ΠΑΝΕΠΙΣΤΗΜΙΟ ΔΥΤΙΚΗΣ ΑΤΤΙΚΗΣ

ΣΧΟΛΗ ΜΗΧΑΝΙΚΩΝ

ΤΜΗΜΑ ΗΛΕΚΤΡΟΛΟΓΩΝ & ΗΛΕΚΤΡΟΝΙΚΩΝ ΜΗΧΑΝΙΚΩΝ

Διπλωματική Εργασία

Μελέτη και προσομοίωση εγκατάστασης ασύρματης φόρτισης οχημάτων σε δυναμική φόρτιση

Φοιτητής: Νικολάου Νικόλαος

ΑΜ: 04418

Επιβλέπων Καθηγητής

Γεώργιος Βόκας

ΑΘΗΝΑ-ΑΙΓΑΛΕΩ, Φεβρουάριος 2024

UNIVERSITY OF WEST ATTICA

FACULTY OF ENGINEERING

DEPARTMENT OF ELECTRICAL & ELECTRONICS ENGINEERING

Diploma Thesis

Study and simulation of wireless vehicle charging installation in dynamic charging

Student: Nikolaou Nikolaos

Registration Number: 04418

Supervisor

Georgios Vokas

ATHENS-EGALEO, February 2024

Η Διπλωματική Εργασία έγινε αποδεκτή και βαθμολογήθηκε από την εξής τριμελή επιτροπή:

Βόκας Γεώργιος Καθηγητής	Ιωαννίδης Γεώργιος Καθηγητής	Καμινάρης Σταύρος Καθηγητής
Georgios Vokas Digitally signed by Georgios Vokas Date: 2024.04.01 14:46:36 +03'00' (Υπογραφή)	Digitally signed by Georgios Ioannidis Date: 2024.04.02 08:58:31 +03'00' (Υπογραφή)	Stavros Kaminaris Digitally signed by Stavros Kaminaris Date: 2024.04.01 16:32:18 +03'00' (Υπογραφή)

ΔΗΛΩΣΗ ΣΥΓΓΡΑΦΕΑ ΔΙΠΛΩΜΑΤΙΚΗΣ ΕΡΓΑΣΙΑΣ

Ο κάτωθι υπογεγραμμένος Νικολάου Νικόλαος του Ορέστη, με αριθμό μητρώου 04418 φοιτητής του Πανεπιστημίου Δυτικής Αττικής της Σχολής ΜΗΧΑΝΙΚΩΝ του Τμήματος ΗΛΕΚΤΡΟΛΟΓΩΝ ΚΑΙ ΗΛΕΚΤΡΟΝΙΚΩΝ ΜΗΧΑΝΙΚΩΝ,

δηλώνω υπεύθυνα ότι:

«Είμαι συγγραφέας αυτής της διπλωματικής εργασίας και ότι κάθε βοήθεια την οποία είχα για την προετοιμασία της είναι πλήρως αναγνωρισμένη και αναφέρεται στην εργασία. Επίσης, οι όποιες πηγές από τις οποίες έκανα χρήση δεδομένων, ιδεών ή λέξεων, είτε ακριβώς είτε παραφρασμένες, αναφέρονται στο σύνολό τους, με πλήρη αναφορά στους συγγραφείς, τον εκδοτικό οίκο ή το περιοδικό, συμπεριλαμβανομένων και των πηγών που ενδεχομένως χρησιμοποιήθηκαν από το διαδίκτυο. Επίσης, βεβαιώνω ότι αυτή η εργασία έχει συγγραφεί από μένα αποκλειστικά και αποτελεί προϊόν πνευματικής ιδιοκτησίας τόσο δικής μου, όσο και του Ιδρύματος. Παράβαση της ανωτέρω ακαδημαϊκής μου ευθύνης αποτελεί ουσιώδη λόγο για την ανάκληση του διπλώματός μου. Επιθυμώ την απαγόρευση πρόσβασης στο πλήρες κείμενο της εργασίας μου μέχρι ……………………… και έπειτα από αίτησή μου στη Βιβλιοθήκη και έγκριση του επιβλέποντος καθηγητή.»

Ο Δηλών

Νικολαου Νικόλαος

Ν.Νικολάου

(Υπογραφή φοιτητή/~~ήτριας~~)

Ευχαριστώ την οικογένεια μου.

Περίληψη

Στη σύγχρονη εποχή, η επιτακτική ανάγκη για τεχνολογίες φιλικές προς το περιβάλλον οδήγησε στην εμφάνιση και τον πολλαπλασιασμό των ηλεκτρικών οχημάτων, σηματοδοτώντας μια παραδείγματική αλλαγή στον τομέα των μεταφορών.Μια σημαντική καινοτομία σε αυτόν τον τομέα είναι η ανάπτυξη ηλεκτρικών οχημάτων ασύρματης φόρτισης, η οποία έχει συγκεντρώσει σημαντική προσοχή για έρευνα και ανάπτυξη. Ο πρωταρχικός στόχος αυτών των καινοτομιών είναι ο μετριασμός των εκπομπών από τα συμβατικά οχήματα, τοποθετώντας τα ηλεκτρικά αυτοκίνητα στο μέλλον των μεταφορών και συμβάλλοντας σε έναν πιο βιώσιμο κόσμο.

Τα ηλεκτρικά αυτοκίνητα κατατάσσονται κυρίως σε δύο κύριες κατηγορίες: υβριδικά και αμιγώς ηλεκτρικά αυτοκίνητα. Τα υβριδικά ηλεκτρικά αυτοκίνητα χρησιμοποιούν ένα συνδυασμό κινητήρων εσωτερικής καύσης και πηγών συνεχούς ρεύματος επί του οχήματος τόσο για την πρόωση όσο και για τη φόρτιση, προσφέροντας μια μεταβατική τεχνολογία προς την πλήρη ηλεκτροκίνηση. Από την άλλη πλευρά, τα αμιγώς ηλεκτροκίνητα οχήματα βασίζονται αποκλειστικά σε εξωτερικές πηγές ενέργειας, καθιστώντας αναγκαία τη χρήση εξειδικευμένων φορτιστών για την αναπλήρωση των μπαταριών τους. Παρά την ευρεία υιοθέτηση της αγώγιμης φόρτισης, η μέθοδος αυτή παρουσιάζει αρκετές προκλήσεις, όπως η ανάγκη για φυσικές συνδέσεις, οι οποίες μπορεί να είναι δυσκίνητες και μη πρακτικές.

Η ασύρματη μεταφορά ενέργειας αναδεικνύεται ως μια πολλά υποσχόμενη λύση, παρουσιάζοντας σημαντικές προόδους στην αποδοτικότητα, στην ανοχή της λανθασμένης ευθυγράμμισης και στους μειωμένους χρόνους φόρτισης. Οι βελτιώσεις αυτές είναι αποτέλεσμα εκτεταμένων προσπαθειών έρευνας και ανάπτυξης, με στόχο να καταστεί η ασύρματη φόρτιση όχι απλώς μια βιώσιμη εναλλακτική λύση, αλλά μια προτιμώμενη μέθοδος για τη φόρτιση των ηλεκτρικών οχημάτων.

Η παρούσα διπλωματική εξετάζει τη τεχνολογία δυναμικής φόρτισης των ηλεκτροκίνητων οχημάτων, αντιμετωπίζοντας την επείγουσα ανάγκη μείωσης των εκπομπών και των αποβλήτων. Η έμφαση δίνεται στην ανάλυση εγκαταστάσεων ασύρματης φόρτισης οχημάτων σε σενάρια δυναμικής φόρτισης, με στόχο την προσομοίωση πραγματικών καταστάσεων για την ολοκληρωμένη κατανόηση και την ανάπτυξη πρακτικών λύσεων. Το θεωρητικό υπόβαθρο που παρέχεται είναι απαραίτητο για την εδραίωση της κατανόησης και τη διασφάλιση της ακρίβειας των αποτελεσμάτων, αποτελώντας το θεμέλιο πάνω στο οποίο μπορούν να οικοδομηθούν πρακτικές εφαρμογές.

Οι προσομοιώσεις παίζουν καθοριστικό ρόλο σε αυτή την έρευνα, στοχεύοντας στην κατανόηση της συμπεριφοράς ενός δυναμικού συστήματος φόρτισης που χρησιμοποιεί την τεχνολογία επαγωγικής μεταφοράς ενέργειας με συντονισμό. Μέσω αυτών των προσομοιώσεων, η διπλωματική εργασία παρέχει πολύτιμες γνώσεις σχετικά με το πώς οι μεταβολές στο διάκενο και την κακή ευθυγράμμιση

επηρεάζουν την απόδοση του συστήματος, θέτοντας τις βάσεις για μελλοντικές εξελίξεις και βελτιστοποιήσεις.

Εν κατακλείδι, η παρούσα διπλωματική εργασία χρησιμεύει ως ολοκληρωμένος οδηγός και ερευνητική βάση για την κατανόηση και την προώθηση της τεχνολογίας των ηλεκτρικών οχημάτων ασύρματης φόρτισης, με ιδιαίτερη έμφαση στη δυναμική φόρτιση. Υπογραμμίζει τη σημασία της συνεχούς καινοτομίας και έρευνας στον τομέα αυτό για την ικανοποίηση των αυξανόμενων απαιτήσεων για βιώσιμες και αποδοτικές λύσεις μεταφορών. Οι συνεχιζόμενες προσπάθειες έρευνας και ανάπτυξης είναι ζωτικής σημασίας για την αντιμετώπιση των υφιστάμενων προκλήσεων, τη βελτίωση των επιδόσεων και της ασφάλειας του συστήματος και τη διασφάλιση της πρακτικής εφαρμογής αυτής της τεχνολογίας σε πραγματικές συνθήκες.

Λέξεις – κλειδιά

Ηλεκτρικά αυτοκίνητα, Ασύρματα συστήματα φόρτισης, Αμοιβάια επαγωγή, Μοντελοποίηση, Προσωμοίωση.

Abstract

In the contemporary era, the imperative for environmentally friendly technologies has led to the advent and proliferation of electric vehicles (EVs), marking a paradigm shift in the transportation sector. A significant innovation in this domain is the development of electric wireless charging vehicles, which has garnered considerable attention for research and development. The overarching aim of these innovations is to mitigate emissions from conventional vehicles, positioning EVs as the future of transportation, and contributing to a more sustainable world.

EVs are predominantly classified into two main categories: hybrid and pure EVs. Hybrid EVs utilize a blend of internal combustion engines and on-board DC sources for both propulsion and charging, offering a transitional technology towards full electrification. Pure EVs, on the other hand, rely solely on external energy sources, necessitating the use of specialized chargers to replenish their batteries. Despite the widespread adoption of conductive charging, this method presents several challenges, including the need for physical connections, which can be cumbersome and impractical.

Contactless power transfer (CPT) emerges as a promising solution, showcasing remarkable advancements in efficiency, misalignment tolerance, and reduced charging times. These improvements are the result of extensive research and development efforts, aiming to make wireless charging not just a viable alternative, but a preferred method for EV charging.

This thesis delves into the dynamic charging technology of EVs, addressing the urgent need to reduce emissions and waste. The focus is on analyzing wireless vehicle charging installations in dynamic charging scenarios, aiming to simulate real-life situations for a comprehensive understanding and the development of practical solutions. The theoretical background provided is essential for solidifying understanding and ensuring accurate results, forming the foundation upon which practical applications can be built.

Simulations play a crucial role in this research, aiming to understand the behavior of a dynamic charging system that utilizes resonant inductive power transfer technology. Through these simulations, the thesis provides valuable insights into how variations in gap and misalignment affect the system's performance, setting the stage for future developments and optimizations.

In conclusion, this thesis serves as a comprehensive guide and research basis for understanding and advancing the technology of electric wireless charging vehicles, with a particular focus on dynamic charging. It underscores the importance of continuous innovation and research in this field to meet the growing demands for sustainable and efficient transportation solutions. The ongoing research and development efforts are crucial for overcoming existing challenges, optimizing system performance and safety, and ensuring the practical implementation of this technology in real-world scenarios.

Keywords

Electric vehicles, Wireless charging systems, Mutual Inductance, Modeling, Simulation.

Table of Contents

List of Figures

List of Abbreviations

Abbreviations	
AC	Alternating current
AGC	automatic gain control
BJT	Bipolar junction transistor
BMS	battery management system
CMOS	complementary metal-oxide-semiconductor
CPT	Contactless power transfer
CWPT	capacitive wireless power transfer
DC	Direct current
DCS	dynamic charging systems
DR	depletion region
EEFF	effective dielectric constant
EMF	electromagnetic field
EMI	electromagnetic interference
EV	Electric Vehicle
FT	ferrite toroid
HBT	heterojunction bipolar transistors
HF	High Frequency
ICNIRP	International Commission on Non-Ionizing Radiation Protection
ID	drain current
IDSS	the greatest JFET current
IGBT	insulated-gate bipolar transistor
IMD	intermodulation distortion
IPT	inductive power transfer
JFET	Junction field-effect transistor
LF	Low Frequency
MGWPT	magnetic gear wireless power transfer
MMIC	monolithic microwave integrated circuit
MOSFET	Metal-oxide-silicon field-effect transistor
PM	permanent magnets
PMA	Power Matters Alliance
PWM	Pulse-width modulation
Q	quality factor
RF	Radio frequency
RIPT	Resonant Inductive Power Transfer
SMD	Surface mount gadget
SOC	State of Charge
SRD	Step-recovery diode
SRF	Self-resonant frequency
VCO	Varactor diode
VDS	drain-to-source voltage
VGS	negative voltage
VHF	very high frequency
VSWR	voltage standing wave ratio
VZ	Zener voltage
WEVCS	wireless electric vehicle charging system

WHO	World Health Organization
WPT	wireless power transfer
XP	Primary winding
XS	Secondary winding

INTRODUCTION

In modern times, the need for technologies that protect the environment is becoming increasingly important. So electric vehicles (EVs) are coming to serve those needs. Continuous research and development have resulted in a key breakthrough that allows power to be delivered without the use of wires, and as a result of this, electric wireless charging vehicles are becoming more and more a subject for research, study and improvement.

The goal is to decrease the emissions caused from conventional vehicles. Bearing that in mind and having increased well-to-wheel efficiency EVs are viewed as the future of transportation. There are many types of electric vehicles. The two main categories are the hybrid EVs and the pure EVs. Hybrid EVs using a small size internal combustion engine for traction and charging the on-board energy sources, as well as on-board DC-sources like batteries. In the other hand pure EVs need to receive energy from the grip through on/off-board chargers in order to charge the batteries.

Batteries and ultra-capacitors can be recharged using conductive or contactless methods with on-board chargers. Wires are used in conductive charging to connect an electric vehicle's charger to the power grid supply. Despite being widely used, conductive charging has drawbacks such as the requirement for connecting wires, galvanic separation for on-board electronics, elevated weight and bulk of chargers, and the matter of safety in wet conditions.

The constraints of contactless power transfer (CPT) have improved as a result of research articles published in recent years, including improvements in power transfer with efficiency, improvements in misalignment tolerance, and reductions in charging time.

Subject of the thesis

The subject of the thesis is the study of EVs and especially the dynamic charging technology of them. The necessity for lowering the emissions and reducing wastes, makes the study of wireless vehicle charging installation in dynamic charging an important and topical issue.

Purpose and objectives

The purpose of the thesis is to analyze the wireless vehicle charging installation in dynamic charging and to simulate as close as a real situation in order to be able to identify if it is possible or not, to create systems like that in the real world.

The objectives of this thesis include

- The creation of a guide in wireless charging technology as well as EVs.
- The correlation between gap, misalignment with efficiency of a power dynamic charging system.

- The creation of a useful model that can be easily adjusted and utilized for simulations in order to optimize the dynamic wireless technology.

Methodology

The initial step was to gather material and understand it. Next, the creation of a theoretical background for a complete understanding of wireless charging systems and electric vehicles. Then a mathematical model and a model in the MATLAB/Simulink environment was created. Last but not least a test was made to ensure the correct operation of the model and any errors were addressed. Finally, the simulations were conducted which led to the conclusions.

Innovation

The thesis serves as a comprehensive guide and research basis for understanding and advancing the technology of electric wireless charging vehicles, with a particular focus on dynamic charging.

Structure

The thesis consists of 6 chapters.

Chapter 1 introduces a theoretical background of basic electrical and electronic engineering that is going to be needed for this thesis.

Chapter 2 presents targeted knowledge on wireless charging systems, methods of charging, the separation of static and dynamic wireless charging as well as some standards for EVs.

Chapter 3 delves into the creation of a dynamic wireless charging model, the theoretical knowledge of the parts that contains.

Chapter 4 presents the simulations and the results.

Chapter 5 analyses each simulation.

Chapter 6 concludes the thesis by reviewing the contributions. Suggestions for future research in this field are stated as well.

1 CHAPTER 1: Theoretical Background

1.1 Overview

Studying projects can be challenging and a theoretical background is necessary in order to remember or learn something valuable, leading to more accurate and solid results. This chapter is going to be the theoretical guide that this project may need.

1.2 Passive Components at RF

Lumped (physical) capacitors, inductors, and resistors are not the "unadulterated" components that are thought to function at lower frequency ranges when operating at radio frequencies. Their real essence at greater frequencies includes unwanted capacitances, inductances and resistances, as can be seen in Fig. 1.1; these should be taken into account while designing, reproducing, and formatting any wireless circuit.

In order to reduce losses caused by lead inductance at frequencies that are considered microwaves, all part drive lengths need to be restricted. Additionally, the board that interfaces such uninvolved parts should be converted into transmission line structures. The typical structure is microstrip, that maintains a 50ohm constant impedance throughout its length without adding inductance or capacitance. "Surface mount devices" (SMDs) are ideally suited for diminishing this lead length, and along these lines the series inductance, of any part (Fig. 1.2).

Given that the part's effective operating frequency rises as its size decreases, it is necessary for all lumped components to have as small of a physical structure as possible as the frequency at which each wireless circuit operates increases. This is because a smaller package reduces harmful distributed reactances as well as parallel or series resonances.

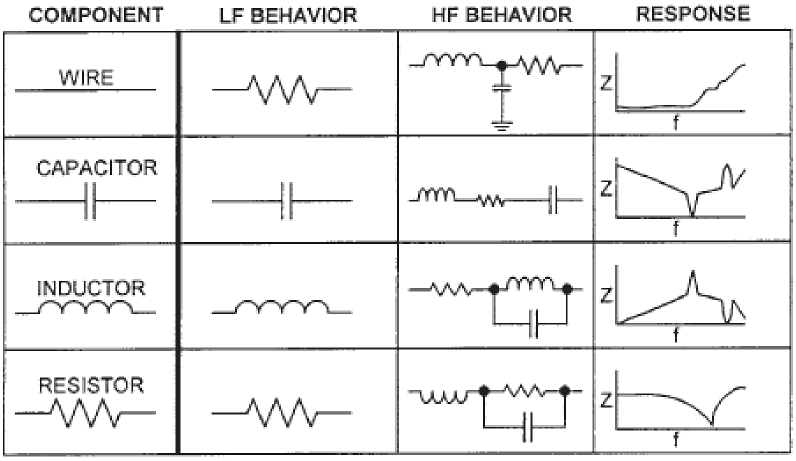

Figure 1.1 The actual behavior of a component at low frequencies (LF) and high frequencies (HF) [1].

(*Cotter W. Sayre, Complete Wireless Design, 2001, page 2*)

Figure 1.2 Resistor mounted on the surface [1].

(*Cotter W. Sayre, Complete Wireless Design, 2001, page 2*)

1.2.1 Resistors

As the frequency of operation is increased, the real value of a resistor will start to decline, as shown in Fig. 1.3. This is due to the dispersed capacitance, which shunts the signal around the component and is always essentially in parallel with the resistor, reducing the resistance's effective value. This dispersed capacitance, as depicted in figure 1.3, becomes increasingly problematic as both the frequency and resistance levels rise. A resistor with a high value might lose a significant amount of the indicated resistance that is shown at relatively low microwave frequencies due to this capacitive effect; if it is not of the high-frequency, thin film variety. Furthermore, the additional reactive effect is insignificant in helping the resistor in keeping its indicated resistance value because the series inductance of the leads of surface mount technology resistors is often fairly low.

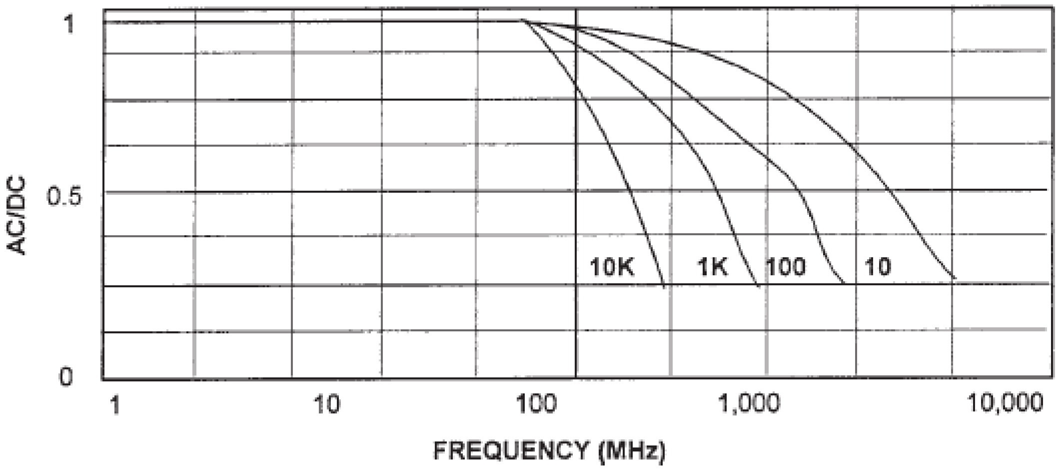

Figure 1.3 DC resistance to AC resistance ratio of an SMD resistor as frequency rises [1].

(*Cotter W. Sayre, Complete Wireless Design, 2001, page 3*)

1.2.2 Capacitors

When choosing capacitors for RF and microwave applications, consideration should be given to both the cost and temperature tolerance of the component as well as its ability to work at such high frequencies appropriately. A capacitor has an unwanted lead inductance, as Fig. 1.1 illustrates, and as the frequency rises, the capacitor's properties start to deteriorate. This impact is generally articulated assuming the lead inductance resounds with the capacitance of the actual capacitor, bringing about a series reverberation or an overall reactance close to 0 ohms (make a capacitor be at resonance mode, may additionally be intended: a capacitor with 0 imaginary part is the kind that creates low impedance which is ideal for coupling and uncoupling at elevated frequencies by bring at resonance its own parasitical inductance along with its own little worth of stamped capacitance at a frequency of interest.). It is crucial to ensure that the circuit's original frequency does not exceed the capacitor's series resonance since the capacitor is going to turn more inductive rather than capacitive over the specified frequency of resonation. It is crucial for coupling and uncoupling capacities, while a capacitor for adjusted circuits ought to have a series resonance easily above its planned frequency. The capacitor is nearer its inductive area the higher its value is, which also decreases the amplitude of this series resonance. As a result, an average larger inductance will be displayed by a greater-value capacitor as opposed to a lower value capacitor. Due to this, a trade-off must be made regarding the capacitor's series resonance and capacitive reactance in coupling operations. To put it another way, assuming the capacitor is selected to function as a j0 type, a coupling capacitor that is predicted to have a capacitive reactance valued at 0.1 ohm at the frequency that matters could in fact be a considerably worse option compared to a capacitor which has a capacitive reactance valued at 5 ohm.

Only specific types of capacitors can operate over real-world temperature variations and at greater frequency ranges while yet retaining an acceptable amount of capacitance tolerance. The different types of capacitors and how they are used in wireless circuits are covered in the sections that come next:

Electrolytic capacitors made of tantalum or aluminum are both used for exceptionally low ranges of frequency coupling and uncoupling purposes. As [1] said: “They have poor equivalent series resistance (ESR) and high DC leakage through the dielectric, and most are polarized. However, they possess a very large amount of capacitance per unit volume, with this value ranging from greater than 22,000 μF down to 1 μF for the aluminum types. Aluminum electrolytics have a limited life span of between 5 to 20 years while tantalums, with their dry internal electrolyte, have a much longer lifetime—and less DC dielectric leakage”. Unluckily, tantalums have a lesser maximum operating voltage rating and a fewer variety of values (in the range of 0.047 ~F and 330 ~F). Metallized film capacitors are frequently employed for low-frequency uncoupling since they are typically effective up to roughly 6 MHz. These capacitors, which come in the polystyrene, metallized paper, polycarbonate, and MylarTM (polyester) families, have capacitance ranging of 10 pF to 10 F. The dielectric layers are able to be finely metallized to create metallized film capacitors. Silver mica capacitors are a more seasoned, less utilized sort of high recurrence capacitor. An older, less common kind of high-frequency capacitor is the silver mica capacitor. They feature a capacitance ranging from 2 to 1500 pF, with a low ESR, and good thermal stability.

Leaded ceramic capacitors are integral components in radio frequency (RF) circuits, functioning effectively up to frequencies as high as 600 MHz. These capacitors manifest in two primary configurations: the single-layer ceramic disk and the multi-layered, monolithic ceramic structure. Their capacitance values span a broad spectrum, ranging from 1.5 picofarads (pF) to 0.047 microfarads (μF). The dielectrics in these capacitors are categorized into three distinct grades, each suited to specific operational requirements.

The first category, COG (NPO), is optimized for applications where temperature stability and precise capacitance values are paramount. These capacitors exhibit superior tolerance, typically 5 percent or better, and offer capacitance values between 10 and 10,000 pF. The second category, as [1] said: "X7R types, with less temperature stability and a poorer tolerance (±10 percent) than COG (with available values of 270 pF to 0.33 μF); and Z5U types, which are typically utilized only for bypass and coupling because of extremely poor capacitance tolerances (±20 percent) and bad temperature stability (with a range of values from 0.001 to 2.2 μF)".

However, in the realm of microwave frequency applications, Surface-Mounted Device (SMD) ceramic and porcelain chip capacitors have become predominant, suitable for RF circuitry up to approximately 15 GHz. Despite their high-quality design for RF and microwave applications, these chip capacitors must maintain relatively low capacitance values to ensure optimal functionality at higher frequencies. This necessity arises from the inherent increase in internal inductance of the capacitor with elevated capacitance values. Typically, a maximum of 10 pF or less is utilized in circuits, contingent on the frequency requirements.

These microwave chip capacitors are available in both multi-layer and single-layer configurations. Multi-layer types are commonly provided in standard SMD packages, whereas single-layer capacitors, due to their non-standard SMD casings, pose more challenges in board mounting. Nevertheless, single-layer capacitors are capable of operating at substantially higher frequencies, potentially reaching tens of GHz, albeit with a reduced capacitance range.

Additionally, certain ceramic and porcelain microwave SMD capacitors incorporate a microstrip ribbon in their structure. This feature facilitates more efficient bonding to the microstrip transmission lines on printed circuit boards, enhancing their integration and performance in complex RF circuitry.

1.2.3 Inductors

In the context of high-frequency applications, inductors often encounter an unintended phenomenon known as distributed capacitance. This capacitance exists in parallel with the inductor's inherent inductance (as illustrated in Fig. 1.1). Consequently, there exists a specific frequency at which the inductor's inductance and the distributed capacitance achieve parallel resonance. This resonance manifests as a pronounced peak in impedance at the resonant frequency. Ideally, this impedance would be infinitely high, barring the presence of minimal wire resistance in series with the inductor.

The frequency at which this resonance occurs is termed the Self-Resonant Frequency (SRF) of the inductor. For effective functionality in a tuned resonant circuit, the SRF must substantially exceed the operational frequency of the circuit, ensuring the maintenance of appropriate impedance levels within the resonant tank circuit. To mitigate the effects of distributed capacitance and thereby elevate the SRF, high-frequency RF inductors are designed with compact form factors. However, this design choice inversely affects the maximum attainable inductance.

As [1] said: "An inductor parameter that is especially important for tuned circuits is the Q, or quality factor, of the inductor. The Q indicates the quality of the inductor at a certain test frequency; Q equals the inductive reactance divided by the combined DC series resistance, core losses, and skin effect of the coil. At low frequencies Q will increase, but at high frequencies the Q of an inductor will begin to decrease as a result of the skin effect raising the resistance of the wire. (Even while this is occurring, the distributed capacitance is also decreasing the desired inductance of the coil. Thus, the Q will soon reach zero, which is the value at its SRF)."

The DC series resistance of the coil, measurable via a standard ohmmeter, represents the intrinsic resistance of the inductor's wire. This resistance not only influences the Q factor (particularly in small, high-value, high-frequency inductors where it can be relatively significant) but also contributes to a notable DC voltage drop across the inductor. This aspect is crucial in applications where excessive DC voltage drop can result in erratic circuit performance due to reduced bias voltages available to the active device.

Finally, high-inductance coils at high frequencies are susceptible to significant losses stemming from the coil form. These losses, encompassing hysteresis, eddy currents, and residual losses, become so pronounced that air-core inductors are often the only viable option. This is due to the minimal loss effects associated with air-core materials compared to other core types.

Design of Inductive Coils: In certain instances, particularly within the scope of small-scale projects or prototypical developments, the requisite specification or variant of an inductor may not be readily accessible. Under such circumstances, it becomes necessary to engage in the design and fabrication of a custom inductor.

When considering the construction of a high-frequency, single-layer air-core coil, typically configured as a helical structure, the determination of the requisite number of coil turns to achieve a specific inductance value can be computed through a designated formula.

$$n = \sqrt{\frac{L[(18d) + (40l)]}{\mathrm{d}}} \tag{1.1}$$

Where n=the quantity of single layer turns needed to achieve the desired inductance (L).

L=desired inductance of the air coil, µh

d=diameter, in inches, of the inside of the coil (the same diameter as the form used to wind the coil)

l=length, in inches, of the coil (if this length is not met after winding the turns, then spread the individual coils outward until this value is reached)

However, it needs be noted that the equation is precise only if the length of the coil is no less than half as long as its diameter, and precision degrades when frequency is raised to a very high frequency (VHF) range and higher. This is a consequence of the conductor thickness's excessive rise with coil diameter. To avoid turn-to-turn shorts, only varnished ("magnet") wire should be used when creating coils.

Toroids are inductors made from ferrite or powdered iron cores that are formed like doughnuts (Fig. 1.4). Ferrite toroidal cores can operate at frequencies as little as 1 kHz and as high as 1 GHz, however the highest frequency that can be achieved with a given toroid depends on the type of ferrite material used in its manufacture. The majority of toroidal designs are low- to medium-power, lower-frequency ones.

Attributable to their minimal magnetic flux leakage and diminished sensitivity to mutual inductance, toroidal inductors are regarded as essential components. In contrast to air-core inductors and transformers, which may necessitate protective measures or alterations to their layout on the printed circuit board (PCB) to prevent electromagnetic interference, the circular geometry of toroidal inductors inherently minimizes the emission of radio frequency interference into adjacent circuits. This characteristic of toroidal inductors enhances their effectiveness, given that nearly all the magnetic flux is contained within the core, facilitating the transfer of energy from the primary winding to the secondary without significant losses.

Additionally, toroidal inductors find applications in the attenuation of low-frequency disruptions caused by transmission systems, effectively preventing the transmission of electromagnetic noise along power conductors into sensitive electronic equipment. By integrating toroidal inductors in a series configuration within power supply lines, a substantial portion of this electromagnetic disturbance is suppressed.

The physical dimensions and material composition of a toroid's core are indicative of its properties. For example, a toroidal core with the designation FT-23-61 suggests that the toroid has a ferrite composition with an exterior diameter of 0.23 inches and utilizes ferrite material denoted by the classification '61'. The designation 'T' typically infers a toroidal shape, as opposed to alternative core geometries.

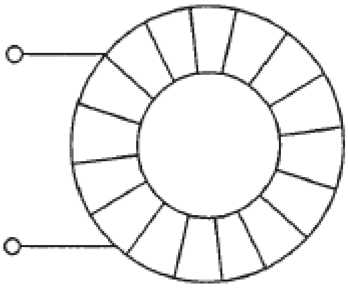

Figure 1.4A toroid core Inductor [1].

(*Cotter W. Sayre, Complete Wireless Design, 2001, page 6*)

Ferrite-based toroidal cores suitable for applications up to 1 GHz are available, with the requisite inductance per turn (A_L) values specified in microhenries (μH) for 100 turns of wire enveloping the core, accessible within the core's technical datasheet. When fabricating a ferrite toroidal inductor or choke, the core dimensions must be chosen to provide sufficient space for the anticipated wire turns.

To determine the precise number of wire turns needed to achieve a given inductance for a ferrite toroidal coil, one may employ the following calculation:

$$N = 100\sqrt{\frac{L}{A_L}} \qquad (1.2)$$

Here N=the quantity of turns of a single-layer coil necessary to procure the target inductance L.

L=inductance desired for the coil, μH

A_L=value, as read on the core’s data sheet, of the chosen size and powdered-iron mix of the core, μH per 100 turns

In the scenario where a ferrite toroidal core is being conceptualized, the engineer would apply the following mathematical expression to compute the necessary turns:

$$N = 1000\sqrt{\frac{L}{A_L}} \tag{1.3}$$

Where N= the count of single-layer windings required

L= the inductance aimed for in millihenries (mH)

A_L= the inductance factor provided in the core's datasheet, which corresponds to the specific core dimensions and ferrite composition, expressed in millihenries per 1000 windings.

Inductive core values, denoted as A_L, typically exhibit a tolerance range of ±20 percent. It is crucial to ensure that the core material does not reach saturation under excessive power conditions, whether from direct or alternating current sources. Fabricating a single-layer toroidal inductor or transformer should be done with a gap of 30 degrees between the start and finish of the winding, as depicted in Fig. 1.5, to curtail distributed capacitance, thereby optimizing the Quality Factor (Q) of the inductor. The composition of the core material is selected to define the upper limit of the operating frequency for the core.

1.2.4 Transformers

RF transformers are frequently bought as complete units, although they can be built in a toroidal shape as well (Fig. 1.6). In low-frequency radio systems, most air cores have been replaced by toroids as interstage transformers (Fig. 1.7).

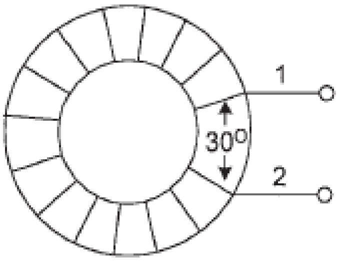

Figure 1.5 Correct methodology for toroidal inductor coil winding [1].

(*Cotter W. Sayre, Complete Wireless Design, 2001, page 8*)

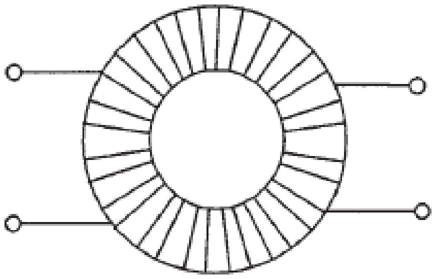

Figure 1.6 Transformer creation utilizing a toroid [1].

(*Cotter W. Sayre, Complete Wireless Design, 2001, page 8*)

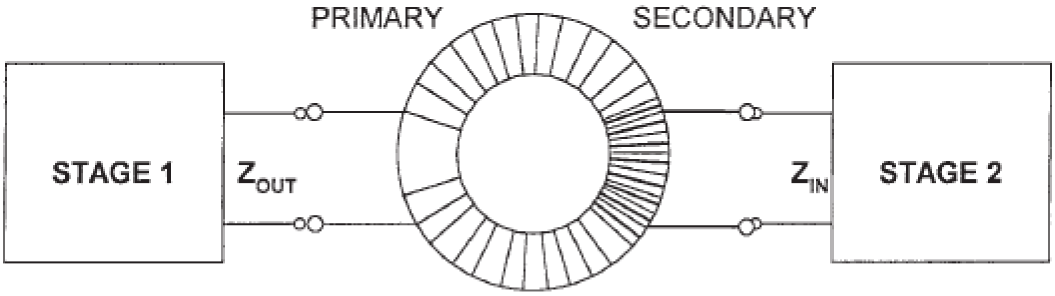

Figure 1.7 Impedance matching with a toroidal transformer [1].

(*Cotter W. Sayre, Complete Wireless Design, 2001, page 8*)

When suitably selected for material properties, toroidal transformers are adept at serving as broadband transformers with operational limits extending to 1 GHz. Yet, the interwinding capacitance becomes increasingly significant as the operational frequency of the broadband transformer ascends. This inherent capacitance acts to diminish the upper frequency limit of the transformer's performance. Mitigation of such effects may be achieved through the utilization of a core with enhanced permeability, facilitating the attainment of the same reactance with fewer windings and consequently reducing distributed capacitance at elevated frequencies.

For toroidal transformers, at the foundational frequency of use, the reactance values of both the primary and secondary windings must surpass the combined reactance of the transformer's source and load by a factor of four or greater. Specifically, the primary winding reactance (Xp) ought to maintain a minimum of 200 ohms, and similarly, the secondary winding reactance (Xs) should uphold 200 ohms at the minimum frequency of operation. For example, with a primary to secondary ratio of 1:1, if a 50-ohm amplifier is connected at the primary and a 50-ohm antenna is linked to the secondary, these conditions should be met.

For the construction of a toroidal transformer, the following procedural steps are advised:

1. Compute the transformer's secondary and primary reactances at the lowest frequency.

$$X_P = 4 \times Z_{OUT} \tag{1.4}$$

$$X_S = 4 \times Z_{IN} \tag{1.5}$$

where X_P = the stipulated primary reactance at the transformer's minimum operational frequency

Z_{OUT} = impedance post the previous stage

X_S = mandated secondary reactance at its minimum frequency

Z_{IN} = impedance before the subsequent stage

2. Proceed to evaluate the inductance of the primary and secondary windings.

$$L_P = \frac{X_P}{2\pi f_{LOW}} \tag{1.6}$$

and

$$L_S = \frac{X_S}{2\pi f_{LOW}} \tag{1.7}$$

3. Select a core with a high permeability, the smallest size possible, and the capacity to function at the desired frequency. Then, determine the number of primary and secondary turns needed.

$$N_S = 100\sqrt{\frac{L_S}{A_L}} \tag{1.8}$$

Or

$$N_S = 1000\sqrt{\frac{L_S}{A_L}} \tag{1.9}$$

$$N_P = N_S\sqrt{\frac{L_P}{L_S}} \tag{1.10}$$

4. Lastly, wrap the toroid with the primary in a single layer. At one end, coil the secondary over the primary winding (Fig. 1.8). Step-up transformer windings should be reversed.

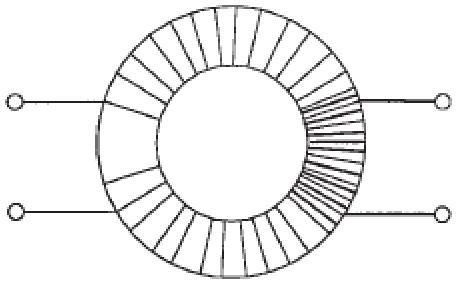

Figure 1.8 Illustration of optimal toroidal transformer winding technique [1].

(*Cotter W. Sayre, Complete Wireless Design, 2001, page 10*)

1.3 Semi-Conductors

1.3.1 Introduction

Semiconductor technology, in contrast to the vacuum tubes used historically, presents compactness, reliability, robustness, and operates with minimal bias voltages. These semiconducting devices are employed for a multitude of functions including the amplification, modulation, and detection of electrical signals, in addition to generating radio frequency (RF) through oscillation. Integral to the functionality of integrated circuits, semiconductors are the cornerstone upon which contemporary wireless apparatuses are built. Presented here is a concise synopsis of the prevalent semiconductor elements.

1.3.2 Diodes

PN junction diodes. The creation of PN junction diodes (Figure 1.9) involves the union of N-type and P-type semiconductor substances. In the N-type region, an abundance of electrons exists as the principal charge carriers, whereas holes, which are the minority carriers, are considerably less prevalent. The process known as doping introduces foreign atoms into the intrinsic semiconductor matrix, resulting in an imbalance of charge carriers: an increase in electrons for N-type and a proportional increase in holes for P-type. This is typically achieved by incorporating pentavalent impurities for N-type and trivalent for P-type, compared to silicon's tetravalent structure.

In this context, the flow of current in P-type semiconductors is predominantly facilitated by the movement of holes, while in N-type semiconductors, it is the electrons that chiefly contribute to conductivity. With zero applied voltage across a diode (Figure1.10), diffusion causes electrons to migrate towards the P-type region, and holes towards the N-type, leading to the formation of a depletion zone at the PN junction, characterized by a scarcity of free charge carriers and the establishment of an electric field.

The inherent electric field within the depletion zone of a silicon-based PN junction typically presents a potential barrier of approximately 0.7 V, which acts to obstruct the free movement of charge carriers, thereby maintaining the equilibrium. Augmenting the majority carrier concentration in this region would be counteracted by the electric field of the potential barrier.

When the diode junction is subject to forward bias, the potential barrier is diminished, facilitating charge carrier recombination and allowing current to flow (Figure 1.11). The positive terminal of the bias repels holes toward the junction, while the negative terminal attracts electrons, culminating in the flow of charge and the establishment of an electric current across the junction.

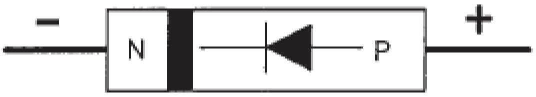

Figure 1.9 Semiconductor diode [1].

(*Cotter W. Sayre, Complete Wireless Design, 2001, page 11*)

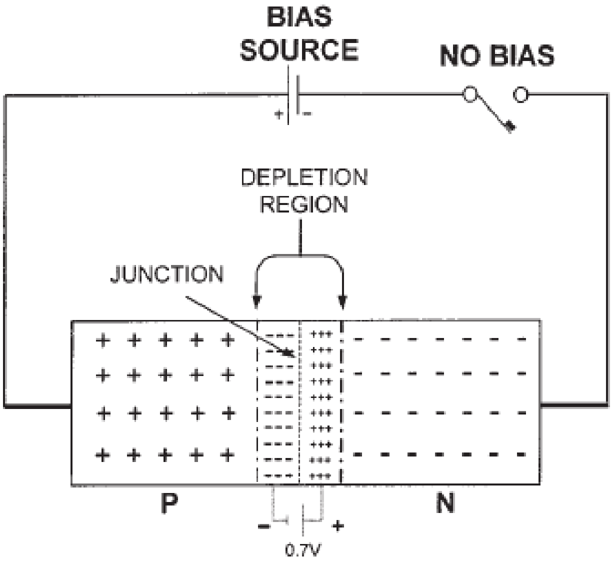

Figure 1.10 A diode in unbiased condition with depletion region [1].

(*Cotter W. Sayre, Complete Wireless Design, 2001, page 11*)

The depletion region will start to grow if a reverse bias is supplied to a diode's terminals, as seen in Figure 1.12. This results from the positive terminal of the battery drawing in electrons while the negative terminal draws in holes, making the diode serve as an extremely high resistance. Only a tiny amount of leakage current will continue to pass through the diode at this point. When breakdown or the barrier potential reaches the bias potential, the depletion region will keep growing until the diode is damaged or destroyed by unchecked reverse current flow.

According to the characteristic curves for a standard silicon diode (Figure. 1.13), no matter how much the forward current increases, a forward-biased silicon will constantly experience a voltage drop of about 0.7 V. diode. This is due to the diode's semiconductor materials' low intrinsic value of dynamic internal resistance.

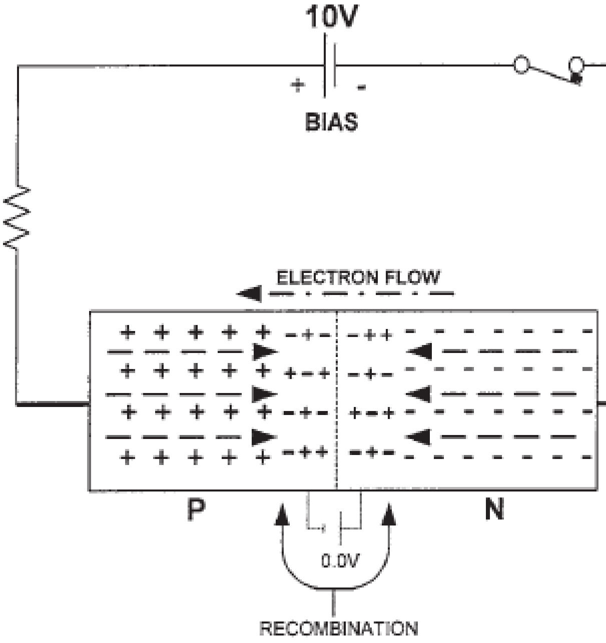

Figure 1.11 Diode conducting under forward bias [1].

(*Cotter W. Sayre, Complete Wireless Design, 2001, page 12*)

For low-current circuits, small diode packages made of plastic and glass (Figure 1.14) are used, whereas power diodes are utilized for large forward currents of up to 1500 A.

Several of the significant rectifier diodes parameters are as follows:

The greatest forward current that a diode may handle before suffering damage to its semiconductor material is known as $I_{F(MAX)}$.

When in reverse bias, a diode's temperature-dependent reverse leakage current (I_R)

The maximum reverse voltage that ought to be applied across a reverse biased diode's terminals is known as PIV.

Zener diodes (Figure 1.15) exploit the capacity of a diode to endure reverse bias through avalanche breakdown without damage. Variations in the current passing through the Zener diode do not affect its voltage drop, making it suitable for voltage regulation in electronic circuits (Figure 1.16). The breakdown voltage of a Zener diode, denoted as Vz, is critical as it specifies the voltage at which it conducts in reverse bias. Each Zener diode, even with the same nominal Vz, may activate at a slightly different voltage due to manufacturing variances, which is why these diodes are available with various tolerance levels, including 20%, 10%, 5%, and 1%.

Temperature fluctuations can alter the voltage ratings of Zener diodes, which is essential for precision circuits. To address this, variants such as temperature-compensated Zener diodes have been developed.

Key specifications of Zener diodes include the following:

- I_{zm}, the maximum current the diode can carry before failure.
- V_z, the Zener voltage that remains constant with varying current levels.
- I_z, the operating current to maintain the diode in its Zener region.
- P_d, the maximum power the diode can dissipate without exceeding its thermal limits.

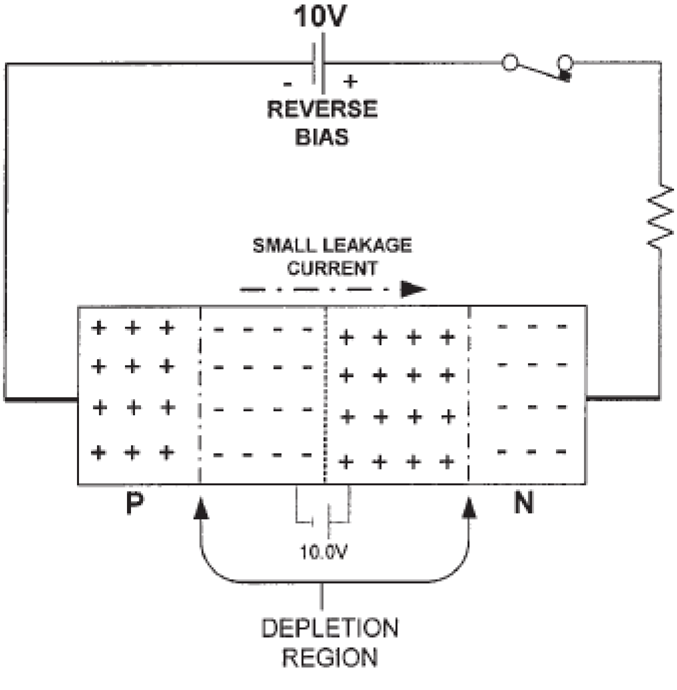

Figure 1.12 Reverse-biased diode showcasing leakage current dynamics. [1].

(*Cotter W. Sayre, Complete Wireless Design, 2001, page 13*)

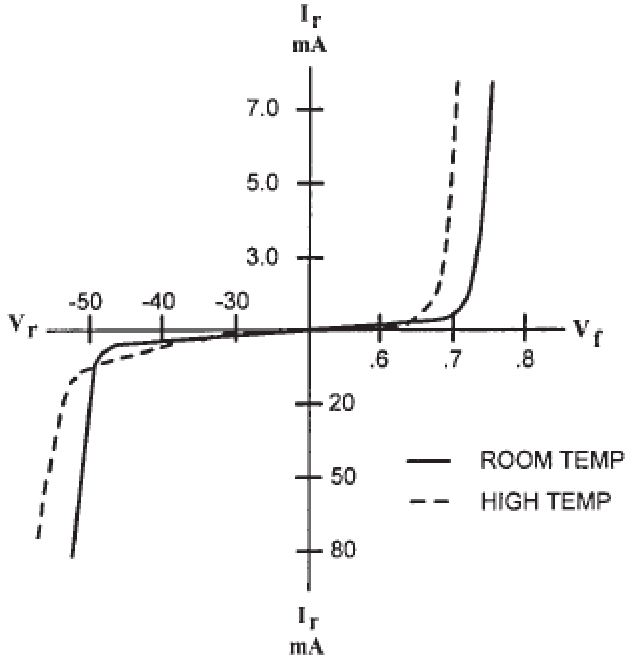

Figure 1.13 Characteristic response curves of a silicon diode [1].

(*Cotter W. Sayre, Complete Wireless Design, 2001, page 13*)

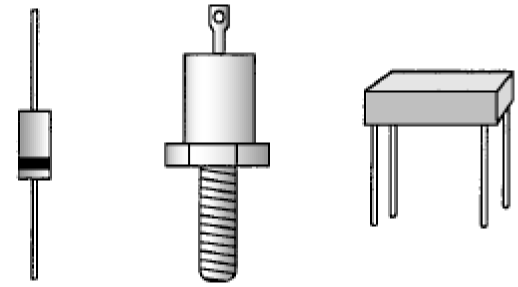

Figure 1.14 Various diode package types: small signal, power, and bridge rectifiers. [1].

(*Cotter W. Sayre, Complete Wireless Design, 2001, page 14*)

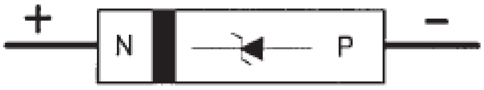

Figure 1.15 Zener diode schematic representation [1].

(*Cotter W. Sayre, Complete Wireless Design, 2001, page 14*)

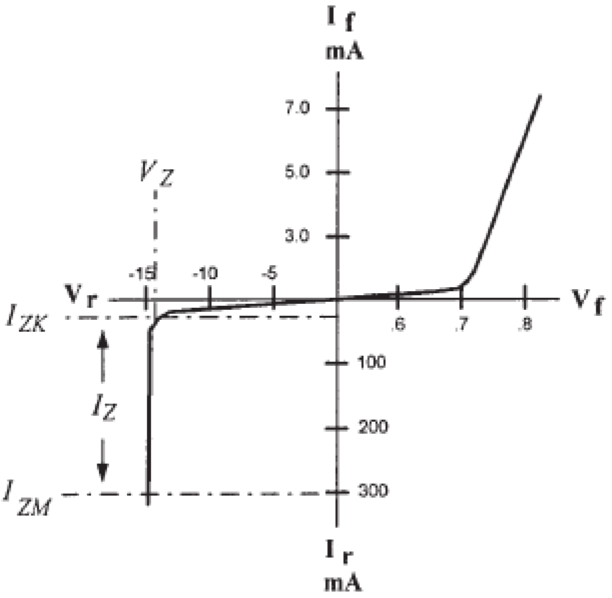

Figure 1.16 Characteristic performance curves of a Zener diode [1].

(*Cotter W. Sayre, Complete Wireless Design, 2001, page 14*)

Varactor diodes. Much like Zener diodes when operated in reverse bias, varactor diodes (Figure 1.17) also exhibit similar behavior. This characteristic can be harnessed beneficially in varactors. It is known that a capacitor's capacitance diminishes with an increase in the dielectric's width. Conversely, a decrease in the width augments the capacitance. In varactor diodes, the depletion zone acts as the dielectric. When reverse bias is applied, this zone becomes broader, which in turn reduces the capacitance as shown in Figure 1.18. Conversely, a decrease in reverse bias will have a direct effect; it narrows the depletion zone and thus enhances the diode's capacitance. In the case of a particular type of varactor, known as the abrupt varactor, these changes in capacitance with respect to reverse voltage can be quite significant. Figure 1.19 illustrates how the capacitance varies in response to the changes in the diode's reverse voltage.

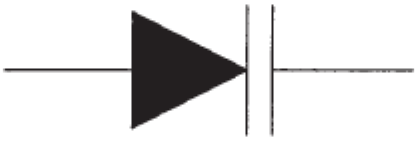

Figure 1.17 Schematic symbol for a varactor diode [1].

(*Cotter W. Sayre, Complete Wireless Design, 2001, page 15*)

Circuits that necessitate a voltage-variable capacitance, like voltage-controlled oscillators and tunable resonant filters, utilize varactors (VCOs). For practically any RF application, they are readily available in a wide range of capacitance values.

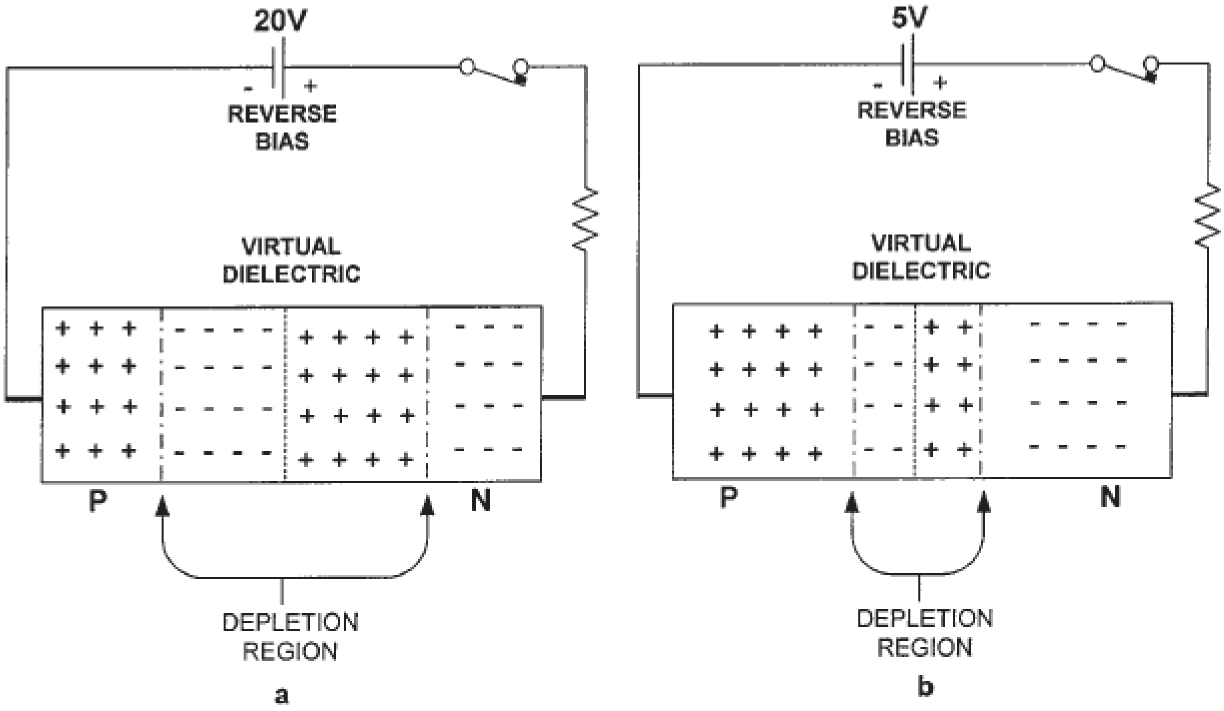

Figure 1.18 The formation of the virtual dielectric in a varactor diode with two different reverse bias voltages: (a) low capacitance; (b) high capacitance [1].

(*Cotter W. Sayre, Complete Wireless Design, 2001, page 15*)

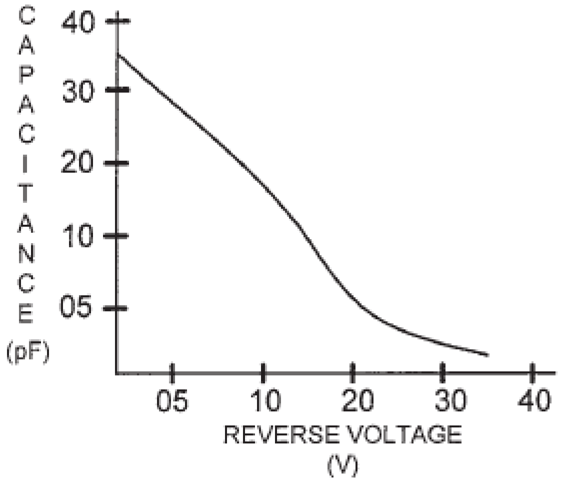

Figure 1.19 Capacitance versus the applied reverse voltage for a varactor diode [1].

(*Cotter W. Sayre, Complete Wireless Design, 2001, page 16*)

PIN diodes incorporate a distinct intrinsic layer situated between a layer doped positively and another doped negatively. These diodes are versatile, serving in roles such as RF signal attenuators and switches. The crucial parameter that determines the operational frequency range of a PIN diode is its carrier lifetime. Below a certain frequency threshold, the PIN diode behaves like a conventional PN junction diode. However, PIN diodes stand out by performing differently than standard PN junction rectifiers when it comes to high-frequency applications (exceeding 50 MHz), where they function more like resistors that are controlled by the current passing through them.

The resistance characteristics of PIN diodes are markedly different from those of typical PN junction rectifiers. They have a variable resistance range that can be finely tuned from approximately 12 ohms to an upper limit reaching tens of kilo-ohms, all controlled via a DC bias current. This bias current is the key to the diode's switching capabilities, allowing it to alternate between a state of minimal resistance (activated) to one of substantial resistance (deactivated). Constant adjustment of this bias current is essential when the PIN diode is employed as an adjustable attenuator, as it does not operate in fixed resistance steps but rather adjusts continuously across the spectrum of its resistance capabilities. The behavior of a PIN diode's resistance in response to varying forward-bias conditions and its impact on RF resistance is graphically depicted in Figure 1.20.

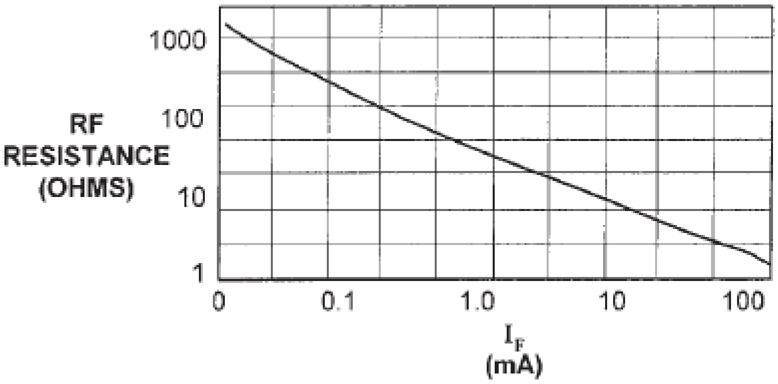

Figure 1.20 PIN diode forward-bias current and RF resistance [1].

(*Cotter W. Sayre, Complete Wireless Design, 2001, page 17*)

Schottky diode. The Schottky diode is made of a metal that is layered on a semiconductor material, causing the development of an electrostatic boundary among the Schottky barrier. Microwave sensors, dual modulators, harmonic oscillators, rectifiers, and mixers all use these diodes. Some Schottky diodes are mechanically robust, have a low forward barrier voltage, and also can operate at frequencies up to 100 GHz.

Zero-bias A sort of diode having a very low forward voltage is a Schottky. Their I-V graphs, which indicate their low forward voltage and the resulting forward current, are shown in Figure 1.21.

Gunn diodes. Within the domain of microwave frequencies, Gunn diodes are capable of functioning as oscillators. These components can achieve oscillation at frequencies surpassing 100 GHz when optimally positioned within a resonant cavity that is compatible. The precise oscillation frequency is contingent upon the duration it takes for an electron to traverse the Gunn diode. As the operational frequency of the Gunn diode rises, the physical thickness of the diode must be reduced, which concurrently limits its ability to dissipate power effectively.

Step-recovery diodes. A unique type of diode utilized in some microwave frequency-multiplication systems is called step-recovery diode (SRD). The SRD performs this purpose by alternating between low and high impedance states. This phase transition might take place in as little as 200 picoseconds, generating a very slight pulse of energy. The best way to understand an SRD is to think of it like a capacitor which retains a charge before rapidly discharging it to produce a pulse rich in harmonics.

1.3.3 Transistors

Bipolar junction transistor (BJT). NPN or PNP doped areas, with NPN being perhaps the most prevalent, make up a bipolar transistor. Charges are provided by the emitter and are controlled by the base. The collector gathers the charges that have not yet reached the base.

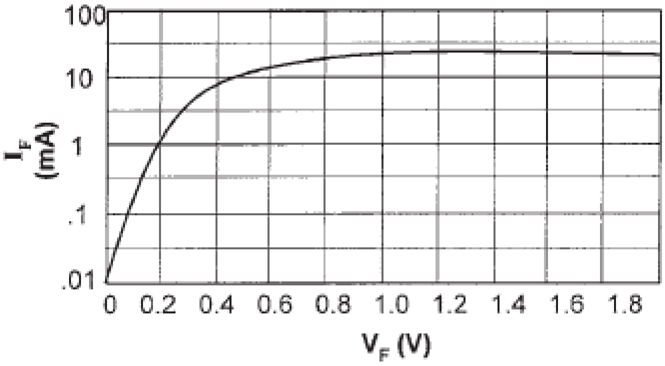

Figure 1.21 Characteristic I-V curves of a Schottky diode under zero-bias [1].

(*Cotter W. Sayre, Complete Wireless Design, 2001, page 18*)

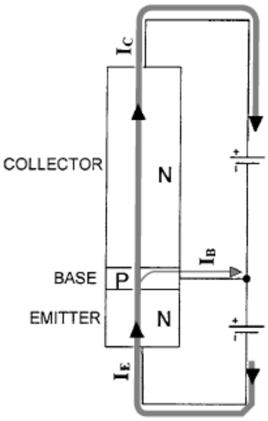

Figure 1.22 The current flow through the emitter, base, and collector of a bipolar NPN transistor [1].

(*Cotter W. Sayre, Complete Wireless Design, 2001, page 18*)

For the foundational design of a basic amplifier, the silicon NPN transistor depicted in Figure 1.22 is configured with its emitter linked to the negative voltage supply and its collector connected to the positive supply, establishing a condition known as reverse bias for the collector. In this architecture, the minimal width of the base region and its limited hole concentration prevent substantial recombination, ensuring the majority of electrons injected from the emitter traverse the base to reach the collector. This mechanism, where over 99 percent of the charge carriers (electrons) injected into the base continue to the collector, results in a negligible base current compared to the emitter and collector currents, a consequence of the transistor's inherent biasing.

Current amplification in a transistor adheres to a proportional relationship, evident from the fact that increases in base current proportionally augment both the emitter and collector currents. This relationship indicates that a minimal increase in base current yields a smaller yet amplified increase in collector current. Amplification occurs when the collector current is directed through an output resistance, generating an amplified voltage.

In a common-emitter transistor configuration, external signals fed into the base-emitter junction encounter minimal resistance, enhancing the admittance of both DC bias and superimposed signal voltages. This is observable in Figure 1.23's graphical representation of the transistor's operational characteristics, showing how the input signal modulates the transistor’s current.

The potential across the transistor's emitter-base junction must surpass approximately 0.6 V for silicon devices before significant current conduction commences. The base bias circuitry is tasked with maintaining this threshold. A semiconductor is capable of amplifying voltages within the active region delineated by the boundaries of saturation and cutoff, offering a finite voltage amplification range.

The operation of a Bipolar Junction Transistor (BJT) can be interpreted as a device where the current regulation is determined by the base current. The low base current modulates the considerably larger emitter-to-collector current, enhancing the output voltage when this collector current is directed through an output load resistance.

Certain high-frequency power transistors may possess intrinsic impedance designed to elevate their ordinarily minimal input and output impedances, which are often as low as 0.5 ohms. Meanwhile, some metal-can transistors are constructed with a quartet of leads, one of which is affixed to the metal enclosure and grounded, functioning as a shield against radio frequency interference.

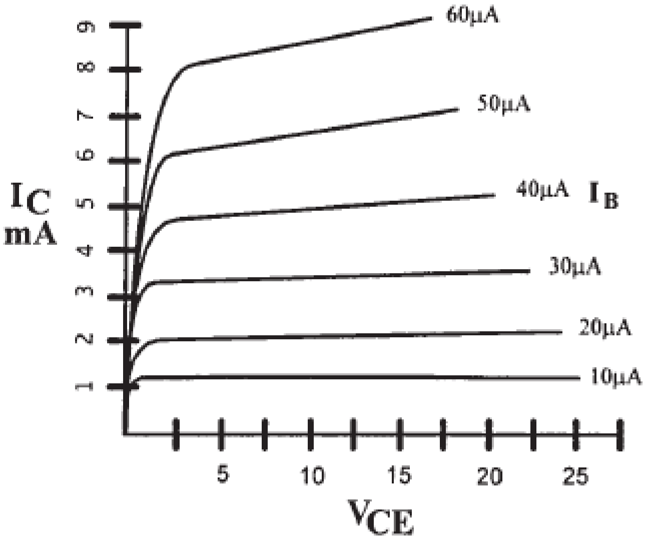

Figure 1.23 The characteristic curves for a bipolar transistor [1].

(*Cotter W. Sayre, Complete Wireless Design, 2001, page 19*)

Listed among the standard specifications for Bipolar Junction Transistors (BJTs) in technical data sheets are:

- The breakdown voltage from collector to base, denoted as $V_{(BR)CBO}$, represents the maximum voltage the collector can withstand from the base before breakdown occurs.
- The absolute maximum power dissipation, P_{DMAX}, is the peak power a transistor can dissipate at a standard ambient temperature of 25°C without incurring damage.
- $T_{J(MAX)}$ indicates the maximum temperature the internal semiconductor junction can sustain before thermal failure.
- The peak allowable collector current is specified as $I_{C(MAX)}$.
- The transition frequency, or f_T, is the frequency at which the transistor operates with a unity gain, also related to the gain-bandwidth product.
- The frequency at which the transistor's current gain drops to 70.7% of its value at low frequencies is termed the beta cutoff frequency, f_β.
- The leakage current, I_{CEO}, is the current that flows from the emitter to the collector when the base is open, and it is contingent on temperature variations.

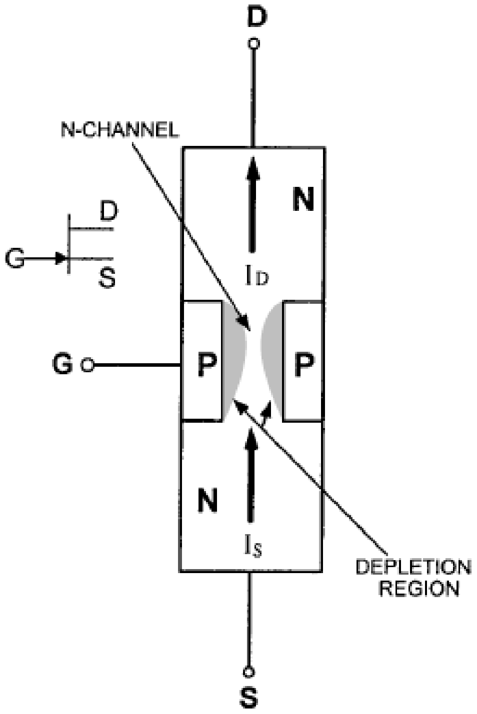

Figure 1.24 Internal structure and current flow in a JFET device [1].

(*Cotter W. Sayre, Complete Wireless Design, 2001, page 21*)

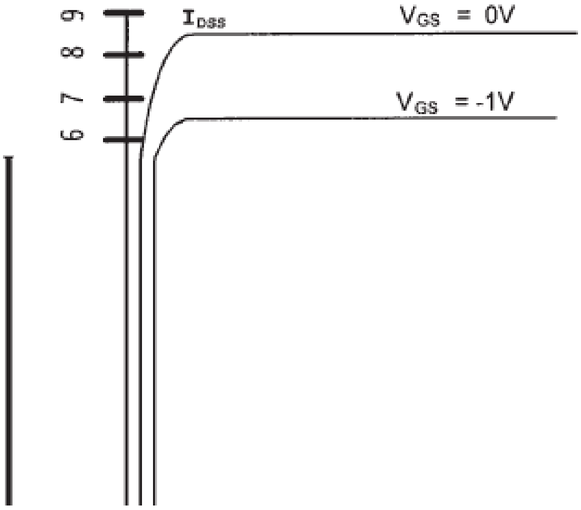

Figure 1.25 Performance curves for a Junction Field-Effect Transistor [1].

(*Cotter W. Sayre, Complete Wireless Design, 2001, page 21*)

Junction field-effect transistor (JFET). The input gates of a JFET have an extremely high low-frequency input resistance because they are constantly reverse biased, making them voltage regulated. Although they produce less inner noise than a BJT and can tolerate inputs of up to several volts (as opposed to a bipolar transistor's few tenths of a volt), junction field-effect transistors exhibit lesser voltage gain and also more signal distortions.

A JFET's structure is comprised of a gate, a source, and a drain, as seen in Fig. 1.24. The drain-to-source voltage (VDS) of the JFET leads the source to be more negative than the drain due to the voltage biasing of the terminals. This enables the drain current (ID) to pass via the N channel from source to drain.

In the absence of a bias voltage at the gate, a JFET is normally on device, as shown by the JFET curves in Fig. 1.25. By doing so, the greatest JFET current (IDSS) is able to pass from the source towards the drain. The depletion region (DR) begins to form inside the N channel of the JFET when a negative voltage (VGS) is applied to the gate and source. As a result of this N channel depletion region's insulating properties, the N channel continues to narrow even as the JFET becomes more and more reverse biased and depleted of all available charge carriers. As the resistance of the channel increases, the JFET's output current through its load resistor decreases, lowering the output voltage of the device across this resistor. As [1] said: "As the negative gate voltage of _V_{GS} is increased, the depletion region continues to widen, decreasing current flow even further— but a point is ultimately reached where the channel is totally depleted of all majority carriers, and no more current flow is possible. The voltage at which the current flow stops is referred to as $V_{GS(\mathrm{OFF})}$. In short, the V_{GS} successfully controls the JFET's channel resistance, and thus its drain current. However, it is important that the drain-to-source voltage V_{DS} should be of a high enough amplitude to allow the JFET to operate within its linear region, or above *pinch-off* (V_P). Pinch-off is simply an area where the drain current will stay constant even if the drain-to-source voltage is increased; now only the gate-to-source voltage can affect the drain current.

A few of the more common JFET parameters are:|"

I_{DSS}, the maximum JFET drain current possible (with a VGS at 0 V)

g_m or g_{fs}, the transconductance gain (or ID/ VGS), measured in siemens or mhos

$V_{DS(MAX)}$, the maximum safe drain-to-source voltage

V_P, the pinch-off voltage, the minimum VDS required for the JFET's linear

operation

P_D, the JFET's maximum power dissipation rating

Metal-Oxide-Semiconductor Field-Effect Transistors (MOSFETs) are fabricated from metal-oxide and silicon and feature a gate architecture insulated from the drain, source, and channel, yielding an active component with an exceptionally high DC input impedance. Nevertheless, the input impedance is not limitless due to the operational characteristics determined by the device's configuration.

Within MOSFET technology, two operational states exist: the enhancement mode, where the device is normally non-conducting, and the depletion mode, in which the device is typically conducting. Voltage application at the gate of an N-channel MOSFET in depletion mode modulates the drain current (Figure 1.26), (Figure 1.27). Incrementing the negative voltage at the gate of the MOSFET to a more positive direction induces a state where no significant drain current exists due to the absence of charge carriers. However, as the gate-to-source voltage (VGS) moves toward a more positive value, the conduction process commences. Unlike Junction Field-Effect Transistors (JFETs), an N-channel MOSFET's drain current continues to increase with a positive VGS and does not peak at zero voltage. The flow of charge carriers at maximum positive VGS results in the maximum drain current.

Depletion MOSFETs are preferred in applications that demand low noise production, such as wireless communications. An example is the dual-gate MOSFET (Figure 1.28), which incorporates two gates within a single device architecture and is often utilized in Automatic Gain Control (AGC) amplifiers and mixers due to its ability to manage the drain current with precision.

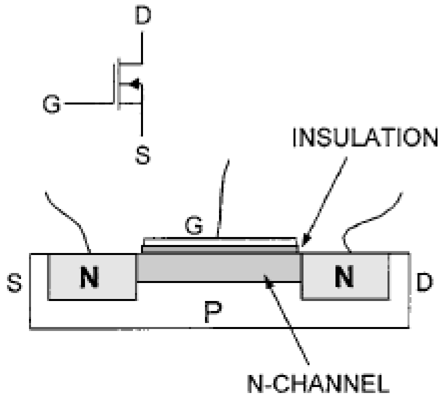

Figure 1.26 Cross-sectional view of an N-channel depletion-mode MOSFET [1].

(*Cotter W. Sayre, Complete Wireless Design, 2001, page 23*)

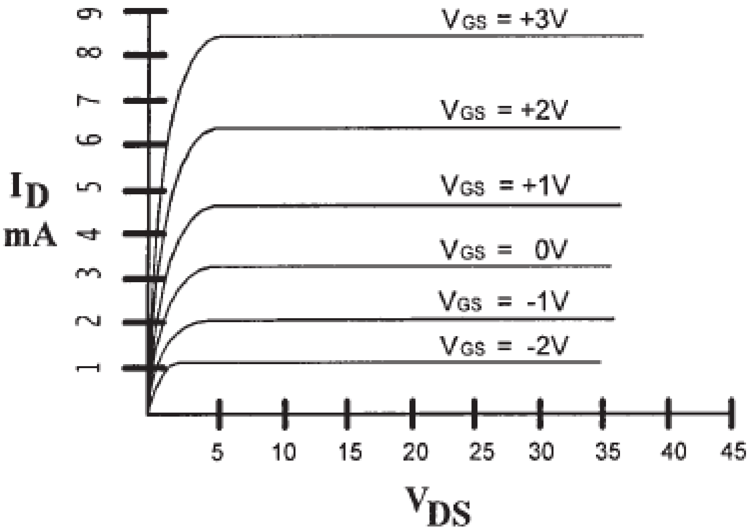

Figure 1.27 The characteristic curves of an N-channel depletion-mode MOSFET [1].

(*Cotter W. Sayre, Complete Wireless Design, 2001, page 23*)

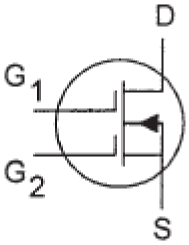

Figure 1.28 Symbolic representation of a dual-gate MOSFET [1].

(*Cotter W. Sayre, Complete Wireless Design, 2001, page 23*)

As previously indicated, the enhancement-mode kind of MOSFET, also known as the E-MOSFET (Figure 1.29) is a typically off transistor. Therefore, as illustrated by the characteristics of Fig. 1.30, essentially no source-to-drain current is flowing since there is no bias across the E-gate. MOSFET's However, nearly any positive voltage applied across the gate will result in the creation of a channel connecting the source and drain of the device (Figure. 1.31). An N-channel is thus formed inside the P-type substrate as electrons are drawn to the gate. This causes an ongoing current flow by allowing electrons to move constantly in the direction of the positively charged drain.

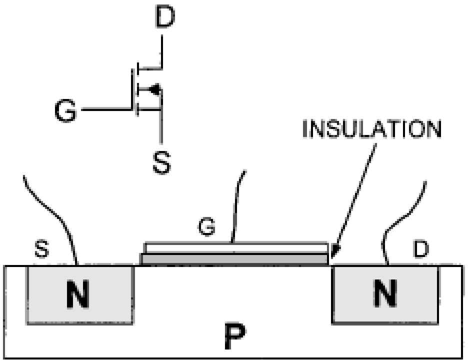

Figure 1.29 The internal structure of an enhancement mode MOSFET [1].

(*Cotter W. Sayre, Complete Wireless Design, 2001, page 24*)

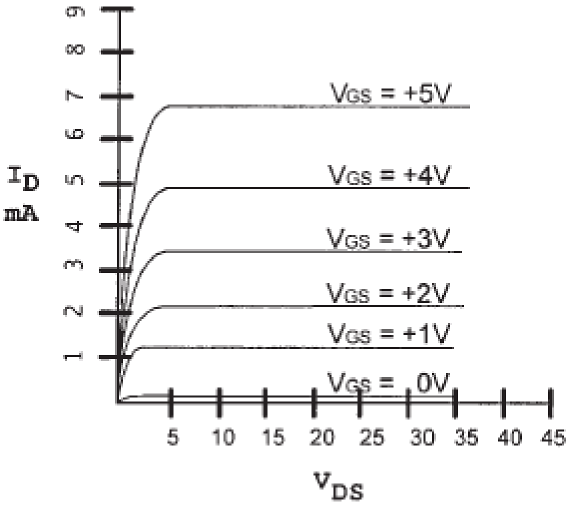

Figure 1.30 The characteristic curves of an enhancement-mode MOSFET [1].

(*Cotter W. Sayre, Complete Wireless Design, 2001, page 24*)

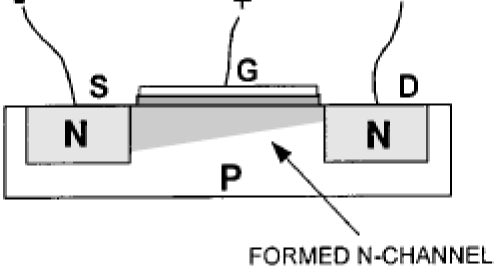

Figure 1.31 The formation of the N channel in an E-MOSFET's substrate by a positive gate voltage [1].

(*Cotter W. Sayre, Complete Wireless Design, 2001, page 24*)

Nevertheless, a 1-V gate threshold voltage must be reached before any appreciable drain current can flow in enhancement-mode MOSFETs. In order to maximize gain and output power, enhancement mode MOSFET power devices actually need to apply a positive gate bias to pass through this gate threshold voltage. Due to this bias requirement, an E-MOSFET cannot operate as a Class C power amplifier by simply applying a zero gate bias to its input, unlike a BJT.

Enhancement-mode MOSFETs are integral to digital integrated circuitry, functioning as voltage-controlled devices within power amplifiers across a spectrum of frequencies, encompassing high, very high, and extremely high-frequency domains. Their superior performance compared to traditional BJTs is attributed to their more favorable gate-driven input impedance, enhanced power-handling capabilities, and a greater resilience against deviations in load impedance. Additionally, MOSFETs inherently have a positive temperature coefficient at elevated current levels, which mitigates the risk of thermal runaway—a scenario where increased temperature leads to a self-sustaining increase in current. This characteristic obviates the potential for a MOSFET to succumb to thermal runaway, consequently reducing the need for additional temperature control mechanisms. MOSFETs also exhibit a higher intrinsic gain per stage compared to BJTs and present a relatively consistent input impedance across a range of input drive levels. However, they can be susceptible to damage under high-stress conditions, such as when exposed to static discharge.

N-channel MOSFETs, frequently employed in radio frequency (RF) applications, and particularly those operating in Class B and Class C amplifiers, exhibit a reduction in gain at lower frequencies—a phenomenon not typically seen in depletion-mode power MOSFETs. Additionally, when compared to BJTs, MOSFETs may demonstrate suboptimal performance regarding intermodulation distortion (IMD) when the devices are driven in parallel configurations.

SiGe BiCMOS technology combines silicon-germanium (SiGe) with complementary metal-oxide-semiconductor (CMOS) technology. The synergy of SiGe with CMOS underpins the functionality of SiGe BiCMOS.

Silicon-germanium heterojunction bipolar transistors (SiGe HBTs) merge silicon (Si) with germanium (Ge) to create devices that can operate at considerably higher frequencies due to their increased gain bandwidth product. This results in a higher operating frequency threshold compared to standard silicon-based transistors. Despite a slight reduction in noise performance and a minor compromise in reliability, SiGe HBTs are expected to see improvements in these areas in the near future.

The capabilities of Gallium Arsenide (GaAs) in facilitating high-frequency operations are now achievable with Silicon-Germanium (SiGe) technology at a cost reduction, estimated to be a fraction of that associated with GaAs fabrication. SiGe also benefits from less complex manufacturing processes and improved yields compared to GaAs. There is a consensus among several industry analyses that for frequencies below 60 GHz, SiGe may eventually supplant GaAs entirely.

The integration of microwave RF front-end components alongside baseband and intermediate-frequency (IF) processing on a single chip is now feasible, thanks to advancements in CMOS and SiGe technologies. This integration paves the way for more cost-efficient semiconductor devices.

Manufacturing costs and component counts for mass-produced electronics such as smartphones, direct-conversion receivers, GPS devices, wireless local area networks (LANs), and other systems with integrated high-volume circuits are projected to decrease significantly.

The strategic significance of SiGe BiCMOS technology has prompted numerous prominent firms to invest in proprietary foundry licenses from IBM for its development and implementation.

The initial offerings, which include lower-density components that are poised to replace GaAs-based devices, are presently available. The prospect of higher-integration devices, which will serve as the core technology in widespread mobile communications, promises future enhancements in cost-effectiveness and operational efficiency for wireless networks.

The initial goods, which are small-density components aimed to replace GaAs devices, are currently becoming available. Higher-integration devices, with cellular phones as the main market, will inevitably be developed, lowering cost and raising efficiency in many high-volume wireless networks.

1.4 Micro strip

1.4.1 Introduction

Microstrip technology, as illustrated in Figure 1.32, serves a variety of roles, including acting as transmission lines, substituting for passive components, tuning electrical circuits, and functioning as filters with high quality factors for microwave frequencies on printed circuit boards. High-frequency surface-mount components such as capacitors, resistors, and transistors can be affixed directly onto the printed circuit board’s microstrip layer, which is typically comprised of copper or gold, due to the microstrip’s characteristic low attenuation and the straightforward nature of its application.

Since microstrip is an unshielded, unbalanced transmission line, it can emit RF radiation. The radiation produced by a correctly ended microstrip is, nevertheless, fairly minimal. Similar to microstrip, stripline (Fig. 1.33) is installed between a PCB's metallization layers and doesn't radiate due of its balanced twin ground planes. The printed circuit board substrate for microstrip and stripline is typically made of Teflon, polystyrene, or fiberglass. Microstrip is simpler and less expensive to produce than stripline since it can be made using regular PCB manufacturing methods.

Low-impedance microstrip lines are wide, while high-impedance microstrip lines are narrow. The conductor width, dielectric thickness, and dielectric constant all influence the characteristic impedance of microstrip. The fact that the impedance of microstrip does not vary with frequency or line length, however, is its most crucial feature. Microstrip and stripline are designed with characteristic impedances that range from 10 to 100 ohms, with 50 ohms being the typical value for transmission line application. In frequencies of functioning at 150 MHz and above, microstrip is particularly prevalent.

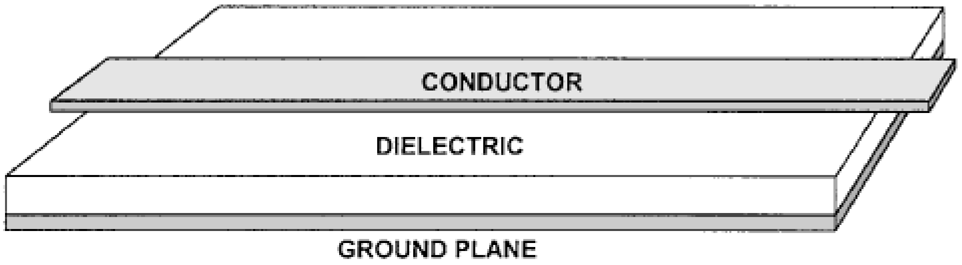

Figure 1.32 Microstrip, showing the dielectric and conductive layers [1].

(*Cotter W. Sayre, Complete Wireless Design, 2001, page 26*)

Figure 1.33 Stripline, showing the dielectric and conductive layers [1].

(*Cotter W. Sayre, Complete Wireless Design, 2001, page 27*)

1.4.2 Microstrip as transmission line

In microwave circuitry, the use of microstrip lines with a characteristic impedance of fifty ohms, and a specified nominal width, is a standard practice to obviate the presence of inductive or capacitive effects along its length. This design consideration ensures the minimization of signal reflection and impedance mismatch losses between discrete circuit elements. Matched impedance conditions between the microstrip and the connected sources and loads ensure that power dissipation occurs primarily through resistive losses rather than reflected energy.

The effective permittivity encountered by a microstrip line deviates from the substrate's relative permittivity due to dielectric flux leakage into the material and surrounding airspace, resulting in a perceived dielectric constant that is a hybrid of the two environments.

To diminish electromagnetic interference and crosstalk, transmission lines on a PCB should be separated by a distance of no less than twice the line width and should be routed to avoid parallel runs. Implementing a ground trace between closely run microstrip lines can further mitigate the likelihood of signal interference. Design strategies also call for the avoidance of impedance discontinuities and the reduction of electromagnetic radiation, which can be induced by abrupt changes or discontinuities in the microstrip path.

Furthermore, when designing microwave circuits with microstrip lines, it is imperative to consider the waveguide effect. Protective metal enclosures for microstrip lines or their associated circuitry should be designed to prevent unintended waveguide behavior, which could significantly alter signal characteristics. The strategic design can overcome these issues, ensuring the integrity of the microstrip's function.

Microstrip transmission line design. To acquire the desired impedance, input several microstrip widths into the following equation.

$$Z_0 = \frac{377}{\left(\frac{w}{h} + 1\right)\sqrt{E_r + \sqrt{E_r}}} \tag{1.11}$$

where Z_0 = typical microstrip impedance, in ohms

W = the microstrip conductor's width (use same units as h)

h = a substrate's thickness between the ground plane and the microstrip conductor (use same units as W)

E_r = board material's dielectric constant

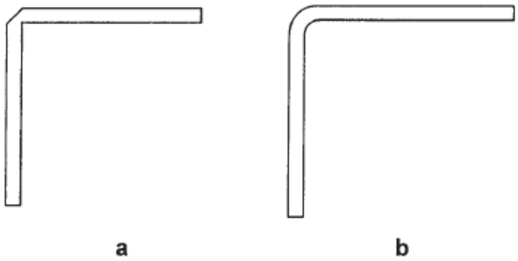

Figure 1.34 Guidelines for managing bends in microstrip lines: (a) mitered bend; (b) curved bend [1].

(*Cotter W. Sayre, Complete Wireless Design, 2001, page 28*)

1.4.3 Microstrip as equivalent components

At microwave frequencies, microstrip transmission line sections on PCBs can be combined to create distributed components like inductors, transformers, and capacitors. A thin trace can be used to create a series or shunt inductor, a large trace can create a shunt capacitor, and changing the size of the microstrip can create a transformer (Fig. 1.37).

Distributed equivalent component design. The comparable component effect will gradually deviate from that of an ideal lumped component if a distributed component is made more than 30 degrees out of the 360 degrees of total wavelength. Simply divide 30 by 360 to find the distance between 30 degrees and 360 degrees. Then, multiply this result by the signal's actual wavelength on the PCB, bearing in mind that the wavelength of the signal on the substrate will differ from its wavelength if it were going through a vacuum.

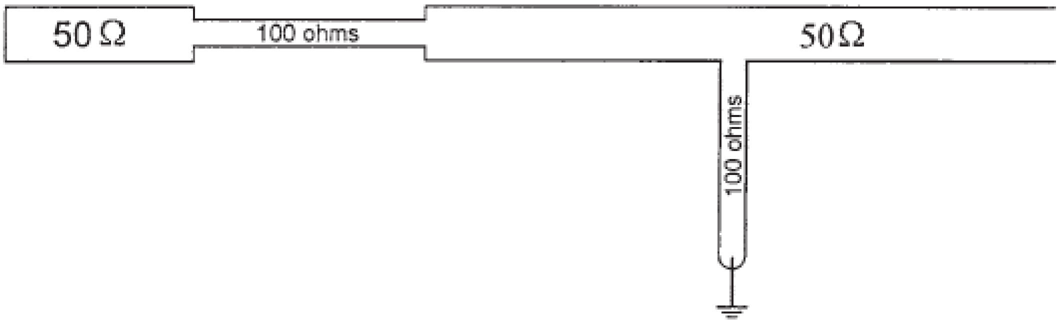

Figure 1.35 A distributed inductor [1].

(*Cotter W. Sayre, Complete Wireless Design, 2001, page 29*)

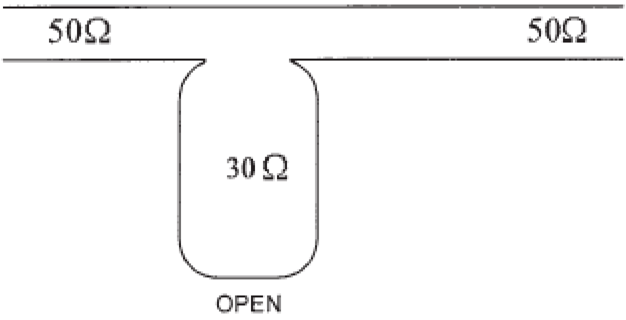

Figure 1.36 A distributed capacitor [1].

(*Cotter W. Sayre, Complete Wireless Design, 2001, page 29*)

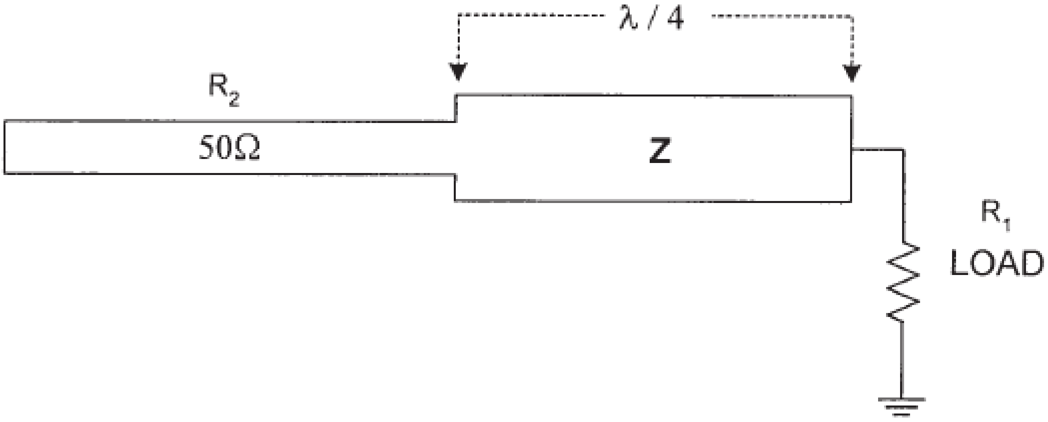

Figure 1.37 Application of a distributed transformer for resistive load matching [1].

(*Cotter W. Sayre, Complete Wireless Design, 2001, page 29*)

To determine the velocity at which a signal propagates along a microstrip line, one must consider the actual wavelength in the medium, which is subject to reduction by the microstrip's substrate material, known as the velocity factor (V_P). Given that the signal traverses both the dielectric of the microstrip and the air above it, the effective dielectric constant (E_{EFF}) must be computed to ascertain the signal's velocity:

$$E_{EFF} = \frac{E_r + 1}{2} + \left(\frac{E_r - 1}{2} \cdot \frac{1}{\sqrt{1 + \frac{12h}{W}}} \right) \tag{1.12}$$

In this expression:

- E_{EFF} is the perceived dielectric constant by the microstrip.
- E_r is the actual dielectric constant of the substrate material on which the microstrip is fabricated.
- h represents the height of the substrate separating the microstrip's top conductor from the ground plane.
- W is the width of the microstrip's conductive trace.

Then:

$$V_P = \frac{1}{\sqrt{E_{EFF}}} \tag{1.13}$$

Here, V_p is the fraction of the speed of light in a vacuum that the signal attains.

The wavelength of the desired signal in a vacuum can then be calculated accordingly.

$$\lambda_{VAC} = \frac{11,800}{f} \tag{1.14}$$

The constant 11,800 is utilized to convert frequency in gigahertz to wavelength in mils, where the speed of light in a vacuum is factored in. To ascertain the wavelength in mils for a signal traversing the microstrip, one multiplies the phase velocity (V_p) by the wavelength in a vacuum (λ_{vac}):

$$\lambda = V_p \times \lambda_{VAC} \tag{1.15}$$

For the design of distributed parallel (shunt) capacitors, the reactive impedance (X_c) can be determined by the standard formula:

$$X_c = \frac{1}{2\pi f C} \tag{1.16}$$

When considering a 30-ohm microstrip impedance, specific calculations are needed to ascertain the appropriate width of the microstrip for this characteristic impedance. Utilizing online calculation tools or appropriate formulas will yield the necessary dimensions for the microstrip.

To enhance the transmission line's performance, a shunt capacitor, which is designed to have an ungrounded open end, may be connected in parallel to a 50-ohm microstrip line through a small interconnecting section. Optimally, dividing the capacitor and positioning each half on opposite sides of the transmission line can further improve performance.

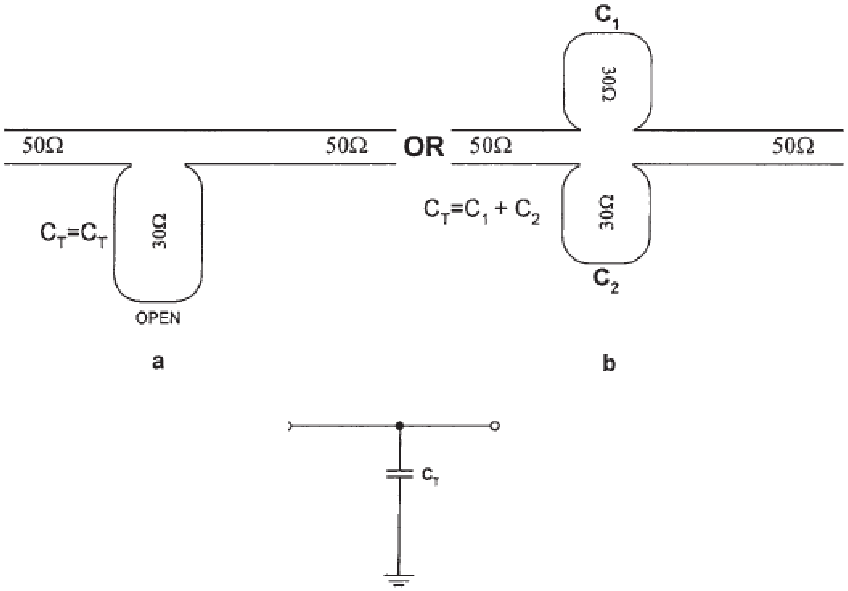

Figure 1.38 Configurations of a distributed capacitor: (a) single unit; (b) dual unit equivalent; (c) lumped element equivalent [1].

(Cotter W. Sayre, Complete Wireless Design, 2001, page 31)

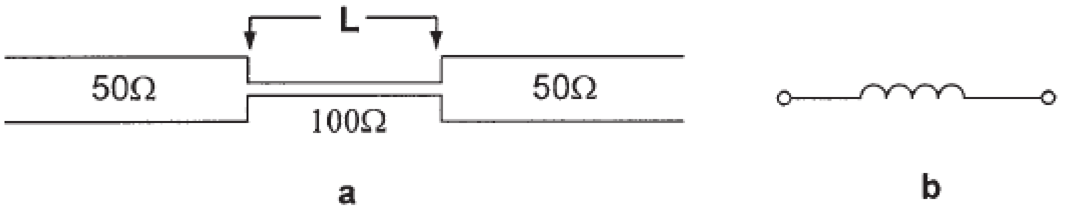

Figure 1.39 (a) A series distributed inductor; (b) equivalent lumped circuit [1].

(*Cotter W. Sayre, Complete Wireless Design, 2001, page 32*)

Third, use the following formula to determine the length of microstrip necessary to create a capacitor with the value X c, as found above:

$$\frac{Arctan\ \frac{30}{X_c}}{360} \times \lambda = Length \tag{1.17}$$

where Xc = Required capacitive reactance in the distributed circuit, expressed in ohms

Length = microstrip Length in mils needed to simulate a lumped component of value Xc (never to exceed 30 degrees, or 12 percent of λ)

λ= wavelength of the desired frequency for the desired substrate (or$V_p \times \lambda$; see formulas above), in mils

Series inductor. The analogous series inductor is positioned between other distributed or lumped components, as depicted in Fig. 1.39, or in series with the 50-ohm microstrip transmission line.

First, using the standard formula, compute the reactance at the frequency of interest while knowing the inductance that the distributed inductor must have.

$$X_L = 2\pi f L \tag{1.18}$$

Second, the substrate's used dielectric should be 100-ohm microstrip (Z_L 100 ohms). Utilize one of the various microstrip calculation tools that are freely available online, or use the microstrip formula above to calculate the microstrip width necessary for this 100-ohm value.

Third, determine how long a microstrip must be to function as an X_L inductor:

$$\frac{Arctan\ \frac{30}{X_L}}{360} \times \lambda = length \tag{1.19}$$

where X_L =Required capacitive reactance in the distributed circuit, expressed in ohms length = microstrip length in mils needed to simulate a lumped component of value X_L (never to exceed 30 degrees, or 12 percent of λ)

λ= wavelength of the desired frequency for the desired substrate (or$V_p \times \lambda$; see formulas above), in mils

Parallel (shunt) inductor. A through connects the equivalent shunt inductor's grounded end (also known as a grounded stub) to the PCB's ground plane, as depicted in Fig. 1.40. A distributed equivalent capacitor to ground can also be used to RF ground it, as will be demonstrated.

First, using the following formula to get the shunt inductor's reactance at the frequency of interest given the necessary inductance for the circuit:

$$X_L = 2\pi f L \tag{1.20}$$

Second, the substrate's dielectric should be 100-ohm microstrip (Z_L = 100 ohms). Utilizing one of the various microstrip calculation tools that are freely available online or by using the microstrip equation previously mentioned, compute the microstrip width necessary for this 100-ohm value.

Third, determine the length of the microstrip needed to convert it into an inductor with the value X_L.

$$\frac{Arctan\,\frac{X_L}{100}}{360} \times \lambda = Length \tag{1.21}$$

Where X_L =Required capacitive reactance in the distributed circuit, expressed in ohms

Length = microstrip Length in mils needed to simulate a lumped component of value X_L (never to exceed 30 degrees, or 12 percent of λ)

λ= wavelength of the desired frequency for the desired substrate (or$V_p \times \lambda$; see formulas above), in mils

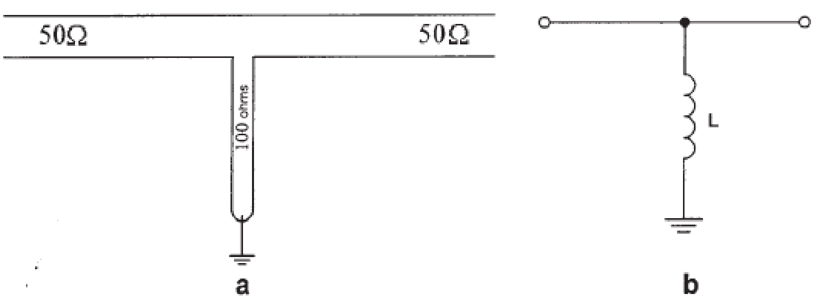

Figure 1.40 (a) A shunt distributed inductor; (b) equivalent lumped circuit [1].

(*Cotter W. Sayre, Complete Wireless Design, 2001, page 29*)

Choke. Distributed choke is designed to provide RF grounding by connecting to the ground through a via or through a distributed or lumped capacitor (Figure 1.41), (Figure 1.42). The width of the choke on the substrate matches that of a microstrip line designed to have a 100-ohm impedance, which corresponds to the microstrip's impedance characteristics rather than a choke's equivalent inductance value. Accurate microstrip dimensions for this specific impedance can be obtained by leveraging computational tools available online or by applying empirical formulas tailored for microstrip design. The physical length of the distributed choke is engineered to be one-quarter of the wavelength $({}^{\lambda}/_{4})$ at the operating frequency, resulting in an electrical length of 90 degrees. When integrated into a distributed circuit at precisely ${}^{\lambda}/_{4}$, the choke behaves as an open circuit at its resonant frequency.

Furthermore, this methodology can be adapted to create an equivalent choke in the bias decoupling circuits. Such a choke, demonstrated in the associated figure, utilizes the quarter-wavelength principle to act as a low-impedance path to ground for RF while providing decoupling for DC biases. The choke's widened structure is instrumental in reducing its impedance, allowing it to act effectively as a shorted stub at the quarter-wavelength, thereby ensuring RF grounding and DC decoupling in the circuit design.

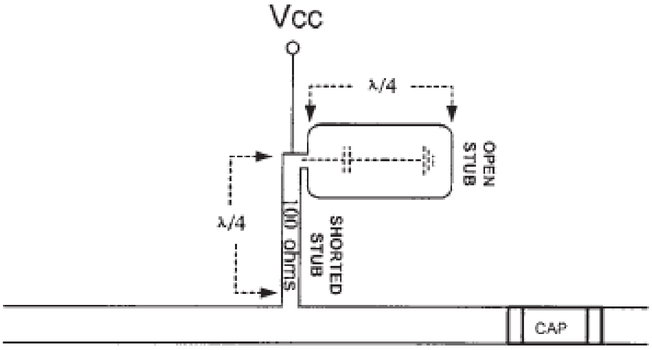

Figure 1.41 Distributed DC bias decoupling [1].

(*Cotter W. Sayre, Complete Wireless Design, 2001, page 34*)

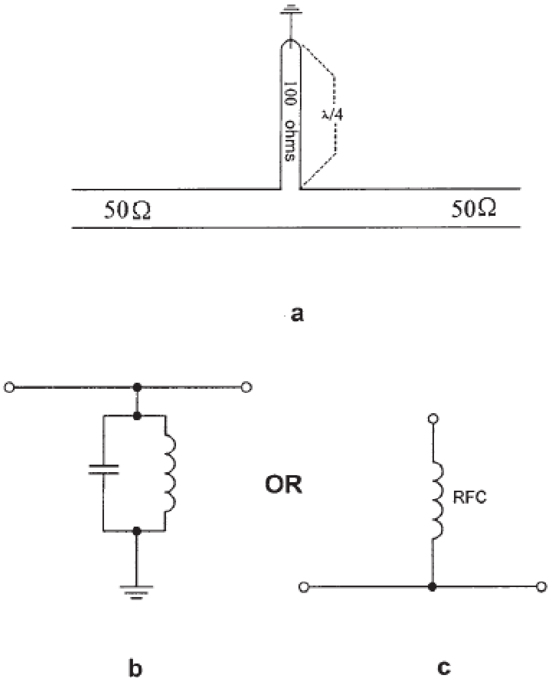

Figure 1.42 (a) A distributed choke; (b) equivalent lumped tank circuit; (c) a lumped choke [1].

(*Cotter W. Sayre, Complete Wireless Design, 2001, page 34*)

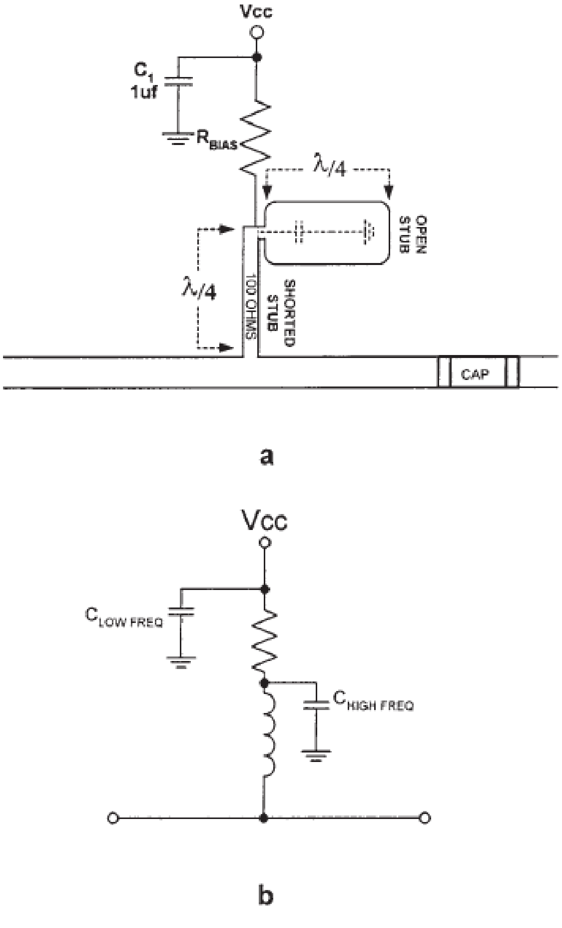

Figure 1.43 (a) Distributed DC bias decoupling; (b) equivalent lumped circuit [1].

(*Cotter W. Sayre, Complete Wireless Design, 2001, page 35*)

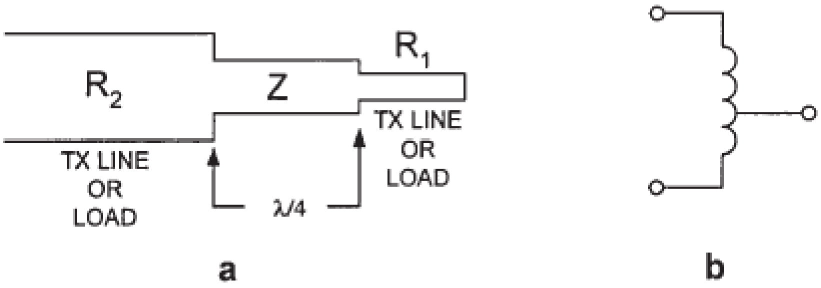

Figure 1.44 (a) A distributed transformer for resistive transformations; (b) equivalent lumped circuit [1].

(*Cotter W. Sayre, Complete Wireless Design, 2001, page 36*)

Transformer. In the context of transformers, specifically the narrowband type as depicted in Figure 1.44, terminations are exclusively resistive. These terminations can be amongst various impedances of microstrip lines, between pairs of resistive elements, or between a pair of reactive elements where the reactance is compensated by discrete components such as capacitors or inductors. The length of the transformer is engineered to be a quarter-wavelength ($^{\lambda}/_{4}$), corresponding to a phase shift of 90 degrees. The impedance transformation characteristic of the device is given by the geometric mean of the impedances of the primary and secondary lines, as expressed by the formula:

$$Z = \sqrt{R_1 R_2} \tag{1.22}$$

Once the impedance has been calculated, determine the necessary width of the Z section by using one of the various microstrip calculating tools that are freely available online or by using the microstrip equation above.

Microstrip component equivalency issues. Only the specific dielectric constant, frequency and board thickness utilized in the initial equivalency calculations will allow inductors, capacitors, transformers and parallel and series tank circuits to operate.

To preserve the effectiveness of the lumped element model in circuit design, the physical dimensions of equivalent capacitive and inductive components should be confined to less than one-eighth of the wavelength (λ). This constraint is crucial due to the velocity factor, which dictates the effective wavelength within the substrate medium, modifying the actual wavelength experienced by the signal compared to free space. All components distributed along the microstrip are influenced by the frequency and the dielectric constant of the substrate, as these parameters dictate the phase velocity (V_p) of the signal.

The integrity of the electric field around the microstrip is susceptible to disruption from the leakage field around the etched copper, which may lead to impedance variations. To mitigate this, it is recommended that shielding be placed no closer than ten times the substrate's thickness from any microstrip-based distributed inductors, capacitors, and the microstrip transmission lines themselves.

Furthermore, as the width of the microstrip conductor increases, there is a subtle adjustment in the calculations for the signal's phase velocity. This adjustment is due to one boundary of the microstrip where the electric field, generated by the propagating signal, is bordered not by the dielectric and ground plane, but by the open air environment.

Fabricating a distributed network of capacitors and inductors for use in a three-pole low-pass filter configuration requires precise calculations, as depicted in Figure 1.45. This figure exemplifies both correct and erroneous methodologies. In Figure 1.45a, calculated lengths of 0.246 inch for series inductors and 0.425 inch for the parallel capacitor are presented, demonstrating accurate microstrip placement for the inductive and capacitive elements. The resulting dimensions of the microstrip elements are functionally viable for the depicted filter design. Notably, the actual length of the capacitor is marginally greater than anticipated, in contrast to Figure 1.45b, where the inductors are significantly shorter than the calculated values.

For ensuring the intended circuit functionality, the dimensions of each distributed element must be meticulously calculated to avoid discrepancies that could lead to circuit malfunction.

When considering distributed circuit elements, it's imperative to account for the capacitive effects introduced by open stubs. Such stubs can exhibit an electrical length approximately 5% longer than their physical length on the printed circuit board (PCB), potentially affecting the resonant frequency. This discrepancy can be corrected by adjusting the physical length of the open stubs, removing the excess 5% to align with the desired electrical performance.

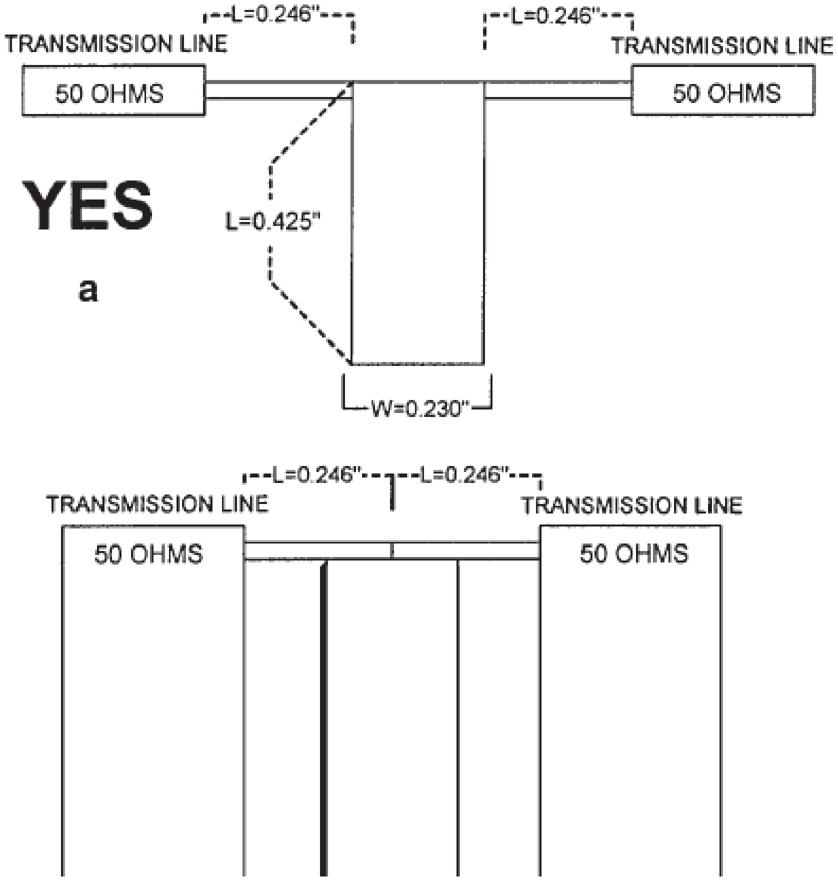

Figure 1.45 Microstrip component layouts: (a) effective design; (b) ineffective design [1].

(*Cotter W. Sayre, Complete Wireless Design, 2001, page 37*)

2 CHAPTER 2: Wireless Charging

2.1 Overview

In this chapter, wireless charging will be analyzed. There will be a general reference to wireless charging. Static and dynamic charging are the two categories of wireless power transfer and needed to be studied in depth. The last goal of this chapter is to provide information about EVs charging standards.

2.2 Introductory remarks

A high-frequency power converter produces high frequency ac power, which is fed to the transmitter in a typical WPT. The transmitter creates a voltage within the receiver by coupling with it through a magnetic, electric or electromagnetic field. Through the use of a power converter, the voltage induced at the receiver is sent to the load in order to adapt the voltage to the requirements of the load. Figure 2.1 shows the diagram of contactless power transfer [2].

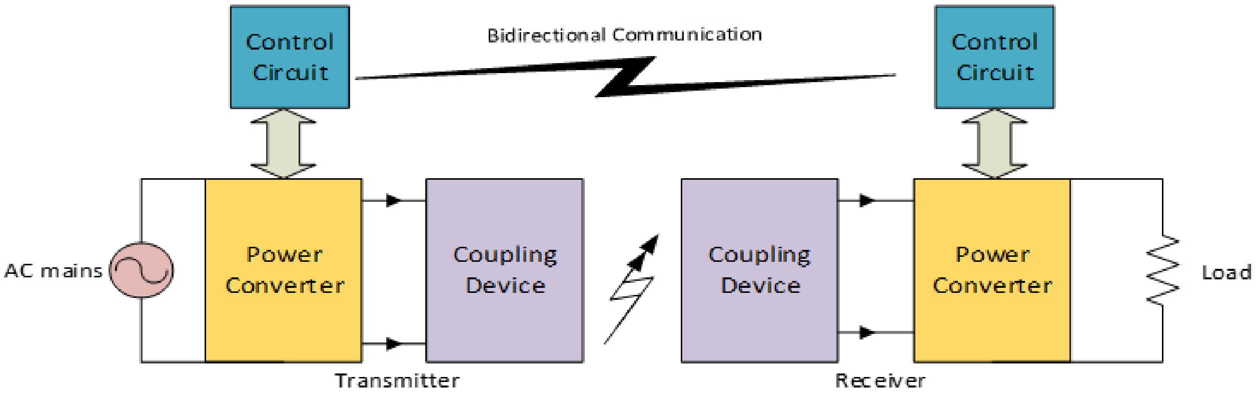

Figure 2.1 Typical diagram of contactless power transfer [2].

For better understanding in the next subchapters electricity, magnetism, electromagnetism, magnetic induction, resonance and resonant magnetic coupling will be condensed.

2.2.1 Electricity

Electricity is defined as the presence or flow of charged particles. Electrons flow (current) through a conductor just like a wire [3]. Electricity represents a form of energy characterized by the flow or movement of electrons between two points in the presence of a voltage disparity, thereby enabling the creation of an electric current.

2.2.2 Magnetism

A moving electric charge's or a particular material's ability to exert an attracting or repulsive force on an object is known as magnetism. Permanent magnets are objects with a constant magnetic field, just like the magnetic field of the earth. Alternating current (AC) flowing through a wire can produce oscillating magnetic fields, which change over time. Illustrations of the magnetic field lines are frequently used to depict and visualize the intensity, direction, and magnitude of magnetic fields (figure 2.2) [3].

Figure 2.2 Magnetic lines [3].

2.2.3 Electromagnetism

The combination of an element's magnetism and electricity produces electromagnetism, a fundamental force in nature. It is often termed as electromagnetic force. The electromagnetic fields are produced by electrical conductors interacting with electrically charged particles and uncharged magnetic force fields. Electromagnets are devices that, when electricity is applied, produce an electromagnetic field. [3].

2.2.4 Magnetic induction

As [4] said: “Induction of magnetism in a body when it is in a magnetic field or in the magnetic flux set up by a magnetomotive force”.

A very effective device for creating or capturing a magnetic flux is a loop or coil composed of conductive elements such as copper and carrying alternating current (AC). A conductive loop will produce an oscillating magnetic field close to it if it is linked to an AC source of power. If an additional conducting loop is located near sufficiently to the first, it may "catch" some of the fluctuating magnetic field, which causes the second coil to produce or induce an electric current. Devices could be powered by the second coil's current production. Magnetic induction, a well-known term for this form of electrical power transmission from one loop or coil to another, is used to describe this process [3].

2.2.5 Resonance

Resonance is a characteristic that can be found in a wide range of physical systems. It can be viewed as the frequency where the energy can be added to an oscillating system most effectively. An oscillating system that utilizes both potential and kinetic energy is a playground swing. The swing's length determines how quickly the kid swings back and forth. If the youngster correctly syncs his arm and leg motion with the movement of the swing, he can help the swing move higher. The child's modest movements effectively transfer energy to the swing, which is swinging at its resonance frequency [3].

2.2.6 Resonant Magnetic Coupling

When two items exchange energy through their fluctuating or oscillating magnetic fields, it is known as magnetic coupling. When the two items' inherent frequencies are almost same, resonant coupling happens [3].

2.2.7 Wireless power transfer methods

As [5] said "Since the introduction of wireless charging systems for EVs, four methods for the design of WEVCS have been utilised: traditional inductive power transfer (IPT), capacitive wireless power transfer (CWPT), magnetic gear wireless power transfer (MGWPT) and resonant inductive power transfer (RIPT)."

2.2.8 Inductive Power Transfer

Nikola Tesla pioneered the development of Traditional Inductive Power Transfer (IPT) in 1914 as a means to transmit power wirelessly. The fundamental block diagram of Traditional IPT is illustrated in Figure 2.3, serving as a foundational element in various Electric Vehicle (EV) charging infrastructures. IPT technology has undergone extensive testing and application across a broad spectrum, ranging from milliwatts to kilowatts, facilitating the contactless transfer of power from a source to a receiver. As [5] said: "In 1996, General Motors (GM) introduced the Chevrolet S10 EV, which was charged by the magne-charge IPT (J1773) system to provide level 2 (6.6 kW) slow and level 3 (50 kW) fast charges [3]. The primary coil, known as a charging paddle (inductive coupler) of the magne-charge, was inserted into the vehicle charging port where the secondary coil received power and allowed to charge the EV". A significant milestone in IPT technology occurred when the University of Georgia demonstrated a 6.6 kW Level 2 EV charger, operating at a frequency of 77 kHz and compatible with battery voltages ranging from 200 to 400 V. This universal IPT solution incorporated a 10 KVA coaxial winding transformer, offering notable advantages such as a customizable power range and enhanced flexibility in inductive coupling design. [5].

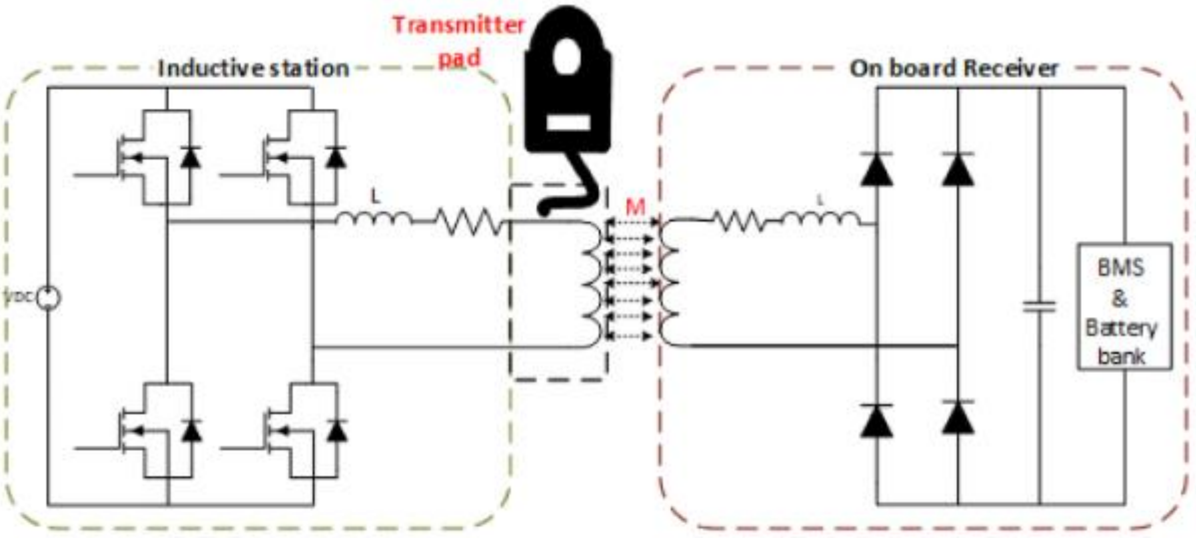

Figure 2.3 Block Diagram of Typical IPT [5].

2.2.9 Capacitive Wireless Power Transfer

The cost-effectiveness and simplicity of Capacitive Wireless Power Transfer (CWPT) technology, facilitated by sophisticated geometric and mechanical configurations of coupling capacitors, prove highly advantageous for low-power applications, including portable electronic devices, mobile phone chargers, and rotating machinery. Figure 2.4, as [5] said: “shows a typical schematic diagram of the series resonant circuit based CPWT. In the CWPT, coupling capacitors are utilised to transfer power from the source to the receiver instead of using coils or magnets. The main AC voltage is applied to an H-bridge converter though power factor correction circuitry. High-frequency AC generated by the H-bridge passes through coupling capacitors at the receiver side. Unlike the IPT, the CWPT operates for both high voltage and low current. In order to reduce impedance between transmitter and receiver sides at the resonant arrangement, additional inductors are added in series with the coupling capacitors”.This configuration facilitates soft switching within the circuitry. Similarly, the received AC voltage is converted to DC for the battery system or load through rectifier and filter circuitry. The efficacy of power transfer in CWPT is predominantly determined by the size of the coupling capacitor and the distance between the two plates. CWPT demonstrates exceptional performance and superior field constraints when the air gap is minimal. However, its application in Electric Vehicles (EVs) has been limited thus far due to the requirement of large air gaps and high-power levels. Recommended air-gap decrease and elevated capacitance coupling methods for the rotating mechanism. To reduce the air distance between the two connecting plates, it is suggested to use the bumper bar of the vehicle as a receiver. At the 540 kHz operating frequency, a static laboratory model with a power output of >1 kW was demonstrated with around 83% efficiency from the DC supply to the battery bank.

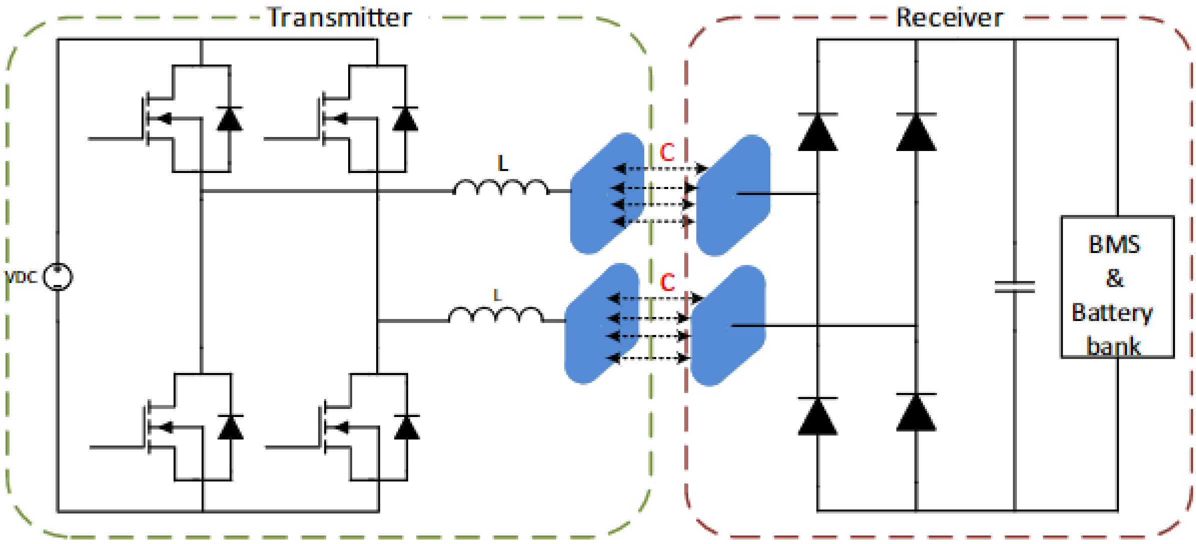

Figure 2.4 Block Diagram of CWPT [5].

2.2.10 Magnetic Gear Wireless Power Transfer

Magnetic Gear Wireless Power Transfer (MGWPT) stands apart from both Capacitive Wireless Power Transfer (CWPT) and Inductive Power Transfer (IPT), as depicted in Figure 2.5. As [5] said: “ In this method, two synchronised permanent magnets (PM) are positioned side-by-side in contrast to other coaxial cable based WEVCS. The main power as the current source is applied to the transmitter winding to produce a mechanical torque on the primary PM. With the utilisation of the mechanical torque, the primary PM rotates and induces a torque on the secondary PM through mechanical interaction. In two synchronised PMs, the primary PM works as the generator mode and the secondary PM receives power and delivers it to the battery through the power converter and BMS”. A laboratory prototype of MGWPT, with a capacity of 1.6 kW, has been developed, demonstrating effectiveness over an air gap distance of approximately 150 mm. However, incorporating this technology into both static and dynamic applications presents numerous challenges. Rotators experienced synchronization speed loss at 150 Hz, significantly impacting power transmission. Continuous speed adjustment is required, facilitated by an advanced feedback system from the battery side to the primary side, to prevent exceeding the upper power limit. The power transfer capability diminishes with increasing axis-to-axis separation between the primary and secondary PMs, as coupling between the synchronized windings decreases abruptly. Consequently, while suitable for stationary WEVCS, MGWPT poses significant challenges for dynamic applications. [5].

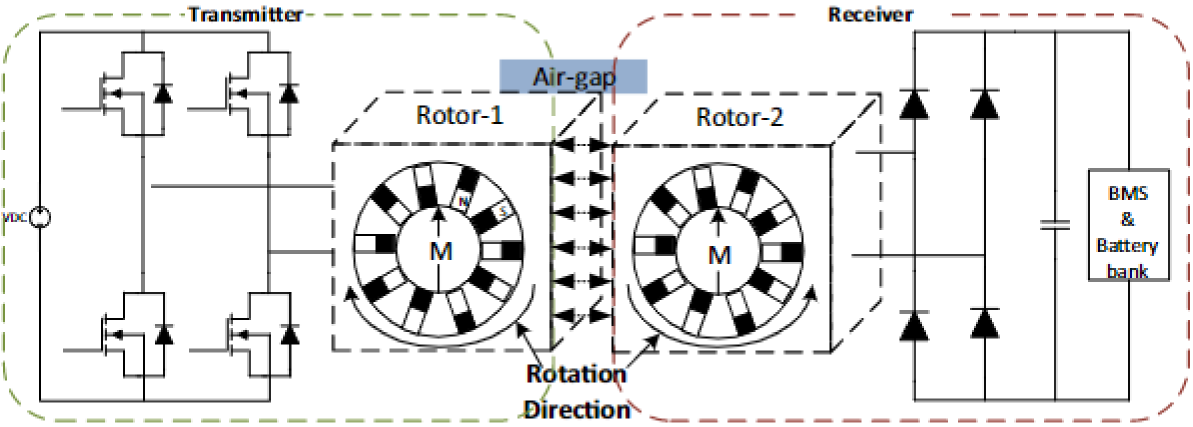

Figure 2.5 Magnetic Gear WPT Diagram [5].

2.2.11 Resonant Inductive Power Transfer

When it comes to creating power electronics and wireless transformer coils, the RIPT is among the most well-known and sophisticated variations of the conventional IPT. The RIPT for electric vehicles is schematically depicted in Figure 2.6. As [5] said: “Like other WPTs, the main AC voltage is converted into the HF AC source and supplied to the transmitter or primary winding. The receiver or secondary coil receives power via varying magnetic fields. The received power is converted to DC for the battery bank of the EVs through additional power electronics and filter circuitry”. In comparison to the conventional IPT, extra compensation networks are added to the main and secondary windings in series and/or parallel topologies, not just to provide the resonant scenario shown in (2.1) but also to lower additional losses.

$$f_{r(p,s)} = \frac{1}{2\pi\sqrt{L_{p,s} \cdot C_{p,s}}} \tag{2.1}$$

As [5] said: “where f r is the resonant frequency of the primary and secondary coils, and L and C are the self-inductance and resonant capacitor values of the transmitter and receiver coils, respectively. When the resonant frequencies of the primary and secondary coils are matched together, efficient power transfer is possible. The operating frequency of the RIPT ranges from tens of kilohertz to several hundred kilohertz. The magnetic flux generated at this frequency range, without any magnetic core, has a significantly adverse effect on the mutual inductance and hence the reduction of the coupling coefficient (k). The value of the coupling coefficient in the RIPT varies from 0.2 to 0.3 due to the minimum height clearance requirement of the EVs, which is 150–300 mm.” The coupling coefficient can be determined using Eq. (2.2). As [5] said: “Lp and Ls are the selfinductance of the transmitter and receiver coils, respectively. Lm is the mutual inductance between the two coils. If the primary and secondary coils are strongly coupled, the mutual inductance value would be higher, and vice versa.”

$$k = \frac{L_m}{\sqrt{L_p L_s}} \tag{2.2}$$

The coupling ratio of the wireless transformer architecture is enhanced by using magnetic ferrite cores in a range of configurations. Skin and proximity impacts can have a significant influence on the conversion efficiency at high frequencies. Individually insulated thin coiled wire-based litz cable is typically taken into account when designing in order to prevent such issues. Additionally, this can lower the parasitic resistance and raise the coil's quality factor (Q). The Q can be determinate by utilizing the (2.3). The frequency (f) and self-inductance (L) of the main or secondary coil are determined by Eq. (2.3), and the coils' resistance is indicated by R.

$$Q = \frac{\omega L_{p,s}}{R_{p,s}} = \frac{2\pi f \cdot L_{p,s}}{R_{p,s}} \tag{2.3}$$

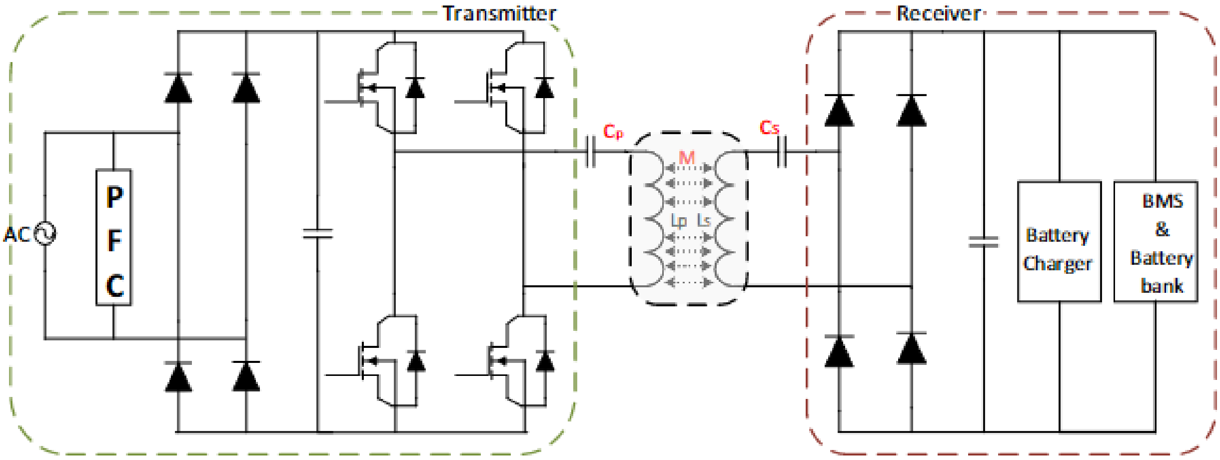

Figure 2.6 RIPT Block Diagram [5].

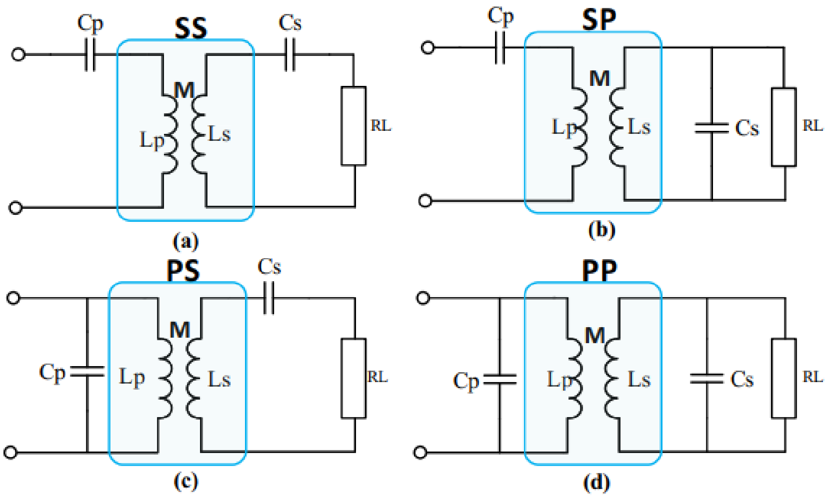

Figure 2.7 Topologies (a) Series-Series, (b) Series-Parallel, (c) Parallel-Series, (d) Parallel-Parallel [5].

Figure designated as 2.6 illustrates the integration of compensation capacitors, configured in both series and parallel arrangements, on the transmitter and receiver ends within static electric vehicle (EV) wireless charging systems to establish Resonant Inductive Power Transfer (RIPT). Figure 2.7 delineates four distinct compensation network topologies, denoted as series-series (SS), series-parallel (SP), parallel-series (PS), and parallel-parallel (PP). Source-side compensation is essential to nullify the phase disparity between the current and voltage, thereby reducing reactive power at the source. Incorporation of a secondary compensation network is pivotal for augmenting power transfer to the load and enhancing system efficiency. The topology selection for the compensation network is predicated on the specific operational demands of the Wireless Power Transfer (WPT) system. PS and PP configurations in the Wireless Charging Systems (WCS) are engineered with protective measures to prevent source coil activation in the absence of the receiver coil. While this ensures operational safety, the system's power transfer capability may be compromised due to misalignment between the source and receiver coils. These configurations necessitate additional series inductors to modulate the source current within the resonant circuit. Capacitance values are contingent upon the magnetic coupling coefficient and the system's quality factor. In SP-compensated WCS, the primary compensation capacitance is unaffected by mutual inductance, thereby facilitating superior power transfer compared to systems with varying mutual inductance. Nevertheless, it is highly sensitive to load variations. The SS topology is particularly advantageous for EV applications due to two primary benefits: firstly, the capacitance values at both the source and receiver are invariant with respect to load conditions and mutual inductance, allowing the resonant frequencies of both sides to be solely dependent on their respective self-inductances. Secondly, such systems sustain a unity power factor by consuming active power at the resonant frequency since the impedance reflected from the receiver coil does not contribute an imaginary component to the transmitter coil. Consequently, an SS topology-based WCS can be a more effective charging mechanism for batteries, potentially providing consistent voltage and current. An additional table enumerates the various advantages and attributes of the differing compensation networks employed in EV WPT systems [5].

Table 1 [50]

Advantages and attributes of compensation networks				
Attributes	SS	SP	PS	PP
Power transfer capability	H	H	L	L
Sensitivity of power factor over distance	L	L	M	M
Alignment tolerance	H	H	M	L
Impedance at resonant state	L	L	H	H
Frequency tolerance on efficiency	L	H	L	H
Suitable for EV application	H	H	M	M
H: High, M: Moderate, L: Low				

Table 2 shows the characteristics of applicable topologies for compensation.

Table 2

Compensation topologies characteristics [52]							
Applicable Topologies for compensation	Characteristics						
	Sending side capacitor	Receiving side capacitor	Load	Appropriate for WCV	Misalignment tolerance	Power tranfer	P.F vs distance
Series-Series (SS)	$\frac{1}{\omega^2 * L_1}$	$\frac{1}{\omega^2 * L_2}$	$\frac{\omega * L_2}{Q_2}$	H	H	H	L
Series-Parallel (SP)	$\frac{1}{\omega^2 * \left(L_1 - \frac{M^2}{L_2}\right)}$	$\frac{1}{\omega^2 * L_2}$	$\omega * L_2 * Q_2$	H	H	H	L
Parallel-Series (PS)	$\frac{1}{\omega^2 * \left(L_1 - \frac{\omega^2 * M^4}{L_1 * R_L^2}\right)}$	$\frac{1}{\omega^2 * L_2}$	$\frac{\omega * L_2}{Q_2}$	M	M	L	M
Parallel-Parallel (PP)	$\frac{1}{\omega^2 * \left(L_1 - \frac{M^2}{L_2}\right) + \frac{\frac{M^4}{L_2^4} * R_L^2}{L_1 - \frac{M^2}{L_2}}}$	$\frac{1}{\omega^2 * L_2}$	$\omega * L_2 * Q_2$	M	L	L	M
L: Low level, M: Medium level, H: High level							

2.2.12 Comparison of methods

In the realm of Wireless Power Transfer (WPT) methodologies for Electric Vehicles (EVs), a comparative analysis reveals a spectrum of efficiencies, costs, and complexities. Four predominant technologies—Inductive, Capacitive, Permanent Magnet, and Resonant Inductive—are juxtaposed on the basis of various performance metrics.

The Inductive WPT approach is characterized by its moderate to high efficiency and cost, paired with a medium level of Electromagnetic Interference (EMI). Operating within the 10-50 kHz frequency range, it exhibits a balance in terms of size, design complexity, and power level, rendering it highly compatible with Wireless Electric Vehicle Charging Systems (WEVCS).

Contrastingly, the Capacitive method demonstrates lower efficiency and cost while maintaining a medium EMI profile. Functioning at a higher frequency domain of 100-600 kHz, this technology benefits from minimal spatial volume, yet its design intricacy and power output are moderate, translating to a modest suitability for WEVCS integration.

The Permanent Magnet variant, while spanning a broad frequency range from 0.05 to 500 kHz, is marked by lower efficiency and a notable cost premium. It is distinguished by its substantial EMI, size, and design complexity, which collectively contribute to a reduced adaptability for WEVCS, paralleled by a moderate to low power delivery capacity.

Resonant Inductive technology, on the other hand, asserts itself with medium to high efficiency and a corresponding cost. It is advantaged by a low EMI signature within a 10-150 kHz operational bandwidth. This method strikes a median in size and design complexity while offering a moderate power level. Notably, it is deemed highly suitable for WEVCS applications.

In summation, when considering the suitability for WEVCS, Inductive and Resonant Inductive methods are superior, attributed to their higher efficiency metrics. Capacitive and Permanent Magnet methods, albeit economical, exhibit constraints in efficiency and WEVCS compatibility. Therefore, the selection of an appropriate WPT technology necessitates a balanced consideration of efficiency, cost, operational frequency, EMI, and system integration compatibility.

Table 3 [50]

Overview of different methods of Wireless Power Transfer (WPT) for EVs.

WPT methods	Performance			Price	Size/ Volume	Complexity of design	Power Level	Suitability for WEVCS
	Efficiency	EMI	Frequency Range (kHz)					
Inductive	M/H	M	10–50	M/H	M	M	M/H	H
Capacitive	L/M	M	100–600	L	L	M	L	L/M
Permanent magnet	L/M	H	0.05–0.500	H	H	H	M/L	L/M
Resonant inductive	M/H	L	10–150	M/H	M	M	M/L	H

Table 4 confirms that the more suitable method of wireless power transfer for EVs is the inductive couple, as it is considered the only applicable technology for eRoad.

Table 4 [51]

Comparisons of characteristics of wireless charging technologies.

Charging Tchnology	Charging Efficiency	Power	Air gap Tollerance	Applicable for eRoad
Microwave	76%	1.4kW	10 cm	No
Capacitive	83%-90%	3kW	15-30 cm	No
Magnetic Gear	81%	1.6kW	15 cm	No
Inductive Coupled	71%-96%	Up to 250kW	7.5-50 cm	Yes

2.3 Static wireless charging

All EVs experience issues with their batteries, such as their large weight, high expense, a lengthy charging process, and a limited driving range. The configuration a route's availability of a significant number of electric charging stations considered to be a practical solution to this issue. Because wired chargers are stationary, a vehicle must stop at a charging point for charging purposes. Additionally, the mechanical Connectors need to be regularly serviced. Dealing with the wiring and mechanical connectors provide a risk, especially in both wet and dry conditions. The deployment of a wireless network can help solve these issues. An EV must still need a stationary wireless charging method to halt for charging, but maintaining and connecting movable connectors are not a hassle.

An EV must be positioned on the wireless charger at a charging station in order to be charged utilizing the IPT static wireless charging method. It is not necessary for the battery or the car to be physically connected to the charging system. To a limited extent, misalignment between the assembly mounted on the EV and the charging surface is permissible. Given that the car is stopped for a set period of time, this strategy is suitable for use in offices and shopping centers. Similar to conductive charging technologies, this method requires a sizable battery pack. Large battery issue is helped by a dynamic charging method [6].

2.4 Dynamic wireless charging

The WPT technology is most suited for dynamic wireless charging since it enables the charge of the vehicle when it is in motion. Additionally, this extends its range, reduces the driver and passengers time, and enhances their safety. Since charging no longer requires mechanical connectors, the cost of maintenance is also decreased. One approach of using EVs is to charge them using roads dynamic WPT. With this technique, the WPT dynamically charges the EV and does not need much time to complete charging. This method enables charging for public transportation to occur even when a passenger exits or boards a taxi or bus. Highways could potentially make advantage of this concept.

EVs can be reliably charged along some routes. This will decrease the vehicle's weight, complexity, starting cost, and battery pack size. Utilizing this method also extends range. For dynamic charging, there are two different kinds of magnetic couplers. A single longitudinal coupler is set down in the first form, whereas the coupler is separated into segments in the second version. Comparing the segmented coupler to the longitudinal coupler, it is more beneficial. With the segmented coupler technique, just the segment that houses the vehicle's current receiving system is powered up. Power losses are lessened as a result. High initial costs, the need for construction to be dispersed maybe along highways, and challenging scheduling planning are issues associated with this technology. Just a few dynamic charging systems are currently on the market, and this approach is still under development. A suggested methodology is side LCC. This method can be used to get around IPT charger issues.

Low efficiency represents one of the main drawbacks of dynamic wireless power transfer. Numerous technologies, including effective pickup modules, compelling pickup tuning, pickup voltage schemes, and resonant inverters for wireless power exchange, have been presented to obtain higher transfer efficiency.

2.5 Projects of dynamic wireless charging

Dynamic wireless charging represents a groundbreaking approach in the evolution of electric vehicle technology, aiming to address the critical challenge of range anxiety and charging convenience. This innovative concept leverages inductive charging systems. Key projects in this field are exploring various technical aspects, such as the optimization of coil alignment, efficiency of power transfer, and integration with existing road infrastructures. These projects are critical in demonstrating the feasibility of dynamic wireless charging systems in real-world scenarios, and they contribute significantly to the development of sustainable transportation solutions. By potentially enabling continuous charging, these systems could revolutionize the electric vehicle industry, enhancing the usability of electric vehicles and supporting the transition to a more environmentally friendly mode of transportation.

Table 5 presents a summary of eRoad Projects for field test and evaluation with valuable information about efficiency, power, air gap and frequency.

Table 5

Summary of eRoad Projects for Field Test and Evaluation [53,54,55,56]

Organization	Project	Country	Cost	Air Gap	Efficiency	Power	Frequency
KAIST	OLEV 1st gen.	South Korea	-	10 cm	80%	3 kW	20 kHz
	OLEV 2nd gen.	South Korea	-	17 cm	72%	6 kW	20 kHz
	OLEV 3rd gen.	South Korea	$1M/lane-km	17 cm	71%	17 kW	20 kHz

	OLEV 3rd+ gen.	South Korea	-	20 cm	83%	15 kW	20 kHz
	OLEV 4th gen.	South Korea	$0.85M/lane-km	20 cm	80%	25 kW	20 kHz
	OLEV 5th gen.	South Korea	-	20 cm	71%	22kW	20 kHz
Bombardier (Scania)	Primove	Germany	€3.25-6.15M/lane-km	6-10 cm	90%	200 kW	20 kHz
Oak Ridge National Lab	WPT	United States	€1.32M/lane-km	7.5 cm	95%	20 kW	-
Fabric	Victoria	Spain	-	15 cm	83%	50 kW	26 kHz
Utah State University	WPT	United States	-	25-38 cm	90%	30-50 kW	20-140 kHz
VICTORIA / Endesa	-	-	-	15-20 cm	85%	50 kW	26 kHz
INTIS	-	-	-	10 cm	-	30 kW	30 kHz
UTokyo	-	-	-	12 cm	89-93%	2x12 kW	85 kHz
RTRI	-	Japan	-	7.5 cm	70-85%	50 kW 3 × 16.7 kW	10 kHz
ORNL	-	-	-	10 cm	75%	1.5 kW	23 kHz
Fabric – Qualcomm	-	France	-	12.5 cm - 17.5 cm	80%	20 kW - 40 kW	-
Fabric	-	Italy	-	25 cm	70-80%	20 kW × 3 – 100 kW	10-150 kHz
ORNL	-	-	-	12.-17 cm	90-95%	20 kW	22-23 kHz
University of Auckland	-	New Zealand	-	50 cm	85%	20-30 kW	12.9 kHz
Railway Technical Research Institute	-	Japan	-	0.75 cm	-	50 kW	10 kHz
Flanders Drive with industries and universities	-	-	-	10 cm	88-90%	80 kW	20 kHz
EV System Lab & Nissan Research Center	-	-	-	10 cm	>90%	1 kW	90 kHz
North Carolina State University	-	USA	-	17 cm	77-90%	0.3 kW	100 kHz

Table 6

Electreon Projects [57]				
Project	Country	Period	Cost	Size
Tel Aviv University Station	Israel	2020-2022	-	700 meters of wireless Electric Road for dynamic charging of e-bus, ad part of a 5km route between university bus terminal and railway station, with additional static wireless charging at the station
Tel Aviv Commercial Deal	Israel	2021-2026	$9.4 M	Static wireless charging at bus terminals, starting with Reading Terminal in Tel Aviv, for 200 e-buses

Arena of the future	Italy	2020-2023	-	Initially, 1.05 km of wireless Electric Road for dynamic charging of an e-bus and passenger electric vehicle, followed by additional integration for an e-van and a static wireless charging station in later phase
eCharge (BASt)	Germany	2021- To be confirmed	-	100m of wireless Electric Road for dynamic charging of e-van
Smartroad Gotland	Sweden	2019-2023	$14.8 M	Initially 1.65 km of wireless Electric Road for dynamic charging of e-bus and heavy-duty e-truck, as part of a 4.1 km rout between the airport and town center, followed by an additional static wireless charging station in later phase.
Port of Karlsruhe (EnBW)	Germany	2020-2026	-	Initially, 100m of wireless Electric Road for dynamic charging of an e-bus with additional static wireless charging station at the client's facilities, followed by an additional 500m of wireless electric Road in later phase
Michigan DOT	USA (Michigan Central Sation & Michigan Avenue)	2022-2024	-	1.61 km of wireless Electric Road for dynamic charging of multiple vehicle types, with additional static wireless charging station in the vicinity
ASPIRE Demonstration Utah	USA	2022	-	50m of wireless Electric Road for dynamic charging of an e-truck
Electra Afikim Commercial Deal	Israel	2022- To be confirmed	-	Static wireless charging at the Afikim bus lot/terminal in Rosh HaAyin for 30 e-buses
E|MPOWER	Germany	2024- To be confirmed	-	100 km of wireless Electric Road for dynamic charging of multiple vehicle types
Balingen (ELINA)	Germany	2022-2023	-	101 km of wireless Electric Road for dynamic charging of an e-bus, with additional static wireless charging stations along the bus route
Trondheim Electric Road	Norway	2024- To be confirmed	-	Wireless Electric Road for dynamic charging of an e-bus
Charge as you Drive	France	2024- To be confirmed	-	2 km of wireless Electric Road for dynamic charging of e-bus and heavy-duty e-truck, with an additional static wireless charging station
SITEC	China (Shandong Province)	2023- To be confirmed	-	Tens of kilometers of wireless Electric Road for dynamic charging of e-bus and heavy-duty e-truck, with up to hundreds of additional static wireless charging station deployed throughout several phases
BDX	Sweden	2024-2026	-	Two static wireless charging spots for last mile delivery e-van

Electreon technology is vehicle and Original Equipment Manufacturer (OEM) agnostic, indicating its compatibility with any road vehicle equipped with an Electric Vehicle (EV) battery, including e-trucks, e-buses, e-taxis, e-vans, and passenger EVs. The technology operates on the principle of inductive coupling, involving roadway infrastructure composed of copper charging coils, termed "segment" coils, embedded beneath the asphalt. These coils, when in proximity to copper coils installed in the "receiver" beneath the vehicle, generate a magnetic field that facilitates the wireless transfer of electricity. The roadway coils are connected to the electrical grid and wirelessly transmit electricity to the receiver mounted on the vehicle, which then channels the electricity to the EV battery for charging. Electreon entire system is designed to be completely subterranean, eliminating the presence of exposed wires, cords, or infrastructure. This significantly reduces maintenance needs, wear and tear, weather damage, and risks of vandalism.

Recent reports, particularly from a project in Sweden where temperatures can be extremely low, underscore the technology's capability to function effectively in various weather conditions and real-world roadway scenarios. These reports highlight the system's ability to maintain the road’s structural integrity, even with the frequent passage of heavy vehicles over the segment coils installed underneath the asphalt.

2.6 Electric Vehicles Charging Standards

For portable electronics like cell phones, there were no power standards even at the start of the twenty-first century. This led to various plugs for several phone models. There have been attempts to establish a unified standard for wirelessly charging electronic gadgets in order to avoid such issues. Progress in this field was only partially realized, though, as three guidelines for wireless power transfer had been created by 2015: the QI standard, the Power Matters Alliance (PMA) and the Alliance for Wireless Power (A4WP). However, the last two (PMA and A4WP) later united to become the AirFuel Alliance standard in 2015 [7].

2.6.1 The QI standard

The Wireless Power Consortium created the first wireless power transfer standard, known as the Qi standard (from the Chinese for the flow of life energy), which was released to the public in 2008. Then, in 2010, an upgraded version of this guideline became available. Nokia was the producer who promoted this standard. Later, more well-known businesses joined this standard.

This standard, which is devoted to such transfer based on IPT technology, is the leading one for energy transfer. This standard enables the charging of devices with a rated power of 5 to 15 W, such as smartphones. To compensate, attempts are being undertaken to raise the charging capacity from 30 to 60 W, which will enable the wireless power supply of electrical devices with higher power requirements, such as laptops and tablets. However, this standard has limitations, including heating since temperature affects how well energy is transmitted, the requirement for adjustments (such equalizing the transmitter and receiver), and the ability to charge only one device.

According to the QI standard, three transmitter types—guided positioning, free positioning (shifting the primary coil), and free positioning—can be used to achieve the required charging effect (the QI coil matrix) [7].

2.6.1.1 Guided Positioning

This standard instructs the user whether the locations of the primary and receiver match. In case of a mismatch, the client is instructed on how to reposition the receiver and transmitter in order to ensure the most effective charging. The magnet within the transmitter pulls the receiver carrying the magnetic attractor, making the correct matching feasible. Figure 2.7 depicts a sample of this kind of transmitter.

In accordance with the Qi-guided positioning standard, this figure shows a typical setup of the transmitter and receiver for power transfer. As can be seen, a magnet M located inside the coil in the middle of the transmitter is responsible for drawing the attractor found inside the receiver to it. In this instance, positioning the magnet directly over the attractor will guarantee a flawless alignment of both coils [7].

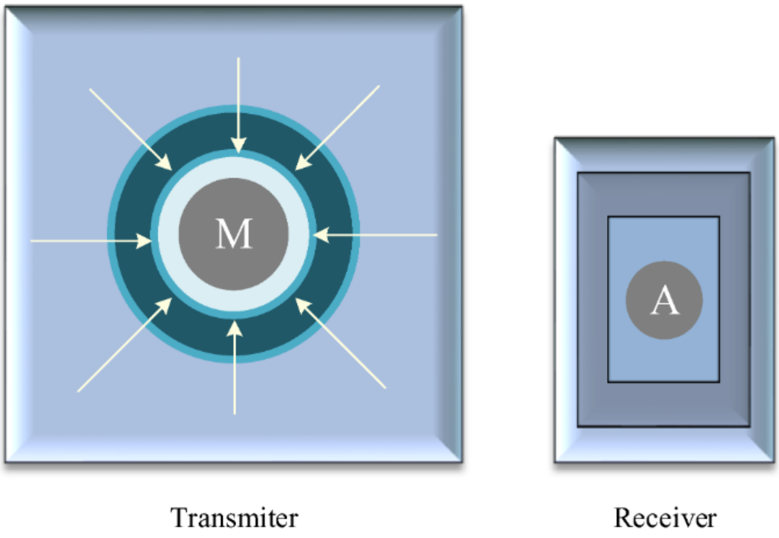

Figure 2.8 Guided Positioning Transmitter [7].

2.6.1.2 Free Positioning—Moving the Primary Coil

In this instance, the orientation of the receiver is carried out by adjusting the primary coil's location to move it toward the receiver in order to appropriately align the transmitter and the receiver (Figure 2.8). To that aim, a receiver identification and tracking system is built within the transmitter. The transmitter advances the coil on the primary winding side toward the receiver once it has located the receiver. The utilization of just one coil in the transmitter is a benefit of this approach, just like in the scenario of guided location. The adoption of a suitable mechanism that enables altering the horizontal position of the coil in the transmitter is necessary for the precise modification of the distance between the coils.

The x- and y-axes in figure 2.8 show that the coil may be moved either horizontally or vertically based on where the receiver is [7].

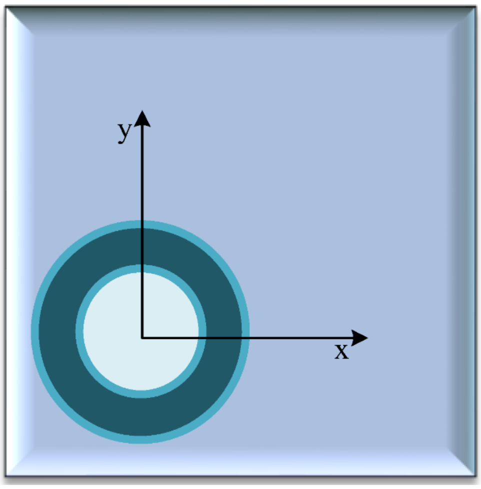

Figure 2.9 Free positioning transmitter-Moving the Coil [7].

2.6.1.3 *Free Positioning—Coil Matrix*

This kind of transmitter has a number of coils arranged in an array covering the whole surface. The transmitter and receiver are set up differently in this scenario. The coils are placed in layers, typically creating three layers, to achieve a uniform distribution of the magnetic force. The magnetic field produced by the sandwiched coils is comparable to the magnetic flux produced by the alternatives that were previously mentioned. This sort of transmitter has the benefit that the transmitter and receiver can be placed anywhere as long as they are inside the range of the magnetic force, therefore accurate alignment of their positions is not necessary. The difficulty of executing serial and multilayer placing of the transmitter coils on the PCB, and maintaining the quality at a sufficient level, is a drawback of this technique. Figure 2.9 depicts an illustration of how a transmitter with coils grouped in layers might be implemented.

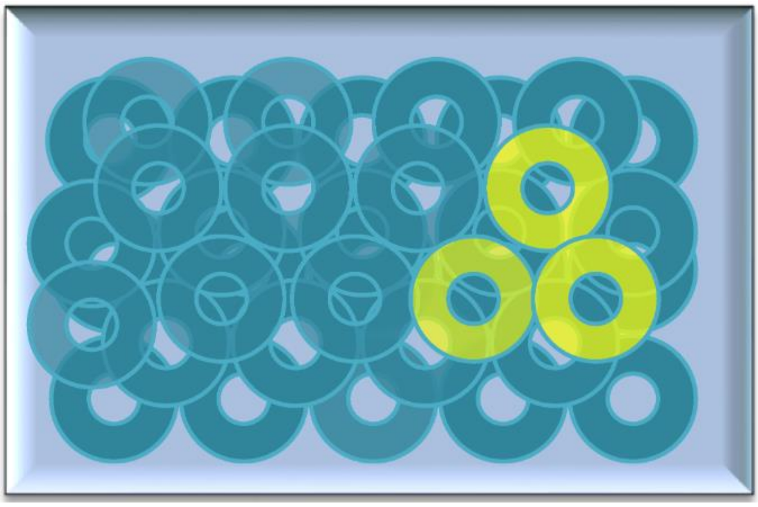

Figure 2.10 Free Positioning Transmitter-Matrix Coil [7].

This figure depicts a transmitter with several stacked coils covering the whole surface of its enclosure. These coils can't travel in the receiver's direction. On the other side, the transmission of electricity starts as soon as the receiver comes into contact with the magnetic flux produced by a few of the transmitting coils (such as those highlighted in yellow).

2.6.2 AirFuel Standard

The PMA, a nonprofit group that created an energy transfer procedure utilizing both IPT methods, introduced the Power Matters Alliance Standard. The AirFuel Alliance standard was established, as was previously noted, as an outcome of the merger of the PMA organization and the A4WP. Very well-known companies have all implemented this standard. The AirFuel Standard now focuses primarily on RF energy resonance and AirFuel Resonant technology. The AirFuel Resonant standard has the benefit of being less expensive and easier to scale than inductive power transfer solutions, as well as being simpler to set up. It was noted that governmental and private infrastructure in Asia uses AirFuel Resonant technology. Using this method, energy may be transmitted at a frequency of 6.78 MHz over long ranges (up to several meters) between transmitter and receiver.

3 CHAPTER 3: Dynamic Charging System Analysis

The development of electric vehicles (EVs) has been a major area of focus in the automotive industry due to concerns about climate change and air pollution [8]. One of the key challenges facing EVs is the limited range of the vehicles on a single charge. To address this challenge, dynamic charging systems (DCS) have been proposed, which allow for charging of the EV battery while the vehicle is in motion. DCS can potentially extend the range of the vehicle, making it more practical for long-distance travel [9].

This chapter aims to provide a theoretical analysis and modeling of a dynamic charging system for electric vehicles. The chapter will begin with a literature review of the current research in the field, followed by an overview of the key concepts and technologies related to dynamic charging systems. The theoretical analysis and modeling will then be presented, including the development of mathematical models for the components of the system and the integration of these models into a complete system using MATLAB/Simulink [10]. Finally, the chapter will discuss the implications of the findings for the design and operation of dynamic charging systems, as well as the limitations of the study and recommendations for future research [11].

3.1 Overview

Dynamic charging systems have been the subject of significant research in recent years, with the aim of extending the range and practicality of electric vehicles [12]. Early research focused on developing inductive power transfer (IPT) technology, which enables the transfer of electrical energy wirelessly between two coils [13]. Since then, researchers have investigated various approaches to dynamic charging systems, including track-based, road-based, and hybrid systems [14].

Recent advancements in dynamic charging systems have focused on improving the efficiency and safety of the technology. For example, researchers have developed more efficient power electronics, better communication systems between the charging infrastructure and the vehicle, and improved methods for controlling the power transfer between the coils [15]. Additionally, researchers have investigated the impact of dynamic charging systems on the grid, considering issues such as grid stability, load balancing, and the integration of renewable energy sources [16].

Dynamic charging systems consist of several components, including the primary and secondary coils, power electronics, and communication systems [17]. The primary coil is typically installed in the charging infrastructure, while the secondary coil is mounted on the underside of the electric vehicle. When the vehicle is positioned over the primary coil, an alternating magnetic field is created, inducing an electrical current in the secondary coil, which is then used to charge the battery [18].

There are several approaches to dynamic charging systems, including track-based, road-based, and hybrid systems. Track-based systems use conductive rails to transfer electrical energy to the vehicle, while road-based systems use embedded coils in the road surface to charge the vehicle wirelessly. Hybrid systems combine both approaches, with conductive rails used for high-power charging and embedded coils used for low-power charging [19].

3.2 Theoretical Analysis

The foundation of dynamic charging lies in wireless power transfer (WPT) principles. Unlike traditional charging methods that require physical connectors, WPT facilitates the transmission of electrical energy through electromagnetic fields. This not only enhances the convenience factor but also promises continuous vehicle operation, minimizing the interruptions commonly associated with conventional charging stations [5].

Power electronics form the backbone of the energy conversion and regulation process in DCS [20]. Components such as rectifiers, inverters, and DC-DC converters are integral to this system. They ensure that the energy flow between the primary and secondary coils is not only stable but also maximally efficient [21].

3.2.1 AC Source (Grid):

The grid is the primary source of electrical power in most countries. It consists of power generation stations, transmission lines, and distribution networks. The AC source in our model represents the final distribution phase, delivering standardized voltage and frequency to consumers [22][23].

3.2.2 Rectifier

Rectifiers can be single-phase or three-phase, depending on the AC source and the required DC output. They use semiconductor devices, primarily diodes, to allow current flow in only one direction, effectively converting AC to DC [24][25].

3.2.3 High-Frequency (HF) Inverter

The HF inverter's role is to produce a high-frequency AC waveform from the DC output of the rectifier. This is achieved using switching devices like MOSFETs or IGBTs. The high frequency is essential to reduce the size of the transmitter coil and improve the efficiency of energy transfer [26][27].

3.2.4 Transmitter and Receiver Coil

The coils operate on the principle of magnetic resonance. The transmitter coil, when energized by the HF inverter, creates a magnetic field. The receiver coil, tuned to the same frequency, captures this field. The efficiency of this energy transfer depends on the coupling coefficient between the coils and their design [28][16].

3.2.5 Vehicle Rectifier

The vehicle rectifier, similar to the primary rectifier, converts the high-frequency AC from the receiver coil back into DC. This DC is then used to charge the EV's battery. The design considerations for this rectifier include minimizing losses and ensuring compatibility with the battery's charging specifications [24][29].

3.2.6 Li-ion Battery

Lithium-ion batteries are favored in EVs due to their high energy density, long cycle life, and decreasing costs. The battery management system (BMS) ensures safe charging and discharging, prolonging the battery's lifespan [30][31].

3.3 Modeling

Creating a comprehensive model of a dynamic charging system requires the integration of various parameters [32]. These include the specifications of the coils embedded in the road and those attached to the EV, the intricacies of the power electronics involved, and the dynamics of the vehicle itself. Such a model offers a holistic view, encompassing both the electrical and mechanical dimensions of the charging process [11].

In this study the focus will be on the electrical dimensions of the charging process.

3.3.1 Power Electronics Model

The power electronics in the DCS primarily comprise of a full-bridge rectifier, a DC-DC converter, and an inverter. The full-bridge rectifier is responsible for transforming the alternating current voltage obtained from the secondary coil into direct current voltage. The DC-DC converter is tasked with voltage level regulation to optimize power transfer. Subsequently, the inverter reconverts the direct current voltage back to alternating current voltage to energize the primary coil.

The operational states of the system can be segregated into four distinct modes, contingent on the power converter's switching state. The power electronics model can be established employing state-space representation, a mathematical modeling technique that represents a physical system as a set of input, output, and state variables related by first-order differential equations [33].

3.3.2 Primary Coil Model

The primary coil can be represented as a current source in parallel with an inductance L_1 and resistance R_1. The primary coil is driven by an AC source, the amplitude of which is controlled by a feedback system to ensure safe and efficient power transfer. The primary current I_1 can be expressed as: [34]

$$I_1(t) = I_{1m} \cdot cos(\omega t + \theta_1) \tag{3.1}$$

The magnetic field B generated by the primary coil can be modeled using Ampere's law and expressed as:[29]

$$B(t) = \mu_0 \cdot N_1 \cdot \frac{I_1(t)}{2\pi r} \tag{3.2}$$

3.3.3 Secondary Coil Model

The secondary coil, which is situated on the vehicle's underside, can be approximated as a series RLC circuit, incorporating an inductance L_2, a resistance R_2, and a capacitance C_2. The potential difference across the secondary coil can be formulated as:[35]

$$V_2(t) = V_{2m} \cdot cos(\omega t + \theta_2) \tag{3.3}$$

Employing Faraday's law of electromagnetic induction, the current I2 flowing through the secondary coil can be expressed as:[36]

$$I_2(t) = C_2 \cdot \frac{dV_2(t)}{dt} \tag{3.4}$$

3.3.4 Gap and Misalignment

The gap refers to the physical distance between the transmitter and receiver coils in a WPT system. This distance can vary based on the application. For instance, in electric vehicle charging, the gap might be the distance between the road surface (where the transmitter coil is embedded) and the vehicle's undercarriage (where the receiver coil is located) [37].

The efficiency of power transfer is inversely proportional to the gap. As the gap increases, the magnetic coupling between the coils decreases, leading to reduced power transfer efficiency. However, advancements in resonant inductive coupling have shown promise in mitigating the adverse effects of increased gaps [17].

Misalignment refers to the relative positioning of the transmitter and receiver coils. Perfect alignment means that the coils are centered with respect to each other. However, in real-world scenarios, perfect alignment is challenging to achieve consistently, especially in dynamic applications like electric vehicle charging [38].

There are two primary types of misalignments:

- Lateral Misalignment: This occurs when the coils are displaced horizontally with respect to each other.
- Angular Misalignment: This happens when the coils are tilted or rotated relative to each other [39].

Misalignment can lead to a significant drop in power transfer efficiency. The magnetic fields generated by the coils may not overlap perfectly, resulting in reduced coupling. Moreover, misalignment can also lead to increased electromagnetic emissions, which can interfere with other electronic systems and pose safety concerns [40].

Several strategies have been proposed to address the challenges posed by gap and misalignment:

- Adaptive Tuning: By adjusting the resonant frequencies of the transmitter and receiver circuits, the system can maintain optimal power transfer even in the presence of varying gaps and misalignments [41].
- Multiple Coils: Using arrays of coils instead of single coils can increase the tolerance to misalignment [42].
- Positioning Feedback: Implementing sensors and feedback mechanisms to adjust the position of the receiver coil or modify the power transfer parameters in real-time [43].

3.3.5 Safety

Technologies that involve the transfer of energy wirelessly, has raised concerns about the safety of passengers due to exposure to electromagnetic fields (EMFs) [44]. The primary concern with EMF exposure is its potential impact on human health. Prolonged or high-level exposure to EMFs has been studied for possible links to various health issues, including thermal (burns) and non-thermal (changes in cell structure, increased risk of cancer, and effects on the nervous system) effects [55][46].

To address these concerns, international organizations have established safety standards and guidelines for EMF exposure:

- International Commission on Non-Ionizing Radiation Protection (ICNIRP): ICNIRP provides guidelines on exposure limits for electric, magnetic, and electromagnetic fields. For frequencies used in dynamic charging, the guidelines focus on limiting the exposure to levels where no adverse health effects are observed [47].
- World Health Organization (WHO): WHO recognizes the guidelines set by ICNIRP and emphasizes the importance of adhering to these guidelines to ensure public safety [48].

Several strategies have been proposed and implemented to minimize EMF exposure in dynamic charging systems:

- Shielding: Using electromagnetic shields, such as ferrite plates, to reduce the EMF levels inside the vehicle [49].
- Optimized Coil Design: Designing the transmitter and receiver coils in a way that confines the magnetic field to a limited space, thus reducing unwanted EMF emissions [43].
- Adaptive Power Control: Adjusting the power transfer dynamically based on the vehicle's requirements and the distance between the coils, ensuring that the system operates at the lowest necessary power level [48].

4 CHAPTER 4: Implementation of EV Dynamic Charging System Simulation

4.1 Overview

The simulation of the EV dynamic charging system is pivotal in understanding its feasibility, efficiency, and challenges. This chapter delves into the intricacies of the simulation process, the tools used, and the results derived.

4.2 Simulation model

As it was mentioned previously, for the creation of the model and the simulation there is going to be MATLAB/Simulink utilization. First there will be a step-by-step explanation of the model and afterwards a presentment of the assumptions and the parameters considered.

4.2.1 Model creation

In order to create a dynamic charging system, it’s necessary to have an AC voltage source, a rectifier, series RLC branch, a HF inverter, a mutual inductance, a vehicle rectifier as well as a li-ion battery.

4.2.1.1 AC Voltage Source

AC Voltage Source can be found in the library browser, if “AC Voltage Source” searched. For this model an ideal sinusoidal AC Voltage Source is utilized with parameters as shown in the figure below.

Figure 4.1 AC Voltage Source

.

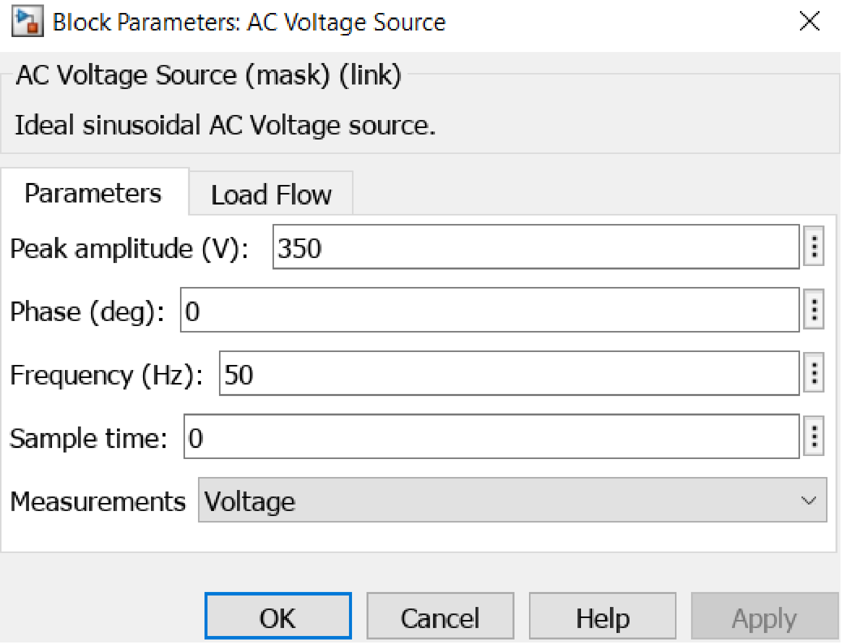
Block Parameters: AC Voltage Source

AC Voltage Source (mask) (link)

Ideal sinusoidal AC Voltage source.

Peak amplitude (V): 350

Phase (deg): 0

Frequency (Hz): 50

Sample time: 0

Measurements: Voltage

Figure 4.2 AC Voltage Source parameters

4.2.1.2 Rectifier

Rectifier can be found in the library browser, if "Universal bridge" searched. For this model the Universal Bridge utilized with parameters as shown in the figure below.

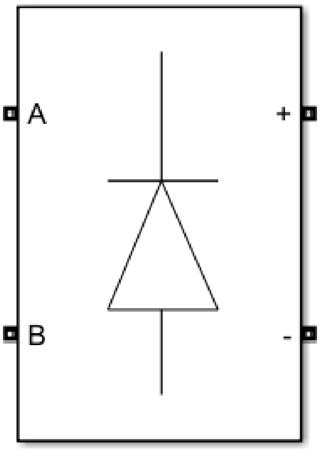

Figure 4.3 Rectifier.

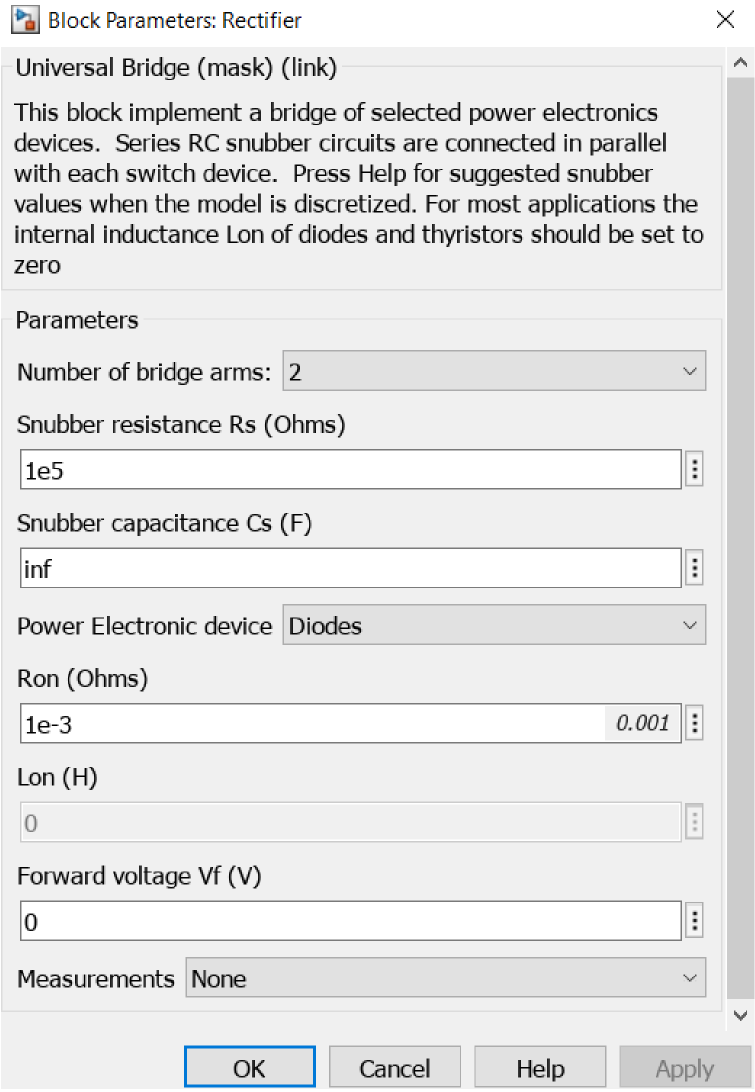

Block Parameters: Rectifier

Universal Bridge (mask) (link)

This block implement a bridge of selected power electronics devices. Series RC snubber circuits are connected in parallel with each switch device. Press Help for suggested snubber values when the model is discretized. For most applications the internal inductance Lon of diodes and thyristors should be set to zero

Parameters

Number of bridge arms: 2

Snubber resistance Rs (Ohms): 1e5

Snubber capacitance Cs (F): inf

Power Electronic device: Diodes

Ron (Ohms): 1e-3 (0.001)

Lon (H): 0

Forward voltage Vf (V): 0

Measurements: None

Figure 4.4 Rectifier parameters.

4.2.1.3 Series RLC branch

Series RLC branch can be found in the library browser, if “Series RLC branch” searched. For this model the utilization of many RLC branches is needed. Specifically, there are L in series (L_1), C parallel before the HF inverter (C_1), C in series after the HF inverter (C_2) and C in series after the mutual inductance (C_3) as show in picture (figure4.5). The parameters of each branch are shown in figures below.

Figure 4.5 Series RLC branch.

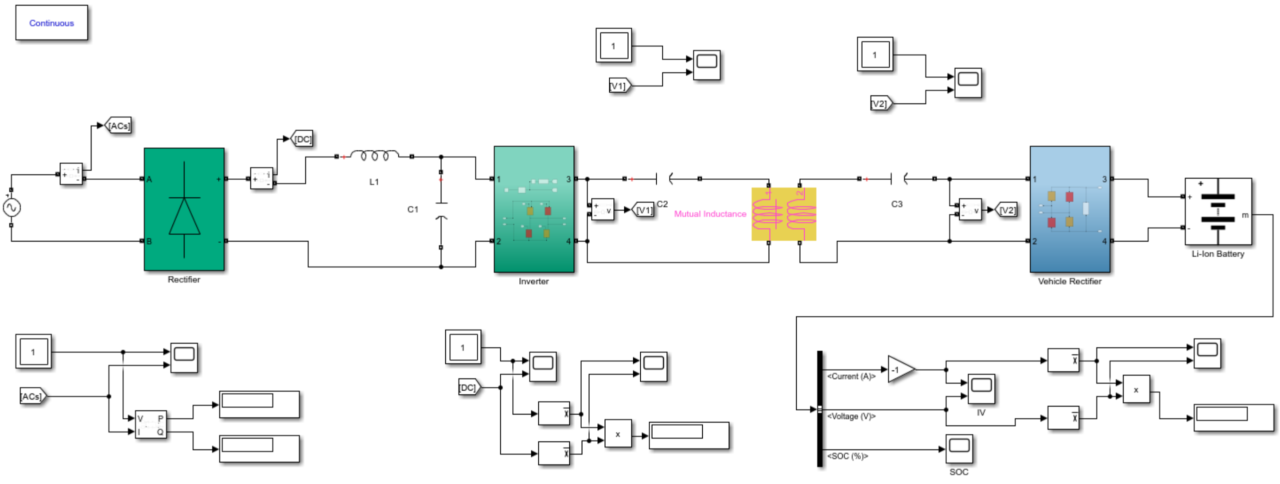

Figure 4.6 Simulation System.

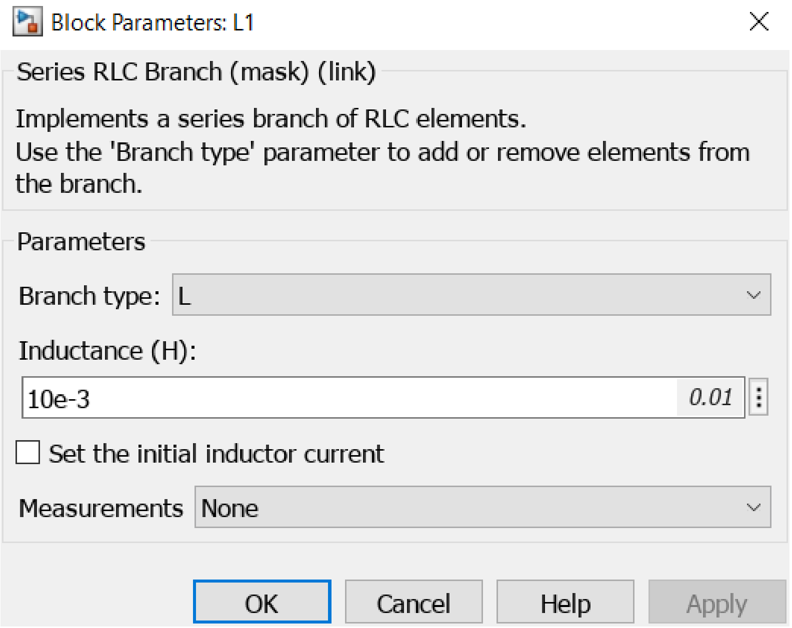

Block Parameters: L1

Series RLC Branch (mask) (link)

Implements a series branch of RLC elements.
Use the 'Branch type' parameter to add or remove elements from the branch.

Parameters

Branch type: L

Inductance (H): 10e-3 0.01

☐ Set the initial inductor current

Measurements None

Figure 4.7 L_1 parameters.

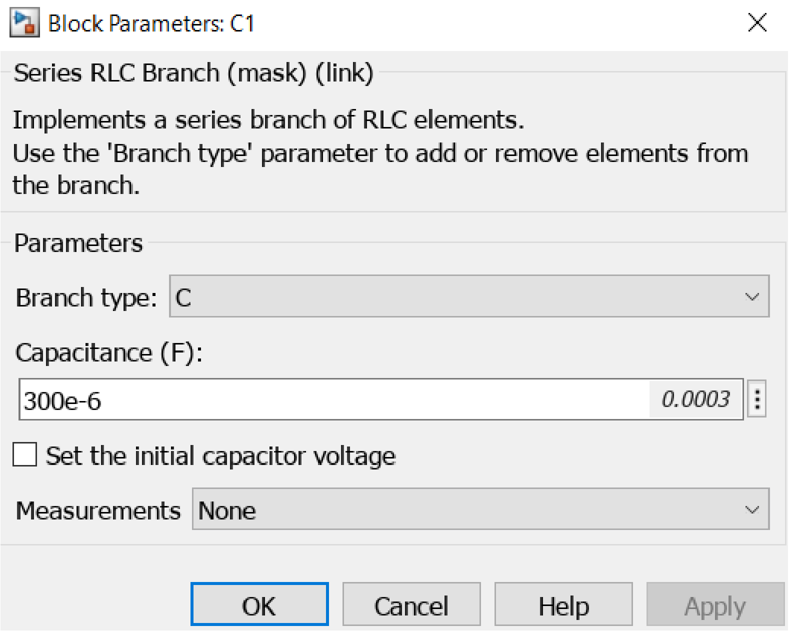
Block Parameters: C1

Series RLC Branch (mask) (link)

Implements a series branch of RLC elements.
Use the 'Branch type' parameter to add or remove elements from the branch.

Parameters

Branch type: C

Capacitance (F):

300e-6 0.0003

☐ Set the initial capacitor voltage

Measurements None

Figure 4.8 C_1 parameters.

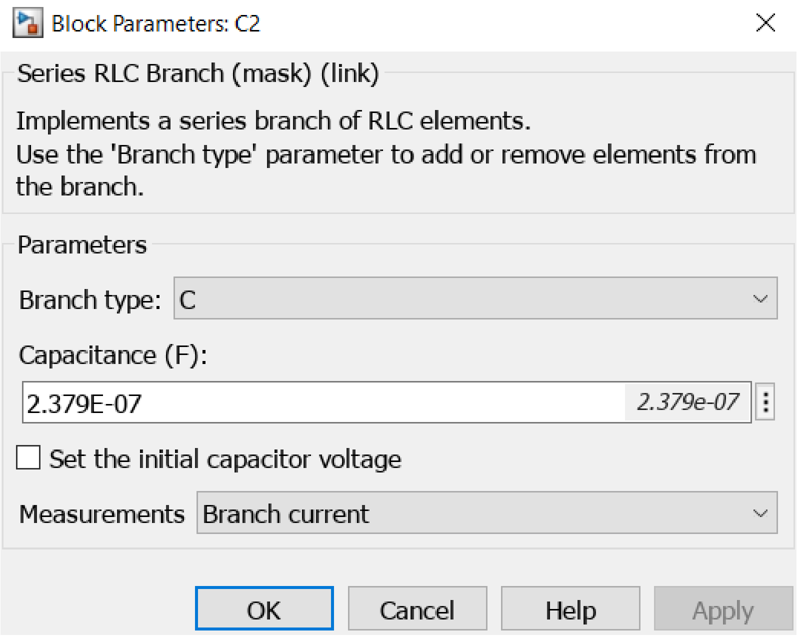
Block Parameters: C2

Series RLC Branch (mask) (link)

Implements a series branch of RLC elements.
Use the 'Branch type' parameter to add or remove elements from the branch.

Parameters

Branch type: C

Capacitance (F):

2.379E-07 2.379e-07

☐ Set the initial capacitor voltage

Measurements Branch current

Figure 4.9 C_2 parameters.

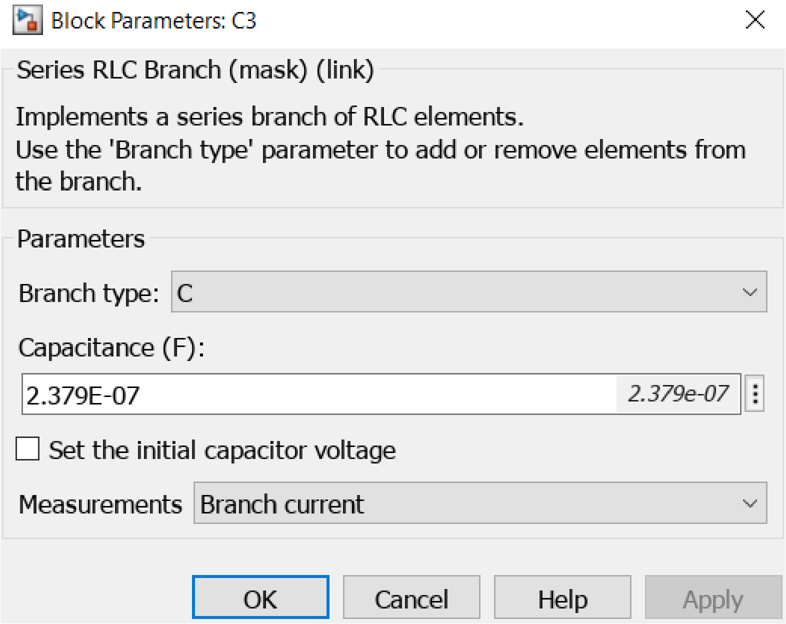

Series RLC Branch (mask) (link)

Implements a series branch of RLC elements.
Use the 'Branch type' parameter to add or remove elements from the branch.

Parameters

Branch type: C

Capacitance (F): 2.379E-07 2.379e-07

☐ Set the initial capacitor voltage

Measurements Branch current

Figure 4.10 C_3 parameters.

4.2.1.4 HF inverter

In order to create a high frequency inverter four IGBT/DIODE needed, as well as a signal to control the opening and closing of the IGBTs. Starting with the signal, one requires a constant, a PWM generator, a logical operator (NOT), a data type conversion, and two Goto blocks. Then using the signal and the four IGBTs a high frequency inverter can be structured. Both signal and inverter can be depicted in figure 4.11 as well as their parameters in the figures bellow.

All IGBTs have the same parameters and all blocks can be found in the library browser by searching each block name.

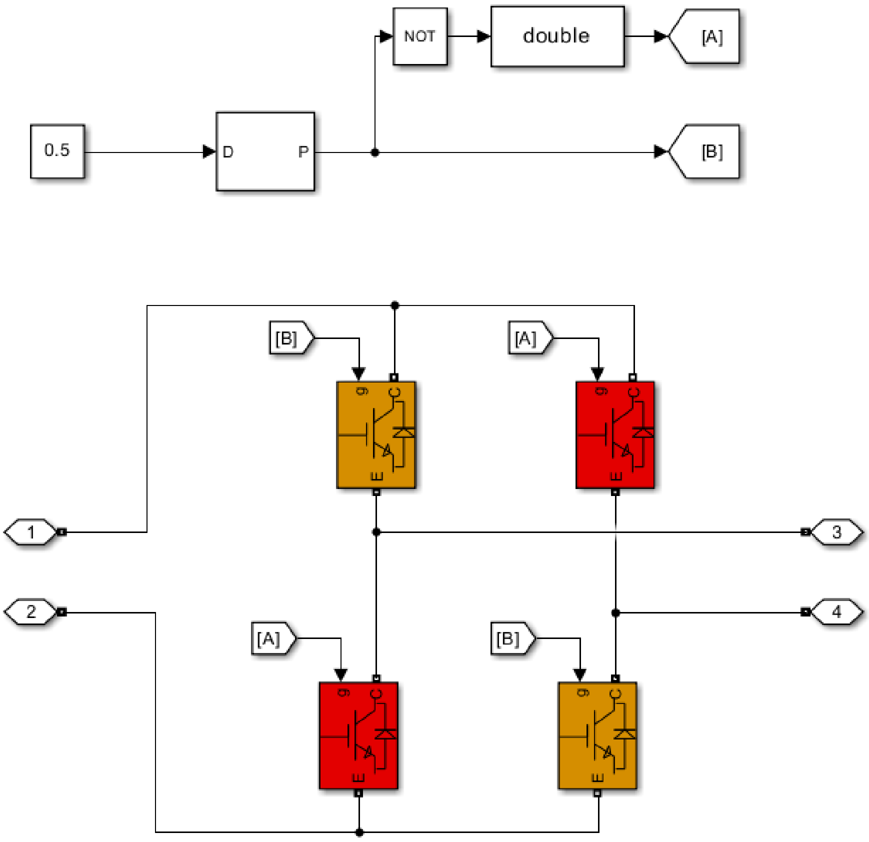

Figure 4.11 High Frequency Inverter.

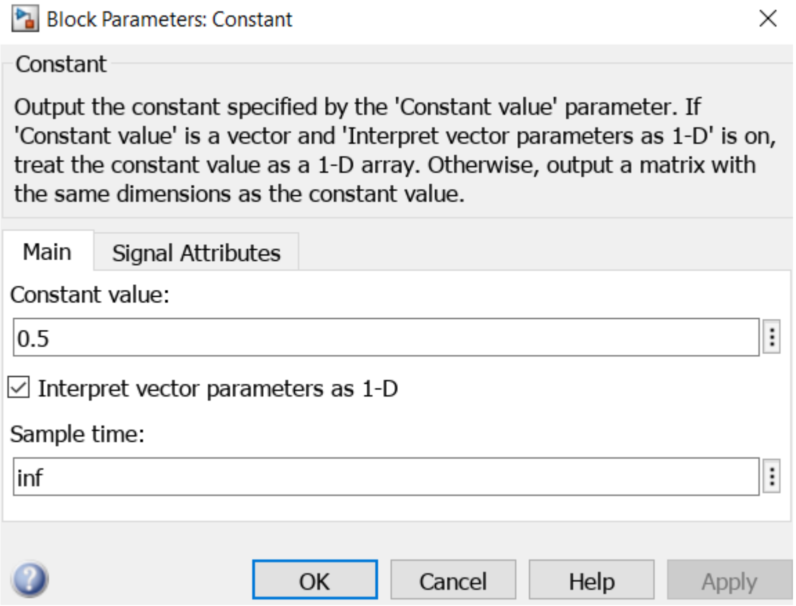

Constant

Output the constant specified by the 'Constant value' parameter. If 'Constant value' is a vector and 'Interpret vector parameters as 1-D' is on, treat the constant value as a 1-D array. Otherwise, output a matrix with the same dimensions as the constant value.

Constant value: 0.5

☑ Interpret vector parameters as 1-D

Sample time: inf

Figure 4.12 Constant block parameters.

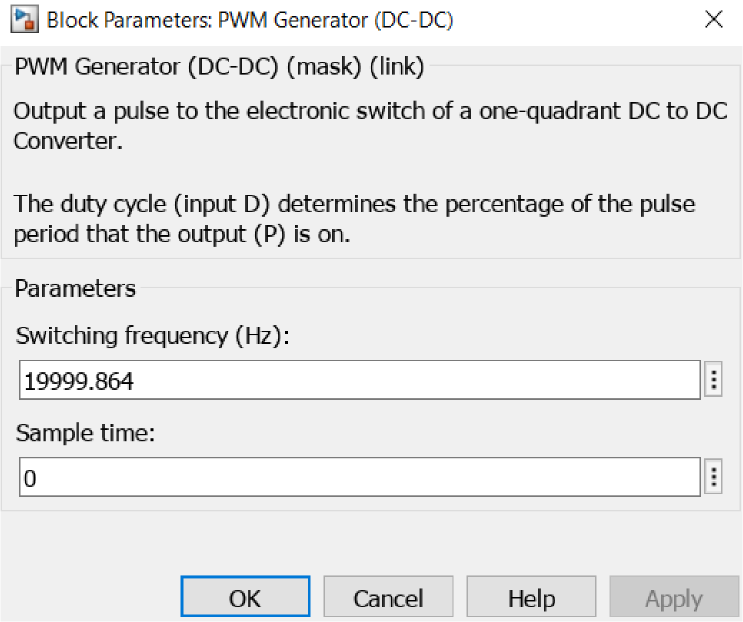

Block Parameters: PWM Generator (DC-DC)

PWM Generator (DC-DC) (mask) (link)

Output a pulse to the electronic switch of a one-quadrant DC to DC Converter.

The duty cycle (input D) determines the percentage of the pulse period that the output (P) is on.

Parameters

Switching frequency (Hz): 19999.864

Sample time: 0

Figure 4.13 PWM Generator block parameters.

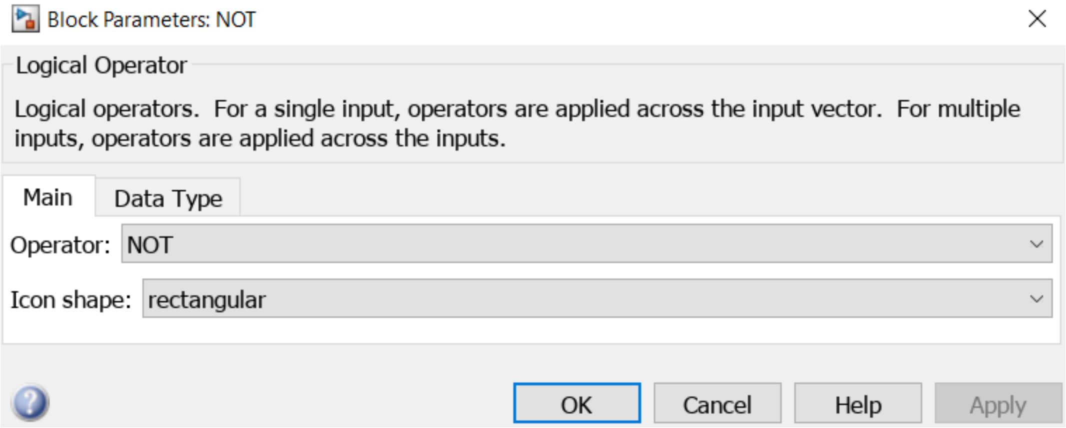

Block Parameters: NOT

Logical Operator

Logical operators. For a single input, operators are applied across the input vector. For multiple inputs, operators are applied across the inputs.

Operator: NOT

Icon shape: rectangular

Figure 4.14 Logical Operator block parameters.

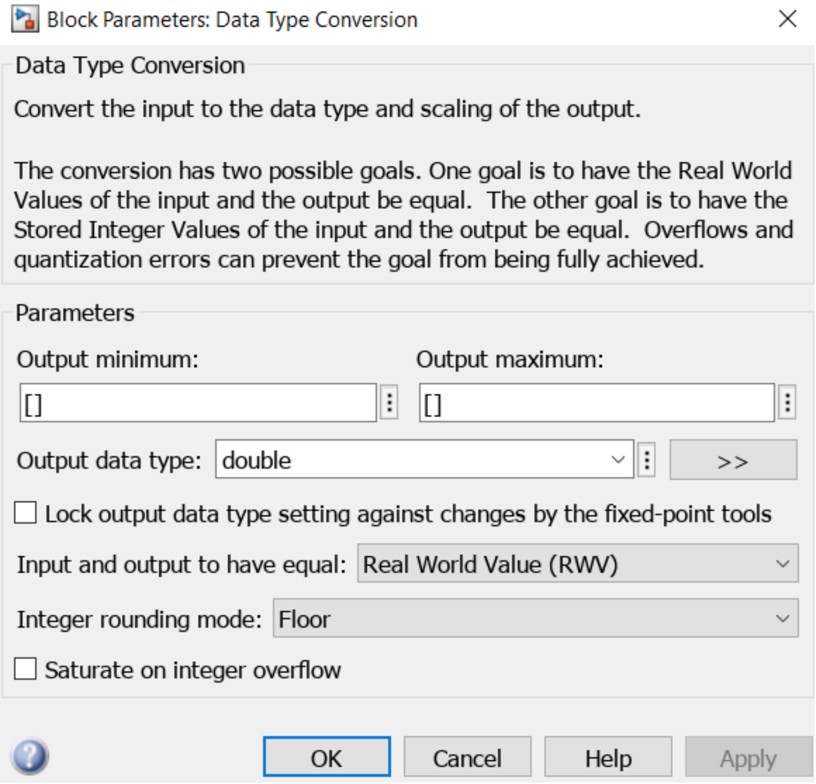

Block Parameters: Data Type Conversion

Data Type Conversion

Convert the input to the data type and scaling of the output.

The conversion has two possible goals. One goal is to have the Real World Values of the input and the output be equal. The other goal is to have the Stored Integer Values of the input and the output be equal. Overflows and quantization errors can prevent the goal from being fully achieved.

Parameters

Output minimum: []

Output maximum: []

Output data type: double

☐ Lock output data type setting against changes by the fixed-point tools

Input and output to have equal: Real World Value (RWV)

Integer rounding mode: Floor

☐ Saturate on integer overflow

Figure 4.15 Data Type Conversion block parameters.

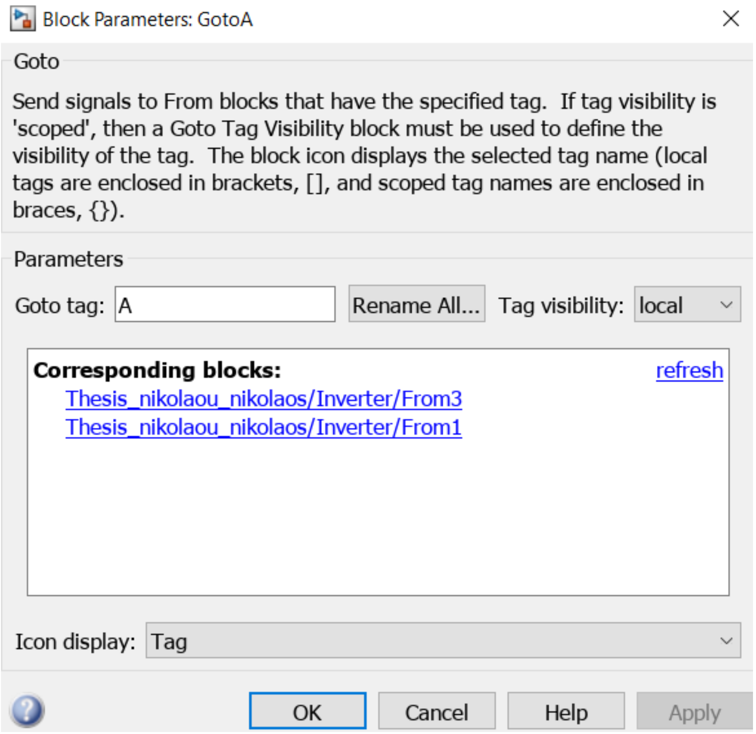

Block Parameters: GotoA

Goto

Send signals to From blocks that have the specified tag. If tag visibility is 'scoped', then a Goto Tag Visibility block must be used to define the visibility of the tag. The block icon displays the selected tag name (local tags are enclosed in brackets, [], and scoped tag names are enclosed in braces, {}).

Parameters

Goto tag: A

Tag visibility: local

Corresponding blocks:

Thesis_nikolaou_nikolaos/Inverter/From3

Thesis_nikolaou_nikolaos/Inverter/From1

Icon display: Tag

Figure 4.16 GotoA block parameters.

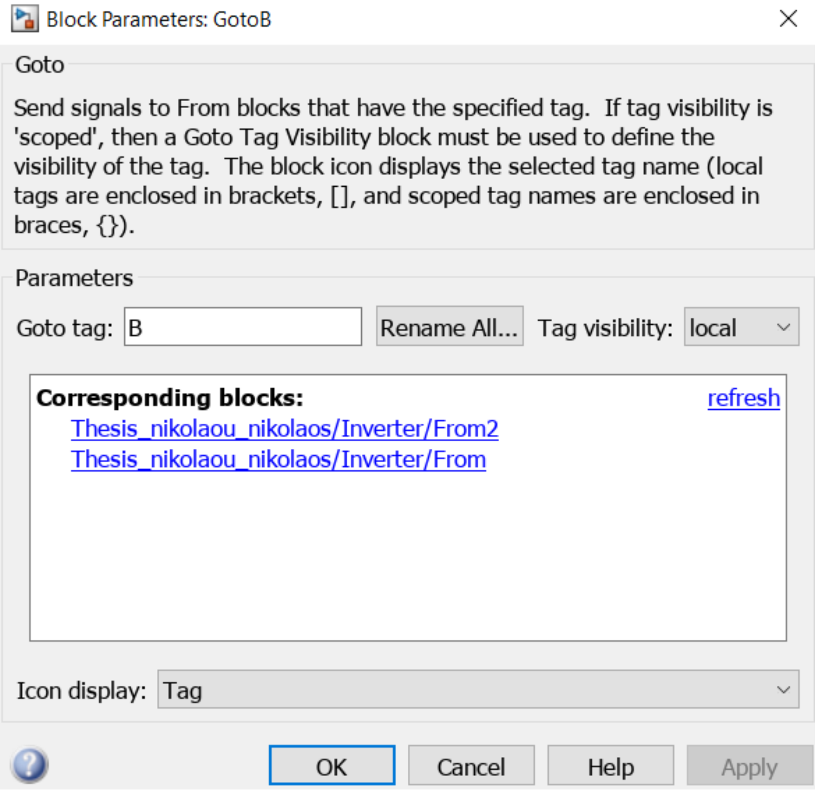

Goto

Send signals to From blocks that have the specified tag. If tag visibility is 'scoped', then a Goto Tag Visibility block must be used to define the visibility of the tag. The block icon displays the selected tag name (local tags are enclosed in brackets, [], and scoped tag names are enclosed in braces, {}).

Parameters

Goto tag: B

Rename All...

Tag visibility: local

Corresponding blocks:

refresh

Thesis_nikolaou_nikolaos/Inverter/From2

Thesis_nikolaou_nikolaos/Inverter/From

Icon display: Tag

Figure 4.17 GotoB block parameters.

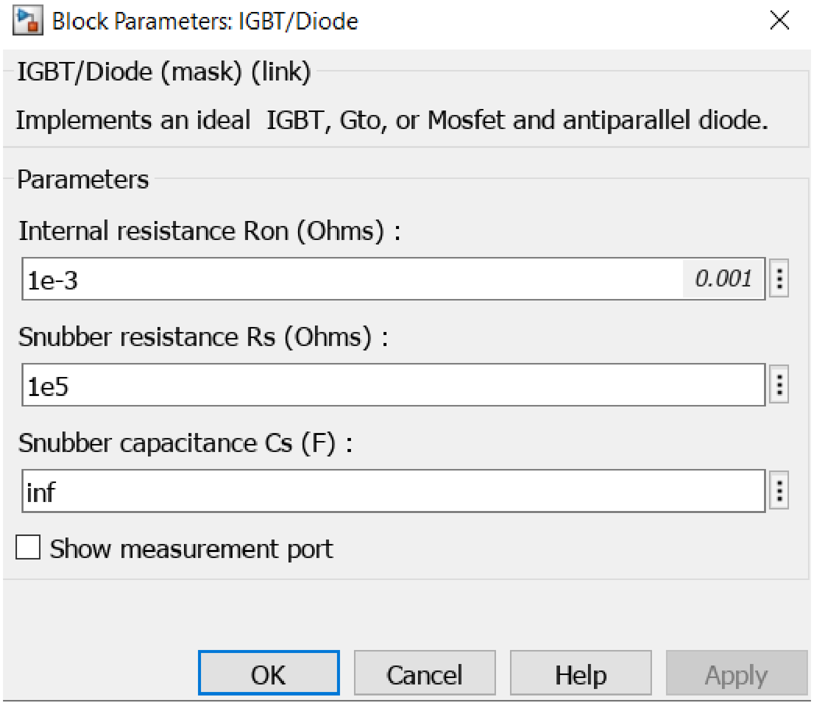

IGBT/Diode (mask) (link)

Implements an ideal IGBT, Gto, or Mosfet and antiparallel diode.

Parameters

Internal resistance Ron (Ohms) : 1e-3 (0.001)

Snubber resistance Rs (Ohms) : 1e5

Snubber capacitance Cs (F) : inf

☐ Show measurement port

Figure 4.18 IGBT/Diode block parameters.

4.2.1.5 Mutual inductance

Mutual inductance can be found in the library browser, if “Mutual inductance” searched. For this model a two windings mutual inductance with equal mutual terms is used with parameters as shown in the figure below. Parameters of mutual inductance will change depends on simulation.

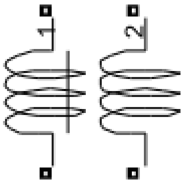

Figure 4.19 Mutual inductance.

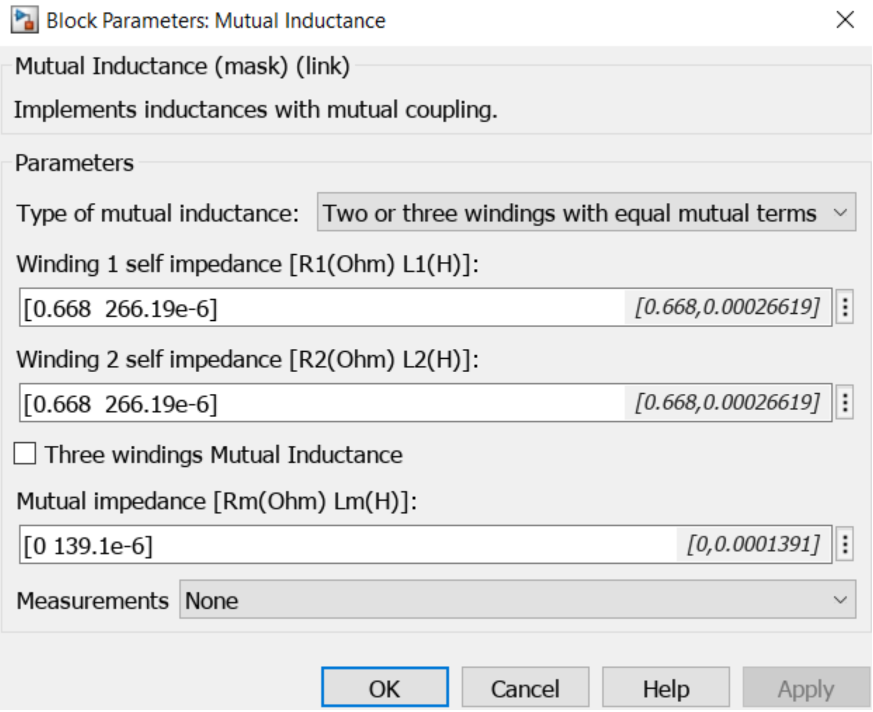

Block Parameters: Mutual Inductance

Mutual Inductance (mask) (link)

Implements inductances with mutual coupling.

Parameters

Type of mutual inductance: Two or three windings with equal mutual terms

Winding 1 self impedance [R1(Ohm) L1(H)]: [0.668 266.19e-6] [0.668,0.00026619]

Winding 2 self impedance [R2(Ohm) L2(H)]: [0.668 266.19e-6] [0.668,0.00026619]

☐ Three windings Mutual Inductance

Mutual impedance [Rm(Ohm) Lm(H)]: [0 139.1e-6] [0,0.0001391]

Measurements None

Figure 4.20 Mutual Inductance block parameters.

4.2.1.6 Vehicle rectifier

In order to create the vehicle rectifier four Diodes required as well as a RLC branch. While the diodes in a full-wave bridge rectifier undertake the initial AC-to-DC conversion, the capacitor is indispensable for refining this output. It acts as a buffer, a smoother, and a ripple minimizer, ensuring that the rectified DC output is both stable and efficient for downstream applications. Specifically, the primary responsibility of the capacitor in this configuration is to smooth out the pulsating DC waveform. Without the parallel-connected capacitor, the rectified output manifests as a series of peaks, corresponding directly to the AC waveform's peaks. The capacitor acts as a temporary energy storage device; it charges during voltage peaks and releases energy during the valleys, effectively filling in the gaps. The resultant waveform, therefore, becomes steadier, resembling a more constant DC voltage.

Ripple voltage is an undesirable byproduct of the rectification process. It refers to the AC components that remain superimposed on the DC output. A crucial function of the capacitor is to minimize this ripple, ensuring the output is as "clean" as possible. The capacitance value plays a decisive role here: larger capacitors typically yield reduced ripple voltages, though practical considerations and diminishing returns limit the viable capacitance value.

Vehicle rectifier can be depicted in figure 4.21 as well as its components parameters in the figures bellow.

All blocks can be found in the library browser by searching each block name.

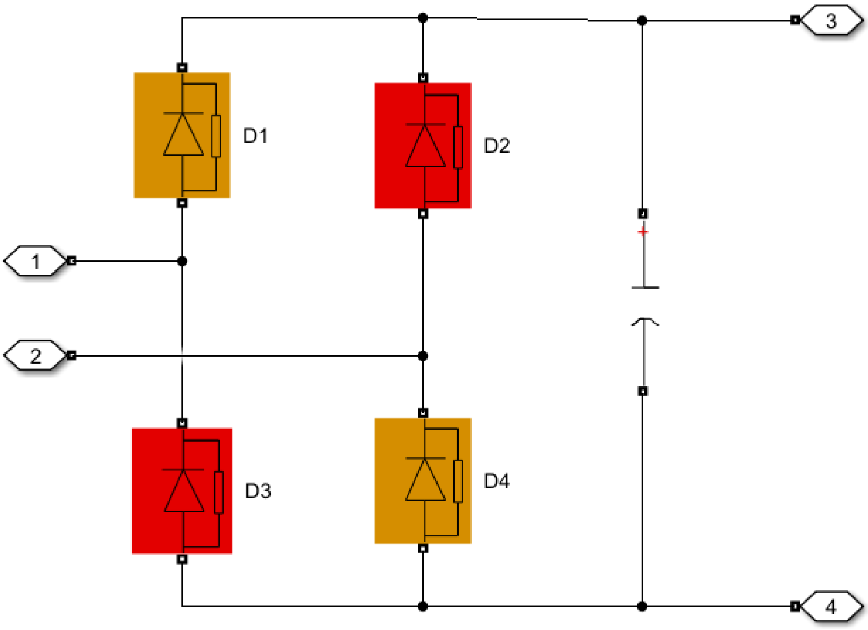

Figure 4.21 Vehicle rectifier.

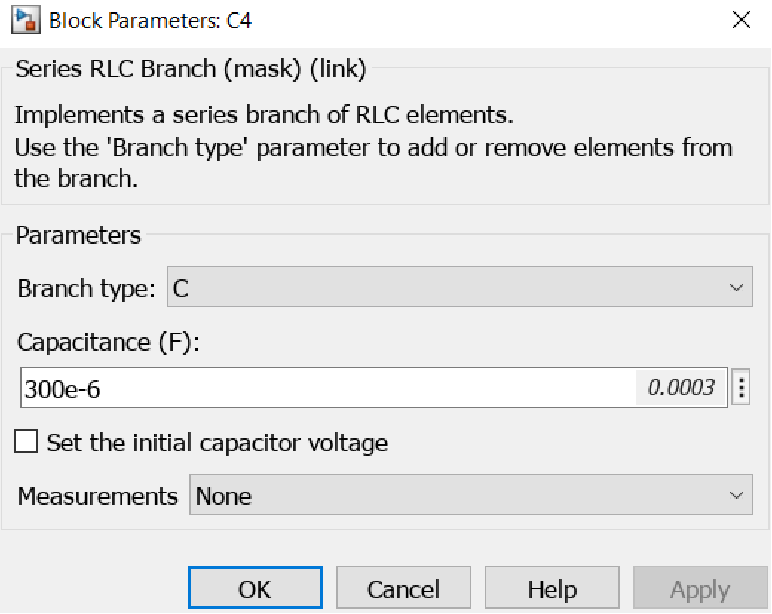

Block Parameters: C4

Series RLC Branch (mask) (link)

Implements a series branch of RLC elements.
Use the 'Branch type' parameter to add or remove elements from the branch.

Parameters

Branch type: C

Capacitance (F): 300e-6 0.0003

☐ Set the initial capacitor voltage

Measurements None

Figure 4.22 C_4 block parameters.

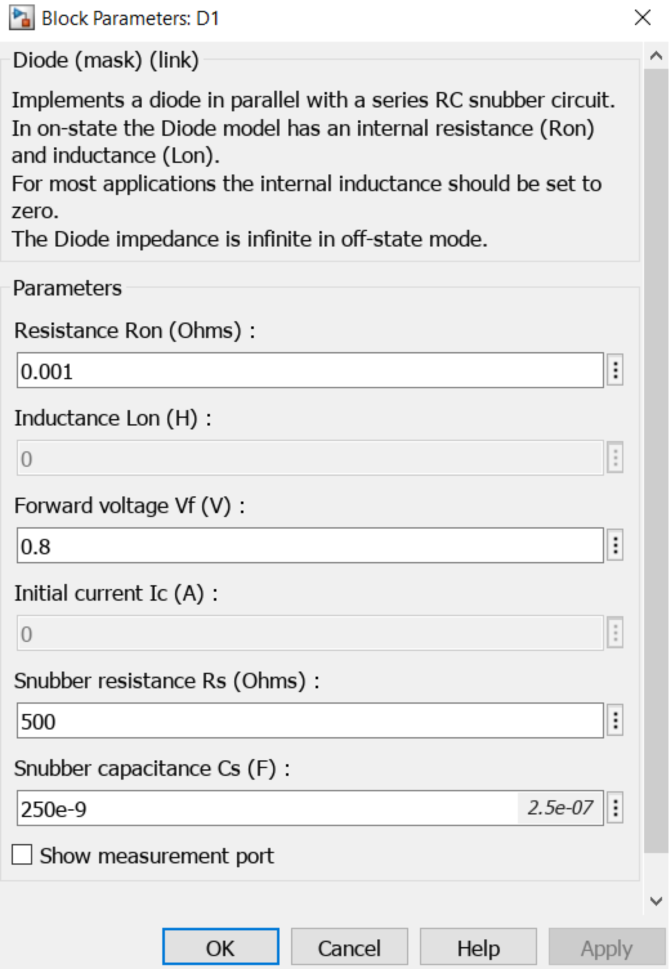

Block Parameters: D1

Diode (mask) (link)

Implements a diode in parallel with a series RC snubber circuit.
In on-state the Diode model has an internal resistance (Ron) and inductance (Lon).
For most applications the internal inductance should be set to zero.
The Diode impedance is infinite in off-state mode.

Parameters

Resistance Ron (Ohms) : 0.001

Inductance Lon (H) : 0

Forward voltage Vf (V) : 0.8

Initial current Ic (A) : 0

Snubber resistance Rs (Ohms) : 500

Snubber capacitance Cs (F) : 250e-9 2.5e-07

☐ Show measurement port

Figure 4.23 D_1 block parameters.

4.2.1.7 Li-ion battery.

Li-ion battery can be found in the library browser, if “Battery” searched. For this model a li-ion battery will be used as it is the most common battery in electric vehicles with parameters as shown in the figure below.

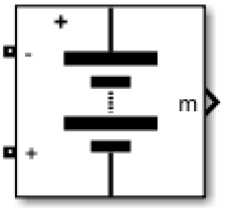

Figure 4.24 Li-Ion Battery.

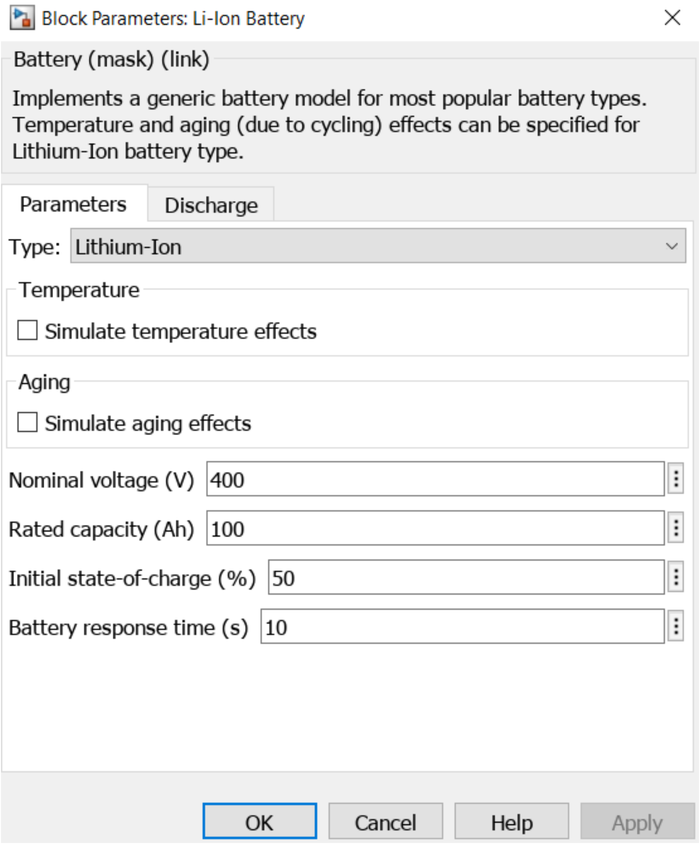

Block Parameters: Li-Ion Battery

Battery (mask) (link)

Implements a generic battery model for most popular battery types. Temperature and aging (due to cycling) effects can be specified for Lithium-Ion battery type.

Type: Lithium-Ion

Temperature

☐ Simulate temperature effects

Aging

☐ Simulate aging effects

Nominal voltage (V) 400

Rated capacity (Ah) 100

Initial state-of-charge (%) 50

Battery response time (s) 10

Figure 4.25 Li-Ion Battery block parameters.

4.2.1.8 Mathematical model

When it comes to creating power electronics and wireless transformer coils, the RIPT is among the most well-known and sophisticated variations of the conventional IPT. The RIPT for electric vehicles is schematically depicted in Figure 2.6. Similar to other WPTs, the primary winding or transmitter receives power from the HF AC source that has been converted from the main AC voltage. Power is sent to the receiver or secondary coil using various magnetic fields. Additional power circuits and filter circuitry transform the received electricity to DC for the battery system of the EVs.

For this model resonant inductive power transfer will be utilized in series-series topology. The calculation of the resonance frequency of primary and secondary coil can be calculated by (2.1) as it mentioned in 2.2.11.

$$f_{r(p,s)} = \frac{1}{2\pi\sqrt{L_{p,s} \cdot C_{p,s}}} \tag{4.1}$$

The coupling coefficient can be determined using Eq. (2.2).

$$k = \frac{L_m}{\sqrt{L_p L_s}} \tag{4.2}$$

The coil's quality factor Q can be determinate by utilizing the (2.3).

$$Q = \frac{\omega L_{p,s}}{R_{p,s}} = \frac{2\pi f \cdot L_{p,s}}{R_{p,s}} \tag{4.3}$$

The capacitance of transmitter and receiver can be given by

$$C_{p,s} = \frac{1}{\omega_0^2 L_{p,s}} \tag{4.1}$$

The total efficiency is

$$\eta = \frac{P_{in}}{P_{out}} \tag{4.2}$$

In order to achieve maximum wireless power transfer and efficiency

$$C_p = C_s\,, L_p = L_s\,, \omega_{Cp} = \omega_{Cs}$$

For a 20kHz system with self-inductances 0,00026619 H the calculated parameters are

$$C_p = C_s = 2{,}379E - 07\ F\,, L_p = L_s = 0{,}00026619\ H\,, \omega_{Cp} = \omega_{Cs} = \ 125662{,}8516$$

The self-resistance of the coils 0,663 Ω and the internal resistance of the battery at 0,04 Ω.

4.2.1.9 Subsystem

For the model a subsystem has been created that can calculates the mutual inductance considering the axial distance between the coils as well as the lateral misalignment between them. It also considers the angle of angular misalignment.

The equation that represents the mutual inductance M’ between two filamentary circular coils that may have lateral and angular misalignments is the follow:

$$M' = \frac{\mu_0 \cdot N_1 \cdot N_2}{4 \cdot \pi} \int_0^{2\pi} \int_0^{2\pi} \frac{r_1 r_2 (\sin\theta \sin\varphi + \cos\alpha \cos\theta \cos\varphi) d\theta d\varphi}{\sqrt{(r_1 \cos\theta - r_2 \cos\varphi)^2 + (r_1 \sin\theta - r_2 \sin\varphi \cos\alpha - c)^2 + (r_2 \sin\varphi \cos\alpha - d)^2}}$$

Where:

- M’ is the mutual inductance with misalignments.
- μ0 is the magnetic permeability of vacuum.
- N1, N2 are the number of turns of the two coils.
- r1, r2 are the radii of the two coils.
- Θ, φ are the angular positions along the coils.
- α is the angle of angular misalignment.
- c is the lateral misalignment between the coils.
- d is the axial distance between the coils.

MATLAB function has been created in order to calculate by utilizing the equation mentioned before. The subsystems consist four constants and three variables as it can depicted in figure 4.26.

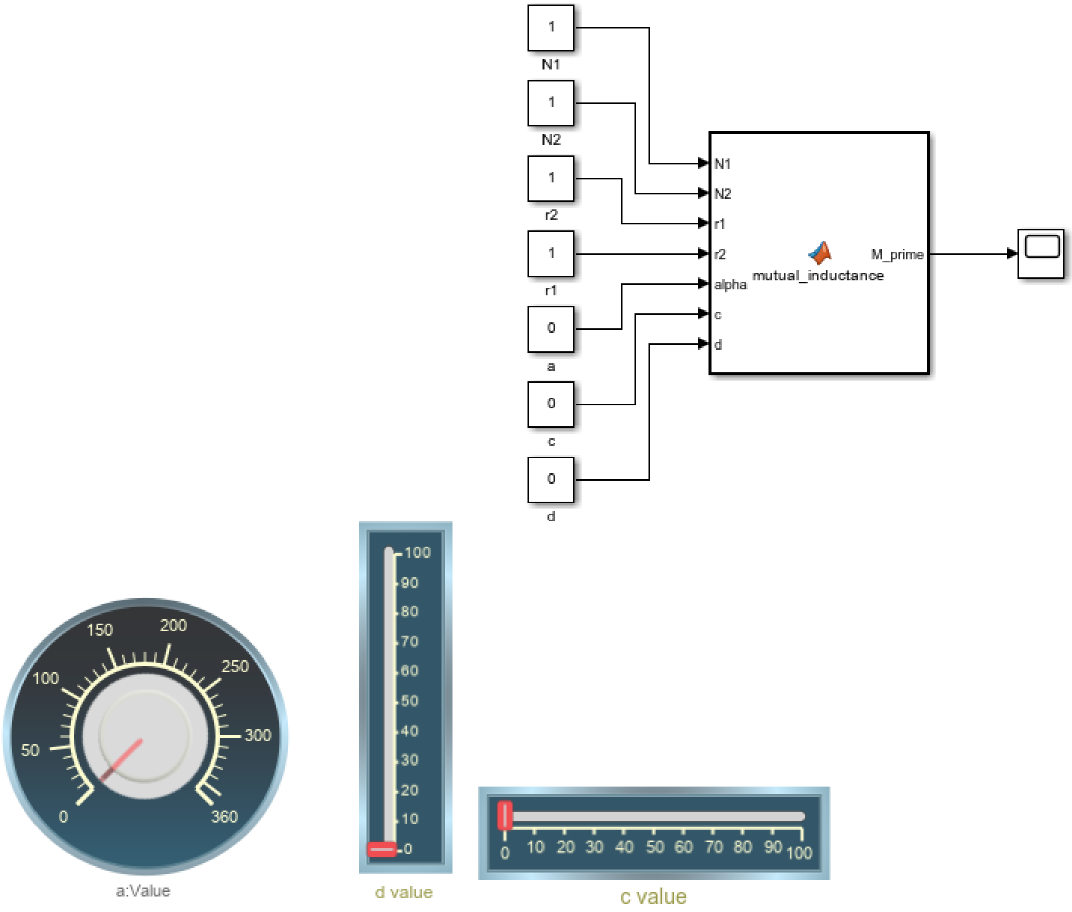

Figure 4.26 Mutual Inductance Calculation Subsystem.

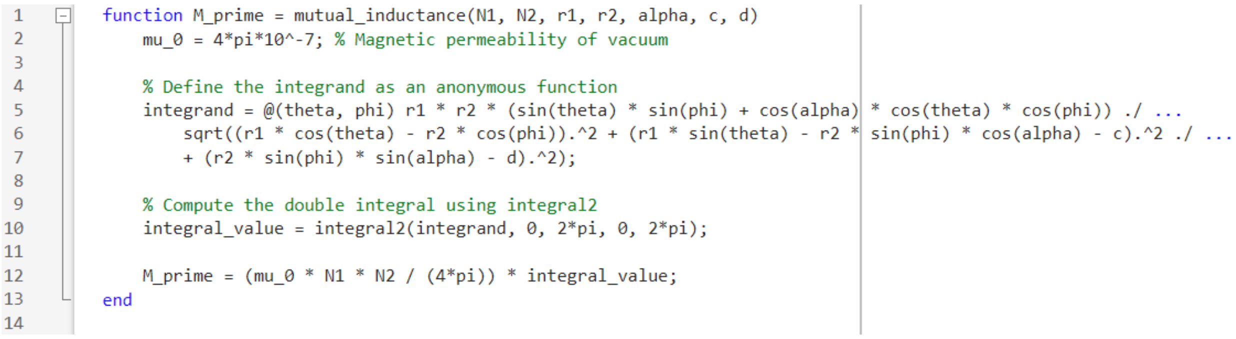

```
function M_prime = mutual_inductance(N1, N2, r1, r2, alpha, c, d)
    mu_0 = 4*pi*10^-7; % Magnetic permeability of vacuum

    % Define the integrand as an anonymous function
    integrand = @(theta, phi) r1 * r2 * (sin(theta) * sin(phi) + cos(alpha) * cos(theta) * cos(phi)) ./ ...
        sqrt((r1 * cos(theta) - r2 * cos(phi)).^2 + (r1 * sin(theta) - r2 * sin(phi) * cos(alpha) - c).^2 ./ ...
        + (r2 * sin(phi) * sin(alpha) - d).^2);

    % Compute the double integral using integral2
    integral_value = integral2(integrand, 0, 2*pi, 0, 2*pi);

    M_prime = (mu_0 * N1 * N2 / (4*pi)) * integral_value;
end
```

Figure 4.27 Function

4.2.2 Assumptions

In the simulation of the EV dynamic charging system, several key assumptions were made to set the context and boundaries. The study is based on a standard typical electric vehicle model with a battery capacity of 100Ah. The vehicle is envisioned to travel on a straight, flat road with minimal incline or decline, and without any sudden accelerations or decelerations. The charging infrastructure on the road consists of filamentary circular coils, each connected to a consistent voltage source. Vehicle speed has not been considered. Clear weather conditions are assumed, devoid of any rain, snow, or other environmental factors that might influence charging efficiency. There's an implicit assumption of perfect alignment between the embedded road coils and the vehicle's receiving coil, ensuring optimal power transfer. If there is any misalignment, it can be calculated with the help of the subsystem mentioned before and then the mutual inductance value can be added to the simulation. The simulation does not consider any external electromagnetic interference that might disrupt the wireless power transfer. The vehicle's battery typically starts at a 50% state of charge in all scenarios unless stated otherwise. Overheating or overcharging are not considered. The simulation overlooks potential disruptions or changes in driving behavior due to other vehicles on the road. The energy source for the road coils is consistently reliable, with no fluctuations in power supply. Other vehicle systems, such as air conditioning or entertainment, are believed to have a negligible impact on the battery's state of charge. Lastly, the road surface is in optimal condition, free from potholes, debris, or other obstacles that might affect the vehicle's trajectory or alignment with the charging coils.

4.3 Simulation 1

In the first simulation the mutual inductance calculated 139.1e-6 H (0.0001391) as it depicted in figure 4.28. Parameters values for this calculation are shown there too. Assuming perfect alignment and a typical gap of 100mm in order to calculate the efficiency.

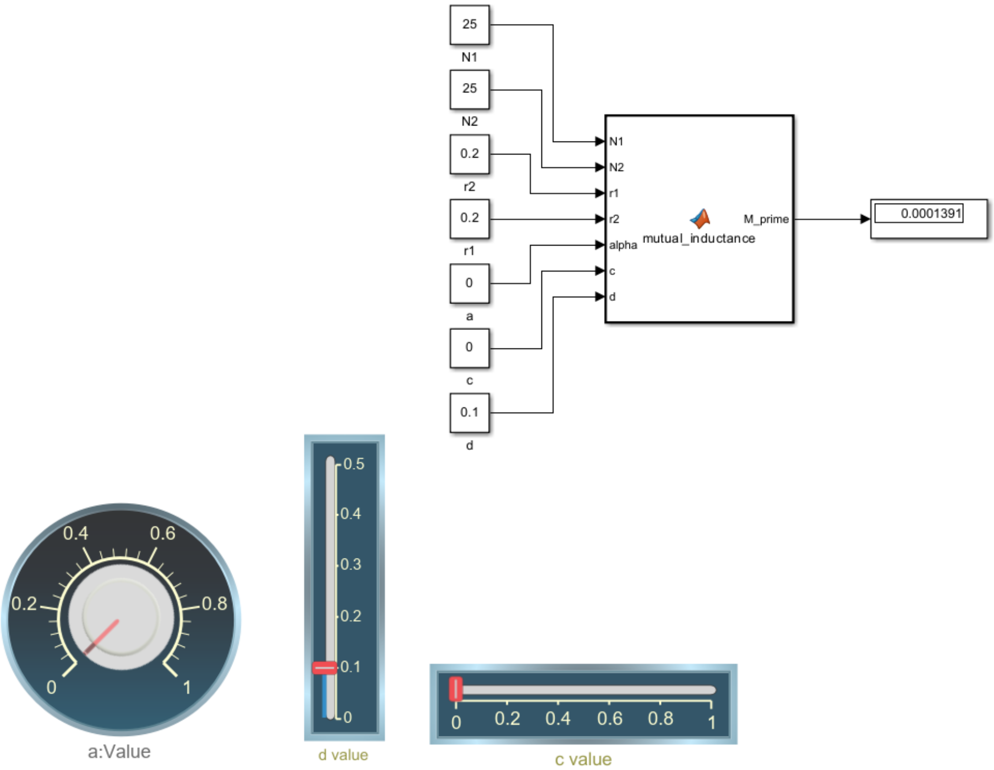

Figure 4.28 Mutual Inductance calculation for simulation 1.

The calculated value has to be added in the block parameters of the mutual inductance (figure 4.29)

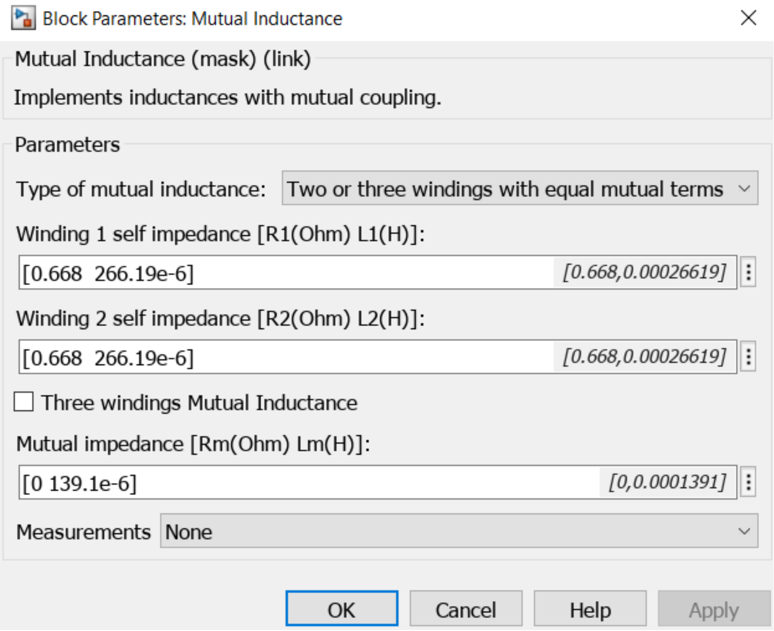

Block Parameters: Mutual Inductance

Mutual Inductance (mask) (link)

Implements inductances with mutual coupling.

Parameters

Type of mutual inductance: Two or three windings with equal mutual terms

Winding 1 self impedance [R1(Ohm) L1(H)]: [0.668 266.19e-6] *[0.668,0.00026619]*

Winding 2 self impedance [R2(Ohm) L2(H)]: [0.668 266.19e-6] *[0.668,0.00026619]*

☐ Three windings Mutual Inductance

Mutual impedance [Rm(Ohm) Lm(H)]: [0 139.1e-6] *[0,0.0001391]*

Measurements None

Figure 4.29 Mutual Inductance block parameters for Simulation 1.

The whole system of the simulation can be depicted in figure 4.30. Values such as $P_{in,\ ac}$, $Q_{in,\ ac}$, P_{dc} after the rectifier, $P_{bat,\ input}$ are shown in display blocks. Specifically $P_{in,\ ac} = 6005W$, $Q_{in,\ ac} = 2405Var$, $P_{dc} = 5945W$ and $P_{bat,\ input} = 5096W$.

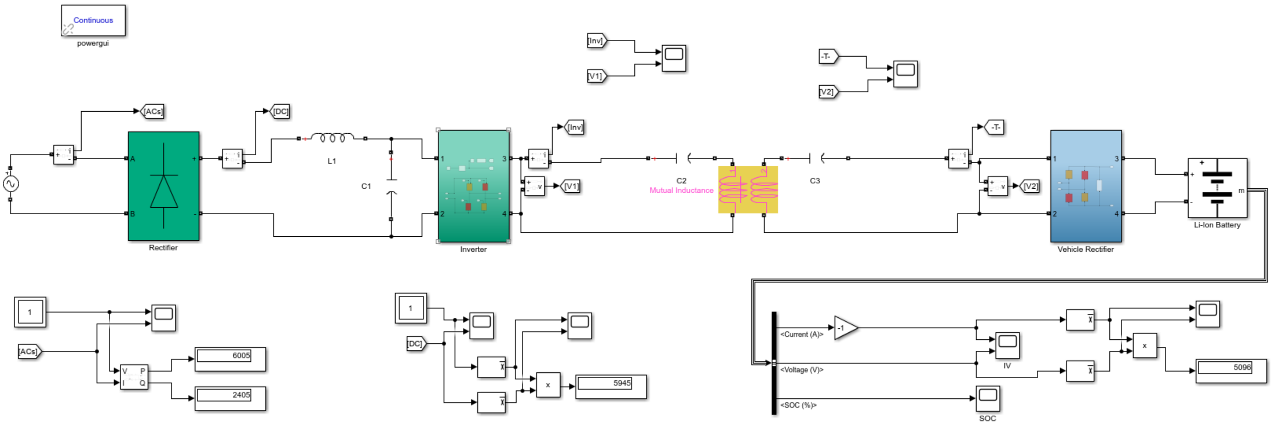

Figure 4.30 Charging system of Simulation 1.

From the AC source Scope (Figure 4.31), Voltage and current are measured. Scopes waveform shows voltage peak value at 350 Volt and current at 52.5 Ampere.

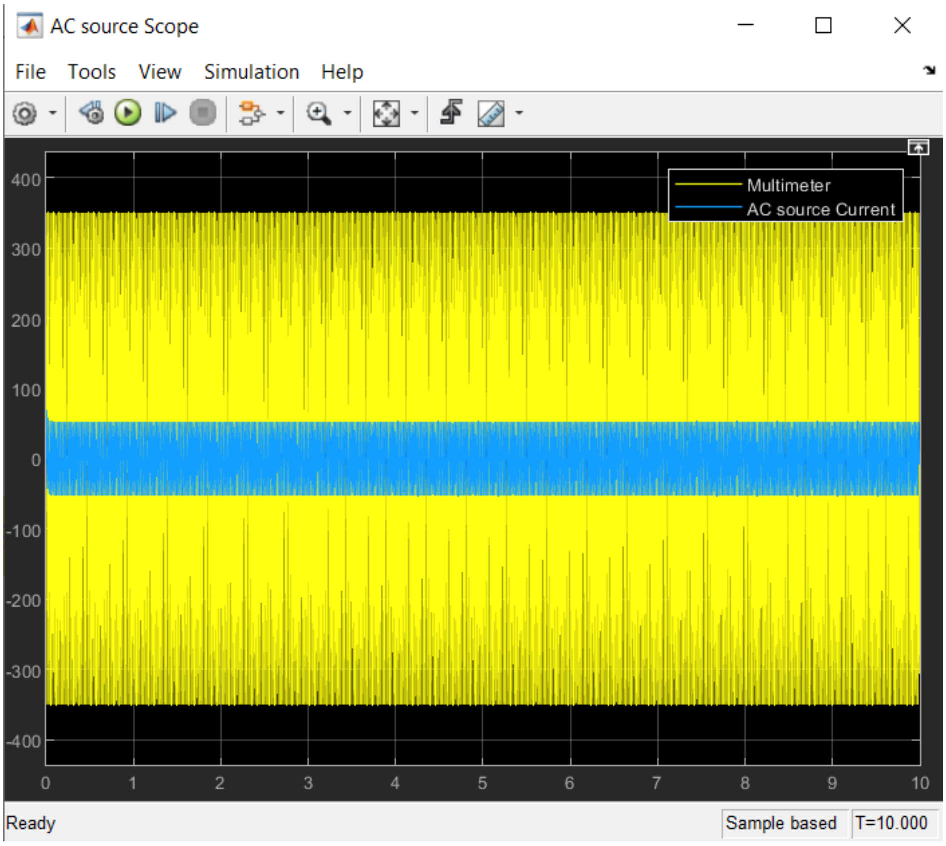

Figure 4.31 AC source Scope of Simulation 1.

The DC Scope (Figure 4.32), shows DC measurements after the rectifier and with the process of considering mean values DC Scope1 (Figure 4.33) shows voltage dc value of 293 volt and dc current value of 20.25 Ampere. Measurements can be taken by using the cursor measurements button located rightmost in toolbar.

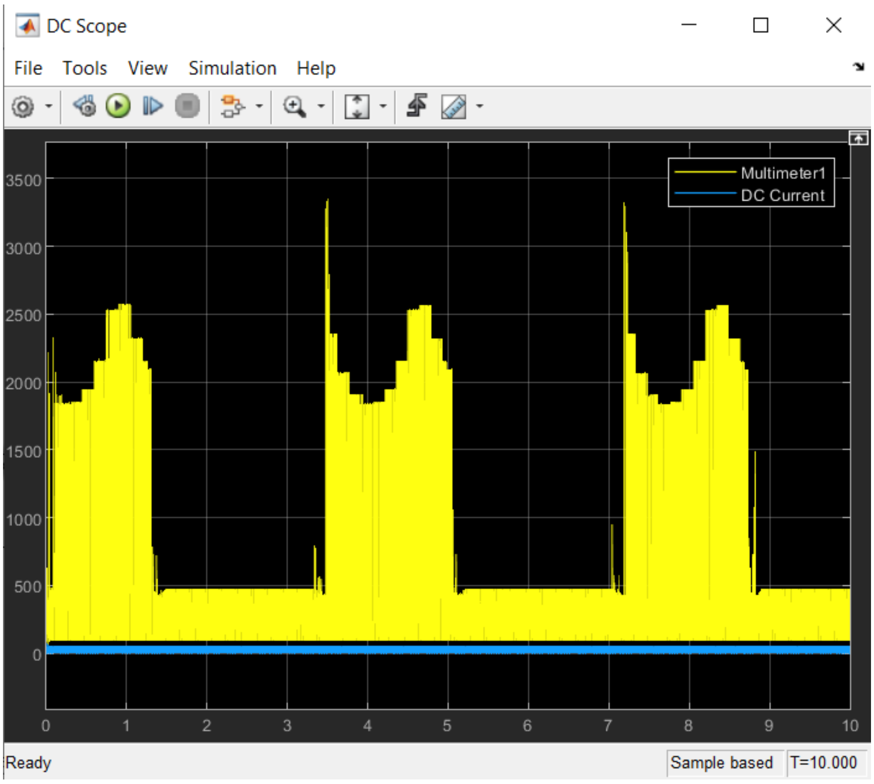

Figure 4.32 DC Scope of Simulation 1.

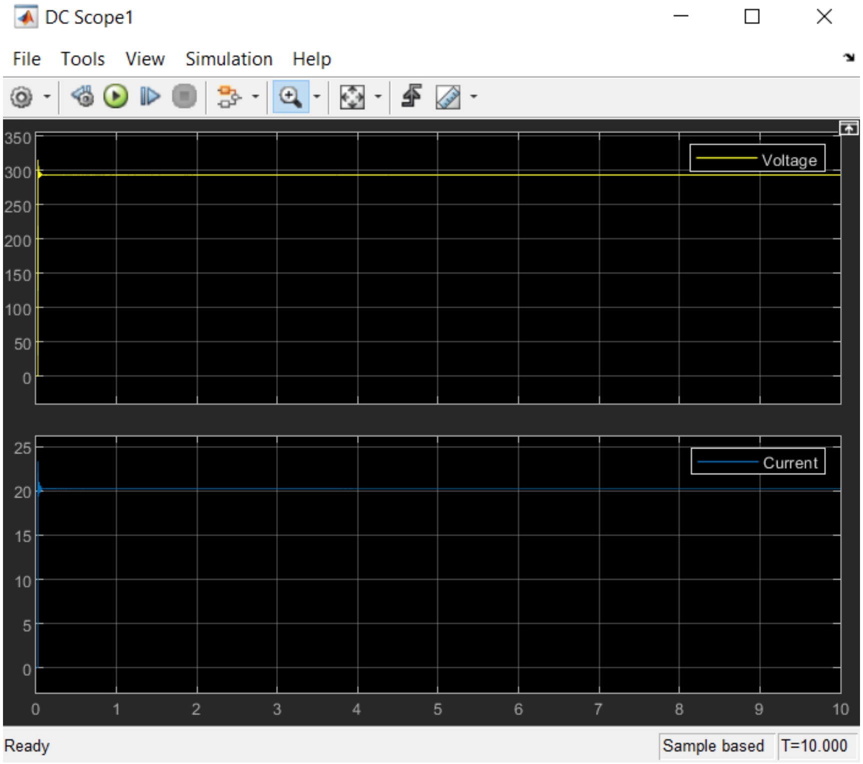

Figure 4.33 DC Scope1 of Simulation 1.

From the HF Scope (Figure 4.34) information about the waveforms of current and voltage after the high frequency inverter can be taken. Peak value of current shown 33 Ampere and voltage 455 volt.

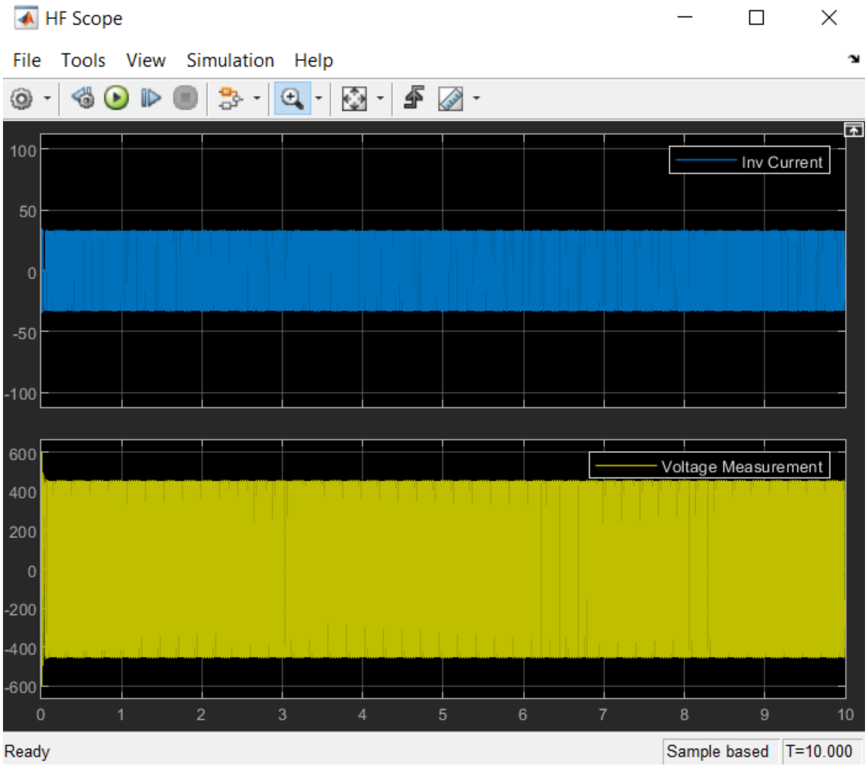

Figure 4.34 HF Scope of Simulation 1.

From the Vehicle Rectifier Scope (Figure 4.34), voltage and current are measured before the vehicle rectifier. Scopes waveform shows voltage peak value at 433.5 Volt and current at 32 Ampere.

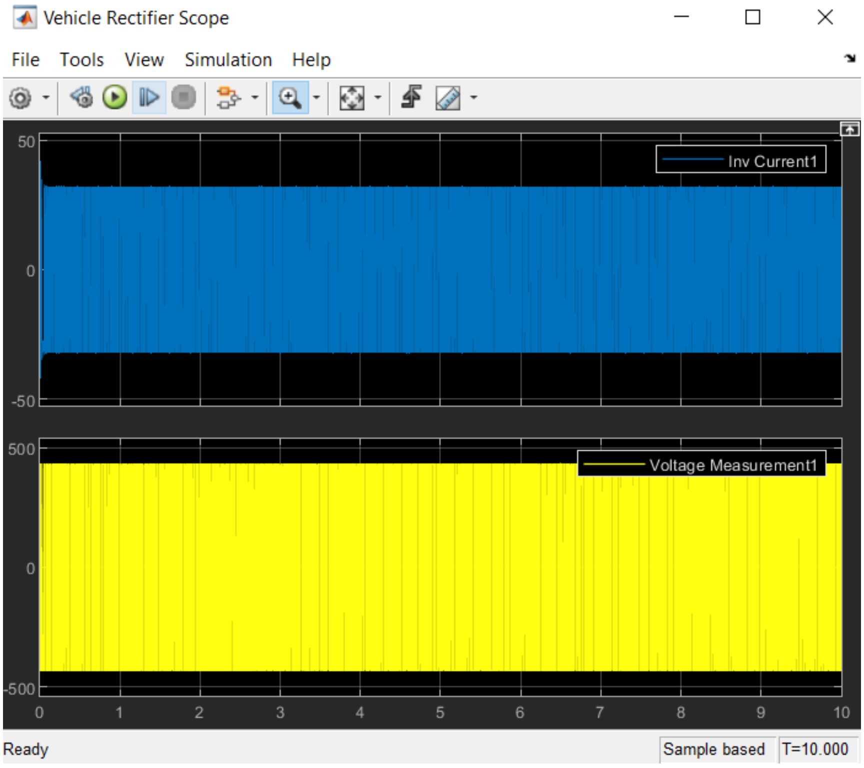

Figure 4.35 Vehicle Rectifier Scope of Simulation 1.

The IV Scope (Figure 4.36), shows DC measurements at the battery and with the process of considering mean values Battery Scope (Figure 4.37) shows dc voltage value of 431.5 volt and dc current value of 11.8 Ampere.

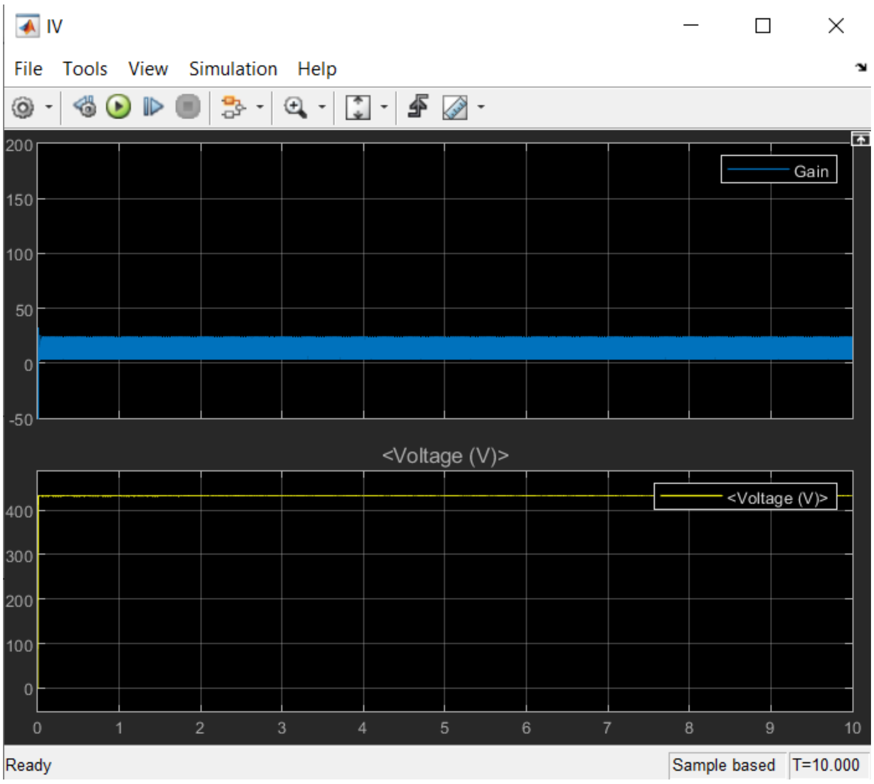

Figure 4.36 IV Scope of Simulation 1.

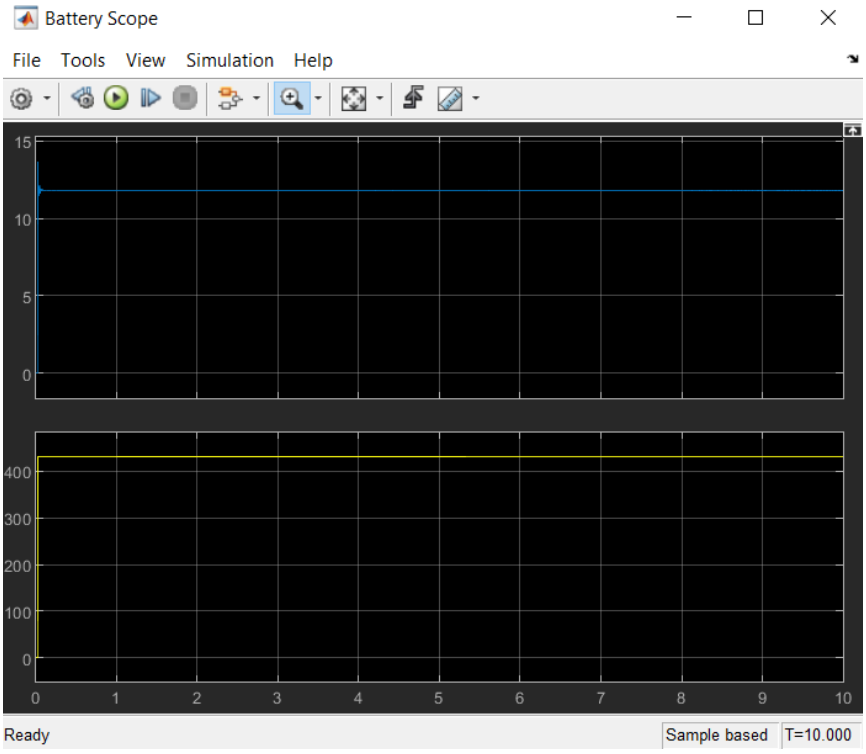

Figure 4.37 Battery Scope of Simulation 1.

The last scope considered; SOC Scope (Figure 4.38) gives information about the state of charge during the process of charging. After the 10 second simulation the soc (%) is 50.0375% with the initial soc at 50%.

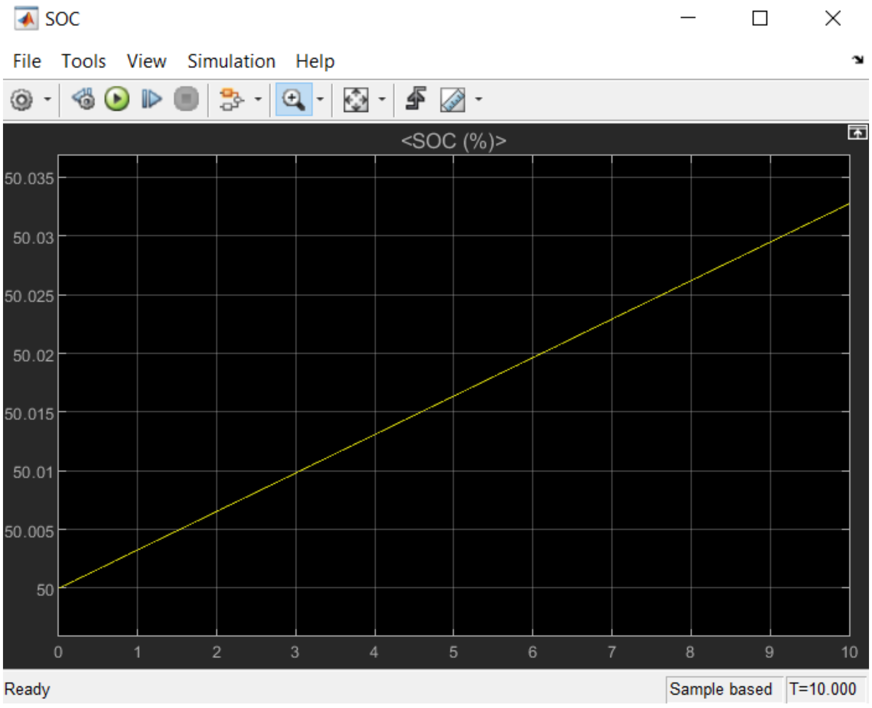

Figure 4.38 SOC Scope of Simulation 1.

As it can observed from the simulation the efficiency of the system is at 84.86%.

4.4 Simulation 2

In the second simulation the mutual inductance calculated 54.67e-6 H (0.00005467) as it depicted in figure 4.39. Parameters values for this calculation are shown there too. Assuming 200mm alignment and a typical gap of 100mm in order to calculate the efficiency.

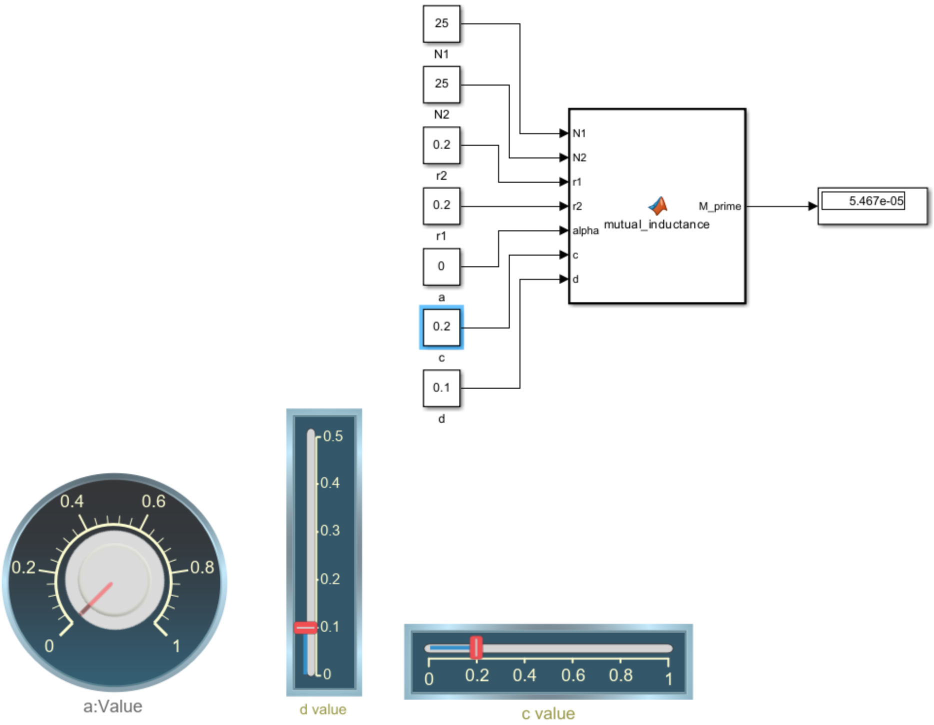

Figure 4.39 Mutual Inductance calculation for simulation 2.

The calculated value has to be added in the block parameters of the mutual inductance (figure 4.40).

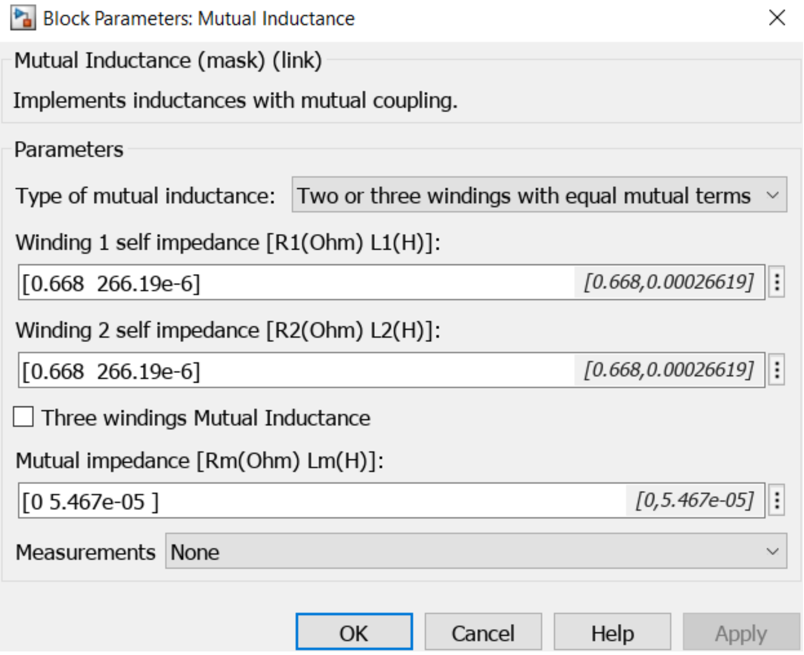

Block Parameters: Mutual Inductance

Mutual Inductance (mask) (link)

Implements inductances with mutual coupling.

Parameters

Type of mutual inductance: Two or three windings with equal mutual terms

Winding 1 self impedance [R1(Ohm) L1(H)]: [0.668 266.19e-6] *[0.668,0.00026619]*

Winding 2 self impedance [R2(Ohm) L2(H)]: [0.668 266.19e-6] *[0.668,0.00026619]*

☐ Three windings Mutual Inductance

Mutual impedance [Rm(Ohm) Lm(H)]: [0 5.467e-05] *[0,5.467e-05]*

Measurements None

Figure 4.40 Mutual Inductance block parameters for Simulation 2.

The whole system of the simulation can be depicted in figure 4.41. Values such as $P_{in, ac}$, $Q_{in, ac}$, P_{dc} after the rectifier, $P_{bat, input}$ are shown in display blocks. Specifically $P_{in, ac} = 13580W$, $Q_{in, ac} = 5442Var$, $P_{dc} = 12050W$ and $P_{bat, input} = 10270W$.

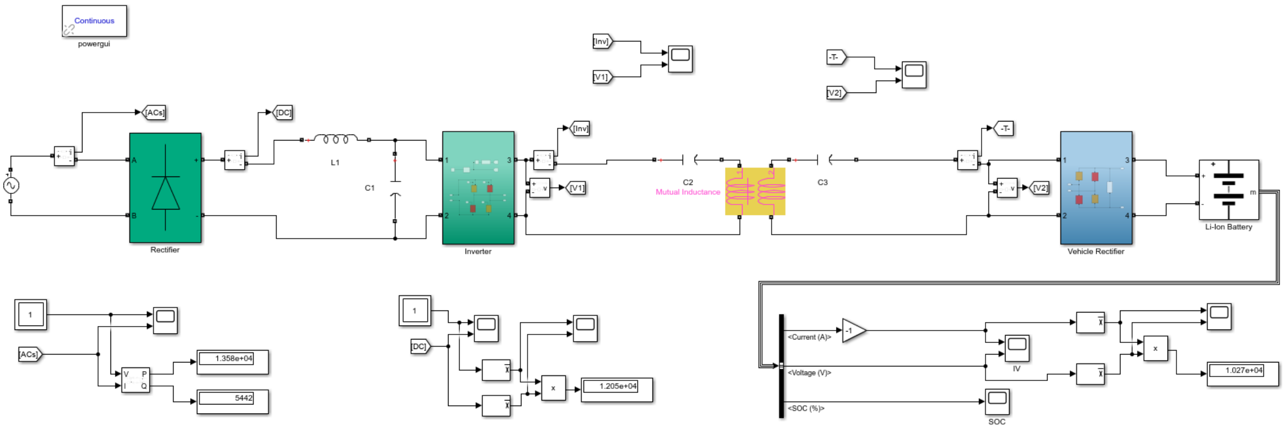

Figure 4.41 Charging system of Simulation 2.

From the AC source Scope (Figure 4.42), Voltage and current are measured. Scopes waveform shows voltage peak value at 350 Volt and current at 99.3 Ampere.

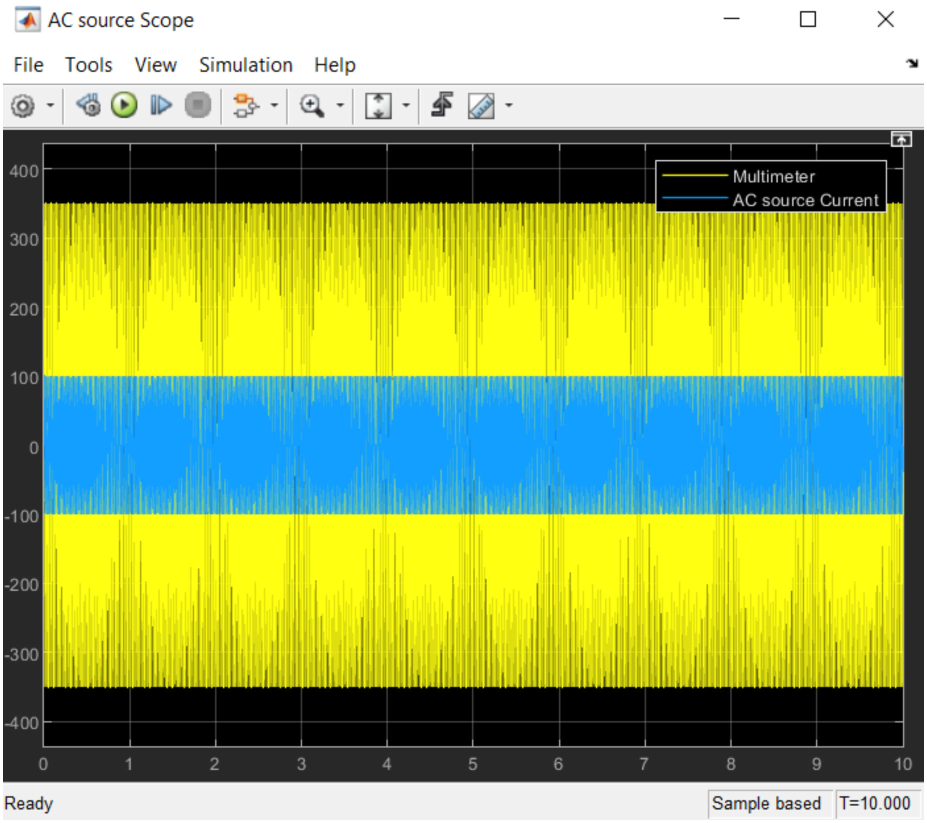

Figure 4.42 AC source Scope of Simulation 2.

The DC Scope (Figure 4.43), shows DC measurements after the rectifier and with the process of considering mean values DC Scope1 (Figure 4.44) shows voltage dc value of 248.5 volt and dc current value of 48.5 Ampere. Measurements can be taken by using the cursor measurements button located rightmost in toolbar.

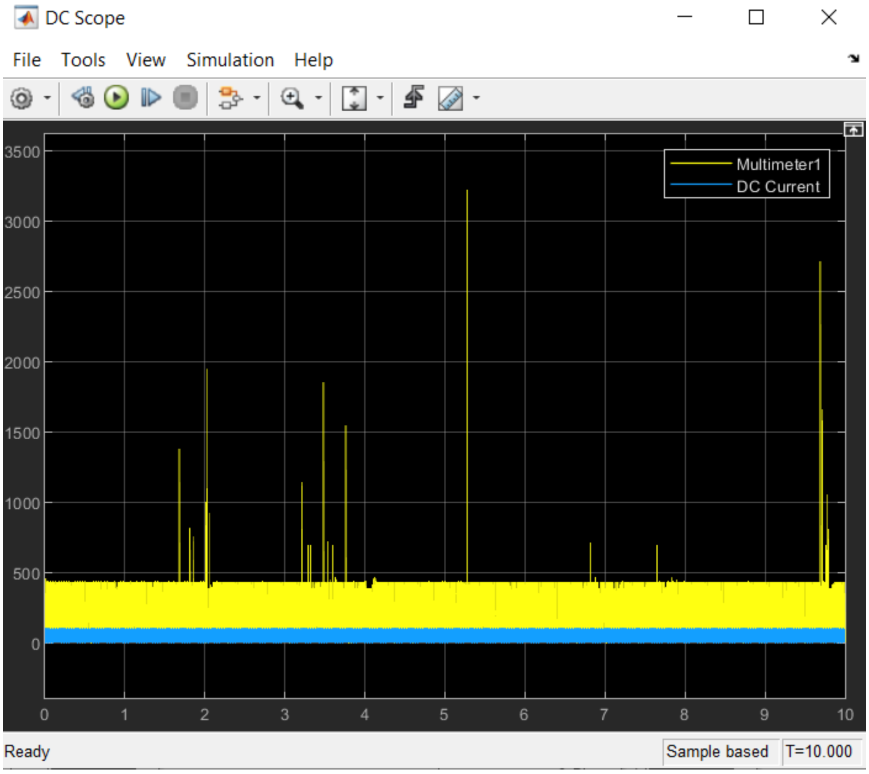

Figure 4.43 DC Scope of Simulation 2.

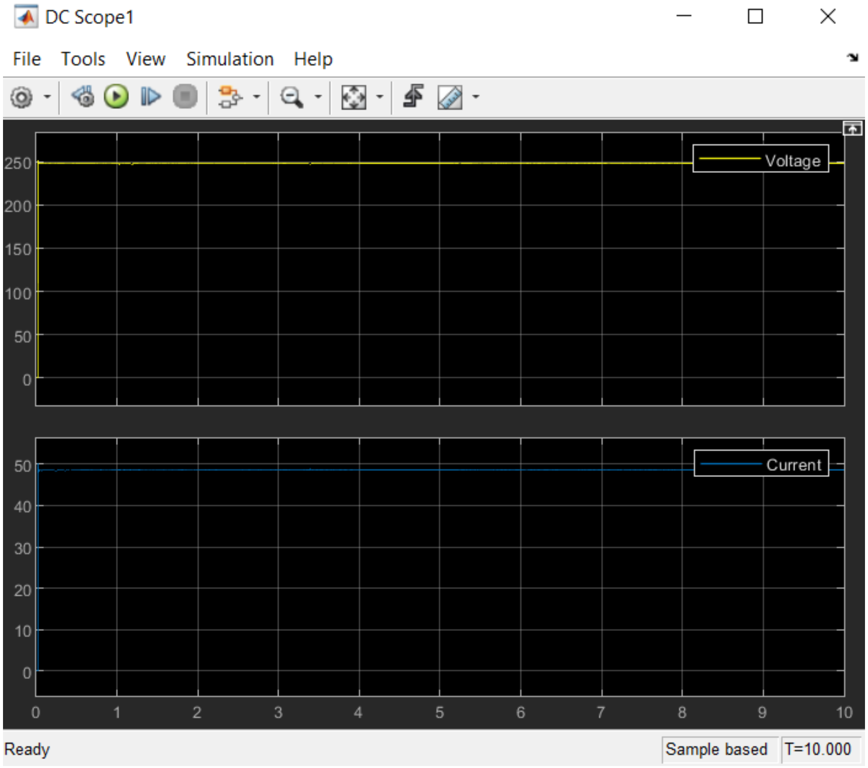

Figure 4.44 DC Scope1 of Simulation 2.

From the HF Scope (Figure 4.45) information about the waveforms of current and voltage after the high frequency inverter can be taken. Peak value of current shown 89 Ampere and voltage 513 volt.

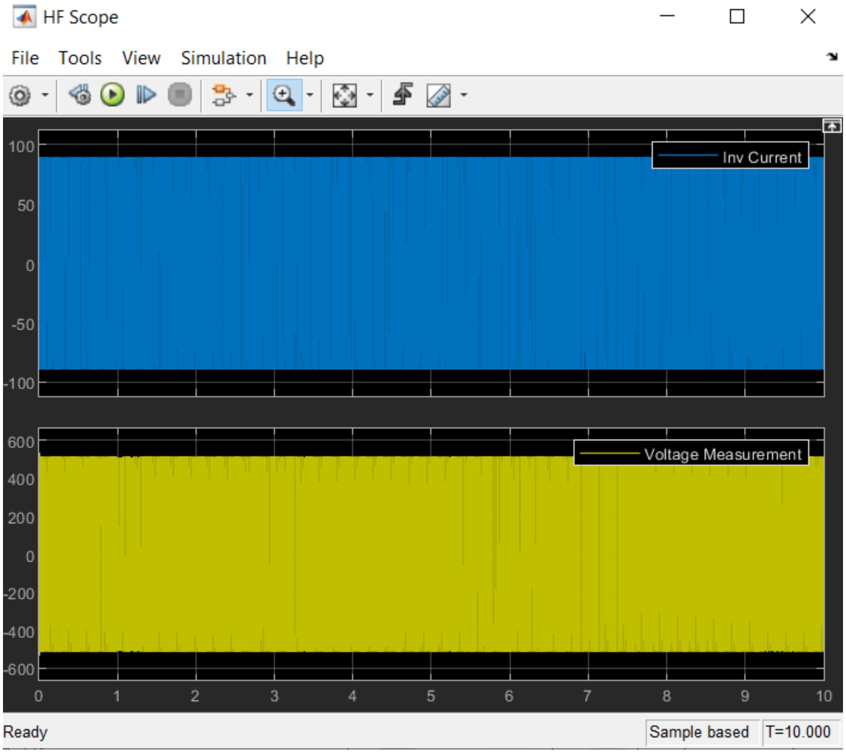

Figure 4.45 HF Scope of Simulation 2.

From the Vehicle Rectifier Scope (Figure 4.46), voltage and current are measured before the vehicle rectifier. Scopes waveform shows voltage peak value at 435 Volt and current at 86 Ampere.

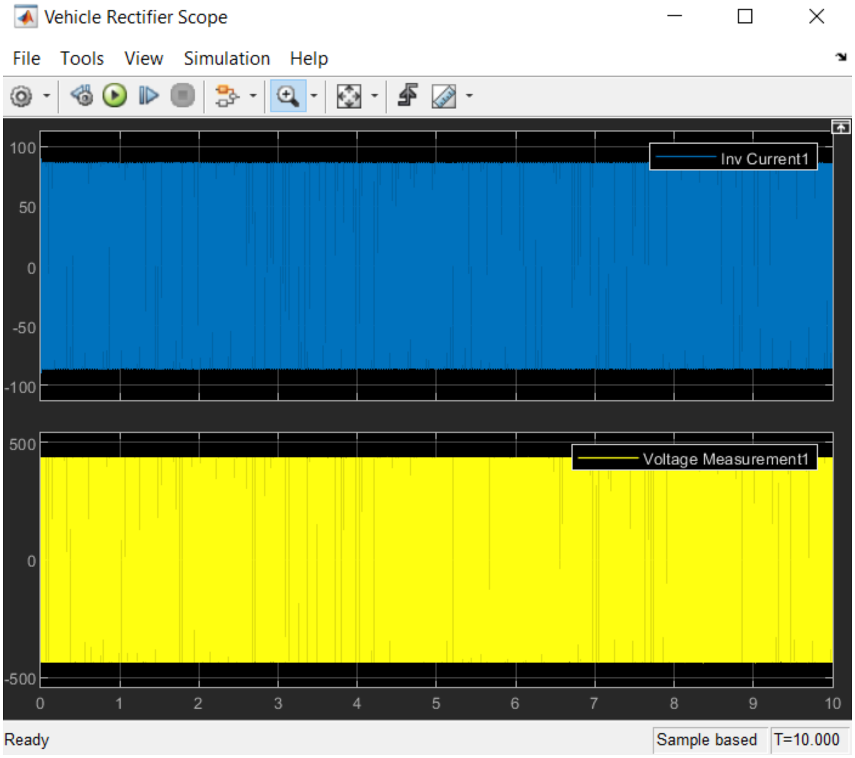

Figure 4.46 Vehicle Rectifier Scope of Simulation 2.

The IV Scope (Figure 4.47), shows DC measurements at the battery and with the process of considering mean values Battery Scope (Figure 4.48) shows dc voltage value of 432.5 volt and dc current value of 27.75 Ampere.

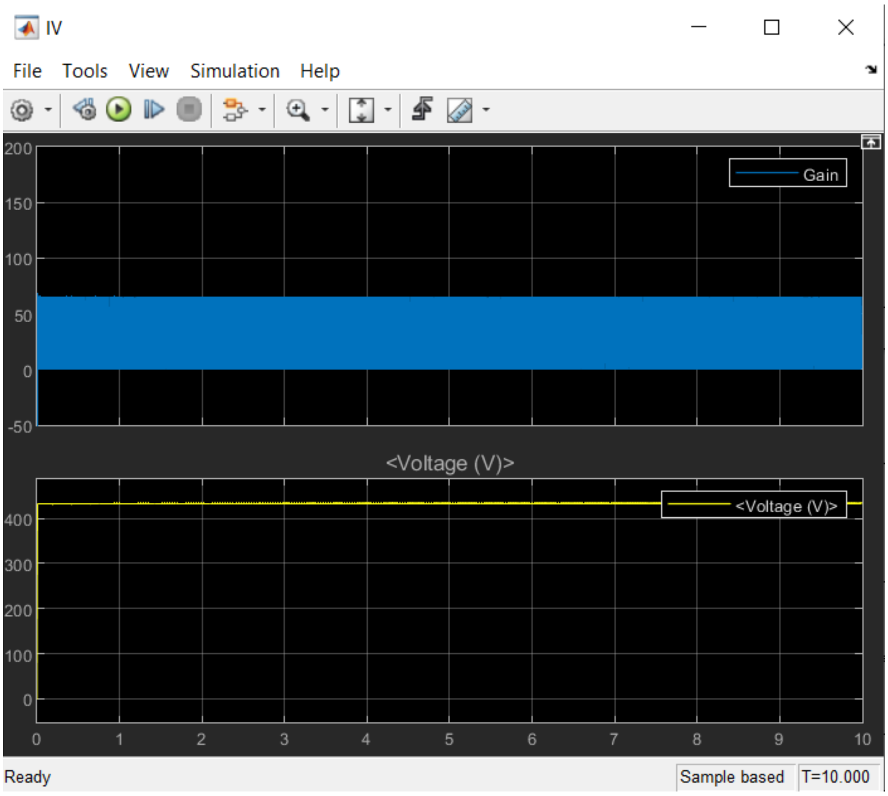

Figure 4.47 IV Scope of Simulation 2.

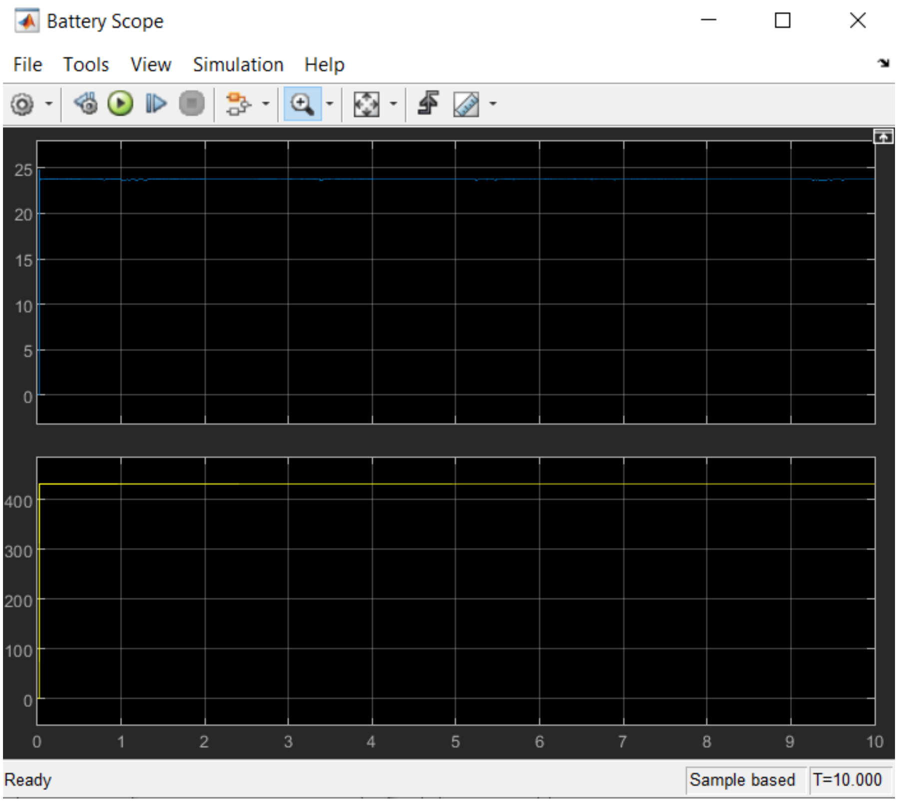

Figure 4.48 Battery Scope of Simulation 2.

The last scope considered; SOC Scope (Figure 4.49) gives information about the state of charge during the process of charging. After the 10 second simulation the soc (%) is 50.066% with the initial soc at 50%.

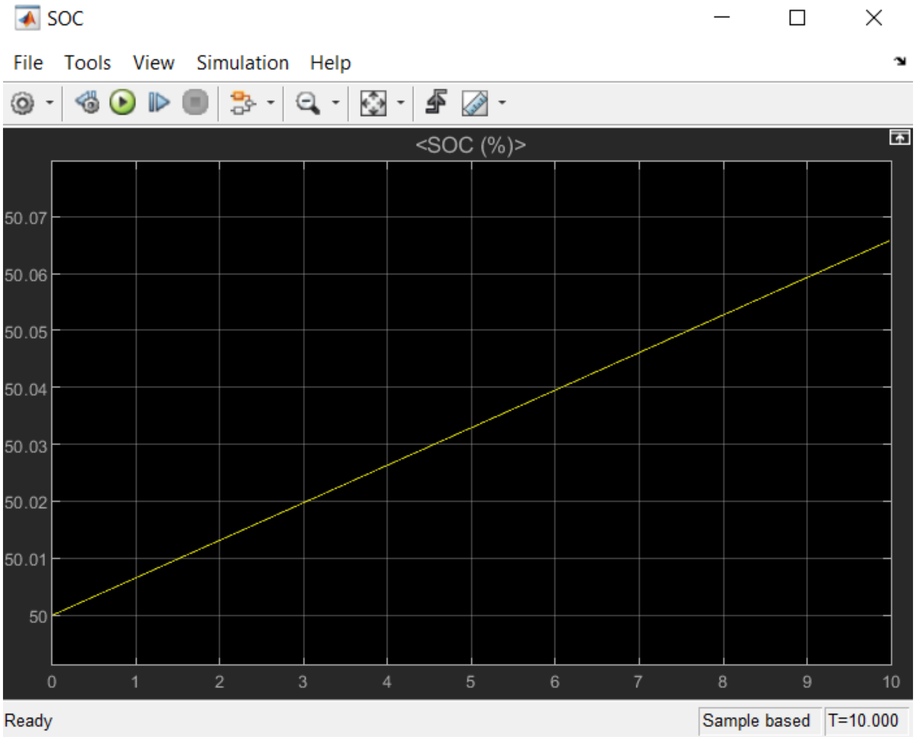

Figure 4.49 SOC Scope of Simulation 2.

As it can observed from the simulation the efficiency of the system is at 75,62%.

4.5 Simulation 3

In the third simulation the mutual inductance calculated 41.94e-6 H (0.00004194) as it depicted in figure 4.50. Parameters values for this calculation are shown there too. Assuming 200mm alignment and a gap of 150mm in order to calculate the efficiency.

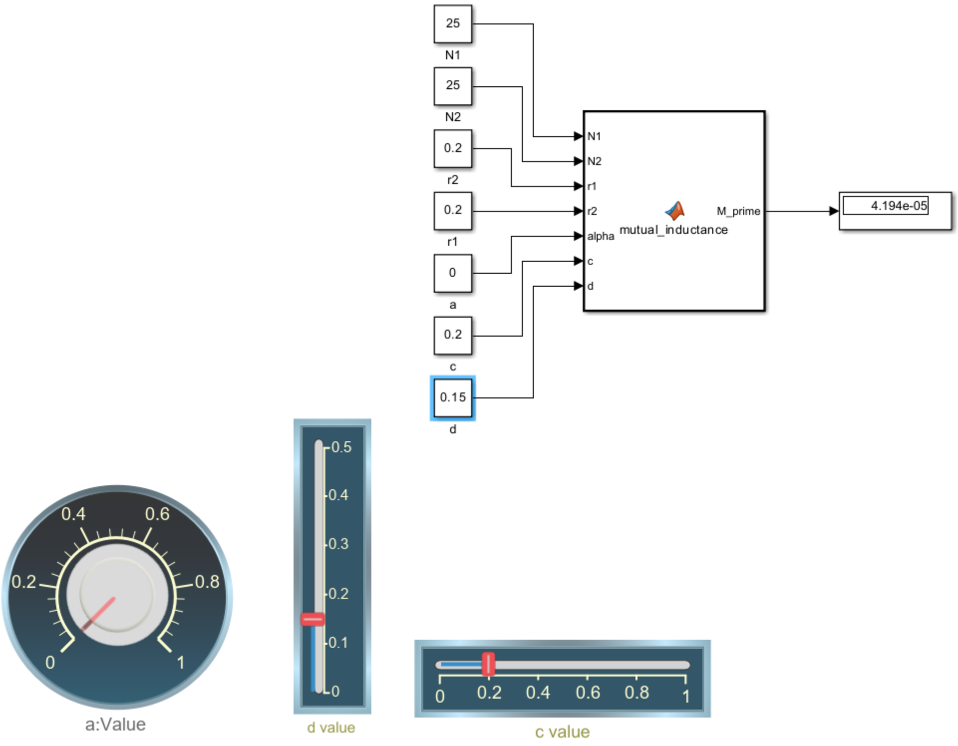

Figure 4.50 Mutual Inductance calculation for simulation 3.

The calculated value has to be added in the block parameters of the mutual inductance (figure 4.51).

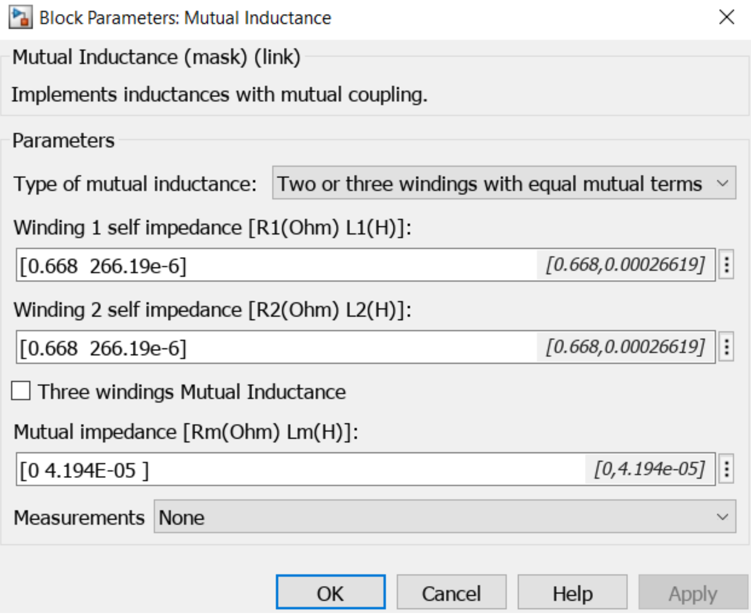

Block Parameters: Mutual Inductance

Mutual Inductance (mask) (link)

Implements inductances with mutual coupling.

Parameters

Type of mutual inductance: Two or three windings with equal mutual terms

Winding 1 self impedance [R1(Ohm) L1(H)]: [0.668 266.19e-6] *[0.668,0.00026619]*

Winding 2 self impedance [R2(Ohm) L2(H)]: [0.668 266.19e-6] *[0.668,0.00026619]*

☐ Three windings Mutual Inductance

Mutual impedance [Rm(Ohm) Lm(H)]: [0 4.194E-05] *[0,4.194e-05]*

Measurements None

Figure 4.51 Mutual Inductance block parameters for Simulation 3.

The whole system of the simulation can be depicted in figure 4.52. Values such as $P_{in,\ ac}$, $Q_{in,\ ac}$, P_{dc} after the rectifier, $P_{bat,\ input}$ are shown in display blocks. Specifically $P_{in,\ ac} = 15940W$, $Q_{in,\ ac} = 6819Var$, $P_{dc} = 13740W$ and $P_{bat,\ input} = 11040W$.

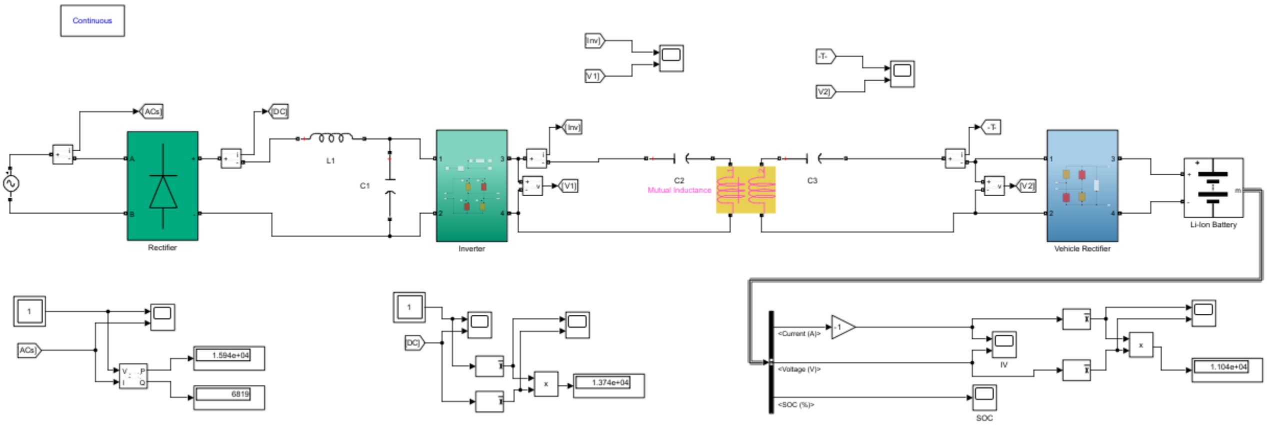

Figure 4.52 Charging system of Simulation 3.

From the AC source Scope (Figure 4.53), Voltage and current are measured. Scopes waveform shows voltage peak value at 350 Volt and current at 112 Ampere.

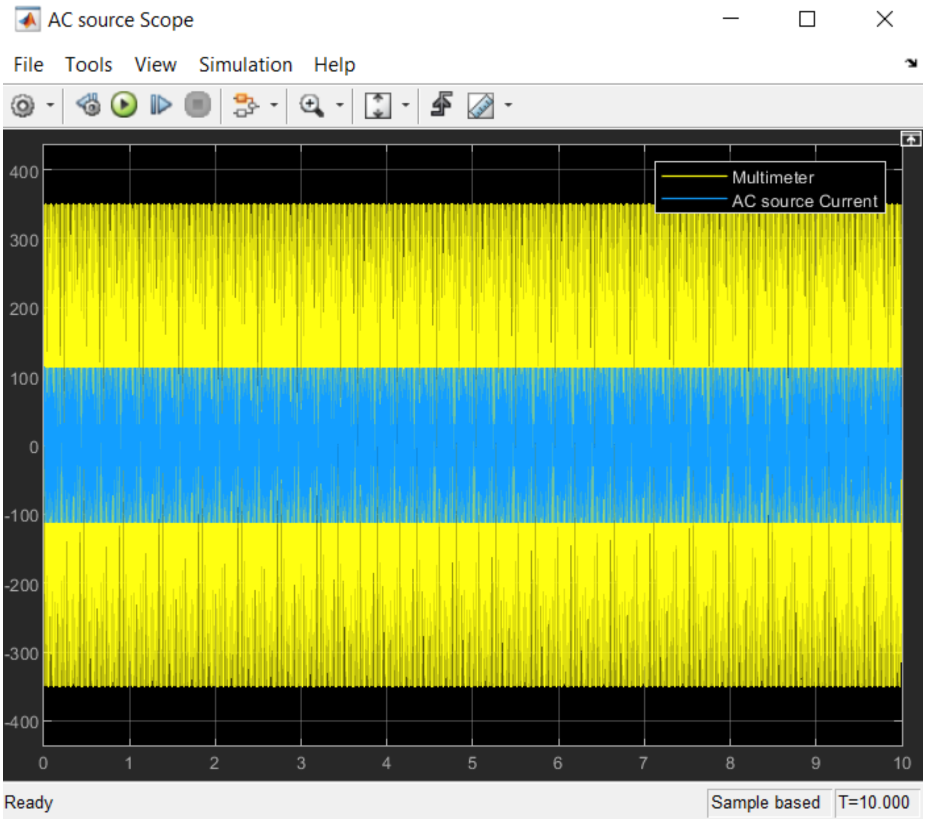

Figure 4.53 AC source Scope of Simulation 3.

The DC Scope (Figure 4.54), shows DC measurements after the rectifier and with the process of considering mean values DC Scope1 (Figure 4.55) shows voltage dc value of 222.69 volt and dc current value of 64.54 Ampere. Measurements can be taken by using the cursor measurements button located rightmost in toolbar.

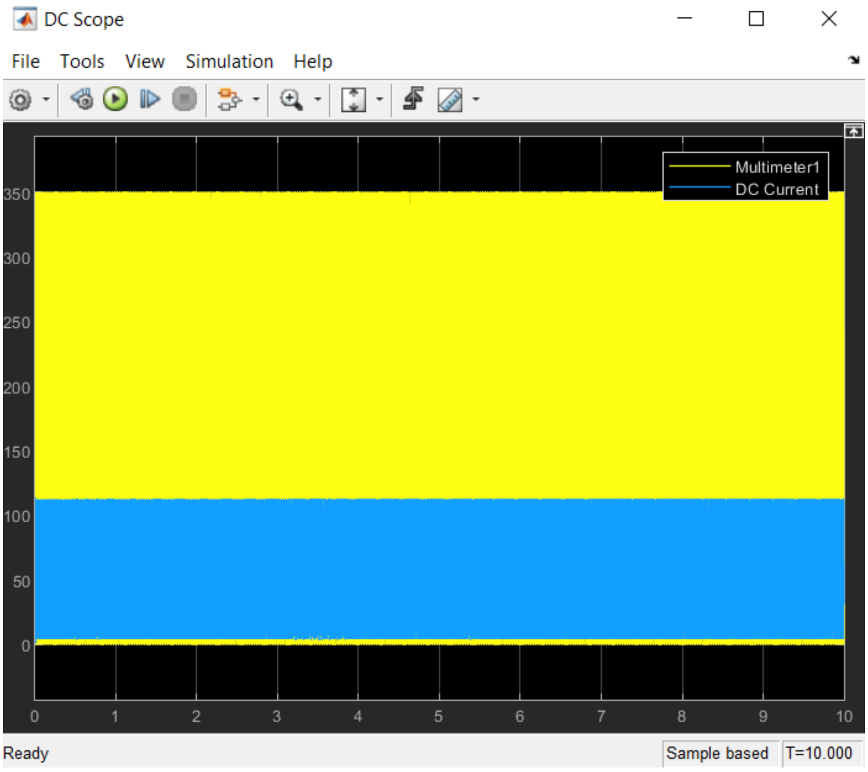

Figure 4.54 DC Scope of Simulation 3.

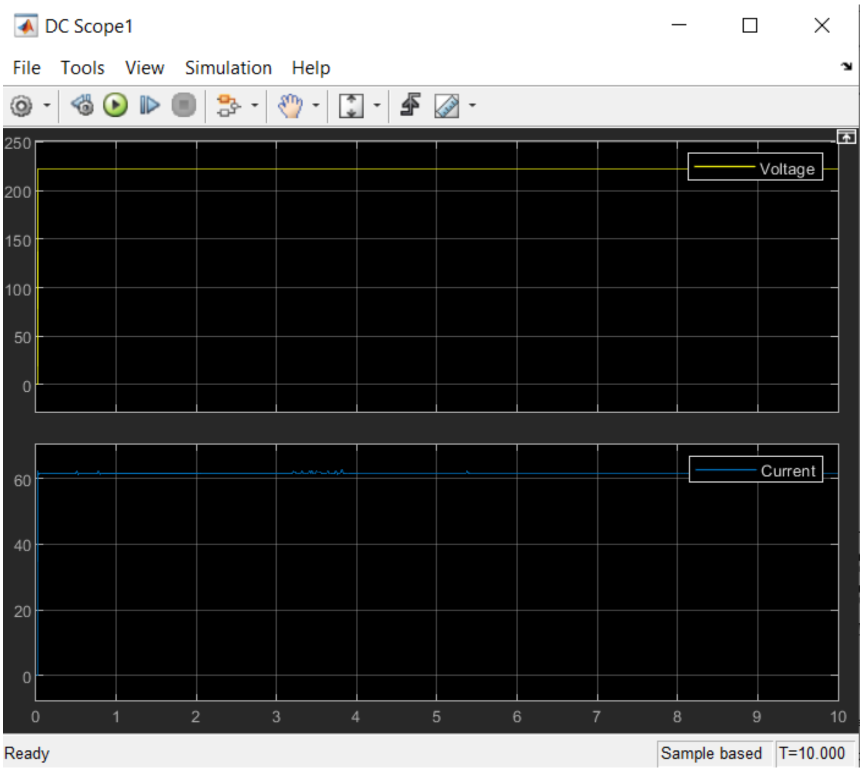

Figure 4.55 DC Scope1 of Simulation 3.

From the HF Scope (Figure 4.56) information about the waveforms of current and voltage after the high frequency inverter can be taken. Peak value of current shown 118 Ampere and voltage 464,5 volt.

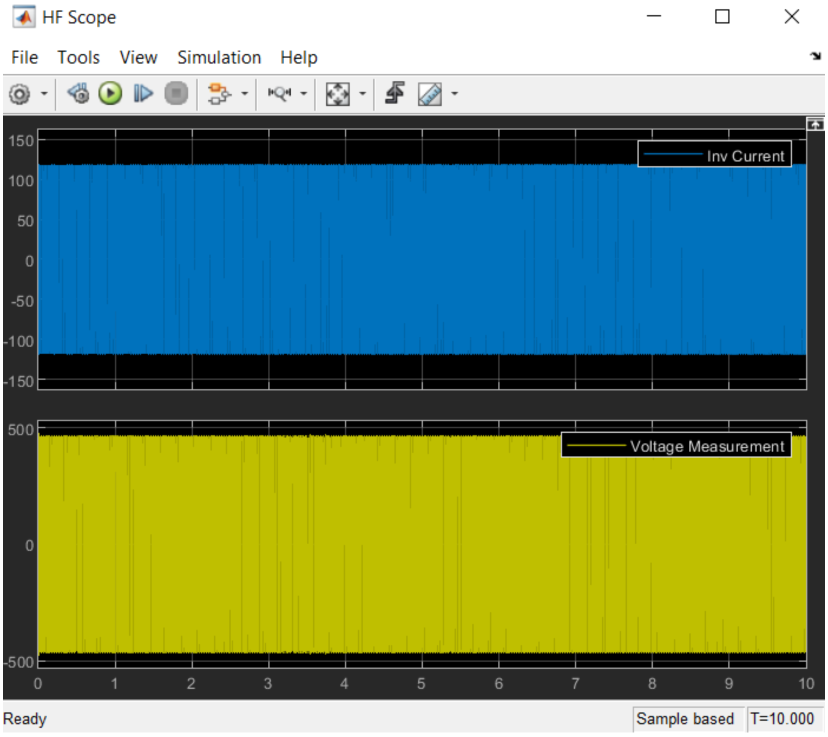

Figure 4.56 HF Scope of Simulation 3.

From the Vehicle Rectifier Scope (Figure 4.57), voltage and current are measured before the vehicle rectifier. Scopes waveform shows voltage peak value at 435 Volt and current at 96.5 Ampere.

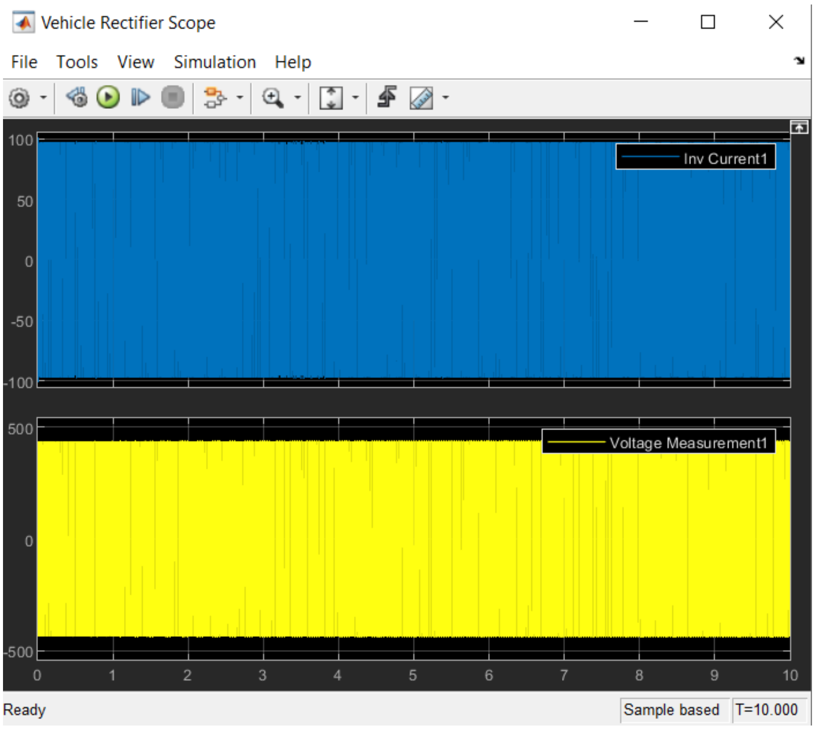

Figure 4.57 Vehicle Rectifier Scope of Simulation 3.

The IV Scope (Figure 4.58), shows DC measurements at the battery and with the process of considering mean values Battery Scope (Figure 4.59) shows dc voltage value of 432.3 volt and dc current value of 25.5 Ampere.

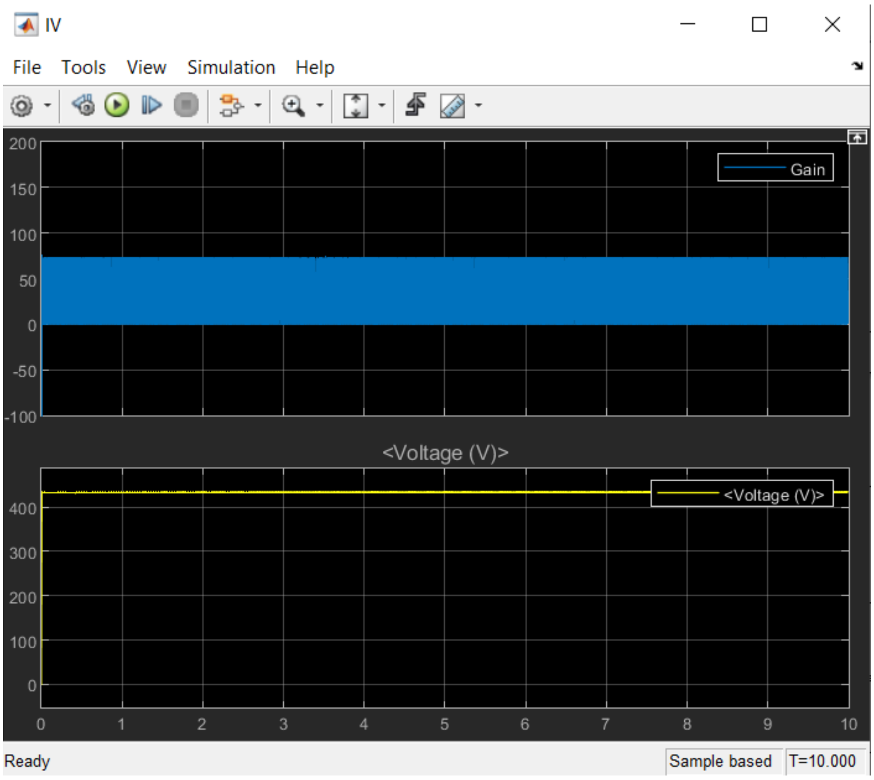

Figure 4.58 IV Scope of Simulation 3.

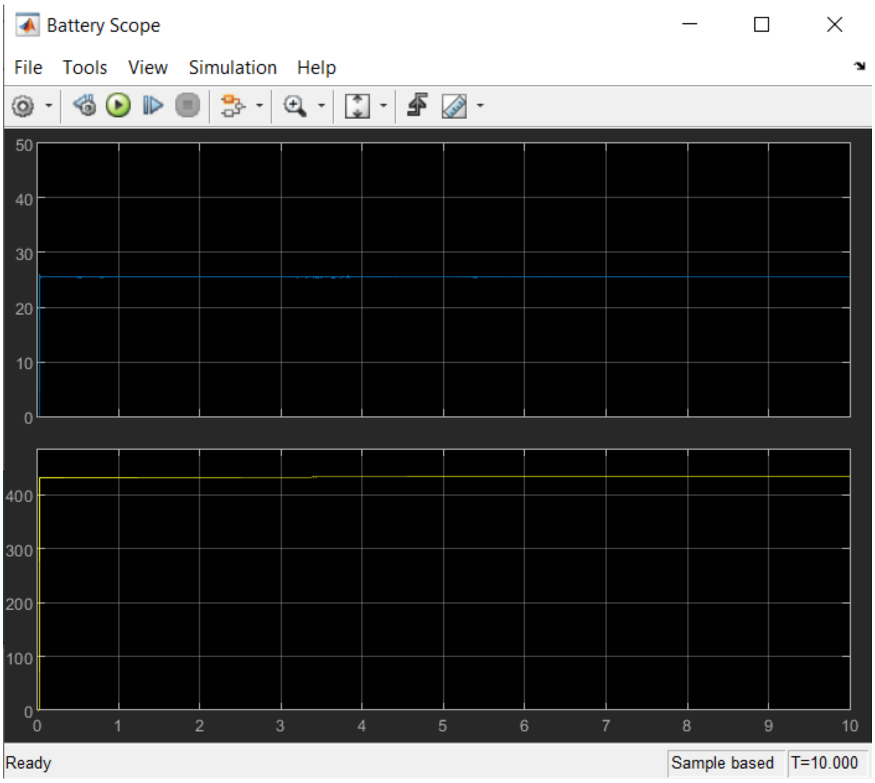

Figure 4.59 Battery Scope of Simulation 3.

The last scope considered; SOC Scope (Figure 4.60) gives information about the state of charge during the process of charging. After the 10 second simulation the soc (%) is 50.0708% with the initial soc at 50%.

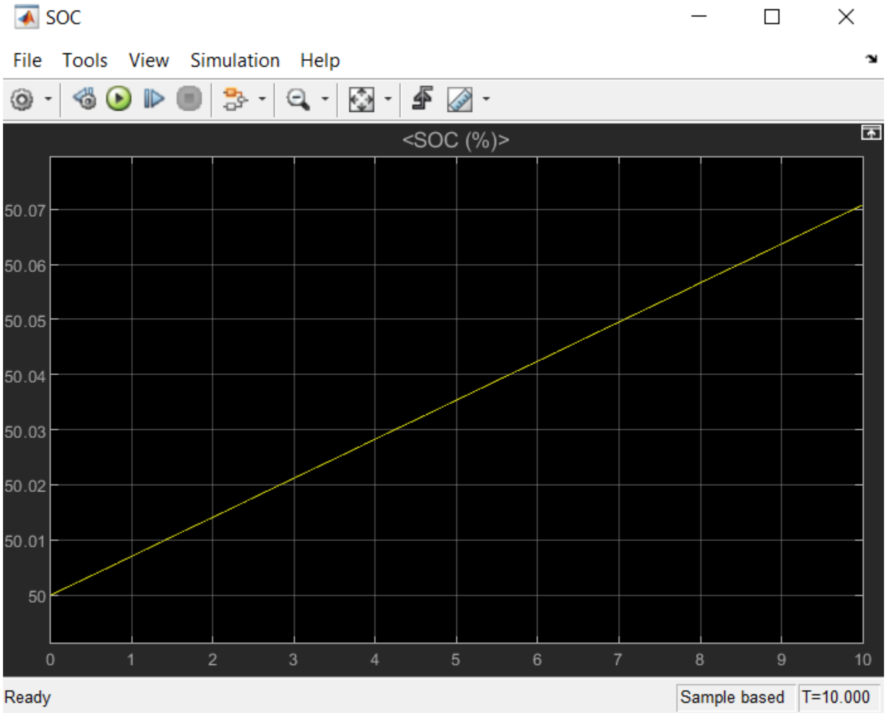

Figure 4.60 SOC Scope of Simulation 3.

As it can observed from the simulation the efficiency of the system is at 69.26%.

4.6 Simulation 4

The forthcoming simulation study is designed to investigate the behavior of the power transfer system as it transitions from Resonant Inductive Power Transfer (RIPT) to standard Inductive Power Transfer (IPT). This critical shift in operational frequency is anticipated to significantly impact the system's efficiency and also limit the input power.

In this simulation the parameters are like the simulation 1 and the value of frequency is at 17kHz. Mutual inductance is 139.1e-6 H (0.0001391) and the gap is 100mm.

The whole system of the simulation can be depicted in figure 4.61. Values such as $P_{in,\ ac}$, $Q_{in,\ ac}$, P_{dc} after the rectifier, $P_{bat,\ input}$ are shown in display blocks. Specifically $P_{in,\ ac} = 1945W$, $Q_{in,\ ac} = 621.9Var$, $P_{dc} = 1840W$ and $P_{bat,\ input} = 1298W$.

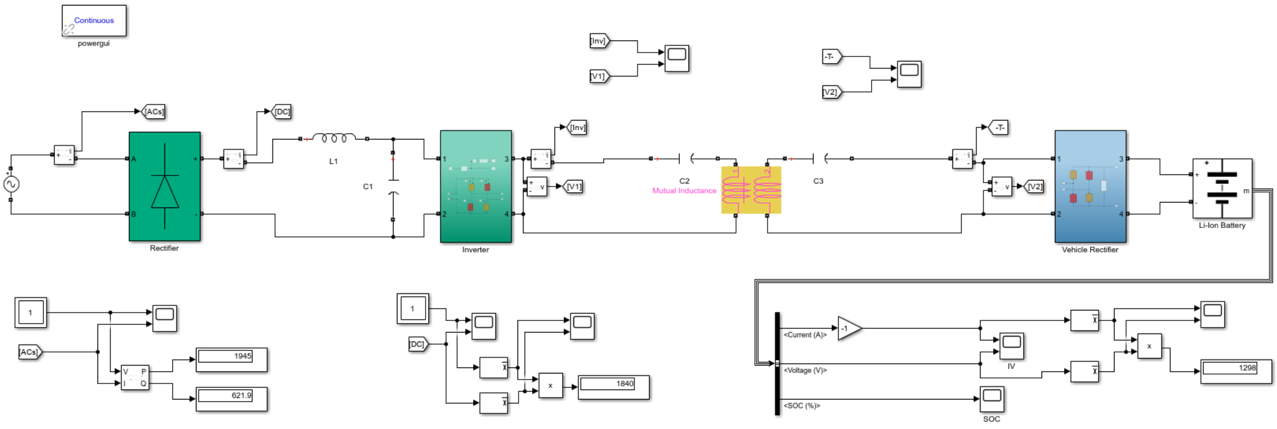

Figure 4.61 Charging system of Simulation 4.

From the AC source Scope (Figure 4.62), Voltage and current are measured.

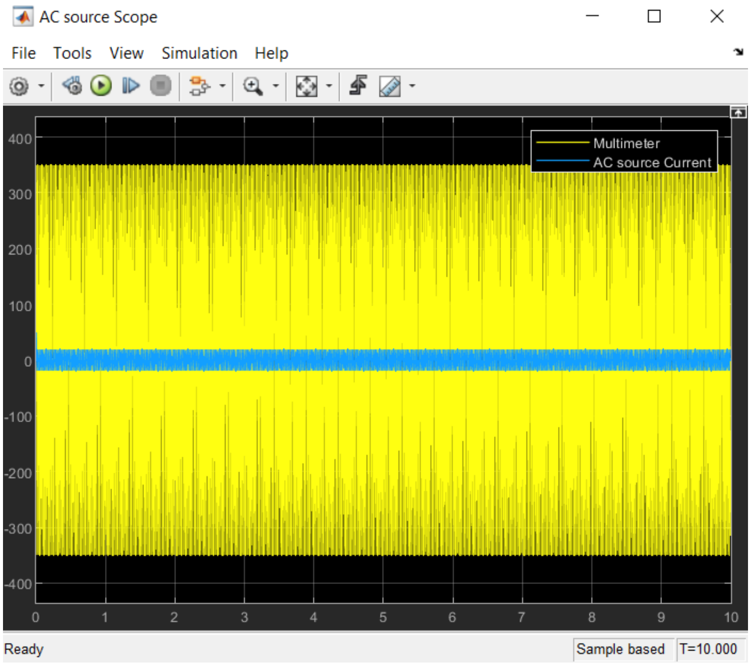

Figure 4.62 AC source Scope of Simulation 4.

The DC Scope (Figure 4.63), shows DC measurements after the rectifier and with the process of considering mean values DC Scope1 (Figure 4.64).

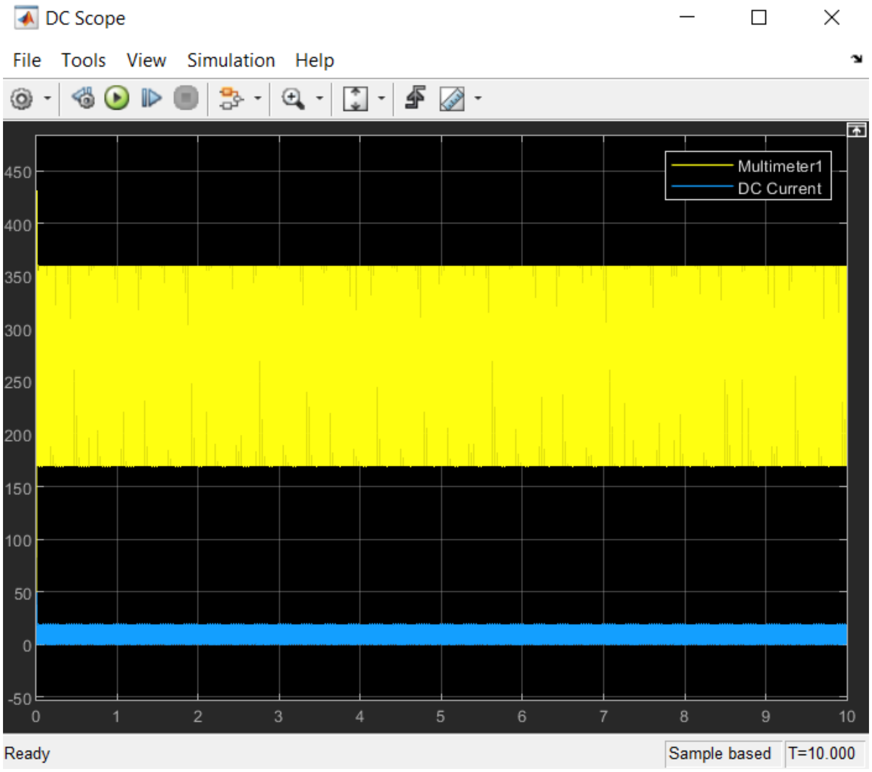

Figure 4.63 DC Scope of Simulation 4.

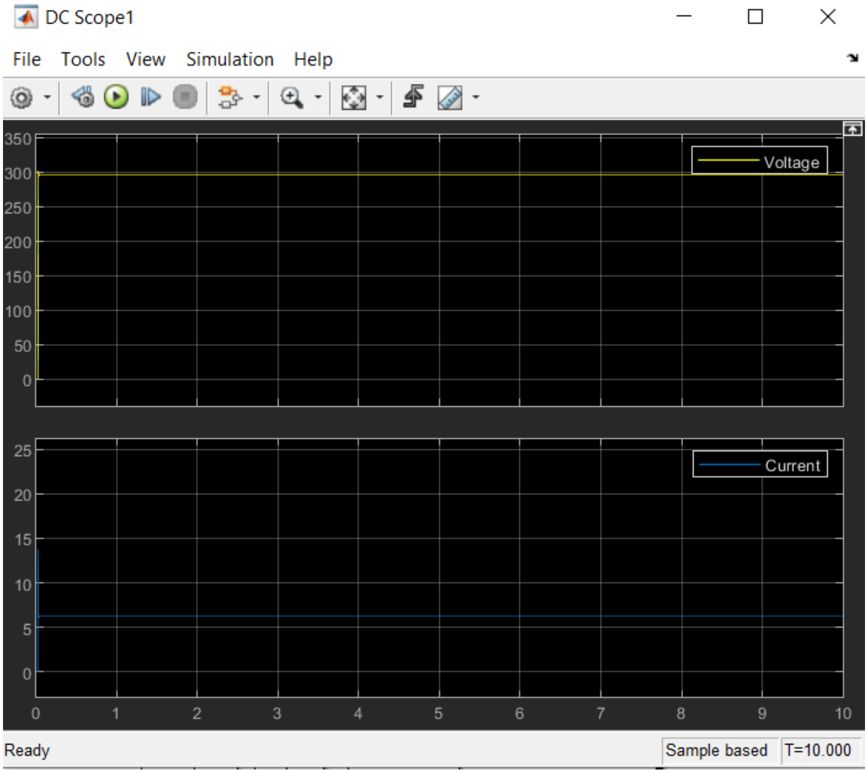

Figure 4.64 DC Scope1 of Simulation 4.

From the HF Scope (Figure 4.65) information about the waveforms of current and voltage after the high frequency inverter can be taken.

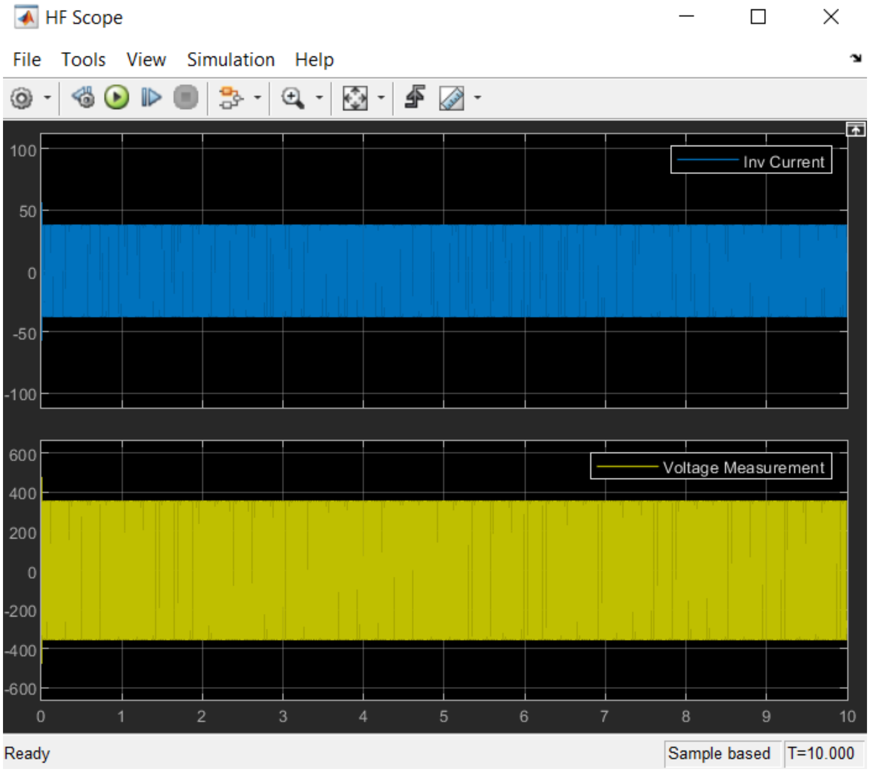

Figure 4.65 HF Scope of Simulation 4.

From the Vehicle Rectifier Scope (Figure 4.66), voltage and current are measured before the vehicle rectifier.

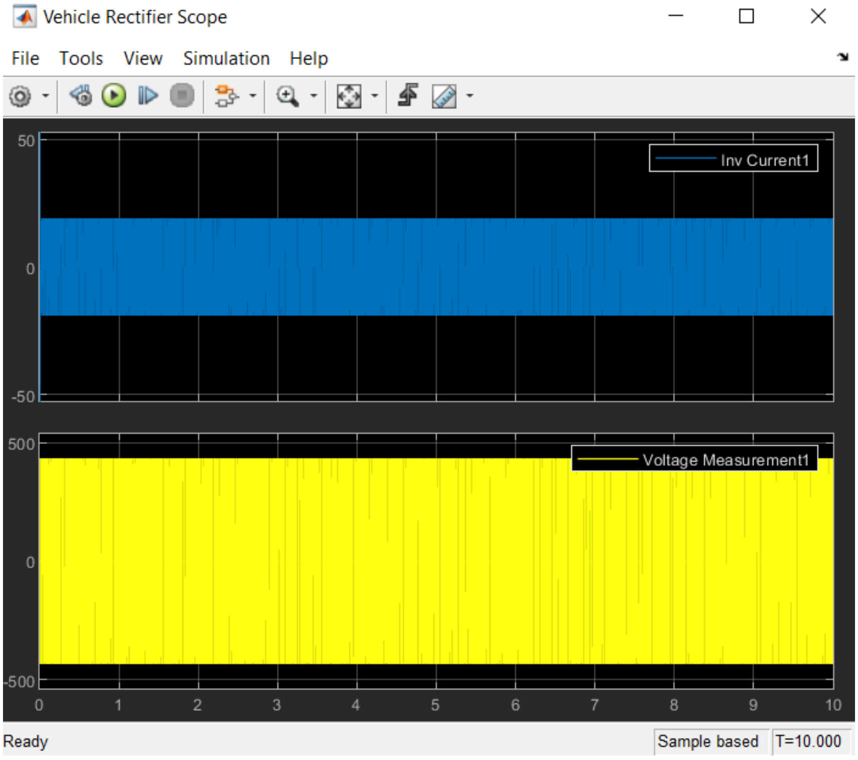

Figure 4.66 Vehicle Rectifier Scope of Simulation 4.

The IV Scope (Figure 4.67), shows DC measurements at the battery and with the process of considering mean values Battery Scope (Figure 4.68).

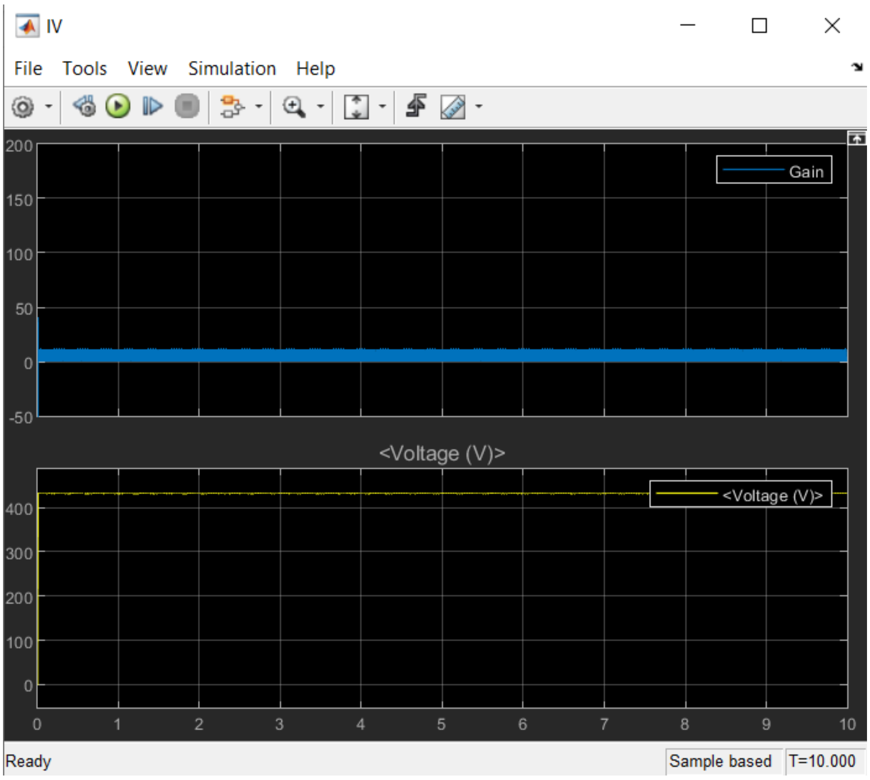

Figure 4.67 IV Scope of Simulation 4.

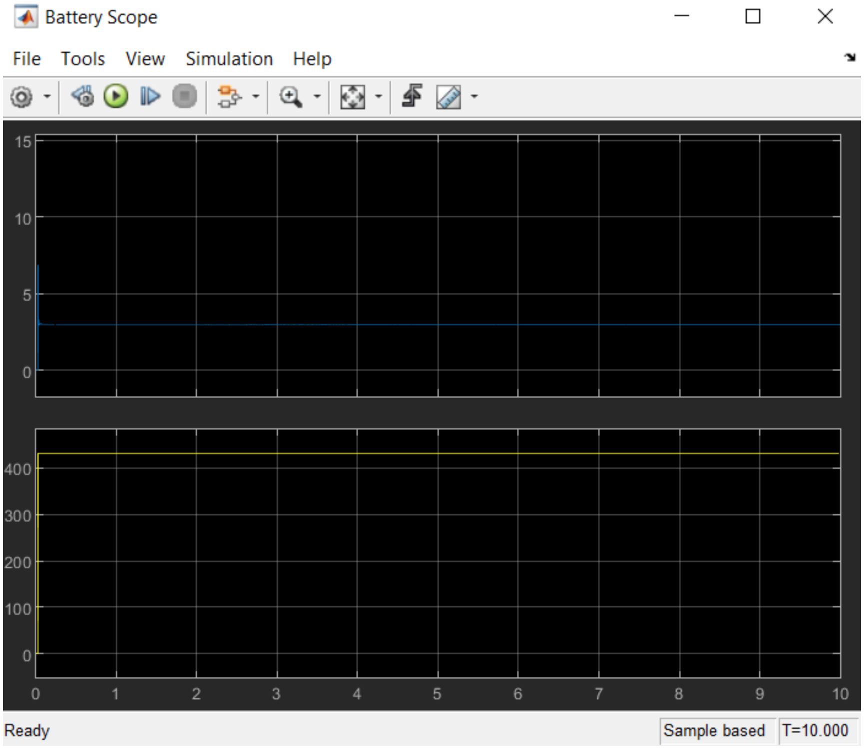

Figure 4.68 Battery Scope of Simulation 4.

The last scope considered; SOC Scope (Figure 4.69) gives information about the state of charge during the process of charging. After the 10 second simulation the soc (%) is 50.0085% with the initial soc at 50%.

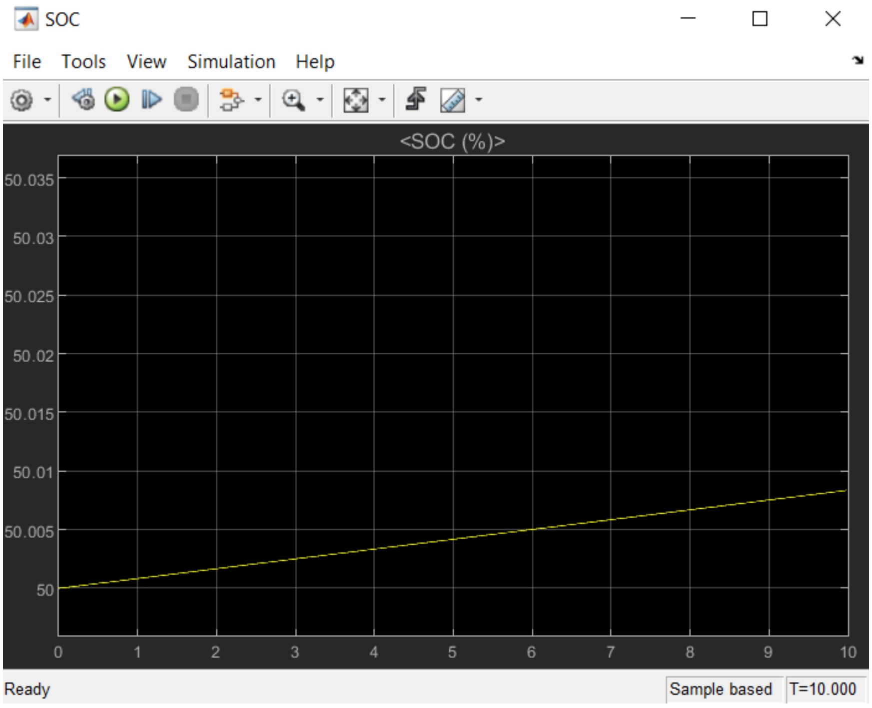

Figure 4.69 SOC Scope of Simulation 4.

As it can observed from the simulation the efficiency of the system is at 66,73%.

This simulation shows that adjusting the frequency far from the resonant can significantly affect the efficiency of the system.

Compare to simulation 1 it can be observed that decreasing the frequency (from 19999.864 Hz to 17000 Hz) it also decreases the current input, resulting a different system behavior as it can observed from the Scopes. State of charge drops from 50.0375% to 50.0058% and the efficiency from 84,86% to 66,73%.

4.7 Simulation 5

The forthcoming simulation study is designed to investigate the behavior of the power transfer system as it transitions from Resonant Inductive Power Transfer (RIPT) to standard Inductive Power Transfer (IPT). This critical shift in operational frequency is anticipated to significantly impact the system's efficiency and also limit the input power.

In this simulation the parameters are like the simulation 1 and the value of frequency is at 23kHz. Mutual inductance is 139.1e-6 H (0.0001391) and the gap is 100mm.

The whole system of the simulation can be depicted in figure 4.70. Values such as $P_{in,\ ac}$, $Q_{in,\ ac}$, P_{dc} after the rectifier, $P_{bat,\ input}$ are shown in display blocks. Specifically $P_{in,\ ac} = 4608W$, $Q_{in,\ ac} = 1582Var$, $P_{dc} = 4212W$ and $P_{bat,\ input} = 3814W$.

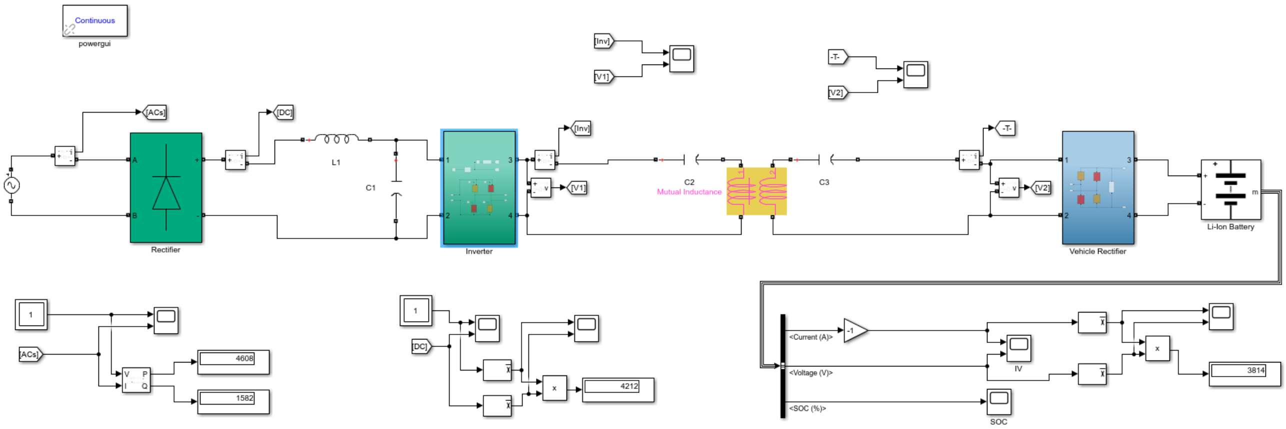

Figure 4.70 Charging system of Simulation 5.

From the AC source Scope (Figure 4.71), Voltage and current are measured.

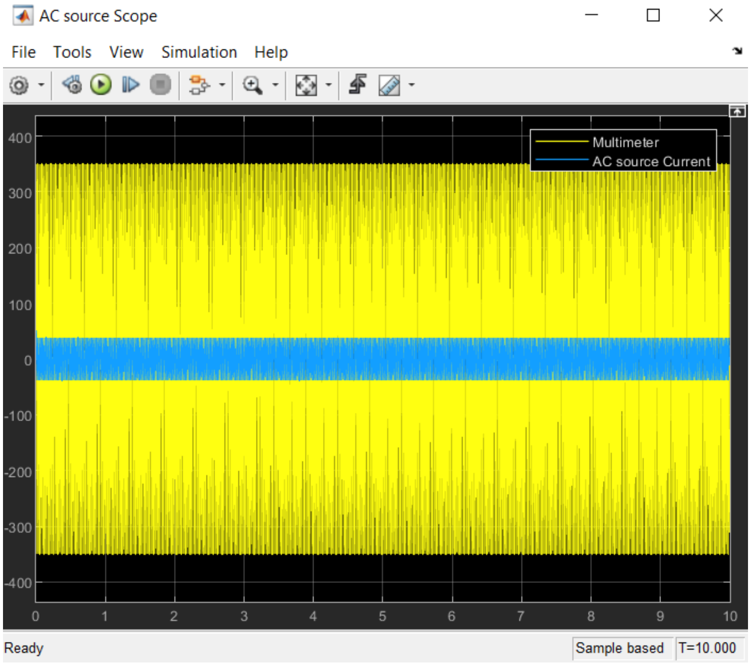

Figure 4.71 AC source Scope of Simulation 5.

The DC Scope (Figure 4.72), shows DC measurements after the rectifier and with the process of considering mean values DC Scope1 (Figure 4.73).

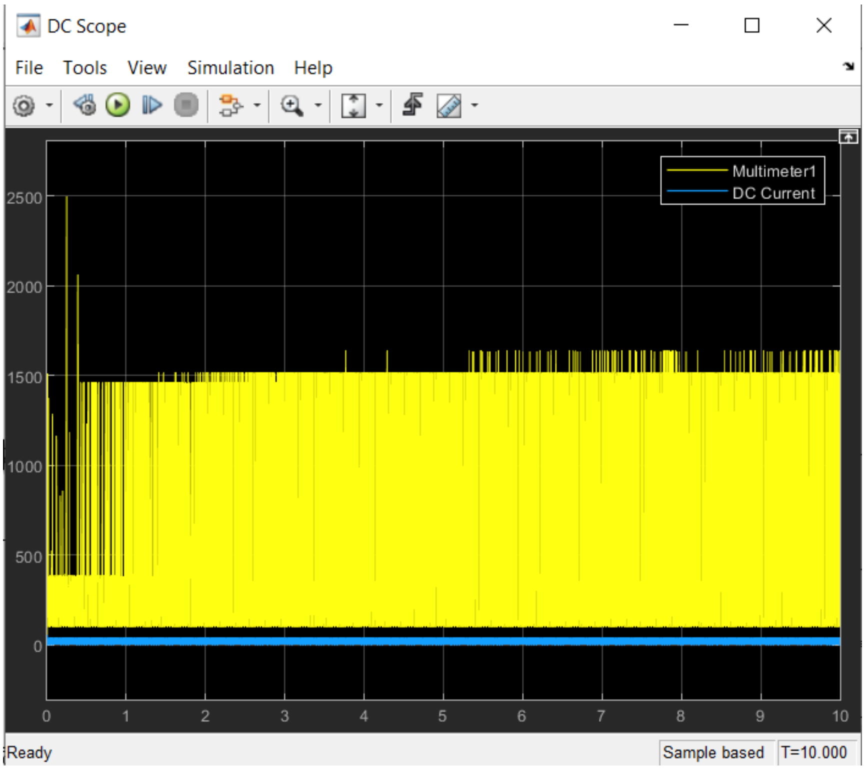

Figure 4.72 DC Scope of Simulation 5.

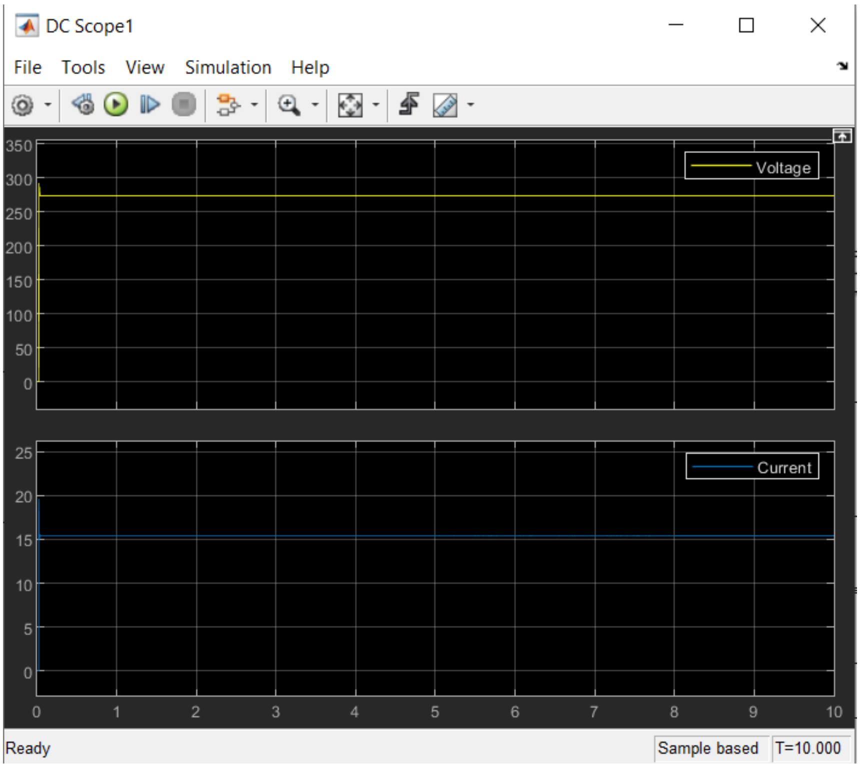

Figure 4.73 DC Scope1 of Simulation 5.

From the HF Scope (Figure 4.74) information about the waveforms of current and voltage after the high frequency inverter can be taken.

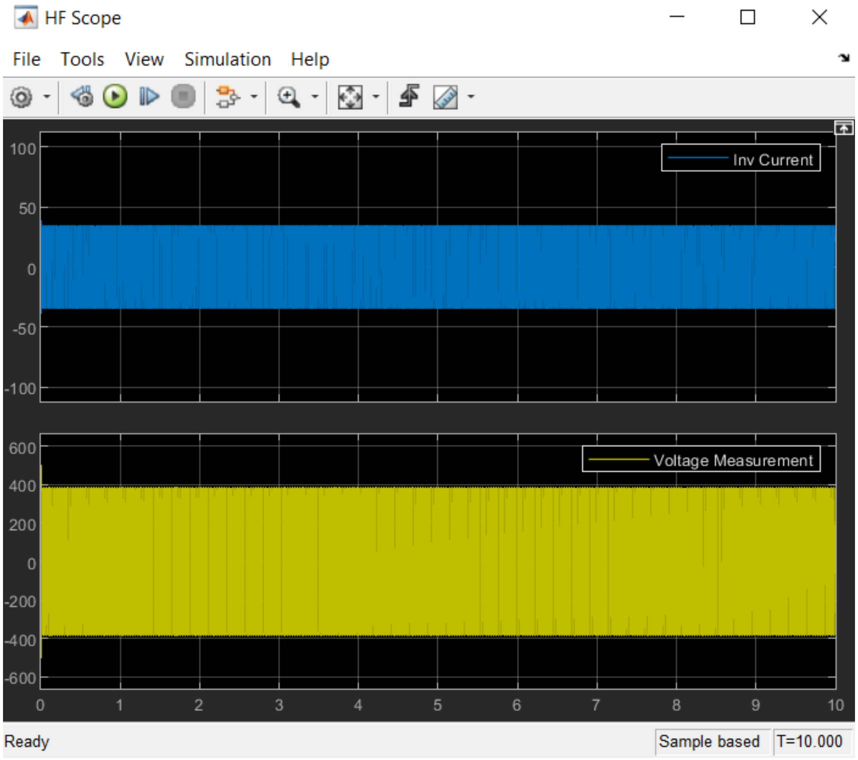

Figure 4.74 HF Scope of Simulation 5.

From the Vehicle Rectifier Scope (Figure 4.75), voltage and current are measured before the vehicle rectifier.

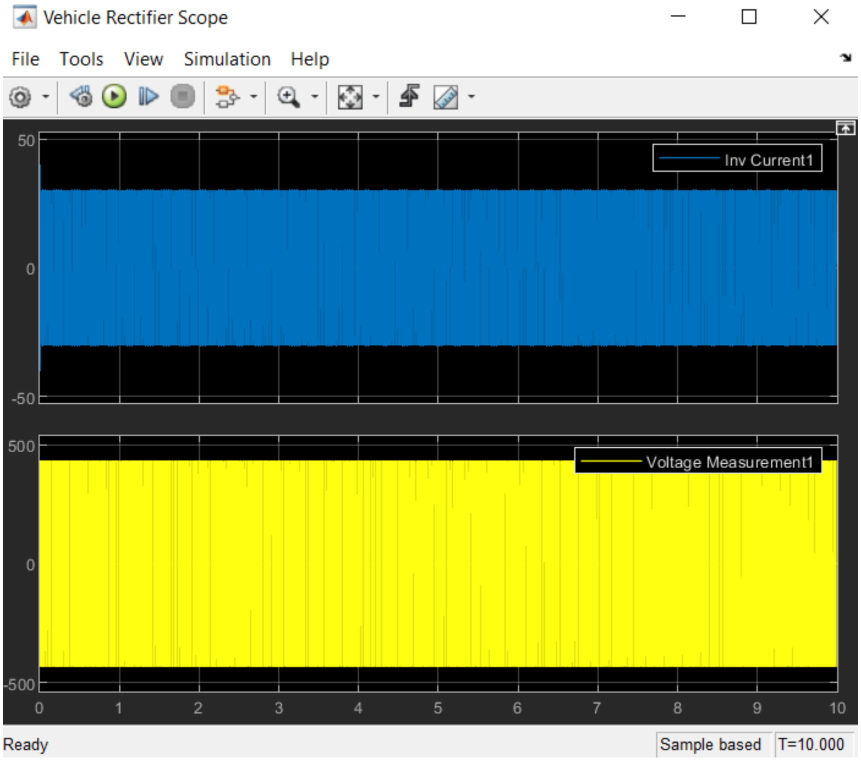

Figure 4.75 Vehicle Rectifier Scope of Simulation 5.

The IV Scope (Figure 4.76), shows DC measurements at the battery and with the process of considering mean values Battery Scope (Figure 4.77).

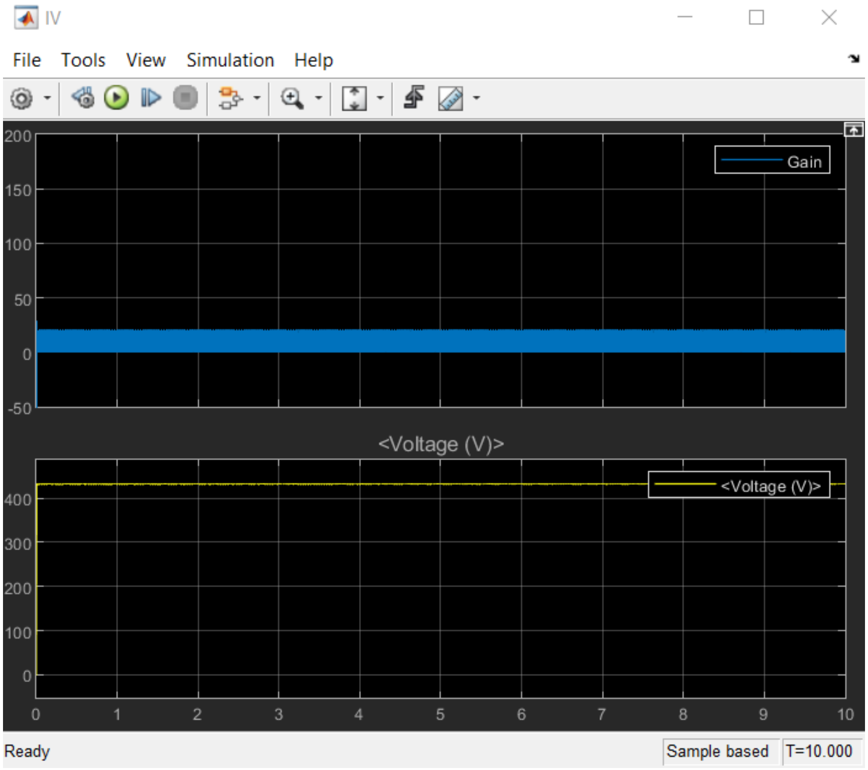

Figure 4.76 IV Scope of Simulation 5.

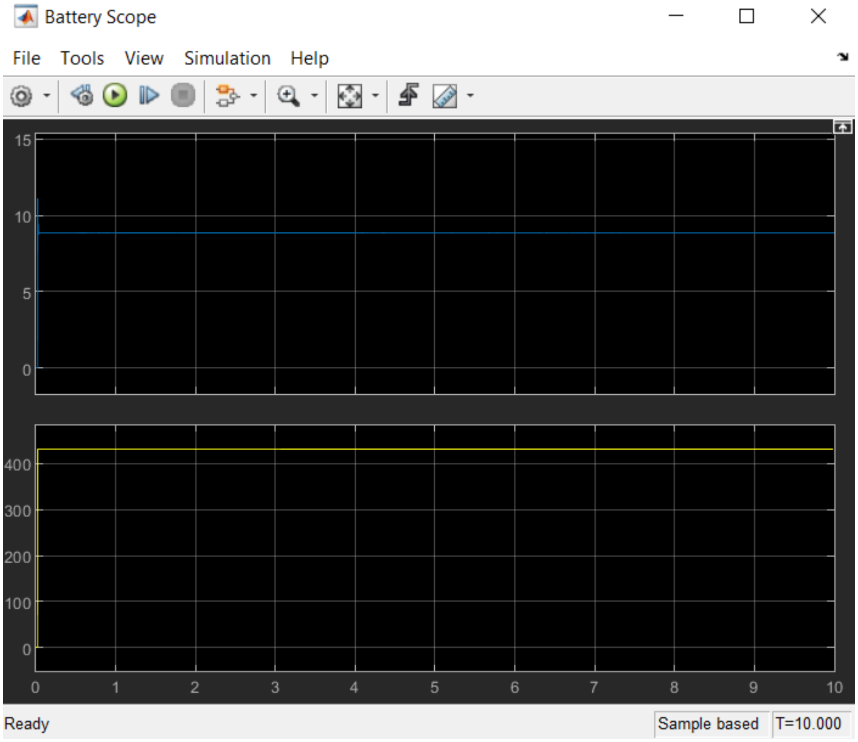

Figure 4.77 Battery Scope of Simulation 5.

The last scope considered; SOC Scope (Figure 4.78) gives information about the state of charge during the process of charging. After the 10 second simulation the soc (%) is 50.025% with the initial soc at 50%.

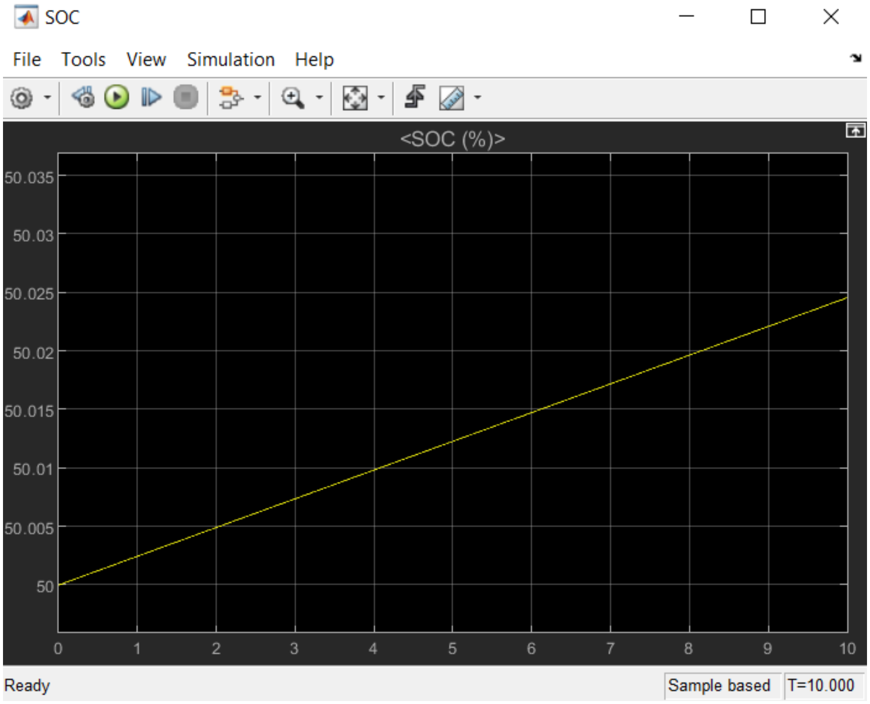

Figure 4.78 SOC Scope of Simulation 5.

As it can observed from the simulation the efficiency of the system is at 82,77%.

This simulation shows that adjusting the frequency far from the resonant can significantly affect the efficiency of the system.

Compare to simulation 1 it can be observed that increasing the frequency (from 19999.864 Hz to 23000 Hz) it also decreases the current input, resulting a different system behavior as it can observed from the Scopes. State of charge drops from 50.0375% to 50.025% and the efficiency from 84,86% to 82,77%.

Comparing simulation 4 and 5 it can be observed that increasing the frequency far from the resonant does not affect the system the same way it does by decreasing it. Specifically, the efficiency drops 2.09% by increasing the frequency 3kHz and it drops 18.13% by decreasing the frequency 3kHz.

4.8 Simulation 6

In the proposed simulation, a key focus will be on the reduction of ohmic losses within the power transfer system. This simulation is aligned with the objectives of the first scenario (simulation 1). However, a significant modification is introduced: the resistances R_1 and R_2, representing the self-impedances of winding 1 and winding 2 respectively, will be adjusted to a value of 0.368 Ω. This adjustment is anticipated to have a substantial impact on the system's overall efficiency, particularly in terms of reducing energy losses attributed to resistance in the windings.

In this simulation the parameters are like the simulation 1 and the value of frequency is at 19999.864 Hz. Mutual inductance is 139.1e-6 H (0.0001391) and the gap is 100mm.

The whole system of the simulation can be depicted in figure 4.79. Values such as $P_{in,\ ac}$, $Q_{in,\ ac}$, P_{dc} after the rectifier, $P_{bat,\ input}$ are shown in display blocks. Specifically $P_{in,\ ac}$ = 5939W, $Q_{in,\ ac}$ = 2384Var, P_{dc} = 5887W and $P_{bat,\ input}$ =5255W.

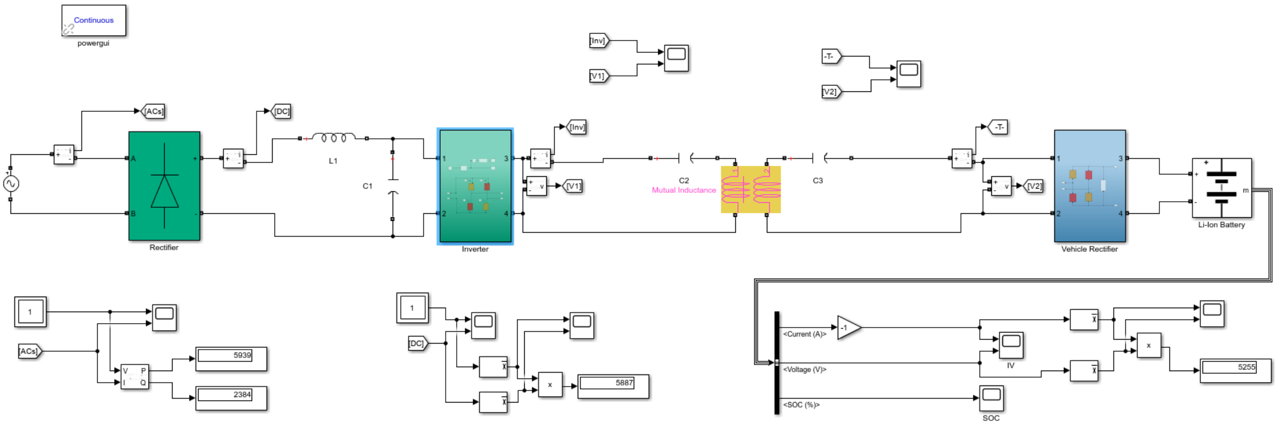

Figure 4.79 Charging system of Simulation 6.

From the AC source Scope (Figure 4.80), Voltage and current are measured. Scopes waveform shows voltage peak value at 350 Volt and current at 52 Ampere.

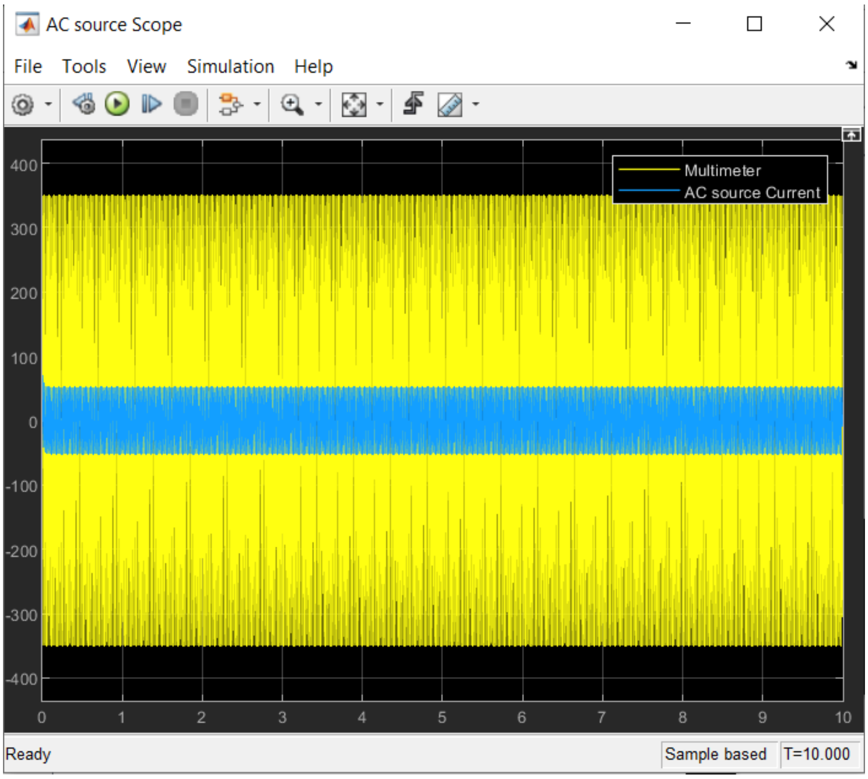

Figure 4.80 AC source Scope of Simulation 6.

The DC Scope (Figure 4.81), shows DC measurements after the rectifier and with the process of considering mean values DC Scope1 (Figure 4.82) shows voltage dc value of 293.5 volt and dc current value of 20 Ampere. Measurements can be taken by using the cursor measurements button located rightmost in toolbar.

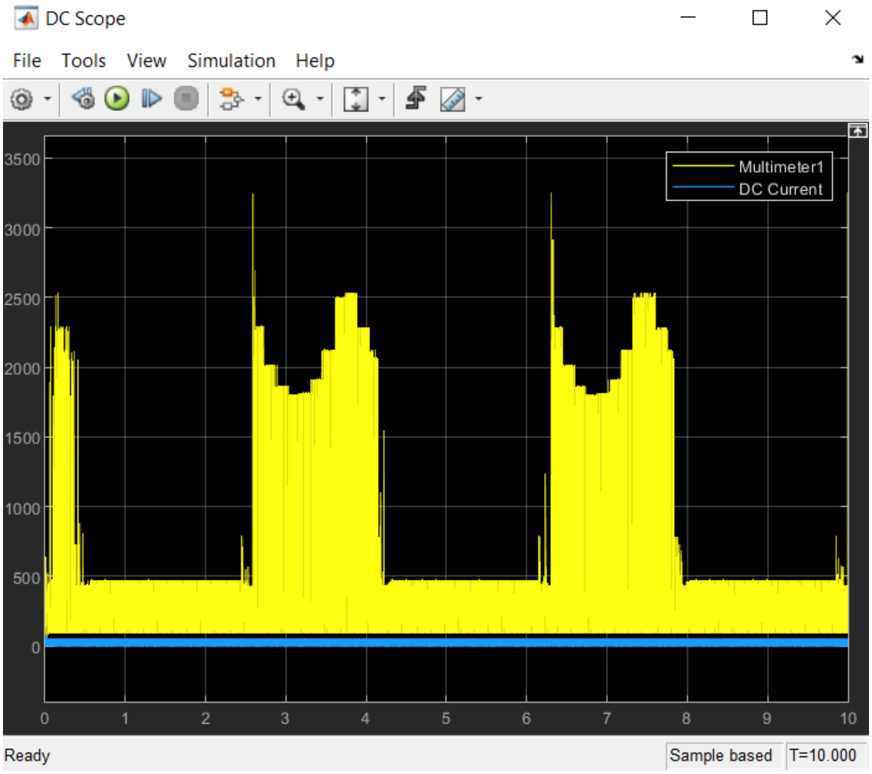

Figure 4.81 DC Scope of Simulation 7.

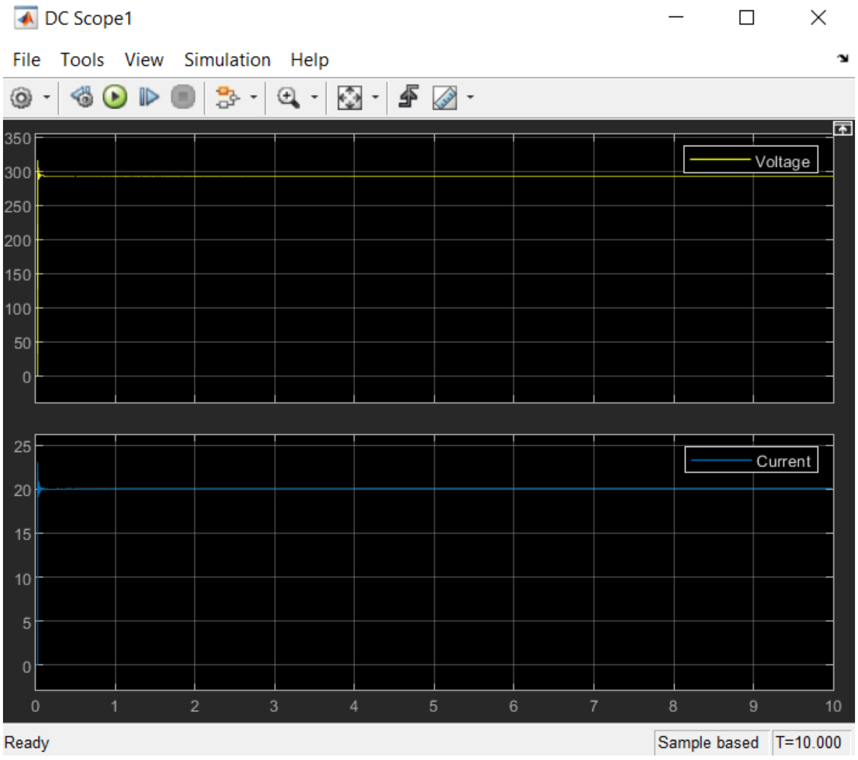

Figure 4.82 DC Scope1 of Simulation 6.

From the HF Scope (Figure 4.83) information about the waveforms of current and voltage after the high frequency inverter can be taken. Peak value of current shown 32.5 Ampere and voltage 452 volt.

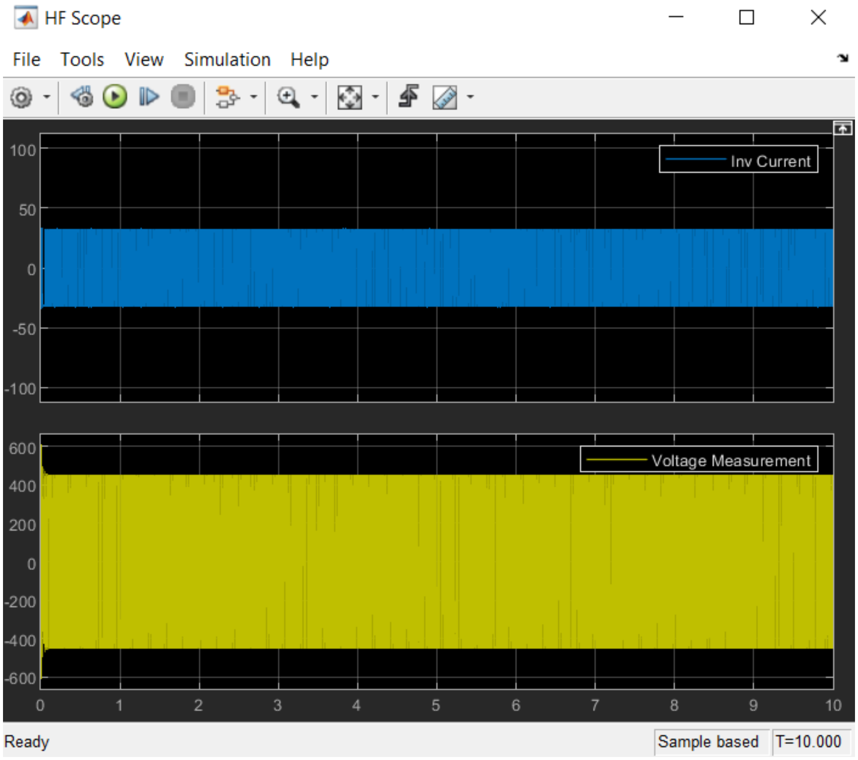

Figure 4.83 HF Scope of Simulation 6.

From the Vehicle Rectifier Scope (Figure 4.84), voltage and current are measured before the vehicle rectifier. Scopes waveform shows voltage peak value at 433 Volt and current at 32.5 Ampere.

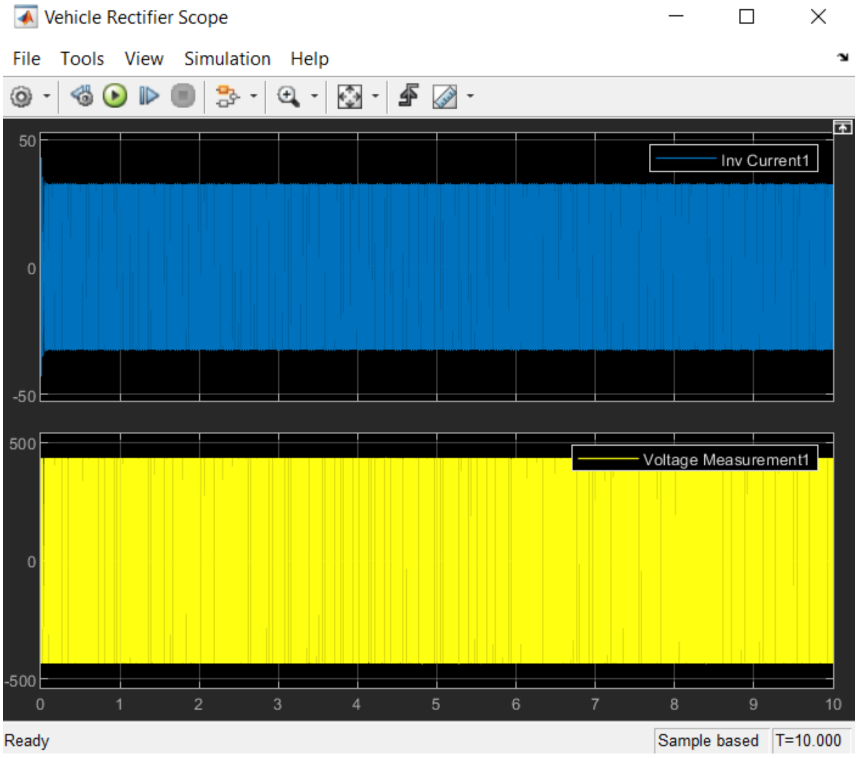

Figure 4.84 Vehicle Rectifier Scope of Simulation 6.

The Battery Scope (Figure 4.85), shows DC voltage value of 431.5 volt and current value at 12.17 Ampere, at the battery considering the mean values.

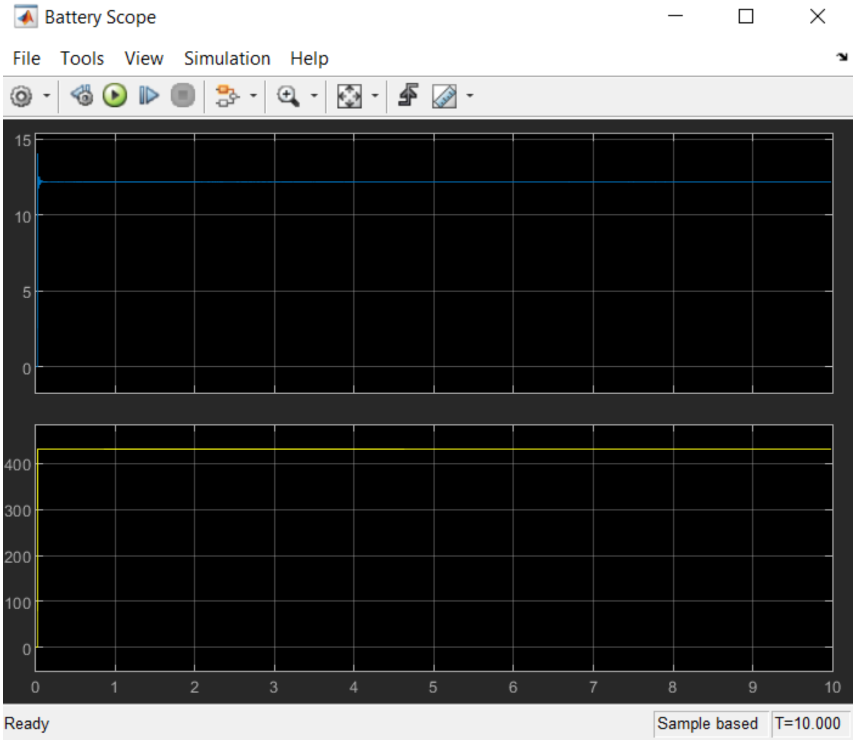

Figure 4.85 Battery Scope of Simulation 6.

The last scope considered; SOC Scope (Figure 4.86) gives information about the state of charge during the process of charging. After the 10 second simulation the soc (%) is 50.033779% with the initial soc at 50%.

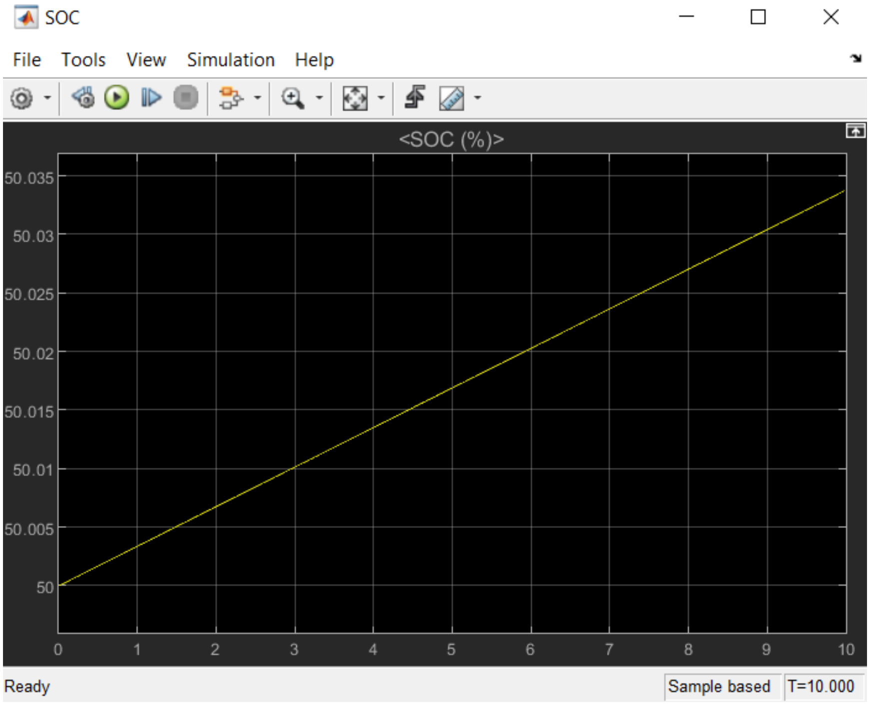

Figure 4.86 SOC Scope of Simulation 6.

As it can observed from the simulation the efficiency of the system is at 88,48%.

Compared to simulation 1 it can be observed that the efficiency increased 3,62%. This result is expected as the ohmic losses decreased.

4.9 Simulation 7

This simulation follows simulation 6 but now the value of frequency is at 19010 Hz in order to limit the power input as close as possible at 6 kW.

The mutual inductance is 54.67e-6 H (0.00005467) and assuming 200mm alignment and a typical gap of 100mm in order to calculate the efficiency.

The whole system of the simulation can be depicted in figure 4.79. Values such as $P_{in,\ ac}$, $Q_{in,\ ac}$, P_{dc} after the rectifier, $P_{bat,\ input}$ are shown in display blocks. Specifically $P_{in,\ ac} = 5973W$, $Q_{in,\ ac} = 2904Var$, $P_{dc} = 5200W$ and $P_{bat,\ input} = 4362W$.

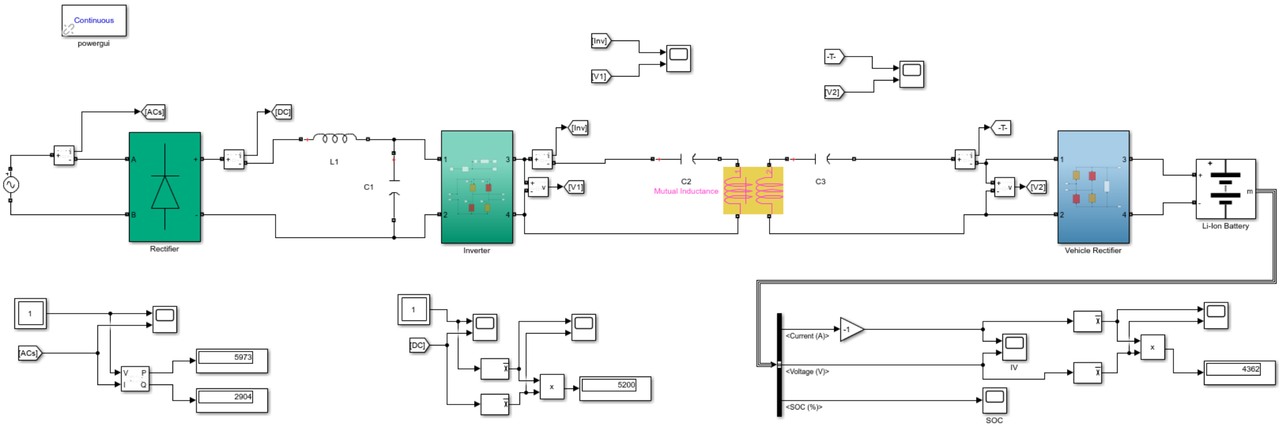

Figure 4.87 Charging system of Simulation 7.

From the AC source Scope (Figure 4.88), Voltage and current are measured. Scopes waveform shows voltage peak value at 350 Volt and current at 43.7 Ampere.

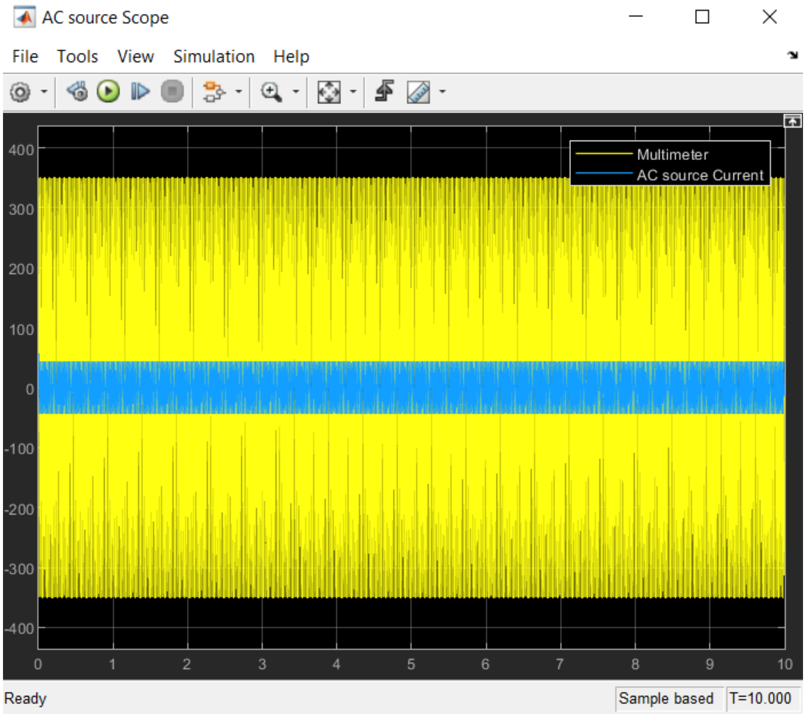

Figure 4.88 AC source Scope of Simulation 7.

The DC Scope (Figure 4.89), shows DC measurements after the rectifier and with the process of considering mean values DC Scope1 (Figure 4.90) shows voltage dc value of 234.5 volt and dc current value of 22.2 Ampere. Measurements can be taken by using the cursor measurements button located rightmost in toolbar.

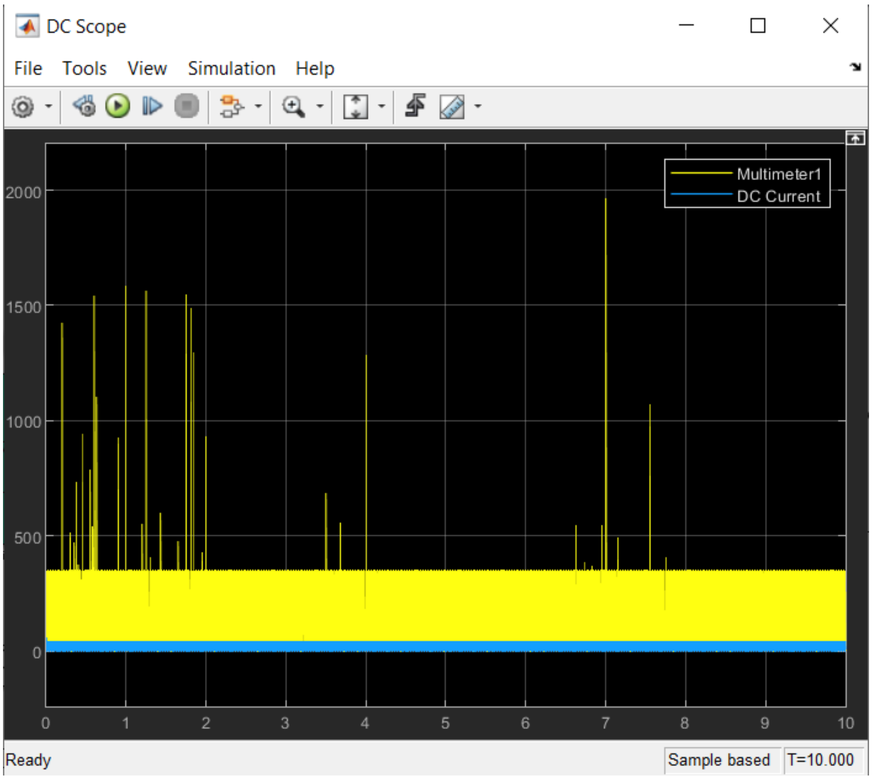

Figure 4.89 DC Scope of Simulation 7.

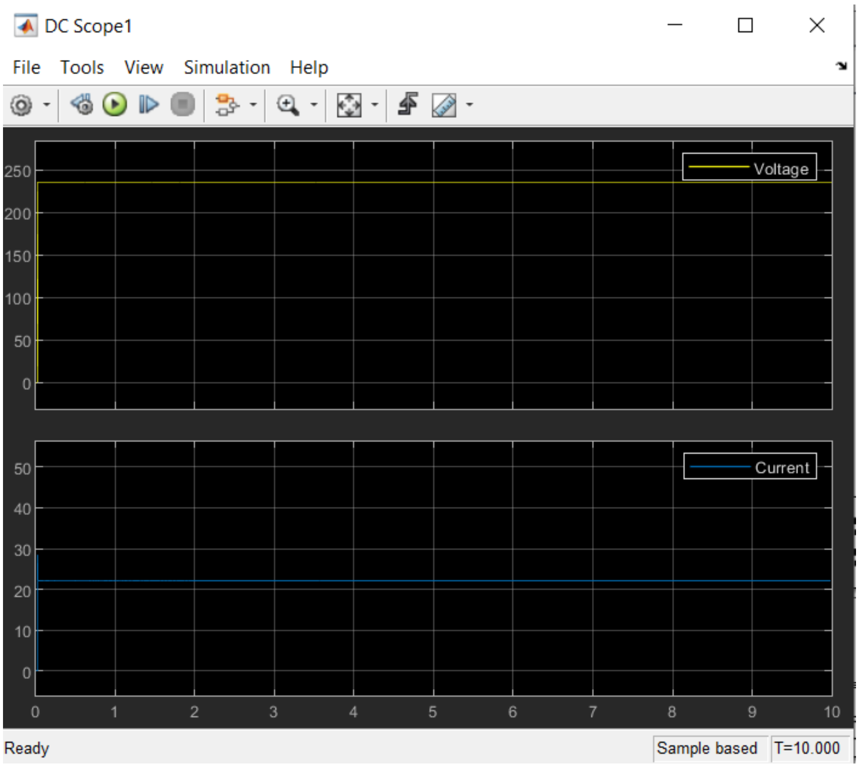

Figure 4.90 DC Scope1 of Simulation 7.

From the HF Scope (Figure 4.91) information about the waveforms of current and voltage after the high frequency inverter can be taken. Peak value of current shown 88.5 Ampere and voltage 305 volt.

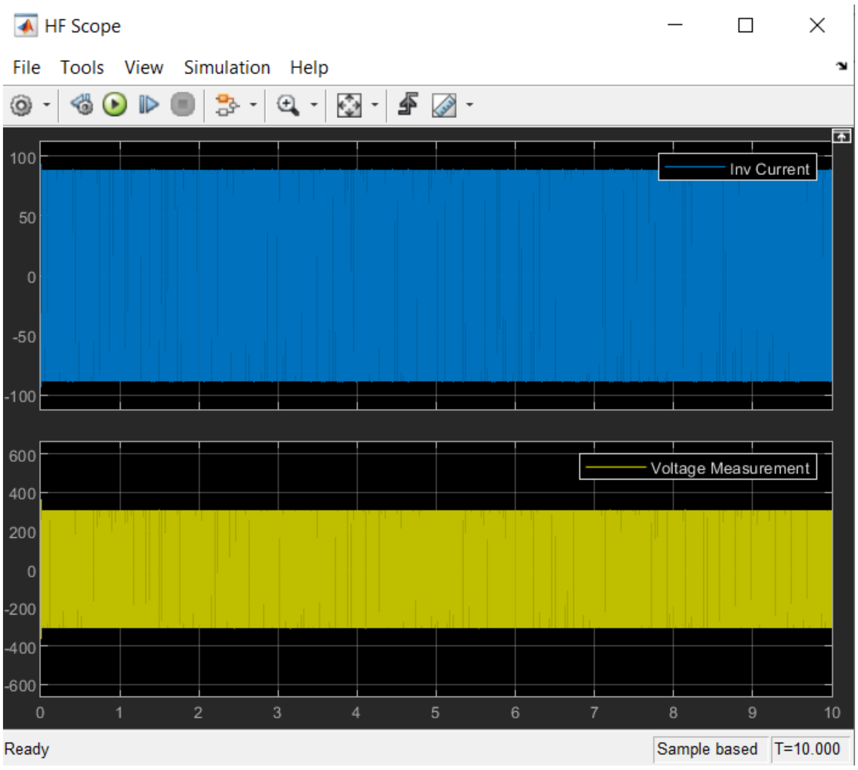

Figure 4.91 HF Scope of Simulation 7.

From the Vehicle Rectifier Scope (Figure 4.92), voltage and current are measured before the vehicle rectifier. Scopes waveform shows voltage peak value at 434 Volt and current at 42.9 Ampere.

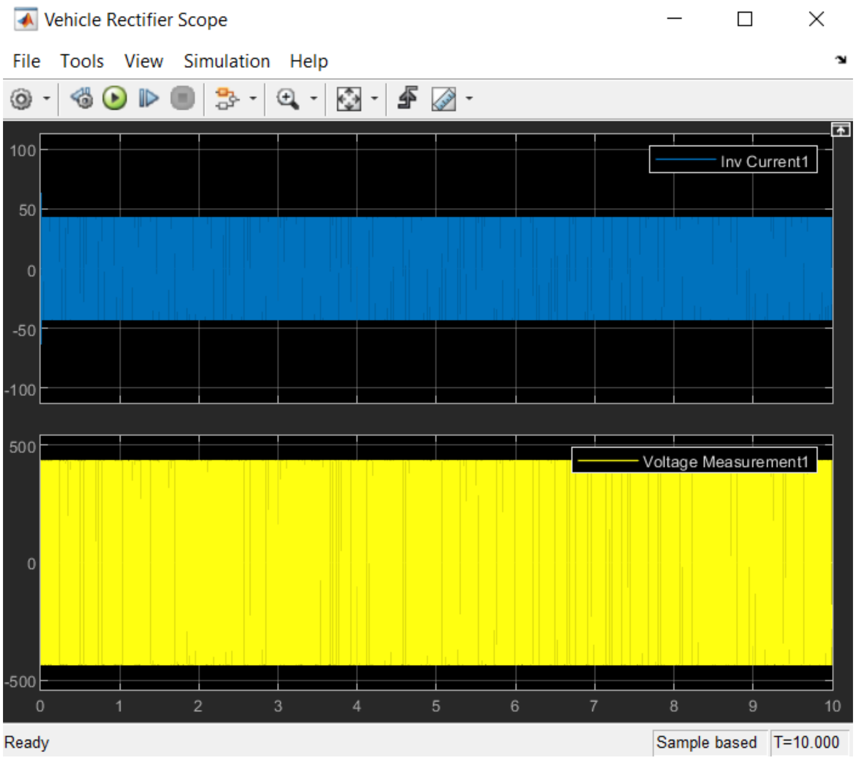

Figure 4.92 Vehicle Rectifier Scope of Simulation 7.

The Battery Scope (Figure 4.93), shows DC voltage value of 431.5 volt and current value at 10.1 Ampere, at the battery considering the mean values.

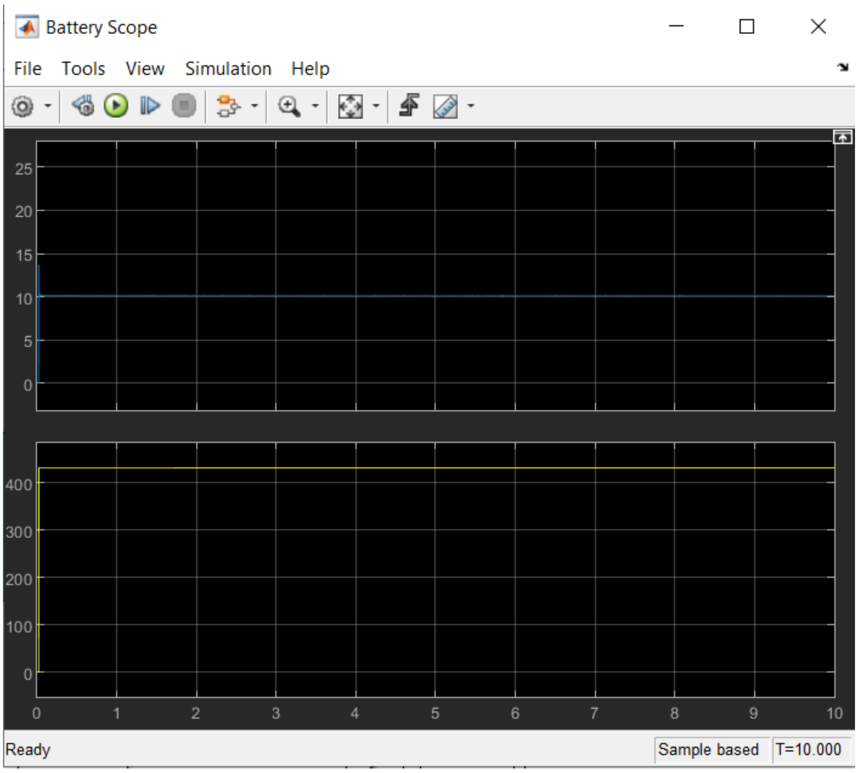

Figure 4.93 Battery Scope of Simulation 7.

The last scope considered; SOC Scope (Figure 4.94) gives information about the state of charge during the process of charging. After the 10 second simulation the soc (%) is 50.028078% with the initial soc at 50%.

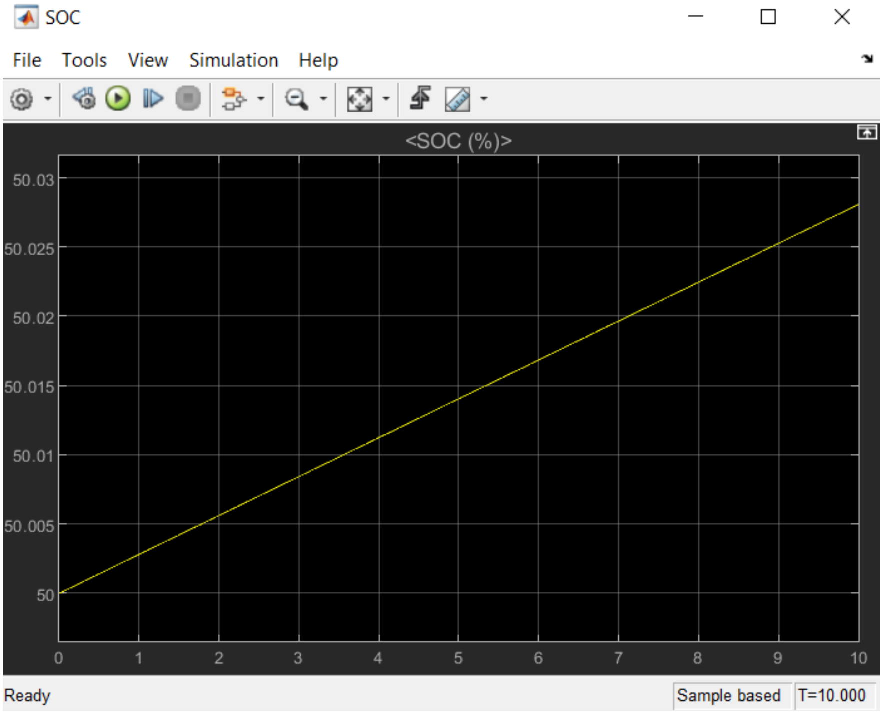

Figure 4.94 SOC Scope of Simulation 7.

As it can observed from the simulation the efficiency of the system is at 73,03%.

Compared to simulation 2 it can be observed that the efficiency decreased 2,59%. This result is expected as the frequency dropped in order to keep the power input at 6 kW, even though ohmic losses decreased.

4.10 Simulation 8

This simulation follows simulation 7 but now the value of frequency is at 19145 Hz in order to limit the power input as close as possible at 6 kW.

The mutual inductance is 41.94e-6 H (0.00004194) and assuming 200mm alignment and a typical gap of 150mm in order to calculate the efficiency.

The whole system of the simulation can be depicted in figure 4.95. Values such as $P_{in, ac}$, $Q_{in, ac}$, P_{dc} after the rectifier, $P_{bat, input}$ are shown in display blocks. Specifically $P_{in, ac} = 5986W$, $Q_{in, ac} = 3018Var$, $P_{dc} = 5274W$ and $P_{bat, input} = 3714W$.

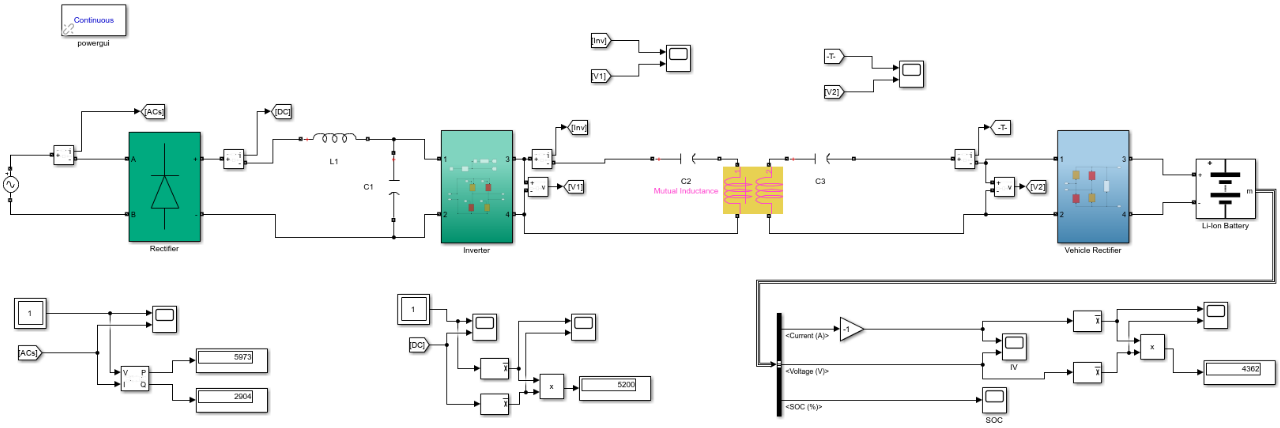

Figure 4.4.95 Charging system of Simulation 8.

From the AC source Scope (Figure 4.96), Voltage and current are measured. Scopes waveform shows voltage peak value at 350 Volt and current at 43.68 Ampere.

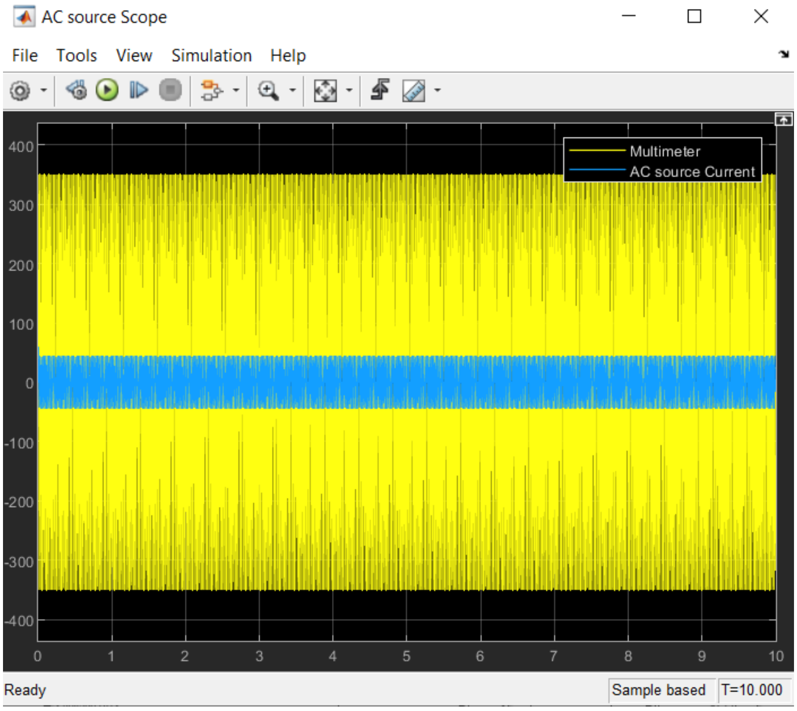

Figure 4.96 AC source Scope of Simulation 8.

The DC Scope (Figure 4.97), shows DC measurements after the rectifier and with the process of considering mean values DC Scope1 (Figure 4.98) shows voltage dc value of 235 volt and dc current value of 22.44 Ampere. Measurements can be taken by using the cursor measurements button located rightmost in toolbar.

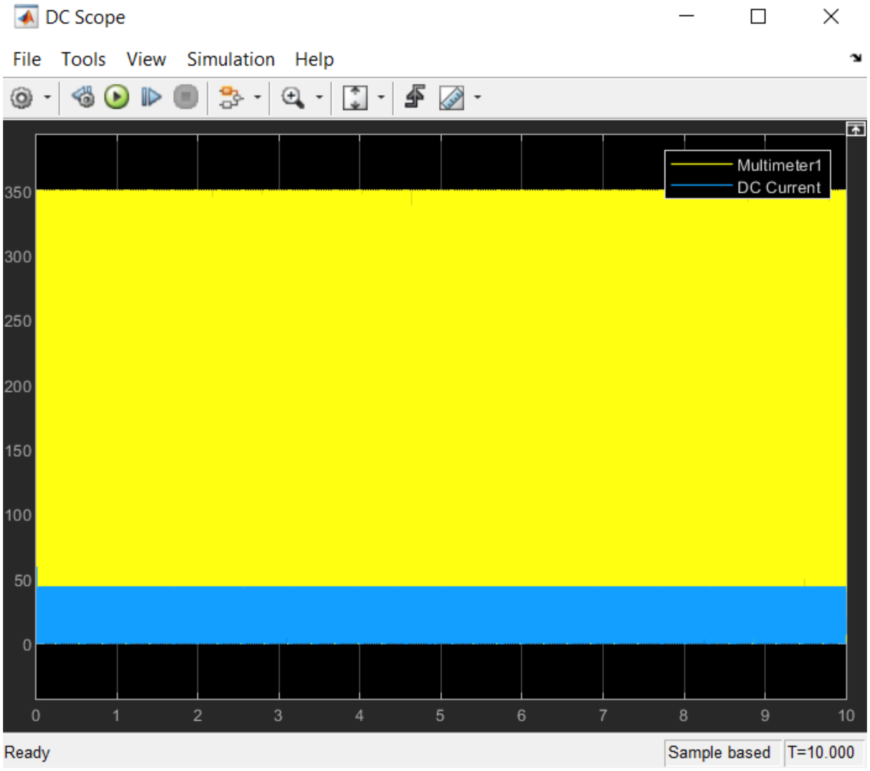

Figure 4.97 DC Scope of Simulation 8.

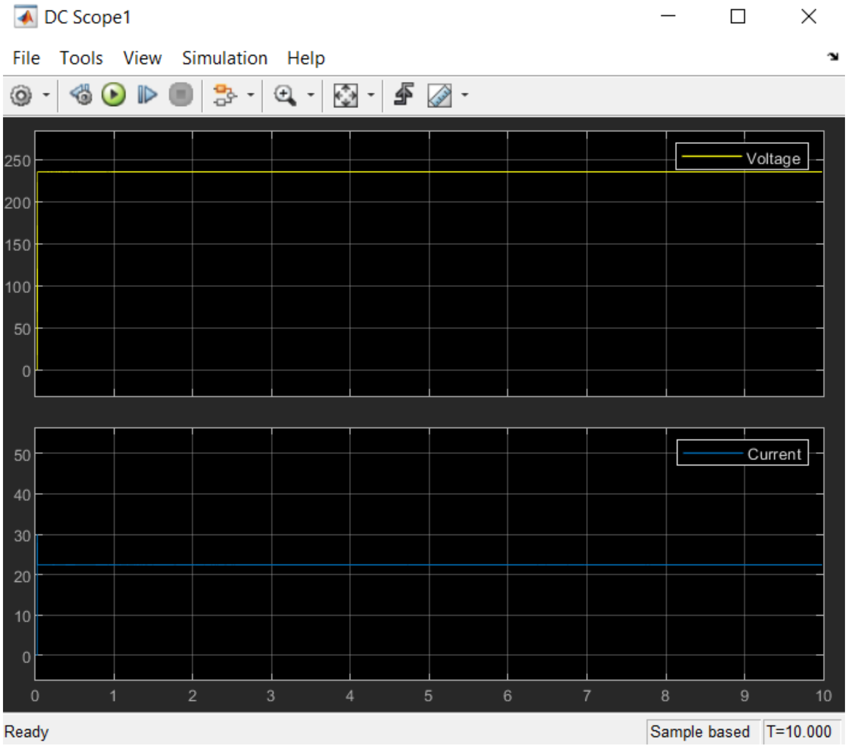

Figure 4.98 DC Scope1 of Simulation 8.

From the HF Scope (Figure 4.99) information about the waveforms of current and voltage after the high frequency inverter can be taken. Peak value of current shown 114 Ampere and voltage 312 volt.

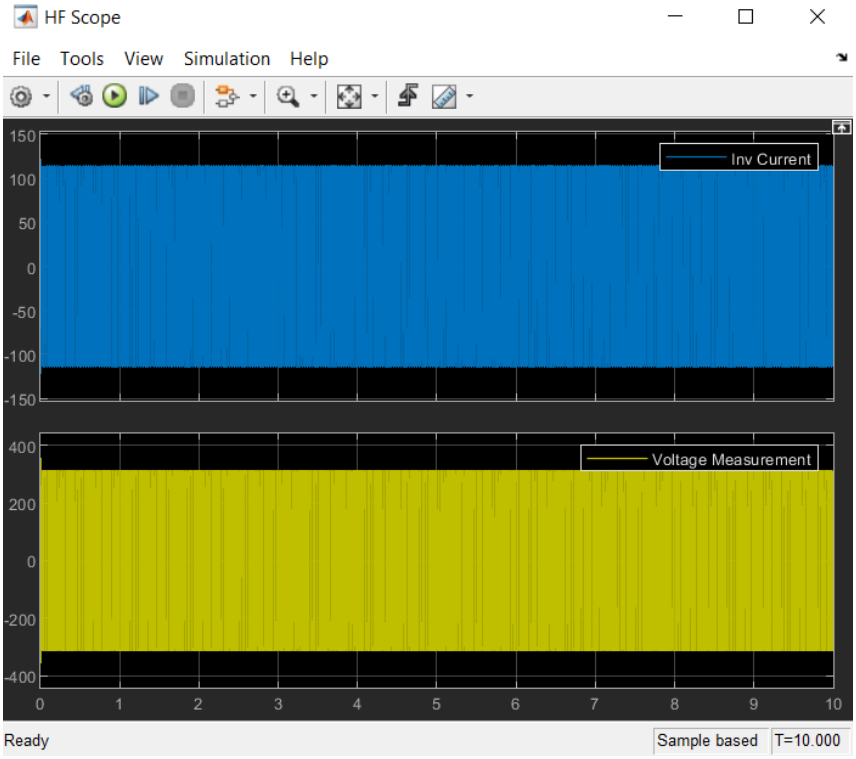

Figure 4.99 HF Scope of Simulation 8.

From the Vehicle Rectifier Scope (Figure 4.100), voltage and current are measured before the vehicle rectifier. Scopes waveform shows voltage peak value at 434 Volt and current at 44 Ampere.

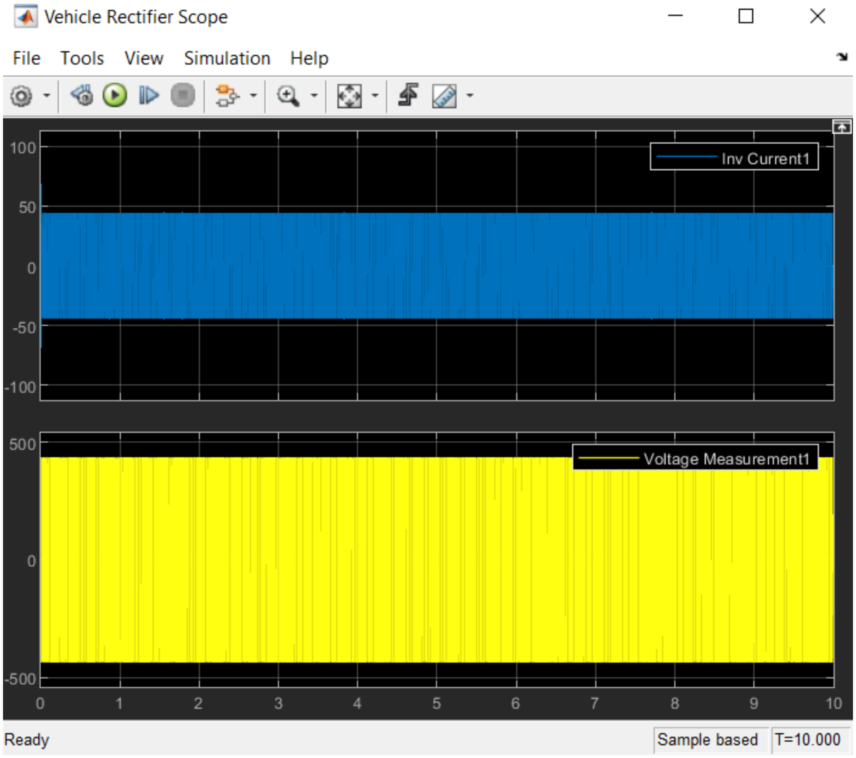

Figure 4.100 Vehicle Rectifier Scope of Simulation 8.

The Battery Scope (Figure 4.101), shows DC voltage value of 431 volt and current value at 8.6 Ampere, at the battery considering the mean values.

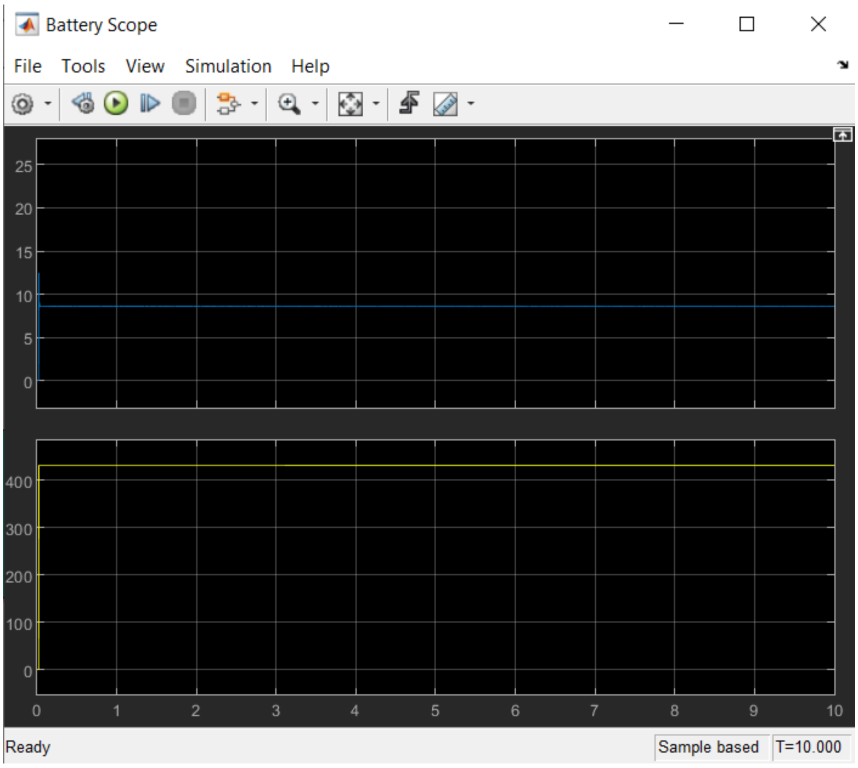

Figure 4.101 Battery Scope of Simulation 8.

The last scope considered; SOC Scope (Figure 4.102) gives information about the state of charge during the process of charging. After the 10 second simulation the soc (%) is 50.023908% with the initial soc at 50%.

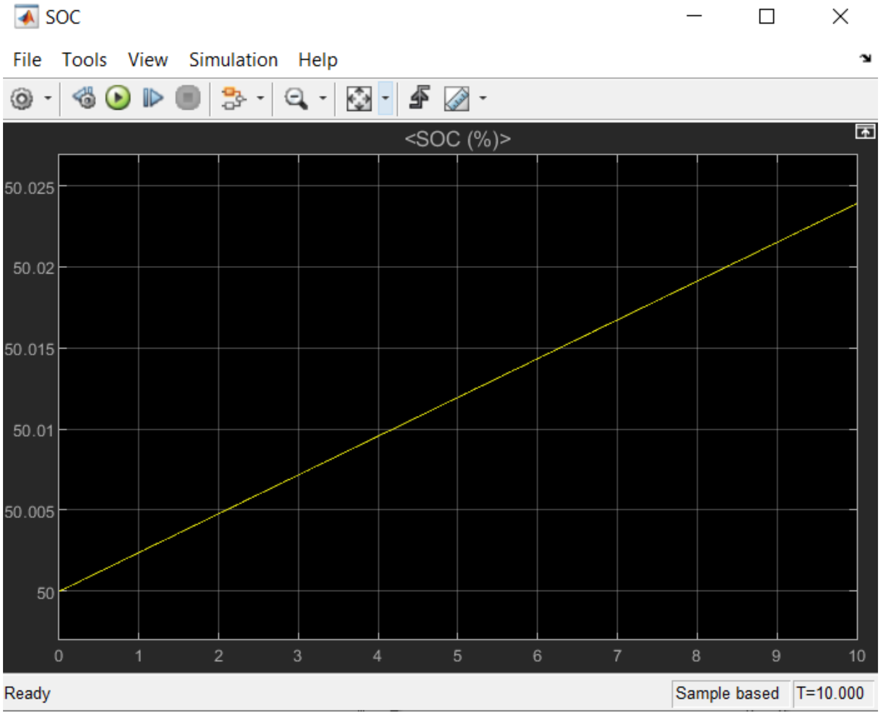

Figure 4.102 SOC Scope of Simulation 8.

As it can observed from the simulation the efficiency of the system is at 62,04%.

Compared to simulation 3 it can be observed that the efficiency decreased 7,22%. This result is expected as the frequency dropped in order to keep the power input at 6 kW, even though ohmic losses decreased.

4.11 Simulation 9

In this simulation the topology of the best performing simulation (simulation 6 at 88,48%) has changed from series-series to series parallel, in order to compare the topologies.

Changing the topology to series parallel requires a change in value of the sending side capacitor from the value of 2.379E-07 to 3.273E-07.

In this simulation the parameters are like the simulation 6 and the value of frequency is at 19999.864 Hz. Mutual inductance is 139.1e-6 H (0.0001391) and the gap is 100mm.

The whole system of the simulation can be depicted in figure 4.103. Values such as $P_{in,\ ac}$, $Q_{in,\ ac}$, P_{dc} after the rectifier, $P_{bat,\ input}$ are shown in display blocks. Specifically $P_{in,\ ac} = 5975W$, $Q_{in,\ ac} = 3530Var$, $P_{dc} = 5682W$ and $P_{bat,\ input} = 4105W$.

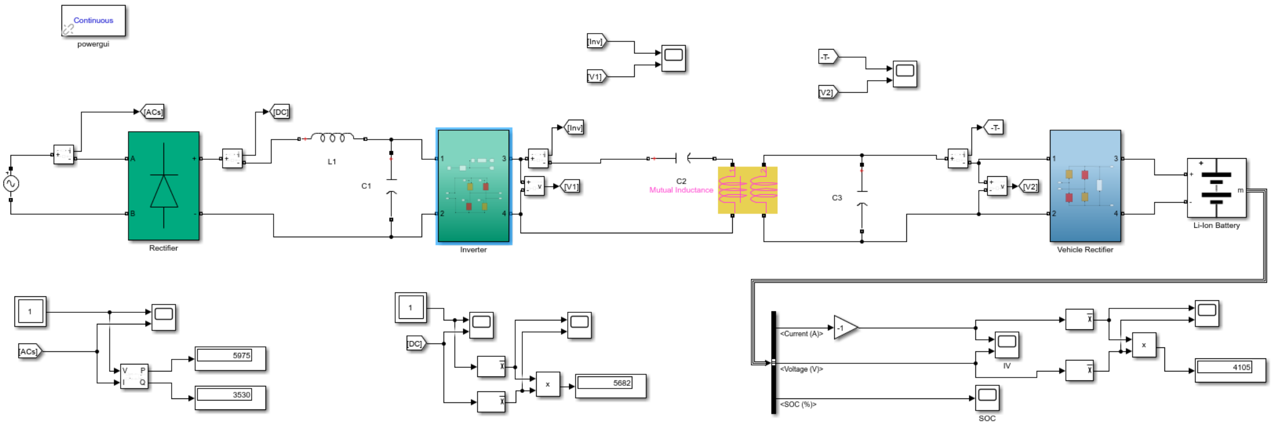

Figure 4.103 Charging system of Simulation 9.

From the AC source Scope (Figure 4.104), Voltage and current are measured. Scopes waveform shows voltage peak value at 350 Volt and current at 48 Ampere.

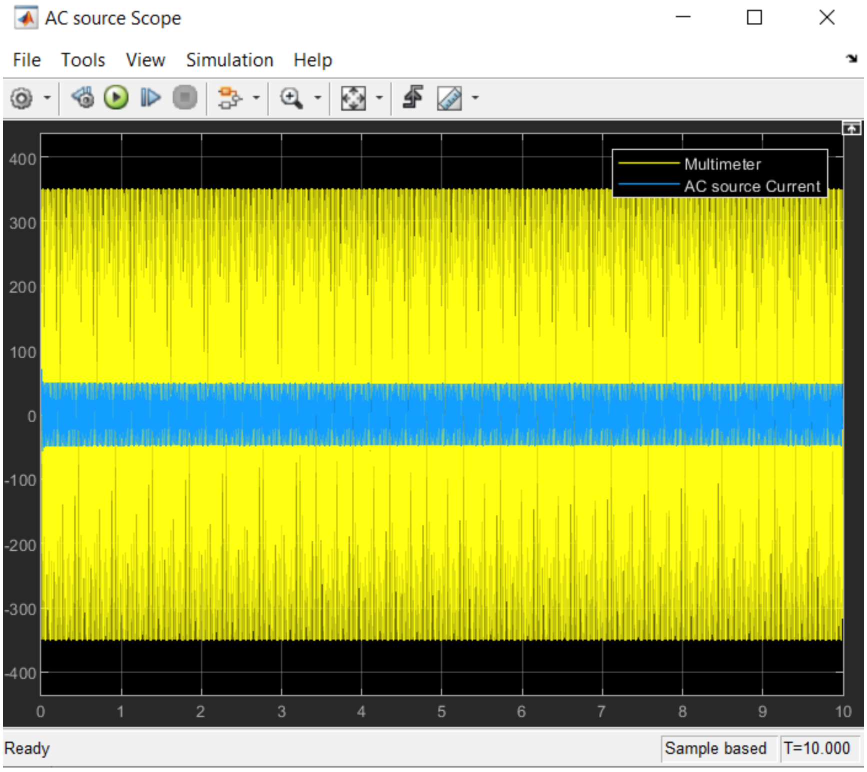

Figure 4.104 AC source Scope of Simulation 9.

The DC Scope (Figure 4.105), shows DC measurements after the rectifier and with the process of considering mean values DC Scope1 (Figure 4.106) shows voltage dc value of 222.75 volt and dc current value varying from 25.5 to 26.4 Ampere. Measurements can be taken by using the cursor measurements button located rightmost in toolbar.

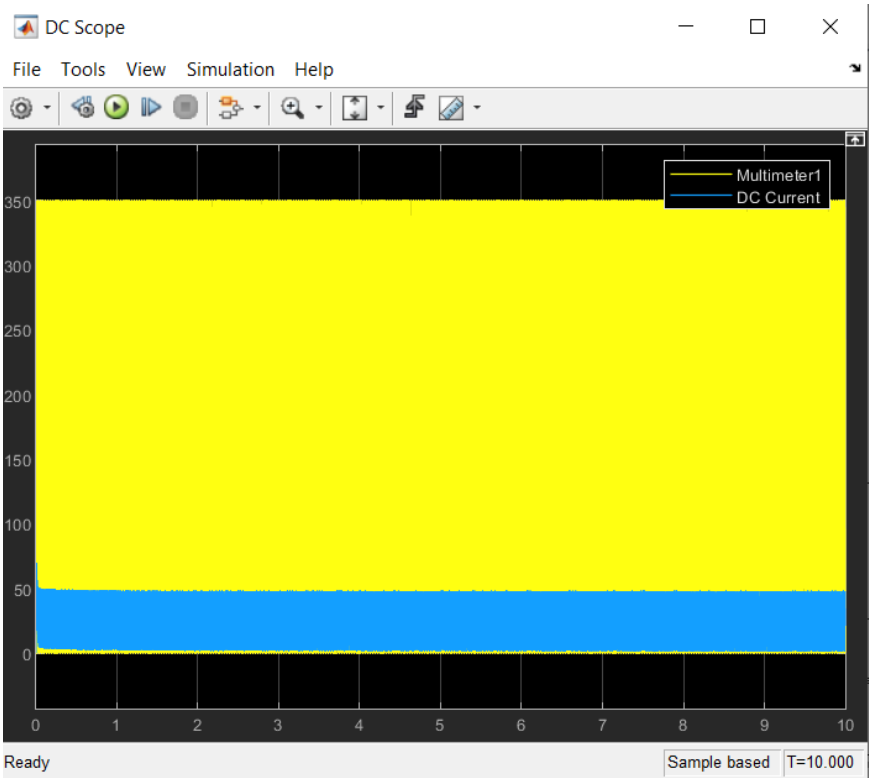

Figure 4.105 DC Scope of Simulation 9.

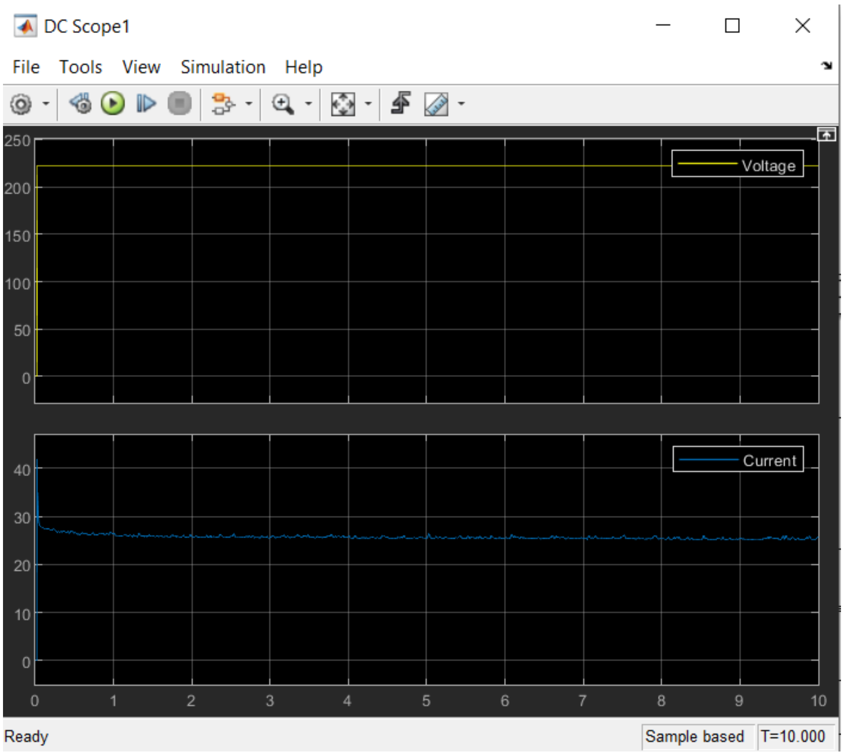

Figure 4.106 DC Scope1 of Simulation 9.

From the HF Scope (Figure 4.107) information about the waveforms of current and voltage after the high frequency inverter can be taken. Peak value of current shown 87 Ampere and voltage 247 volt.

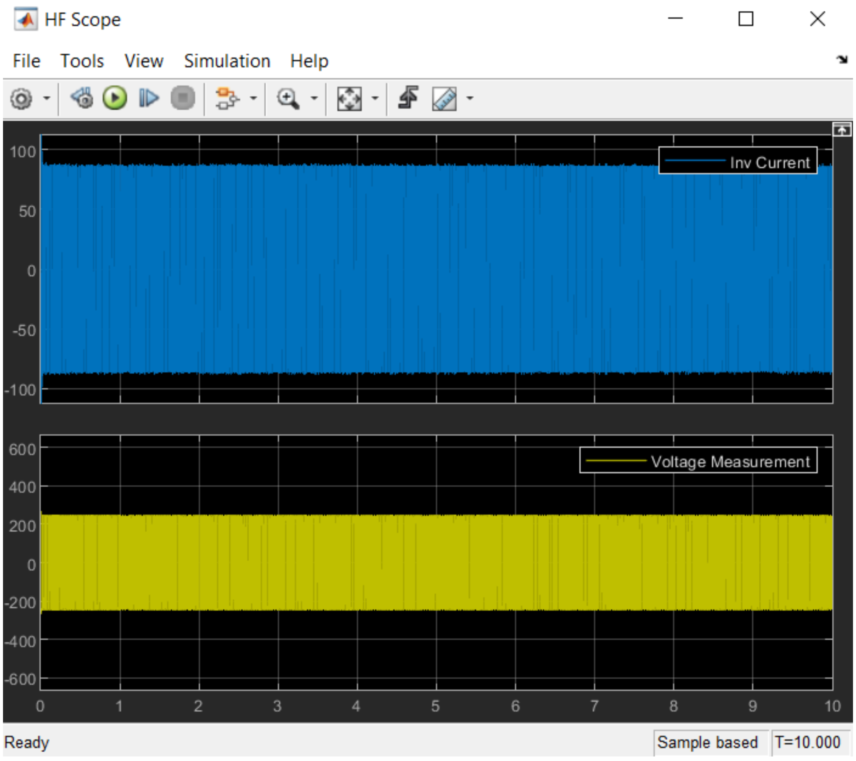

Figure 4.107 HF Scope of Simulation 9.

From the Vehicle Rectifier Scope (Figure 4.108), voltage and current are measured before the vehicle rectifier. Scopes waveform shows voltage peak value at 434 Volt and current at unstable level going sometimes over 200 Ampere.

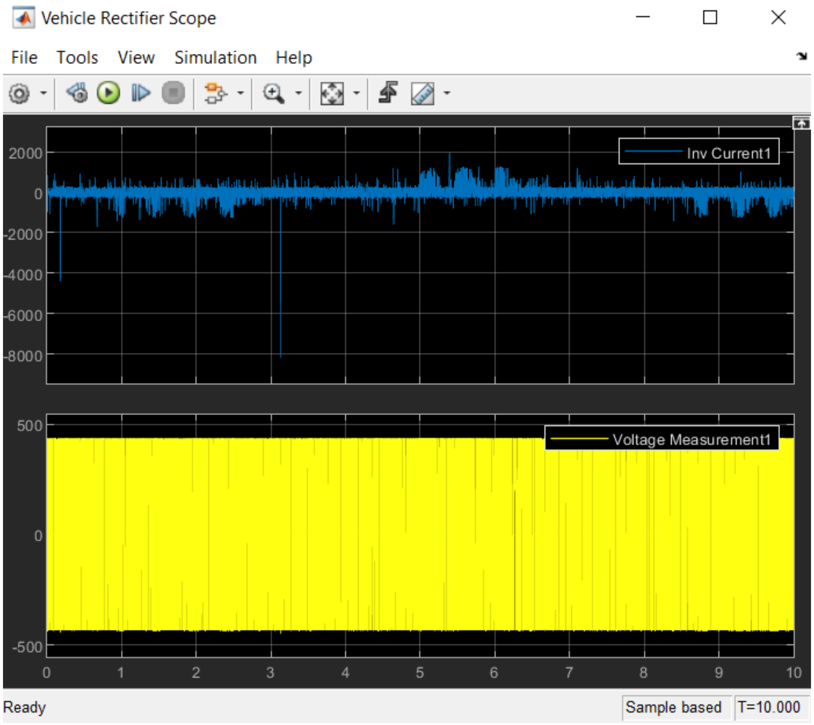

Figure 4.108 Vehicle Rectifier Scope of Simulation 9.

The Battery Scope (Figure 4.109), shows DC voltage value of 431.5 volt and current varying from 9.4 to 10 Ampere, at the battery considering the mean values.

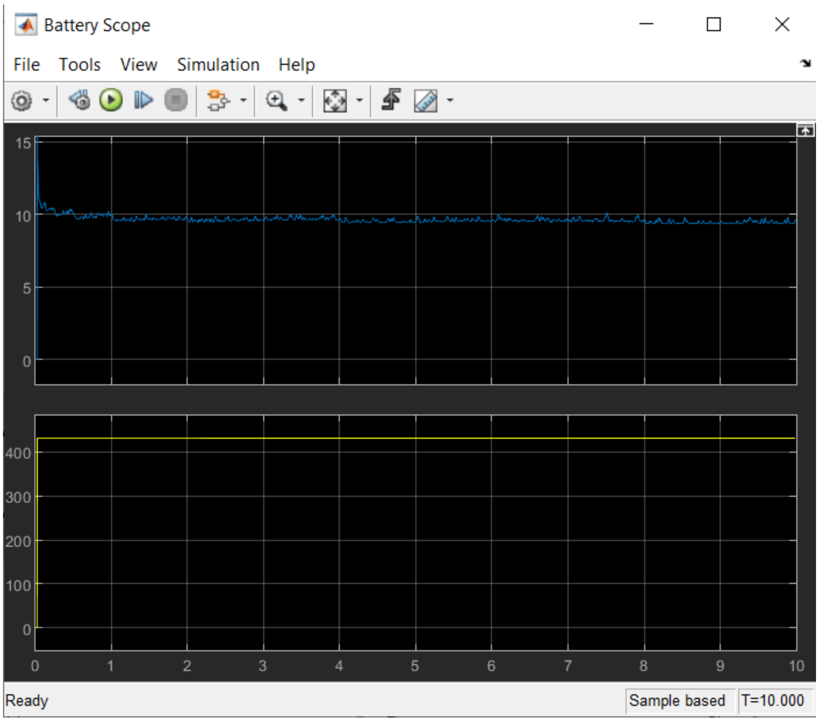

Figure 4.109 Battery Scope of Simulation 9.

The last scope considered; SOC Scope (Figure 4.110) gives information about the state of charge during the process of charging. After the 10 second simulation the soc (%) is 50.02674% with the initial soc at 50%.

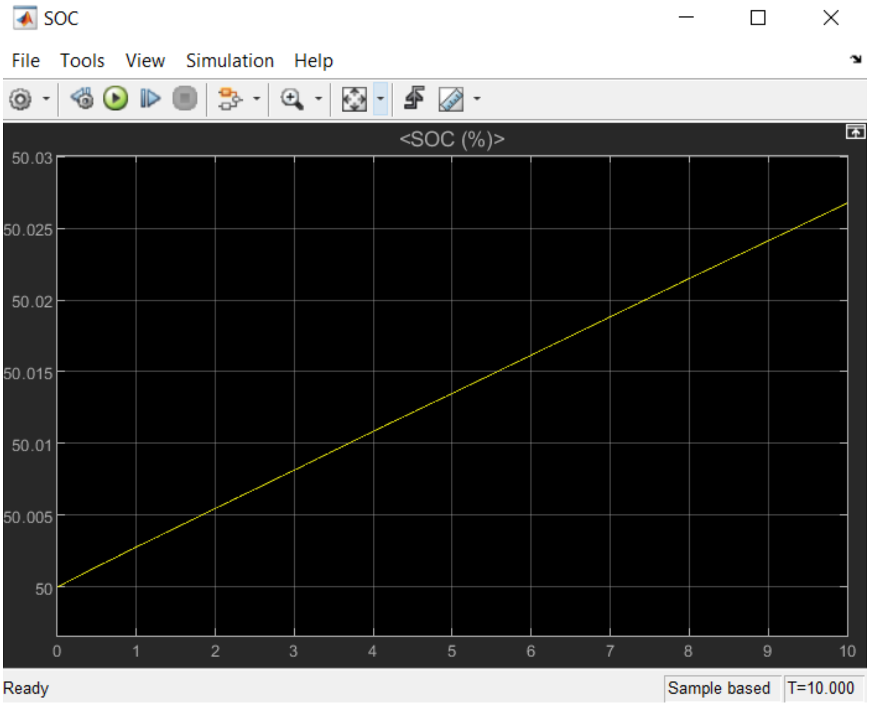

Figure 4.110 SOC Scope of Simulation 9.

As it can observed from the simulation the efficiency of the system is about 68.68%.

Compared to simulation 6 it can be observed that the efficiency decreased 19.8%. As a result, for the current type of model a series series topology considered more efficient that a series parallel.

The results of each simulation have been gathered in table 7.

Results of simulations

Simulation		1	2	3	4	5	6	7	8	9
$P_{in,\ ac}$ (Watt)		6005	13580	15940	1945	4608	5939	5973	5986	5975
$Q_{in,\ ac}$ (Var)		2405	5442	6819	621.9	1582	2384	2904	3018	3530
P_{dc} (Watt)		5945	12050	13740	1840	4212	5887	5200	5274	5682
$P_{bat,\ input}$ (Watt)		5096	10270	11040	1298	3814	5255	4362	3714	4105
AC source Scope	I	52.5	99.3	112	-	-	52	43.7	43.68	48
	V	350	350	350	-	-	350	350	350	350
DC Scope1	I	20.25	48.5	64.54	-	-	20	22.2	22.44	25.5-26.4
	V	293	248.5	222.69	-	-	293.5	234.5	235	222.75
HF Scope	I	33	89	118	-	-	32.5	88.5	114	87
	V	455	513	464.5	-	-	452	305	312	247
Vehicle Rectifier Scope	I	32	86	96.5	-	-	32.5	42.9	44	>200
	V	433.5	435	435	-	-	433	434	434	434
Battery Scope	I	11.8	27.75	25.5	-	-	12.17	10.1	8.6	9.4-10
	V	431.5	432.5	432.3	-	-	431.5	431.5	431	431.5
SOC Scope (%)		50,0375	50,066	50,0708	50,0085	50,025	50,0338	50,0281	50,0239	50,0267
Efficiency (%)		84.86	75.62	69.26	66.73	82.77	88.48	73.03	62.04	68.68

5 Simulations Analysis

Considering simulations 1,2 and 3, it can be observed that as the gap and the misalignment grows, mutual inductance values decrease as well as system's efficiency. Due to the decrease of the total impedance of the system, consumed current grows.

When distance between transmitter and receiver is increased, power rises in the limit. This is proven as it can be observed from simulation 1,2 and 3. Power rises from 6005 Watt to 15940 Watt. When the transmitter is fed in the absence of receiver, absorbed power is very high, which makes necessary the utilization of a control that detects the presence of receiver.

As the current grows, with a constant voltage source, the value of real input power $P_{in,ac}$ increases as well. This is the reason why, despite the fact that the efficiency decreases, the state of charge grows faster.

When misalignment occurs, with a constant frequency, the power transferred to the load increases significantly. However, a solution to that would be a slight increase in the operating frequency. This will keep transferred power constant in its designed value, although this will cause an increase in transmitter current because the system goes out of resonance.

In the first simulation, where there is no misalignment and the gap is 0,1 meters, the efficiency of the system is 84,86%. This is not the best possible outcome, as it is well-known that the efficiency of resonant inductive power transfer can reach even 94%. High value in the ohmic part of both coils self-impedance is the main reason for lower efficiency.

Smaller ohmic part can increase the consumed current in intolerable values. Current limitation controls necessitate as well as battery management system to drop the current in safe values.

In DC Scope of Simulation 1 it can be observed that the voltage is unstable. In order to reduce the "noise" the value of L_1 has to be increased. This will cause more time for the stabilization of the system as well as a drop in efficiency.

Proceeding in simulation 2 it can be observed that by increasing the alignment at 0,2 meters, mutual inductance falls to 54.67e-6 H (from 139.1e-6 H). This resulted a drop in efficiency from 84,86% to 75,62%. It is also observed that the current rises in more than double the amount of the previous simulation.

In simulation 3 where the gap has changed to 0,15 meters and the alignment at 0,2 meters, mutual inductance calculated 41.94e-6 H. The lower the total impedance, the more losses. This resulted a drop of 6,36% (69.26%) from the previous simulation.

Observing this series of simulations make necessary the limitation of the growing current. In real world scenarios current doesn't grow 25,5 amperes to charge the battery. A battery management system is needed to protect the battery and a limitation of consumed $P_{in,\ ac}$.

Simulations 4 and 5 has proved that the input power is controllable by adjusting the frequency. Lowering the frequency lowers the input power and increasing it, input power grows. Decreasing the value of frequency cause greater loses than increasing it.

In real world scenarios power is limited. Also, the ohmic part can be lower with utilization of better materials. The reduction of the ohmic part in simulation 6 has shown 3,62% increased efficiency (compared to simulation 1), with the total efficiency for an almost 6 kW installation reaching 88,48%. In the next two simulations (7 and 8) frequency has been adjusted in order to maintain 6 kW installation. The results prove that it is possible to maintain the input power but it comes with greater loses. Comparing simulation 2 with 7 it can be observed that the efficiency drops from 75,62% to 73,03% and comparing 3 with 8 the efficiency drops from 69,26% to 62,04%.

Considering simulations 6,7 and 8 it can be observed that efficiency has been increased for no misalignment. It can also be observed that with resonant inductive power transfer higher efficiency is achievable and consulting the results of simulations 4 and 5 it is clear which method is better in terms of efficiency.

Simulation 9 has been created in order to observe how, by adjusting the installation from series-series to series-parallel, would affect the system. The best performing simulation has been adjusted and it is clear that the system becomes unstable, with the efficiency reaching 69,68% and the vehicle rectifier scope showing many harmonics.

Overall, the best performing simulation is simulation 6. Efficiency reaching close to currently maximum efficiency of 94%. The gap of 5,52% is because the materials that has been utilized probably have greater ohmic part. Also, operational frequency can contribute in efficiency as well as the gap. Worst performing scenario is 8 because frequency has to be adjusted way out of resonance in order to maintain the 6 kW installation and the system safe from high values of current.

6 CONCLUSIONS

In this thesis, we have embarked on a comprehensive journey to explore the theoretical foundations and practical implementations of dynamic wireless power charging systems, with a particular focus on their applications in electric vehicle (EV) charging. The integration of passive components, semiconductors, and microstrip technologies has provided a robust framework for understanding the intricate behaviors and potentials of these innovative charging systems.

In total, nine simulations were conducted using MATLAB/Simulink. The first three were conducted in order to understand how the system works and to relate gap and misalignment with efficiency. From these 3 simulations it can be observed that as the gap and the misalignment grow, mutual inductance values decrease as well as system's efficiency. Due to the decrease of the total impedance of the system, consumed current grows. In the first simulation, where there is no misalignment and the gap is 0,1 meters, the efficiency of the system is 84,86%. This is not the best possible outcome, as it is well-known that the efficiency of resonant inductive power transfer can reach even 94%. High value in the ohmic part of both coils self-impedance is the main reason for lower efficiency. Proceeding in simulation 2 it can be observed that by increasing the alignment at 0,2 meters, mutual inductance falls to 54.67e-6 H (from 139.1e-6 H). This resulted a drop in efficiency from 84,86% to 75,62%. It is also observed that the current rises in more than double the amount of the previous simulation.

In simulation 3 where the gap has changed to 0,15 meters and the alignment at 0,2 meters, mutual inductance calculated 41.94e-6 H. The lower the total impedance, the more losses. This resulted a drop of 6,36% (69.26%) from the previous simulation.

Proceeding, simulations 4 and 5 were conducted in order to observe how the operational frequency affects the system. Simulations 4 and 5 has proved that the input power is controllable by adjusting the frequency.

Afterwards a series of 3 more simulations were conducted in order to build a real world scenario, which is higher efficiency and controllable power input. In real world scenarios power is limited. Also, the ohmic part can be lower with utilization of better materials. The reduction of the ohmic part in simulation 6 (from 0,668 Ω to 0.368 Ω) has shown 3,62% increased efficiency (compared to simulation 1), with the total efficiency for an almost 6 kW installation reaching 88,48%. In the next two simulations (7 and 8) frequency has been adjusted in order to maintain 6 kW installation. The results prove that it is possible to maintain the input power but it comes with greater loses. Comparing simulation 2 with 7 it can be observed that the efficiency drops from 75,62% to 73,03% and comparing 3 with 8 the efficiency drops from 69,26% to 62,04%.

Simulation 9 has been created in order to observe how, by adjusting the installation from series-series to series-parallel, would affect the system. The best performing simulation has been adjusted and it is clear that the system becomes unstable, with the efficiency reaching 69,68% and the vehicle rectifier scope showing many harmonics.

The following table provides the gathered results of the simulations.

Results of simulations

Simulation		1	2	3	4	5	6	7	8	9
$P_{in,\ ac}$ (Watt)		6005	13580	15940	1945	4608	5939	5973	5986	5975
$Q_{in,\ ac}$ (Var)		2405	5442	6819	621.9	1582	2384	2904	3018	3530
P_{dc} (Watt)		5945	12050	13740	1840	4212	5887	5200	5274	5682
$P_{bat,\ input}$ (Watt)		5096	10270	11040	1298	3814	5255	4362	3714	4105
AC source Scope	I	52.5	99.3	112	-	-	52	43.7	43.68	48
	V	350	350	350	-	-	350	350	350	350
DC Scope1	I	20.25	48.5	64.54	-	-	20	22.2	22.44	25.5-26.4
	V	293	248.5	222.69	-	-	293.5	234.5	235	222.75
HF Scope	I	33	89	118	-	-	32.5	88.5	114	87
	V	455	513	464.5	-	-	452	305	312	247
Vehicle Rectifier Scope	I	32	86	96.5	-	-	32.5	42.9	44	>200
	V	433.5	435	435	-	-	433	434	434	434
Battery Scope	I	11.8	27.75	25.5	-	-	12.17	10.1	8.6	9.4-10
	V	431.5	432.5	432.3	-	-	431.5	431.5	431	431.5
SOC Scope (%)		50,0375	50,066	50,0708	50,0085	50,025	50,0338	50,0281	50,0239	50,0267
Efficiency (%)		84.86	75.62	69.26	66.73	82.77	88.48	73.03	62.04	68.68

In conclusion from the series of simulations and the thesis the foundlings are:

- As the gap and the misalignment grows, mutual inductance values decrease as well as system's efficiency. Due to the decrease of the total impedance of the system, consumed current grows.
- When distance between transmitter and receiver is increased, power rises in the limit.
- When the transmitter is fed in the absence of receiver, absorbed power is very high, which makes necessary the utilization of a control that detects the presence of receiver.
- As the current grows, with a constant voltage source, the value of real input power $P_{in,ac}$ increases as well. This is the reason why, despite the fact that the efficiency decreases, the state of charge grows faster.
- When misalignment occurs, with a constant frequency, the power transferred to the load increases significantly. However, a solution to that would be a slight increase in the operating

frequency. This will keep transferred power constant in its designed value, although this will cause an increase in transmitter current because the system goes out of resonance.

- Smaller ohmic part can increase the consumed current in intolerable values. Current limitation controls necessitate as well as battery management system to drop the current in safe values.
- Simulations 4 and 5 has proved that the input power is controllable by adjusting the frequency. Lowering the frequency lowers the input power and by increasing it, input power grows. Decreasing the value of frequency cause greater loses than increasing it.
- The best performing simulation is simulation 6. Efficiency reaching close to currently maximum efficiency of 94%. The gap of 5,52% is because the materials that has been utilized probably have greater ohmic part. Also, operation frequency can contribute in efficiency as well as the gap. Worst performing scenario is 8 because frequency has to be adjusted way out of resonance in order to maintain the 6 kW installation and the system safe from high values of current.
- This thesis has provided a detailed analysis of dynamic wireless power charging systems, substantiated by practical simulations and theoretical insights. The model that has been created, can be used as a tool for understanding of wireless systems but also can provide real world simulations. The potential of these systems to transform the EV charging infrastructure is immense, promising a future where sustainable transportation is not only achievable but also efficient and reliable.

Βιβλιογραφία – Αναφορές - Διαδικτυακές Πηγές

[1]. *Cotter W. Sayre, Complete Wireless Design, 2001,*

[2]. *Nikolaos Korakianitis, Georgios A. Vokas, Georgios Ioannides, Review of Wireless Power Transfer (WPT) on Electric Vehicles (EVs) Charging,*

[3]. *Nabbel.Pm, A Cost-Effective System for Wireless Power Transmission, 2011*

[4]. *Merriam-Webster.com Dictionary, s.v. "magnetic induction," accessed November 8, 2022, https://www.merriam-webster.com/dictionary/magnetic%20induction.*

[5]. *Chirag Panchal, Sascha Stegen, Junwei Lu, Review of static and dynamic wireless electric vehicle charging system, 2018*

[6]. *Muhammad Amjad, Muhammad Farooq-i-Azam, Qiang Ni, Mianxiong Dong, Ejaz Ahmad Ansari, Wireless charging systems for electric vehicles, 2022*

[7]. *Detka K, Górecki K. Wireless Power Transfer—A Review. Energies. 2022. https://doi.org/10.3390/en15197236*

[8]. *S. Sharma, Y. Chen, and R. He, A Comprehensive Review of Dynamic Wireless Charging for Electric Vehicles: Recent Progress and Perspectives, 2020.*

[9]. *K. Park. Advanced Integrated Communication Systems for Electric Vehicle Wireless Charging, 2018.*

[10]. *J. A. Ferreira, Power electronics for an all-electric transportation system, 2001.*

[11]. *J. Villa, Technological trends, global market, and challenges of electric vehicle charging infrastructure, 2019.*

[12]. *S. Shin, S. Shin, and Y. Kim, Development of an efficient wireless power transfer system using magnetic resonance for electric vehicles, 2017.*

[13]. *J. Sallan, Efficient wireless power transfer system for electric vehicle charging, 2008.*

[14]. *L. Zeng and B. Li, Wireless power transfer for electric vehicle dynamic charging, 2013.*

[15]. *Z. Low, Design and test of a high-power high-efficiency loosely coupled planar wireless power transfer system, 2009.*

[16]. *J. T. Boys, G. A. Covic, and A. W. Green, Stability and control of inductively coupled power transfer systems, 2000.*

[17]. *M. Budhia, G. A. Covic, and J. T. Boys, Design and optimization of circular magnetic structures for lumped inductive power transfer systems, 2011.*

[18]. *H. H. Wu, Design considerations for wireless power transfer coils, 2011.*

[19]. *W. Zhang, A review on the recent development of capacitive wireless power transfer technology, 2017.*

[20]. *M. Kiani and U-M Jow, "Design and optimization of a 3-coil inductive link for efficient wireless power transmission," 2011.*

[21]. *W. Li and C. C. Mi, "Wireless power transfer for electric vehicle applications," 2015.*

[22]. *P. Kundur, "Power system stability and control," 1994.*

[23]. *J. D. Glover, M. S. Sarma, and T. Overbye, "Power system analysis and design," 2010.*

[24]. *M. H. Rashid, "Power electronics handbook," 2012.*

[25]. *R. W. Erickson and D. Maksimovic, "Fundamentals of power electronics," 2001.*

[26]. *D. G. Holmes and T. A. Lipo, "Pulse width modulation for power converters," 2003.*

[27]. *N. Mohan, "Advanced electric drives: Analysis, control, and modeling using MATLAB/Simulink," 2003.*

[28]. *A. Kurs et al., "Wireless power transfer via strongly coupled magnetic resonances," 2007.*

[29]. J. Kim et al., "Design and implementation of shaped magnetic-resonance-based wireless power transfer system for roadway-powered moving electric vehicles," 2011.

[30]. B. Scrosati and J. Garche, "Lithium batteries: Status, prospects and future," 2010.

[31]. G. L. Plett, "Extended Kalman filtering for battery management systems of LiPB-based HEV battery packs: Part 3. State and parameter estimation," 2004.

[32]. C. C. Mi, G. Buja, S. Y. Choi, and C. T. Rim, "Modern advances in wireless power transfer systems for roadway powered electric vehicles," 2016.

[33]. C. Jiang and M. A. Hannan, "In-motion wireless power transfer for electric vehicle charging: Recent progress and perspectives," 2019.

[34]. P. Si, A. P. Hu, S. Malpas, and D. Budgett, "A frequency control method for regulating wireless power to implantable devices," 2008.

[35]. S. Ahson and M. Ilyas, "Electric and Plug-In Hybrid Vehicles: Advanced Simulation Methodologies," 2015.

[36]. W. C. Brown, "The history of power transmission by radio waves," 1984.

[37]. Y. Zhang, Z. Zhao, and K. Chen, "Analysis and optimization of gap and misalignment in wireless power transfer systems," 2017.

[38]. J. L. Villa, J. Sallan, A. L. Osorio, and C. Batlle, "High-misalignment tolerant compensation topology for ICPT systems," 2012.

[39]. N. D. Madzharov, N. J. Hinov, and S. I. Shishev, "Impact of the misalignment on the efficiency of wireless power transfer," 2018.

[40]. S. Ahn and S. Hong, "Effect of misalignment and load variations on wireless power transfer for EV battery charger," 2015.

[41]. J. Lee and Y. Seo, "Adaptive frequency tuning of wireless power transfer system for efficient power transfer," 2016.

[42]. S. I. Babic and C. Akyel, "Improving the efficiency of wireless power transfer by using several resonators in series," 2015.

[43]. S. Y. Choi and S. Y. Jeong, "Robust wireless power transfer using defected ground structure," 2013.

[44]. Z. Bi and C. Mi, "Dynamic charging of electric vehicles by wireless power transfer," 2017.

[45]. ICNIRP, "Guidelines for limiting exposure to time-varying electric and magnetic fields (1 Hz to 100 kHz)," 2010.

[46]. M. H. Repacholi and B. Greenebaum, "Interaction of static and extremely low frequency electric and magnetic fields with living systems: Health effects and research needs," 1999.

[47]. ICNIRP, "Guidelines for limiting exposure to electromagnetic fields (100 kHz to 300 GHz)," 2020.

[48]. World Health Organization, "Electromagnetic fields and public health: Exposure to extremely low frequency fields," 2007.

[49]. W. Zhang and C. Mi, "Compensation topologies of high-power wireless power transfer systems," 2015.

[50]. C. Panchal, S. Stegen, and J. Lu, "Review of static and dynamic wireless electric vehicle charging system," 2018.

[51]. L. Soares and H. Wang, "A study on renewed perspectives of electrified road for wireless power transfer of electric vehicles," 2022.

[52]. *N. Korakianitis, A. Theodorakis, G. A. Vokas, G. Ioannides, and S. Kaminaris, "A Simulation Comparison and Evaluation of Wireless Power Transfer Methods and Topologies Applicable on Static and Dynamic Wireless Electric Vehicles Charging Systems," 2022.*

[53]. *Jon Are Suul, Giuseppe Guidi, "Technology for dynamic on-road power transfer to electric vehicles," 2018.*

[54]. *S. Laporte, G. Coquery, V. Deniau, A.De Bernardinis and N. Hautière, "Dynamic Wireless Power Transfer Charging Infrastructure for Future EVs: From Experimental Track to Real Circulated Roads," 2019.*

[55]. *T. M. Fisher, K. B. Farley, Y. Gao, H. Bai, and Z. T. H. Tse, "Electric vehicle wireless charging technology: a state-of-the-art review of magnetic coupling systems," 2014.*

[56]. *A. Sagar, A. Kashyap, M. A. Nasab, S. Padmanaban, M. Bertoluzzo, A. Kumar, and F. Blaabjerg, "A Comprehensive Review of the Recent Development of Wireless Power Transfer Technologies for Electric Vehicle Charging Systems," 2023.*

[57]. *Electreon Projects: https://electreon.com/projects.*

Παράρτημα Α

Tel Aviv University Station Project, Israel

Port of Karlsruhe (EnBW) Project, Germany